8-2009

Development of Improved Torsional Potentials in Classical Force Field Models of Poly (Lactic Acid)

James Mcaliley
Clemson University, jay.mcaliley@gmail.com

DEVELOPMENT OF IMPROVED TORSIONAL POTENTIALS IN CLASSICAL FORCE FIELD DESCRIPTIONS OF POLY (LACTIC ACID)

A Dissertation
Presented to
the Graduate School of
Clemson University

In Partial Fulfillment
of the Requirements for the Degree
Doctor of Philosophy
Chemical and Biomolecular Engineering

---

by
James Hodges McAliley
August 2009

Accepted by:
Dr. David A. Bruce, Committee Chair
Dr. Douglas E. Hirt
Dr. Robert A. Latour
Dr. Steven J. Stuart
Dr. Mark C. Thies

ABSTRACT

In this work, existing force field descriptions of poly (lactic acid), or PLA, were improved by modifying the torsional potential energy terms to more accurately model the bond rotational behavior of PLA. Extensive calculations were carried out using density functional theory (DFT), for small PLA molecules *in vacuo*, and also using DFT with a continuum model to approximate the electronic structure of PLA in its condensed phase. From these results, improved force field parameters were developed using a combination of the OPLS and CHARMM force fields. The new force field, PLAFF2, is an update to the previously developed PLAFF model developed in David Bruce's group, and results in more realistic conformational distributions during simulation of bulk amorphous PLA. It is demonstrated that the PLAFF2 model retains the accuracy of the original PLAFF in simulating the crystalline α polymorph of PLA. The PLAFF2 model has superior performance to any other publicly available force field for use with PLA; hence, we recommend its use in future modeling studies on the material, whether in its crystalline or amorphous form.

DEDICATION

This dissertation is dedicated to my father, John Eugene McAliley. When I was a kid, I thought my dad must be the smartest man in the world. Today, I still think so. I love you, Dad. Thanks for everything.

ACKNOWLEDGEMENTS

I am very grateful to Dr. David A. Bruce, my advisor, for giving me the opportunity to pursue this degree, and for giving me much-needed guidance along the way. Dr. Bruce has been extremely supportive, not to mention patient, during every step of this process. Thank you so much, Dr. Bruce.

I thank my mother, Linda G. McAliley, who has seen me through the many stages of my development—both personal educational. She has been, and remains, the most enduring constant in my life. Thanks, Mom. I love you.

I thank my wife, İlke E. McAliley, for being as loving and selfless as she is. She stayed by my side during this whole process, listened to all my frustrations, and shared in all my successes. Seni çok seviyorum, canım aşkım benim. Çok teşekkürler sana.

Thanks to my entire family, including the Erdoğan family, for their loving support.

Thanks to my dissertation committee members, for thoroughly reading this dissertation and helping improve it with their many constructive comments: Dr. Douglas E. Hirt; Dr. Robert A. Latour; Dr. Steven J. Stuart, and Dr. Mark C. Thies. Thank you all.

Thanks to the outstanding teachers I've had during my education. There are far too many to name them all, but I specifically thank Mr. V.M. Varner, who taught me to work hard at what I love, and Dr. J.M. Haile, who taught me the economy of thought.

Thanks to Dr. Scott M. Husson, who, in addition to being a skilled instructor, was instrumental in bringing me to graduate school.

Thanks to Dr. Christopher P. O'Brien, whose dissertation was indispensable as I carried out this work.

Corey Ferrier played a big role in getting my research underway. Under her wing, I learned the fine details of Linux and Unix systems. She is an extremely knowledgeable and helpful system administrator, whom I feel priveledged to have worked with.

Special thanks to the CCIT staff, especially the CITI group under direction of J. Barr von Oehsen. We are very lucky to have the level of support that they bring to Clemson computing. Thanks to Karl Lindekugel and Jerome Dugan for helping maintain the computer clusters in the Center for Advanced Engineering Fibers and Films (CAEFF).

Thanks to the vast community of open-source software developers who provided software tools used in this work, especially the following projects: GROMACS, TINKER, Visual Molecular Dynamics (VMD), and Ubuntu Linux.

My fellow researchers at Clemson and CAEFF have provided a wonderfully productive learning environment for my studies. In addition to Dr. Bruce's group, the research groups of Dr. Stuart and Dr. Latour have been kind to include me in their group meetings and discussions. Special thanks to Dr. Vikram Kuppa, Dr. Brad Dickson, Dr. Feng Wang, Galen Collier, Nadeem Vellore, and Ha Nguyen, for thoughtful discussions on theoretical and computational chemistry topics.

The Center for Advanced Engineering Fibers and Films (CAEFF) sponsored this research, through the ERC program of the National Science Foundation under Award Number EEC-9731680. I am indebted to my great country for such assistance.

TABLE OF CONTENTS

LIST OF TABLES

LIST OF FIGURES

CHAPTER ONE

INTRODUCTION

The purpose of this work is to improve the accuracy of existing models for simulating the molecular behavior of polylactide. Polylactide, also called poly(lactic acid) or PLA, is a widely used biocompatible polymer and is also one of the first bioderived polymers to be economically viable as a commodity plastic. It is readily synthesized from low-cost renewable feedstocks, such as corn, making PLA one of the few plastics that can be produced without the need for petroleum feedstocks [*1*]. An equally important aspect that sets PLA apart from petroleum-derived plastics is the timescale on which it biodegrades. Depending on the conditions, composted PLA can decompose into ecologically benign products with a half life of 10 weeks to 2 years, and this rate can be further controlled by the incorporation of comonomers and additives [*2*]. While some progress has been made in synthesizing biodegradable variants of petroleum-based synthetic polymers, for example poly(ethylene terephthalate) [*3*], such materials degrade into forms that are generally harmful to the ecosystem, and therefore, such processes are limited to recycling applications. In 2006, 59 billion pounds of plastic were generated as municipal solid waste in the United States alone, nearly half of which was in the form of packaging materials [*4*]. Overall, less than six percent of this plastic waste

was recovered for recycling. These figures give some indication of the importance of developing biodegradable plastics.

a.)

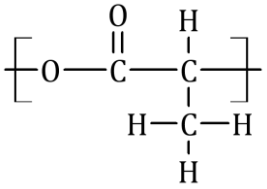

b.)

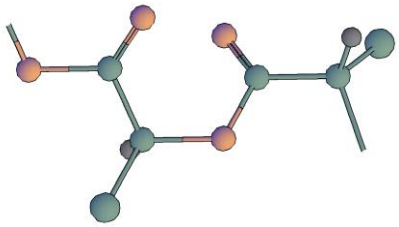

Figure 1.1. Molecular structure of polylactide (PLA). a.) chemical formula of the PLA repeat unit; b.) three-dimensional rendering of a chain segment.

As a result of its unique, environmentally advantageous properties, PLA has received much attention as of late. Commercial scale production has already begun for applications that include food packaging and apparel [*5*]. Additionally, PLA has for some time enjoyed wide applications in the biomedical field. It has a relatively high level of compatibility in human tissue, and its degradability makes it an excellent candidate for *in vivo* biomedical devices, such as absorbable sutures [*6*], tissue scaffolds [*7*], and drug delivery devices [*8*].

Pure, high-molecular-weight PLA is a colorless, rigid, lustrous, thermoplastic polymer, similar to polystyrene in physical properties [*1*]. Despite having these advantageous physical properties, PLA is not ideal for all commercial applications. Compared to its petrochemical derived competitors, PLA has a relatively high

permeability to gases and vapors, is brittle, and also exhibits a high level of creep under prolonged stress [*9*].

Given the shortcomings of PLA, for many applications, the use of additives [*10*], copolymers [*11*] or PLA blends [*11*] is required to achieve the desired material properties. Synthesis and testing of all of the possible combinations of additives, copolymers, and polymer blends is a time consuming and expensive process. Ideally, molecular-level models might be used for prescreening large numbers of proposed polymer systems for their physical and transport properties. In this way, variations that are likely to produce desirable properties may be identified before lab characterization begins. Molecular models might also be used as a tool for understanding the underlying causes that contribute to the behavior and properties of PLA, and such structure-property relationships would be vital to discovering other, improved biodegradable plastic materials.

Further, over the past several decades, molecular modeling has played an increasingly important role in bioengineering and biochemistry. Recent work, done here at Clemson, has shown that these models provide very effective tools in examining surface interactions between proteins and biomaterials [*12-14*]. With the already established use of PLA as a biomaterial, an improved model for PLA would prove very useful in this field.

Given the wide and varying needs for molecular level descriptions of PLA, it is striking that most of the available molecular models have not been well validated in

simulating this material. Molecular simulations are only as accurate as the underlying potential energy model, or force field, used. While many of the potential energy functions used in the field are generally parameterized for small ester molecules, very few have been used for α-polyesters, such as PLA. The α-polyester functionality is sufficiently unique that it requires special treatment in molecular models, since the α-carbon atom is bonded directly to an electron-withdrawing oxygen atom. This is not the case for simple (unpolymerized) esters, in which the α-carbon is usually bonded to alkane substituents. Therefore, when simulating PLA, the use of a model that was not developed for such α-polyesters is probably unwise.

The above discussion suggests that improved force field descriptions of PLA would be of great use to the scientific and engineering communities. Thus, this dissertation is devoted to developing such a model and applying it to PLA. This requires a solid understanding of the essential physics involved in polymer systems, as well as knowledge of the molecular modeling methods and numerical approaches in use today. Thus, Chapter Two focuses on some basic concepts from polymer science, molecular modeling, and numerical methods to lay this groundwork. Chapter Three then discusses some of the important prior work which has been done on molecular modeling of PLA, and Chapters Four and Five detail the development of our particular force field.

Force field parameterization can be a long and difficult process, especially for polymers, where much time is spent waiting for computer simulations to complete. During these periods of waiting, we have tried to anticipate, and address in advance,

problems which might arise in applying our force field to simulate PLA-based systems. Therefore, after making several recommendations for future work in the conclusion of this dissertation (Chapter Six), we include several detailed appendices outlining what we believe are the best current methods for studying gas diffusion and rheology of PLA. These properties are likely to be most relevant in considering PLA-based materials for commodity packaging applications and determining their processability.

CHAPTER TWO

BACKGROUND INFORMATION

This dissertation aims to improve the accuracy of existing models for simulating the molecular behavior of polylactide. As such, there are several different fields of science, engineering, and mathematics which need be applied to achieve this goal. These include some basic concepts from polymer and materials science, quantum mechanics, classical statistical mechanics, classical dynamics, and also mathematical optimization. In this chapter, we give an overview of the important concepts from these fields, which will be used throughout the remainder of this dissertation. Sections 2.1 through 2.3 provide additional background information on the polymer science, quantum and classical molecular modeling, and optimization concepts that are essential to this work. For the sake of completeness, we have chosen to present many of these concepts in some degree of detail; therefore, the reader may wish to skip to Chapter Three and refer back to this chapter only as necessary.

§ 2.1. Polymer Science

On the molecular level, linear polymers such as PLA are best described as long chainlike molecules. The chemical structure is made up of a repeating sequence of atoms, and typical industrial polymers will contain hundreds or even thousands of these repeat units linked in series [*15*]. Thus, molecular dimensions can be orders of

magnitude larger than atomic dimensions, and it is this fact that gives rise to the unique properties of polymers. Their large dimensions result in sluggish response, and relaxation times of polymers can be many orders of magnitude larger than typical liquid or solid chemicals [*16*].

Due to these large relaxation times, material properties of polymers are governed not just by the thermodynamics of the molecular systems (as is often the case for small molecules), but by a complex relationship between dynamics and thermodynamics. Some examples of properties affected by this relationship include: chain conformations, phase transitions, and transport coefficients. The complex interplay of thermodynamics and dynamics is ultimately determined by the polymer's chemical composition, which is often referred to as its *primary structure*. Thus, the primary structure of a polymer is what ultimately determines its properties, and one of the most useful tools a polymer scientist can have is knowledge of these so-called structure-property relationships.

Structure-property relationships can often be understood with the application of simple chemical intuition and heuristics, though sometimes, a detailed understanding of molecular level behavior is needed. When measurements at the molecular level are difficult to obtain, molecular simulation can provide key information in linking the properties of polymers to their primary structure. In this dissertation, we endeavor to develop the necessary models needed to accurately simulate PLA on the molecular level.

§ 2.1.1. Primary Structure

The word *polymer* originates from the Greek *poly*, which means 'many', and *meros*, meaning 'parts'. Thus, the lowest level of structure in a polymer is sometimes referred to as an individual *mer*, though its usage is not well standardized in the literature or in industry. Typically, the term *monomer* refers to the reactant(s) in a polymerization reaction [*17*], which suggests that one *mer* is equivalent to one reactant molecule. For PLA, this leads to confusion, since there are multiple routes to synthesizing the material (see Figure 2.1).

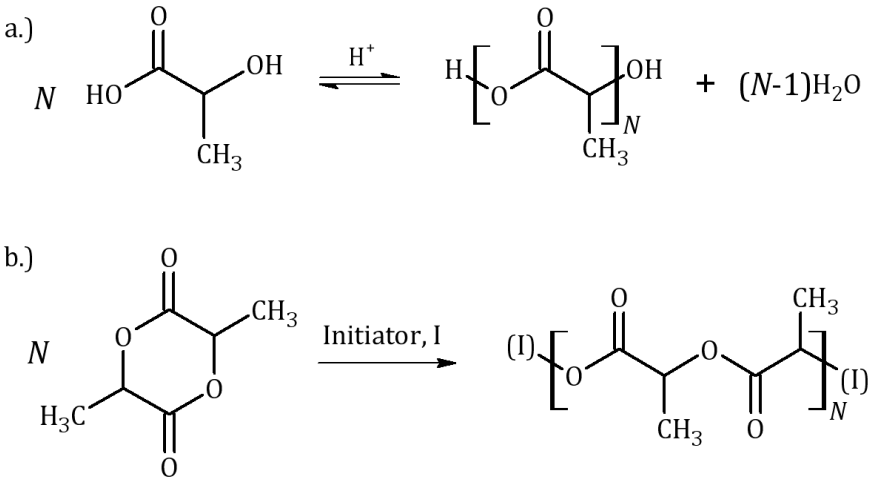

Figure 2.1. Synthesis routes for PLA. In scheme (a), the polymer is formed by condensation polymerization of lactic acid. In scheme (b), the polymer is synthesized via ring-opening polymerization from lactide. This is the origin of the differing names, poly (lactic acid) and polylactide. The products are chemically identical except for end groups.

In a step-growth synthesis, the monomer for PLA is lactic acid, forming poly (lactic acid). However, the step-growth process is generally unsuitable for producing high-molecular weight PLA, and on an industrial scale the plastic is synthesized using a chain-growth reaction. In this case, lactide, the six-membered ring formed upon the double condensation of two lactic acids, is the reactant in the polymerization proper, and thus, is also the monomer. Here arises the term *polylactide*, though polylactide is, essentially, chemically identical to poly (lactic acid) for all but its reaction history (one minor detail lies in the composition of the chain ends, which may contain the chain-growth initiator for polylactide but are hydroxy acids for PLA). In this dissertation, the terms poly (lactic acid), PLA, and polylactide are used interchangeably. However, to avoid confusion, the term *repeat unit* is preferred over monomer, since the repeat unit is unambiguously the nine-atom lactyl residue.

Another primary structure element that characterizes a polymer sample is the molecular weight distribution. In general, it is very difficult to synthesize polymers that have uniform molecular weight, and chain lengths in a polymer sample can vary from extremely long chains down to a single monomer. Thus, molecular weights are routinely reported in the literature as average values. There are two such average molecular weights commonly encountered ($\overline{M}_n$ and $\overline{M}_w$), as represented in the equations:

$$\overline{M}_n = \frac{\sum n_i M_i}{\sum n_i} \tag{2.1}$$

$$\bar{M}_w = \frac{\sum w_i M_i}{\sum w_i} = \frac{\sum n_i M_i^2}{\sum n_i M_i} \tag{2.2}$$

where the summations are taken over all chain lengths present in the sample. In Equation 2.1, the number-averaged molecular weight $\bar{M}_n$ is defined as a weighted average according to the number of chains, n_i, present in the sample for each length i, whereas in Equation 2.2 the weight-averaged molecular weight $\bar{M}_w$ is a weighted average according to the total weight w_i of all chains of length i. The second equality in Equation 2.2 demonstrates that $\bar{M}_w$ can be considered the second moment of the molecular weight distribution, while $\bar{M}_n$ is taken as the first moment. The ratio of these moments ($\bar{M}_w/\bar{M}_n$) is commonly referred to as the *polydispersity index*, which for industrially-produced PLA is approximately 1.4 [*18*].

The primary structure of a polymer is defined not only by the atomic makeup and number of its repeat unit(s), but by the way in which these units are arranged. Repeat units in linear polymers may be arranged in a head-to-tail or tail-to-head fashion, or some combination of the two. Since PLA is polymerized through the formation of an ester bond, the directional nature is inevitably head-to-tail.

The last primary structure element we will discuss involves stereochemistry. For polymers, such as PLA, whose repeat units are chiral, the sequence of stereoconfigurations is important. This primary structure element is referred to as *tacticity*, with *isotactic* denoting repeat units of identical stereoconfiguration, *syndiotactic* denoting an alternating sequence of stereoconfiguration, and *atactic*

signifying a random sequence [*19*]. The source of chirality in PLA is the α-carbon atom, which may have an optical activity of D (an IUPAC absolute stereoconfiguration of R) or L (IUPAC S). The biologically favored enantiomer is usually L, making essentially isotactic polymer commonly abbreviated as PLLA. Similarly, a PLA with an isotactic D arrangement is PDLA, and syndiotactic PLA is PLDLA. Atactic PLA is also easily synthesized. The tacticity of a polymer has implications for crystallization, with only the isotactic and syndiotactic chains being capable of forming crystallites [*19*].

§ 2.1.2. Unperturbed Chain Dimensions

A key molecular property for linear polymers is the unperturbed chain dimension. For polymers in disordered states, such as melts or amorphous rubbers and glasses, an individual chain can take configurations that are either compact or elongated. This property is generally governed by the balance of intermolecular and intramolecular interactions, though in most cases it is accepted that the intramolecular interactions due to angle bending and, particularly, bond rotation play a dominant role [*20*]. Polymers that are relatively stiff in terms of bond rotations tend to favor elongated conformations, while flexible chains favor more compact dimensions. Typical measures of chain dimensions include the radius of gyration, Kuhn length, and characteristic ratio. Each of these can be calculated from the other using simple conversions [*21*].

In this dissertation, all chain dimensions are reported in terms of the characteristic ratio, defined as:

$$C_\infty \equiv \lim_{n\to\infty} \frac{\langle r^2 \rangle}{nl^2} \tag{2.3}$$

where r is the end-to-end distance, taken between the first and last atoms in a polymer chain. The brackets denote a statistical ensemble average, n is the number of backbone bonds in the polymer chain, and l is the length of a single backbone bond [*22*]. In the case of polymers with heterogeneous backbone bond types, such as PLA, it is typical practice to average the backbone bond lengths to obtain a single representative value of l [*23*].

The characteristic ratio arises from the theoretical calculation, described by Flory [*24*], of the average end-to-end distance for a polymer having completely flexible angles and no energy barriers to bond rotation. In such a case, the numerator in Equation 2.3 is equal to its denominator. Thus, the characteristic ratio for real polymers has a lower bound of unity. A value of $C_\infty \cong 1$ suggests a very flexible polymer chain, and higher values suggest stiffer chains.

The characteristic ratio is also a function of temperature, and this dependence comes about due to the ensemble average in Equation 2.3. The brackets in the equation denote a weighted average of all conformational states of the polymer (i.e., bond rotation and angle values), with the individual weights of each state determined via statistical mechanics by its energy and the temperature at which the average is taken. Thus, depending on the energy characteristics of the polymer, C_∞ may increase or decrease with temperature.

The term *unperturbed* chain dimensions is used here to signify that the chain dimensions described by C_∞ are representative of the real conformations inside a bulk polymer under no external strain. This distinction is also needed because experimental methods for determining the characteristic ratio typically involve measurements in dilute solution rather than in the bulk, and alludes to the fact that the choice of solvent may influence the chain conformation. In dilute solution, single polymer chains are isolated. A good solvent for a particular polymer will result in larger chain dimensions, since favorable interactions will incite swelling [*19*].

Due to swelling effects, when measuring chain dimensions via dilute solution experiments, it is preferable to use a solvent that interacts with the polymer chains no more or less than the chains would with like chains. This condition is known as the θ *condition*; it is defined as a solvent composition and temperature which produces the same chain dimensions as a chain in the bulk polymer [*25*]. Each polymer-solvent pair has its own θ *temperature*, while often the term θ *solvent* is used for a solvent that produces the θ condition at or near room temperature. Ideally, dilute solution experiments for determining the unperturbed chain dimensions should be carried out under θ conditions. Unfortunately, the θ condition is by definition on the brink of precipitation for the polymer, making experiments difficult. In practice, measurements in a particular solvent are typically done at higher temperatures, then extrapolated to its θ temperature. This can be done, for example, using the graphical method of

Stockmayer and Fixman [*26*]. The reader is referred elsewhere for a more detailed discussion [*27*].

Estimation of unperturbed chain dimensions from dilute solution experiments can also be complicated by the presence of phase transitions. In the case of PLLA, for example, the tendency for single chains to form crystallites in dilute solution makes determination of the θ temperature problematic, since the crystallites precipitate out of solution before the amorphous polymer would precipitate upon lowering the temperature [*28*]. Glass transitions pose the same difficulty, which brings us to the next two topics: glassy and semicrystalline states of polymers.

§ 2.1.3. The Glass Transition

In an amorphous polymer, the glass transition occurs upon cooling below its *glass transition temperature*, or T_g. Simply put, this marks the region where the polymer changes from a rubbery state to a brittle, glassy state. The glass transition is not a first order thermodynamic phase transition, such as melting or boiling. It resembles a second-order transition, meaning that the volume and entropy are continuous, while their first derivatives exhibit discontinuity with respect to temperature [*29*]. However, observed values for T_g in a polymer will vary depending on the time scale on which the experiments are carried out, and since true second-order thermodynamic phase transitions must occur at fixed temperatures, the observable glass transition is not generally considered a true second-order transition either [*30*].

While the glass transition of polymers has not yet been cast into a single, unified theory, several prominent theories exist that generally fall under one of three categories: free volume theories, kinetic theories, and thermodynamic theories [*31*,*32*]. A brief discussion each of these follows.

§ 2.1.3.1. Free Volume Theories

The term *free volume* refers to the unoccupied spaces within the bulk of a polymer, which are large enough to allow local movement of atoms (see Figure 2.2) [*33*]. A simple analogy is the empty space in a sliding picture puzzle game, as shown in Figure 2.3. Since the individual tiles in the puzzle are constrained to the rectangular grid, motion may occur only if a tile moves into the empty space. This in turn leaves behind a new empty space, into which other units may move. Without the empty space, rearrangement of the tiles is impossible.

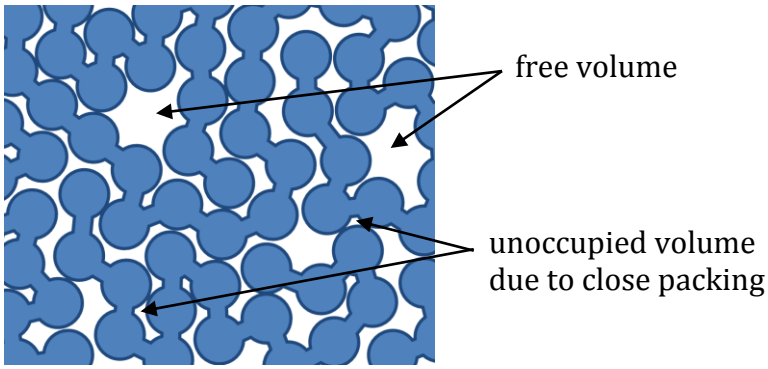

Figure 2.2. Schematic representation of free volume within a polymer. Indicated free volume regions are large enough for neighboring atoms to move into, whereas the indicated unoccupied volume regions occur due to normal random close packing.

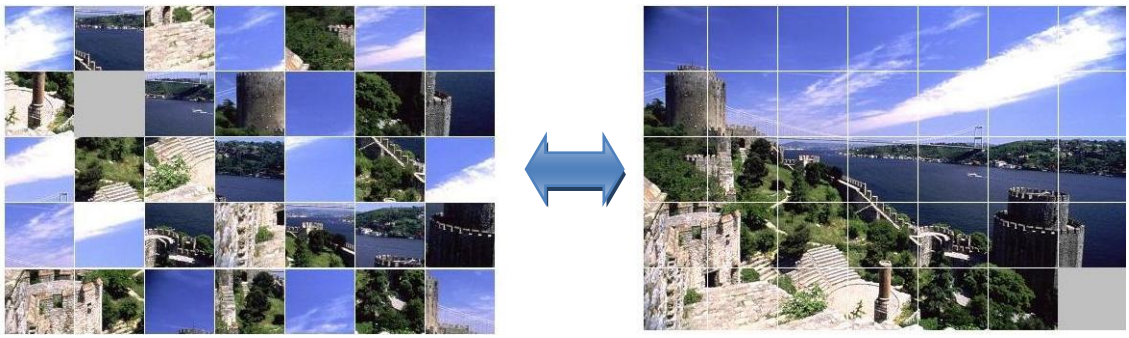

Figure 2.3. Example of a sliding picture puzzle. The empty tile (solid grey) is analogous to the concept of free volume in a polymer. Bulk movement is only possible through a series of local rearrangements, in which the free volume plays a key role.

It is generally accepted that polymers move about in a similar mechanism to the sliding puzzle analogy [*34*]. Movement of polymer chains occurs only when their atoms can find enough empty space in which the coordinated atomic motions necessary for a rearrangement may occur. In most free volume theories, it is hypothesized that the glass transition occurs when the empty spaces within a polymer become too small to allow local rearrangements. In many theories it is assumed that the glass transition marks the onset of an iso-free-volume state, and this is supported by experimental dilatometry measurements [*35-37*]. Without other means for movement, the atomic positions become trapped. Since the packing behavior of polymers is mainly determined by how neighboring atoms interact, one interpretation of free volume theories is that the intermolecular forces play a large role in determining the glass transition, and stronger interactions (more close packing) should result in higher values of T_g.

Free volume theories are well-supported by the success of models such as the Williams-Landel-Ferry (WLF) equation [*38*], which also incorporates kinetic considerations. The WLF equation may be written as:

$$\ln A_T = -\frac{(B/f_0)(T - T_0)}{f_0/\alpha_f + (T - T_0)} \tag{2.4}$$

where B is a constant, and f_0 is the fractional free volume at some reference temperature $T_0 \geq T_g$. That is, f_0 approximates the amount of volume in the bulk polymer that contributes to the free volume as defined in Figure 2.2, divided by the total volume of the system. The parameter α_f is the coefficient of expansion for the free volume, and T is the temperature of interest (also greater than T_g). The *reduced variables shift factor*, A_T, can be any dynamic quantity, taken as a ratio over the reference value. In the most common application of Equation 2.4, A_T is set to the ratio of shear viscosities, η/η_0. In Chapter Five of this work, A_T will be used as a ratio of observation time scales, t/t_0, to facilitate comparison between simulation results and experiments. This proves an invaluable tool, since the time scales in atomistic molecular dynamics and experiments can differ by ten orders of magnitude or more, and polymer behavior is highly dependent on the time scale of the observation.

The WLF model, as written in Equation 2.4, follows directly from the Doolittle equation [*39*] if the free volume is assumed a linear function of temperature. An interesting result of the WLF equation is that its constants are almost invariably the same for all linear polymers, when T_0 is taken as T_g. The values $B/f_0 = 40.16$ and

$f_0/\alpha_f = 51.6$ are taken as universal constants when temperature is specified in °C or K [*40*,*41*]. Thus, as a rule of thumb, a decade decrease in A_T will result in an increase in T_g of about 3 to 4 °C. The effect on T_g may be more pronounced for lower values of A_T. If the constant B is taken as unity (as supported by the data of Doolittle [*39*]), the universal parameters correspond to a fractional free volume of 2.5%. Thus, in free volume theories, 2.5% is commonly interpreted as the critical free volume which causes an onset of the glass transition. Of course, such estimates are dependent on how one defines the free volume and excluded volume, which can differ by an order of magnitude.

§ 2.1.3.2. Kinetic Theories

In kinetic theories of the glass transition, it is assumed that some sort of energy barrier to molecular motion causes trapping of atoms in their local positions. Consider, for example, the two-state glass-forming system shown in Figure 2.4. This imaginary system has a single coordinate along which relaxation may occur, and the potential energy of the system is shown along that coordinate in Figure 2.4a. The system has two potential energy minima, labeled State I and State II, which are separated by some potential energy barrier. The relaxation process, by which the system moves towards its equilibrium state, is governed by the thermal energy of the system, as well as by the observation time scale, t_{obs}. As shown in Figure 2.4b, the spatial probability distribution at equilibrium (plotted as smooth curves) is bimodal for our two-state system, and the

relative probabilities for the two states are a function of temperature. Lower temperatures favor the low energy state, State I, over State II, and at higher temperatures the distribution approaches equal probabilities for all states.

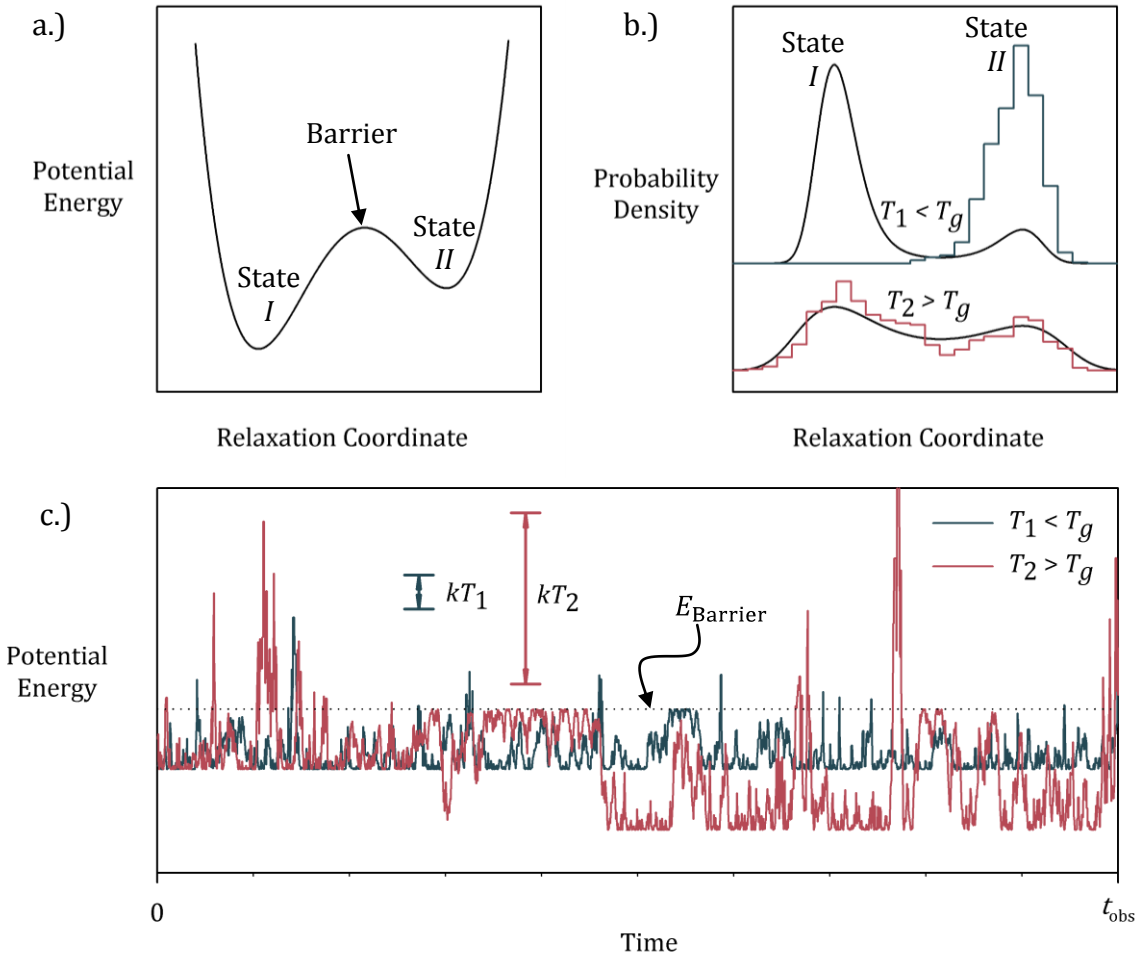

Figure 2.4. Example of a glass forming system with potential energy shown in (a). Histograms in (b) are probability distributions accumulated during an observation time t_{obs}; smooth curves calculated for the system at equilibrium. Plot (c) shows energy fluctuations during the t_{obs} used in (b); dotted line indicates the energy of the barrier.

We see from Figure 2.4b that, at some sub-glass temperature $T_1 < T_g$, our imaginary two-state system becomes trapped in one of the two states. In the figure, the system is trapped in State II, even though the equilibrium distribution requires the system to spend some appreciable amount of time in its other state. This trapping phenomenon disrupts the equilibrium properties of the system, and is the cause of the glass transition. Below T_g, the system has less thermal energy to overcome the barrier and move between its states. In contrast, when the system is at $T_2 > T_g$, the higher amount of thermal energy fluctuations results in a higher likelihood of barrier crossing events. This allows the system to more frequently move back and forth between States I and II, and results in a time-averaged probability distribution much closer to that for the system at equilibrium.

Clearly, the concept of the glassy state, and also the concept of equilibrium, cannot be decoupled from the timescale on which an observation is made. Indeed, the temperature at which the glass transition is observed will depend on the time scale of the observation. For a well-thermalized system (i.e., a system in contact with an energy reservoir), even at very low temperatures there is a small but finite probability that the system could obtain enough potential energy for a barrier crossing event to occur. If one could allow the system enough time for many such events to occur, the long-time average distribution of states would approach the equilibrium distribution. Conversely, even for systems at very high temperatures, reducing the observation time will at some point make the observation of barrier crossings unlikely. For example, if t_{obs} were

reduced to one fourth its value in Figure 2.4c, the system at T_2 would appear to be as glassy as the system at T_1—that is, its observed probability distribution would be just as far from equilibrium.

In kinetic theories of the glass transition, it is recognized explicitly that the glass transition occurs when the relaxation time of chain motion is of the same order of magnitude as the experimental time scale. As in the discussion above, an assumption of the physical type of barrier that causes the kinetic trapping does not play a pivotal role in kinetic theories, as it does in free volume theories. However, in the context of kinetic theory, the glass transition is often thought to be brought about by energy barriers due to bond rotation, since this is the primary mode of molecular movement in polymers. This discussion suggests that the time scale of a molecular simulation will be an important factor in determining T_g, and the occurrence of a glass transition in simulation should be analyzed to determine exactly what type of energy barriers are causing the behavior.

§ 2.1.3.3. Thermodynamic Theories

Thermodynamic theories also exist to explain the glass transition in polymers. These contend that a true second-order glass transition exists at some low finite temperature, but because polymers approach equilibrium very slowly, the transition is observable only over extremely long (near infinite) time scales [*19*]. While these theories are important in reconciling certain paradoxes when considering the entropy of

the glassy state as compared to an ideal crystal, they are of little practical use and hence, are not discussed here further.

§ 2.1.3.4. Summary

In summary, the glass transition in polymers occurs when the molecules become trapped in some local state. It is thought to be affected by two main factors: the packing behavior of amorphous chains due to intermolecular interactions, and energetic barriers to bond rotation. The observed glass transition temperature also depends on the time scale in which an experiment is performed, though if WLF parameters are known for the polymer, T_g may be estimated over a wide range of time scales.

§ 2.1.4. Semicrystalline Polymers

Many polymers are able to crystallize, though extended long range order is not possible under normal conditions as it is for other substances, such as metals. In polymers, crystallization usually results in a hierarchical morphology, as shown in Figure 2.5 [*42*,*43*]. At the lowest level is the lattice arrangement of atoms, which can be determined via wide angle X-ray diffraction (WAXD), among other methods. Typical crystalline conformations for linear polymers include extended (all backbone bonds *trans*) chains, as is the case for polyethylene, or close-packed helices as found in isotactic polypropylene. Often, there are multiple stable crystalline packing arrangements for a polymer, resulting in polymorphism. This is the case for PLA, which forms at least three identifiable polymorphs in addition to the stereocomplexed crystal

observed in blends of PLLA and PDLA [*44*]. The atomic arrangement of the most stable polymorph of PLA (commonly referred to as the α-crystal structure) is thought to be a 10/3 helix, meaning that ten repeat units make exactly three complete turns of the helix [*45*]. This structure can be viewed perpendicular to the helical axis in Figure 2.5a.

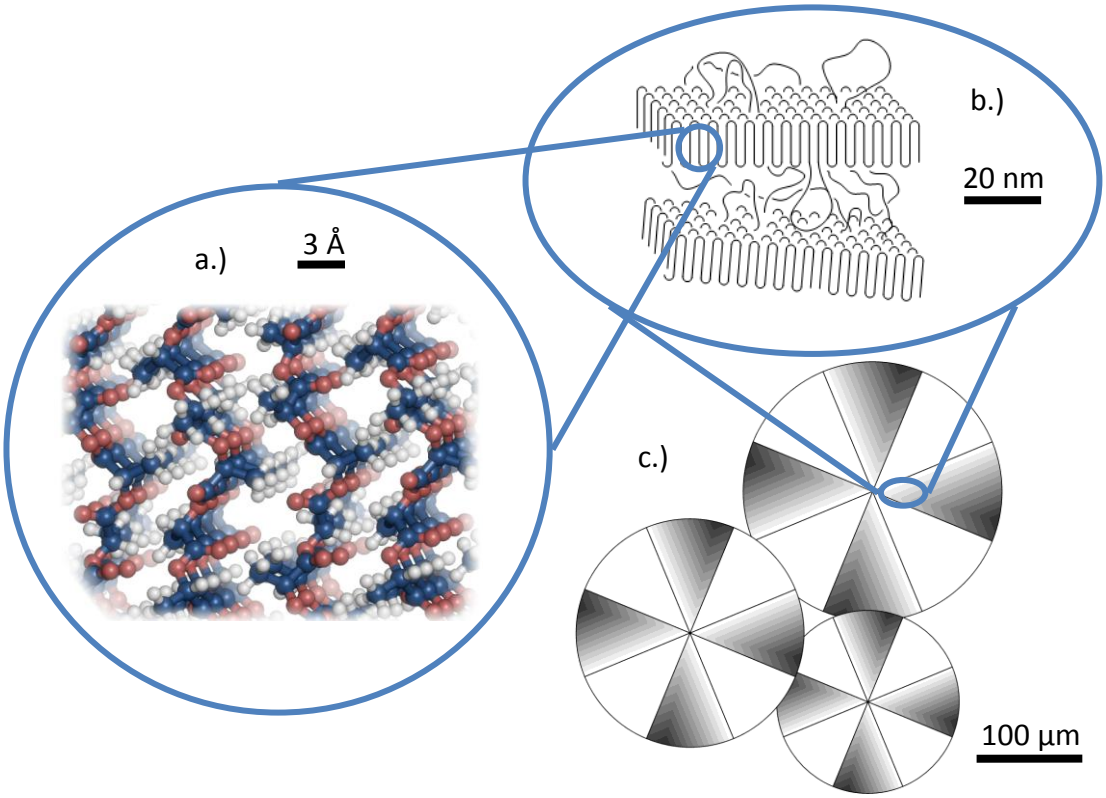

Figure 2.5. Differing levels of morphology in semicrystalline PLA. Inset (a) shows the crystalline lattice on the atomic level; (b) represents the incorporation of crystal packings into chain-folded lamellae; (c) shows the grouping of lamellar sheaths to form spherulites, as they would appear in an optical micrograph. Length scales shown are approximate.

Like the glass transition, the amorphous to crystalline phase transition in a polymer is influenced by kinetic factors as much as it is by thermodynamics. One manifestation of this interchange is the lamellar and spherulitic formation depicted in Figure 2.5b and 2.5c. The most thermodynamically stable configuration of PLA chains would require each chain to adopt a uniform helix throughout its entire length. This would result in the type of long-range order that would occur, for example, if the helices in Figure 2.5a extended infinitely in the vertical direction. However, this arrangement would require some extraordinarily concerted movements of chains, which are physically unrealistic except under extreme stress. Thus, the kinetics of molecular motion demand a compromise, which is thought to occur by chains folding back on themselves, and this is the origin of the chain-folded lamellae depicted in Figure 2.5b.

Authors differ in describing the exact details of lamellar structures, and while this might have bearing on later computational work, such details are not important to this dissertation. For example, the cartoon description of Figure 2.5b probably favors adjacent reentry of chains into the lamellae; however, small angle neutron scattering data suggest more of a switchboard-type configuration tends to occur [*46*]. These matters have been examined in computational studies of isotactic polypropylene, by our colleagues in the Center for Advanced Engineering Fibers and Films (CAEFF) [*47*]. Hence, in later work, one suggested use of the force field model developed in this dissertation is to apply it in conjunction with the methods of Kuppa and Rutledge, for studying the lamellar/interlamellar structure of PLA.

For this work, the important implication of crystalline lamellae formation is its bearing on the observed melting temperature in semicrystalline polymers. In Chapter Five, we will test our force field model to determine how well it estimates the melting temperature of a completely crystalline sample of PLA. Thus, our simulations deal with the ideal, fully extended crystal conformation, and this exhibits melting behavior that is different from real semicrystalline PLA samples. In real samples, the amorphous-crystalline interfacial surface area created by lamellar formation results in an effective lowering of observed melting points, or a melting point depression. This is described by Thompson's rule [*48*]:

$$T_m = T_m^\circ \left(1 - \frac{2\sigma_e}{l\Delta h_f}\right) \tag{2.5}$$

where T_m is the observed melting temperature, T_m° is the melting temperature of the ideal crystal, and Δh_f is the enthalpy of fusion per unit volume crystal. The parameters l and σ_e are the lamellar thickness and the fold surface free energy. Thus, when comparing to experimental results, one can account for the difference in observed and simulated melting temperatures using Equation 2.5.

§ 2.1.5. Sorption

Water uptake is an important process for biodegradation of PLAs, and this is best described in terms of its solubility. The solubility of a penetrant species, i, in a polymer is typically given by:

$$\mathcal{S}_i = \frac{V_i}{VP_i} \tag{2.6}$$

where the volume of penetrant species in the numerator is taken at standard temperature and pressure (STP), which is $273.15\ \mathrm{K},\ 1.013 \times 10^5\ \mathrm{Pa}$. The volume, V, corresponds to the volume in the polymer, and the pressure in the denominator, P_i corresponds to the partial pressure of the penetrant in the gas phase. Equation 2.6 must be evaluated for a system in equilibrium. Solubility is largely dependent on the size of the penetrant in relation to the amount of free volume present in the polymer. The concept of free volume was discussed previously in reference to the glass transition; see, for example, Figure 2.2. Hence, in glassy polymers, solubilities tend to be much lower than in elastomers (the term *elastomer* simply refers to an amorphous polymer above its T_g).

The solubility $\mathcal{S}$ in Equation 2.6 can be viewed as a form of the Henry's Law constant encountered in conventional solution thermodynamics. It gives the equilibrium concentration of a solute in relation to its partial pressure in the gas phase. In addition to the requirement that the temperatures and pressures must be equal in both phases, the equilibrium condition is achieved when:

$$\mu_i^g = \mu_i^p \tag{2.7}$$

where μ_i^g is the chemical potential of the penetrant (species i) in the gas phase, and μ_i^p is the chemical potential of species i immersed in the polymer. Since μ_i^p is a function of

the concentration of i in the polymer, a system out of equilibrium will adjust that concentration until Equation 2.7 is satisfied.

In polymers, the variation of μ_i^p with concentration can be much more complex than the chemical potential in liquid solutions, since penetrants often act as plasticizers (specifically meaning they bring about a lowering of T_g). Thus, in a glassy polymer such as PLA, at some point the addition of more i will bring T_g below ambient conditions, resulting in a dramatic increase in solubility. Additional complexity is brought about simply by the size of polymer molecules, and special theories are needed to study phase behavior in polymer-solute systems. Perhaps the most well-known example of these is the Flory-Huggins theory, which is described in detail in most polymer science texts [*15*,*16*,*19*].

Equation 2.7 allows the solubility to be estimated through molecular simulation, since various methods exist for evaluating the chemical potential μ_i^p (See Appendix A). The enthalpy of solution may also be estimated from simulation methods, and is related to the solubility through the Clausius-Clapeyron equation:

$$\Delta H_s = -R \frac{d \ln \mathcal{S}}{d(1/T)} \tag{2.8}$$

where ΔH_s is the enthalpy of solution evaluated at temperature T, and R is the ideal gas constant. Often, experimental solubilities are measured over a range of temperatures, and Arrhenius plots are constructed to report an apparent activation energy. From

Equation 2.8, it is apparent that the apparent activation energy exhibited by such a plot is the enthalpy of solution ΔH_s.

§ 2.1.6. Diffusion

The permeability of polymers to small molecules is of importance in consumer packaging, as well as other applications, such as membrane separations and controlled release of pharmaceuticals. For example, it might be desired for a polymer to totally block the flux of permeants, as to prevent the introduction of oxygen into a food package, while also thwarting the escape of water. In contrast, for drug release applications, the achievement of a specific, finite diffusion rate may be desired, rather than the complete barriers preferred for food packaging. For membranes, on the other hand, a complete barrier may be desired for some chemical species while allowing other species to pass through freely. The tuning of these properties typically depends on the polymer architecture, composition, and processing conditions used to create the material.

The permeability, $\mathscr{p}$, of a polymeric material to a particular permeant species is usually expressed in terms of the permeant's solubility and diffusivity in the polymer:

$$\mathscr{p} = D \cdot \mathcal{S} \tag{2.9}$$

where D represents the diffusivity and $\mathcal{S}$ the solubility of the permeant species in the polymer, as in Equation 2.6. The permeability relates the amount of permeant flux (flow

per unit area per unit time) to the film thickness and partial pressure difference across the film. The most common units used for $\mathscr{p}$ are:

$$\mathscr{p}\ [=]\ \frac{(\mathrm{cm}^3\ \text{permeant})(\mathrm{cm})}{\mathrm{cm}^2 \cdot \mathrm{Pa} \cdot \mathrm{s}} \tag{2.10}$$

where again the volume of permeant species is taken at STP conditions. Typical values of $\mathscr{p}$ are approximately $10^{-12}\ \mathrm{cm}^2/(\mathrm{Pa} \cdot \mathrm{s})$ for elastomers, and can be as low as $10^{-16}\ \mathrm{cm}^2/(\mathrm{Pa} \cdot \mathrm{s})$ for glassy polymers.

The diffusivity in Equation 2.9 is defined in the regular Fickian sense. Fick's first and second laws are written for an isotropic system as follows:

$$\mathbf{J} = -D\boldsymbol{\nabla}c \tag{2.11}$$

$$\frac{\partial c}{\partial t} = \boldsymbol{\nabla} \cdot (D\boldsymbol{\nabla}c) \tag{2.12}$$

where 2.11 applies to the steady state and 2.12 applies to transient states. In the above equations, $\mathbf{J}$ is the flux, c is the concentration of the diffusing species, t is time, and $\boldsymbol{\nabla}$ is the gradient operator. In equations 2.11 and 2.12, the flux and concentration must be defined consistently; for example, if the concentration is expressed on a mass basis, the flux must be defined relative to the center-of-mass streaming velocity (see reference [*49*] for a useful discussion). For diffusion in one dimension, as is usually the case for polymer films, solution of Equation 2.12 in a Cartesian coordinate system leads to the expression of mass uptake over time:

$$\frac{M}{M_\infty} = k_n t^n \tag{2.13}$$

where M is the mass uptake at time t, and M_∞ is the equilibrium uptake. The parameters k_n and n are constants, with $n = \frac{1}{2}$ when Equation 2.12 is followed (Fickian diffusion). In glassy polymers, however, the observed value of n may often be equal to 1, which is classified as *non-Fickian Case II* diffusion. Concentration profiles are shown in Figure 2.6 for Fickian and Case II non-Fickian diffusion. Diffusion resulting in mass-uptake profiles with $\frac{1}{2} < n < 1$ is termed *anomalous diffusion*.

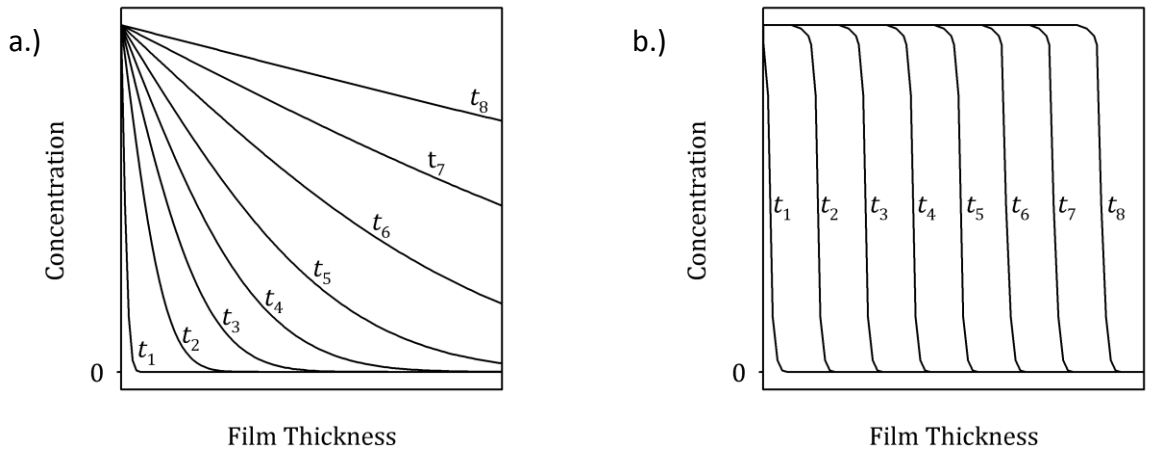

Figure 2.6. Time-dependent concentration profiles typical of transient diffusion through polymer films; a.) Fickian diffusion in an elastomer; b.) Case II non-Fickian diffusion in a glassy polymer. In each case, curves are listed in order of increasing time, i.e., $t_1 < t_2 < \cdots < t_8$.

Non-Fickian behavior in the Case II regime is a result of the fact that D, much like S, is very low for glassy polymers, and it increases drastically upon heating above T_g. Because permeants tend to plasticize glassy polymers, a moving front effect is produced as T_g falls below ambient temperature in regions of increased permeant concentration. This causes the polymer to swell in the plasticized regions, which occurs very fast compared to the rate of diffusion into the glassy region beyond the moving front. It has been noted in the experimental literature that PLA exhibits non-Fickian diffusion at ambient temperatures [*50*]. An understanding of this mechanism is important when comparing simulated diffusion phenomena with experimental results, since conventional methods of simulation are designed for use with constant density systems and employ the Fickian diffusion model. Thus, a proper treatment of gas diffusion in PLA would need to include swelling studies, as well as specialized methods to treat diffusion in glassy materials (see, for example reference [*51*]).

§ 2.1.7. Flow and Rheological Properties

This section concludes the review of polymer science with a discussion of the rheological properties of polymers. From understanding their flow behavior, we may develop a quantitative description of how molecular weight can influence properties, and also define more exactly the concept of relaxation times. The relations presented here will give much insight for interpreting simulation results in later chapters.

The common theme presented in Sections 2.1.1 to 2.1.6 is that the large dimensions of polymer molecules result in physical behavior remarkably different than

ordinary, low molecular weight liquids and solids. This fact is probably most obvious when examining the flow behavior of polymers, since the slow response of polymer molecules results in highly viscous fluids. In what follows, the generalized Newtonian definition of viscosity is adopted, which appears in the equation:

$$\boldsymbol{\tau} = \eta \dot{\boldsymbol{\gamma}} \tag{2.14}$$

where $\boldsymbol{\tau}$ is the stress tensor, $\dot{\boldsymbol{\gamma}}$ is the rate of strain tensor, and η is the generalized Newtonian viscosity, which may depend on $\dot{\boldsymbol{\gamma}}$.

At low molecular weights, the viscosity of a linear polymer increases with the number of backbone atoms as [*19*]:

$$\eta = K_L Z_w^{1.0} \tag{2.15}$$

This equation applies at the zero shear limit, where K_L is a constant and Z_w is the weight-averaged number of backbone atoms, which can be calculated from $\overline{M}_w$ and a knowledge of the primary structure. At higher molecular weights, interchain entanglement occurs and increases the order of chain length dependence to [*19*]:

$$\eta = K_H Z_w^{3.4} \tag{2.16}$$

where a separate constant K_H applies in the high molecular weight regime, and again the equation is valid in the limit of zero shear rate. Equation 2.16 is an empirical relation; theoretically, it has been reasoned that the exponent should be 3.0 rather than 3.4, though this is only true in the limit of infinite molecular weight [*19*]. The critical value of backbone atoms, beyond which Equation 2.16 must be applied in place of 2.15,

is about 300 to 500 atoms for typical polymers. This is referred to as the critical chain length, $Z_{w,c}$, and for PLA occurs near 375 main chain atoms ($\overline{M}_w \approx 9000$ g/mol) . The usual scaling factor of 3.4 has been confirmed to apply to PLA, within the experimental uncertainty of rheological measurements [*52*]. According to the data of Palade et al., the high-molecular weight scaling constant K_H is approximately $2.2 \times 10^{-9}\ \mathrm{Pa \cdot s}$ for linear PLA [*52*].

In addition to their high viscosities, polymers exhibit other flow behavior which cannot be captured by Equation 2.14, due to *viscoelasticity*. The term viscoelasticity refers to the behavior of a material whose response to external stresses is somewhere between that of a Hookean solid and a viscous fluid. This is demonstrated in Figure 2.7, considering the response of a viscoelastic fluid to two types of perturbations. Figure 2.7a shows the typical strain response to a step change in stress, while Figure 2.7b shows the response of stress to a step change in strain. For the viscoelastic fluid in Figure 2.7a, initially, the strain shows a step-like, nearly vertical response as expected of a completely elastic solid. However, the strain continues to increase while the stress is applied, and after the stress is released, it slowly relaxes to some value that is nonzero (permanent deformation). In Figure 2.7b, the viscoelastic fluid initially exhibits an overshooting stress, followed by relaxation processes in which the stress decreases. Upon forcing the sample back to its initial dimensions, the viscoelastic fluid resists initially, and ultimately reaches a stress value of zero. The combination of elastic and viscous properties illustrated in Figure 2.7 is best conceptualized in terms of springs

(representing purely elastic elements) and dashpots (purely viscous). These are represented, in various combinations, in Figure 2.8.

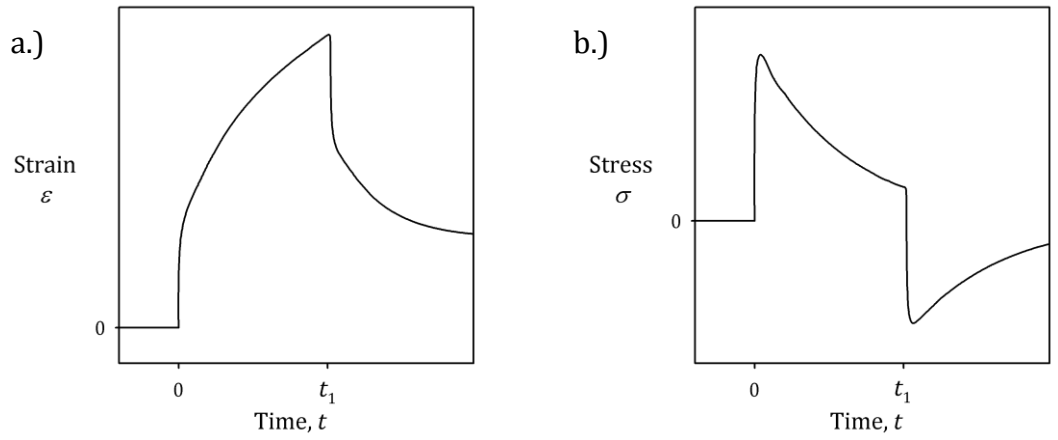

Figure 2.7. Qualitative description of a viscoelastic material's a.) strain response to a step change in stress, and b.) stress response to a small step change in strain. In each case, a positive step change is initiated at time 0 and released at time t_1.

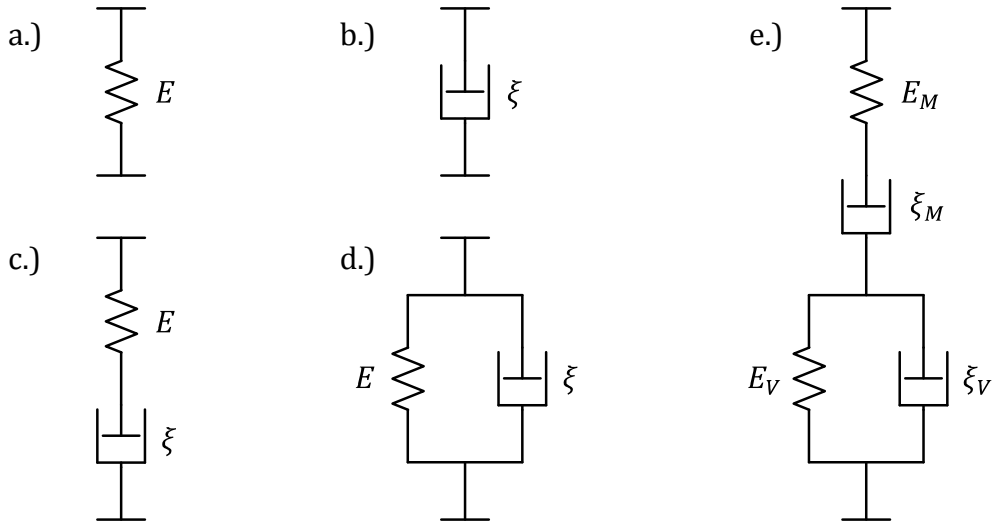

Figure 2.8. Spring and dashpot models; a.) an ideal spring; b.) an ideal dashpot; c.) Maxwell element; d.) Voigt element; e.) combined Maxwell-Voigt element.

The differential equations associated with the spring and dashpot models are as follows. For an ideal spring:

$$\frac{d\varepsilon}{dt} = \frac{1}{E}\frac{d\sigma}{dt} \tag{2.17}$$

where ε is the strain, E is the spring's modulus of elasticity, and σ is the normal stress. For an ideal dashpot, the relevant equation is:

$$\frac{d\varepsilon}{dt} = \frac{\sigma}{\xi} \tag{2.18}$$

with ξ being the viscosity coefficient of the dashpot. Combining these elements in series, *i.e.*, summing their strains, gives the Maxwell model:

$$\frac{d\varepsilon}{dt} = \frac{1}{E}\frac{d\sigma}{dt} + \frac{\sigma}{\xi} \tag{2.19}$$

If the elements are taken in parallel, *i.e.*, equating their stresses, the Voigt model is obtained:

$$\frac{d\varepsilon}{dt} + \frac{E\varepsilon}{\xi} = \frac{\sigma}{\xi} \tag{2.20}$$

Finally, a series of Maxwell and Voigt elements is governed by the simultaneous equations:

$$\frac{d\varepsilon}{dt} = \frac{1}{E_M}\frac{d\sigma}{dt} + \frac{\sigma}{\xi_M} + \frac{1}{\xi_V}[\sigma - E_V\varepsilon_V] \tag{2.21}$$

$$\xi_V \frac{d\varepsilon_V}{dt} + E_V \varepsilon_V = \sigma \tag{2.22}$$

where subscripts define the parameters for the Maxwell and Voigt portions as in Figure 2.8e, and a separate strain ε_V is defined over the Voigt portion of the model.

The qualitative response of the combined spring and dashpot models to step changes in stress and strain are plotted in Figure 2.9, for comparison with the behavior shown in Figure 2.7. The best agreement is obtained by the four-parameter model, illustrated in Figure 2.8e and Equations 2.21 and 2.22. The series of Maxwell and Voigt elements captures the initial elastic response, retarded elastic response, elastic recovery, and permanent deformation of a real viscoelastic fluid.

The physical significance of each element in the four-parameter model is described by Edie [*53*], whom we paraphrase here. Referring to Figure 2.8e, the Maxwell spring stiffness parameter, E_M, represents the elastic straining of the valence angles and bond lengths within the backbone of a polymer chain. The stiffer the spring (higher E_M), the more resistance the polymer has to this type of deformation. The viscosity coefficient in the Maxwell dashpot, ξ_M, corresponds to the friction brought about by the chains slipping past one another during flow. This is the predominant factor governing the material flow. The Voigt element, in the lower portion of Figure 2.8e, is physically interpreted as the mechanism by which the polymer chains rearrange their conformations. The Voigt spring, with stiffness E_V, represents the tendency of the chains to reorient thermally when perturbed from their random coil dimensions. In a

related fashion, the Voigt dashpot, with viscosity coefficient ξ_V, opposes the coiling or uncoiling away from the unperturbed chain dimensions.

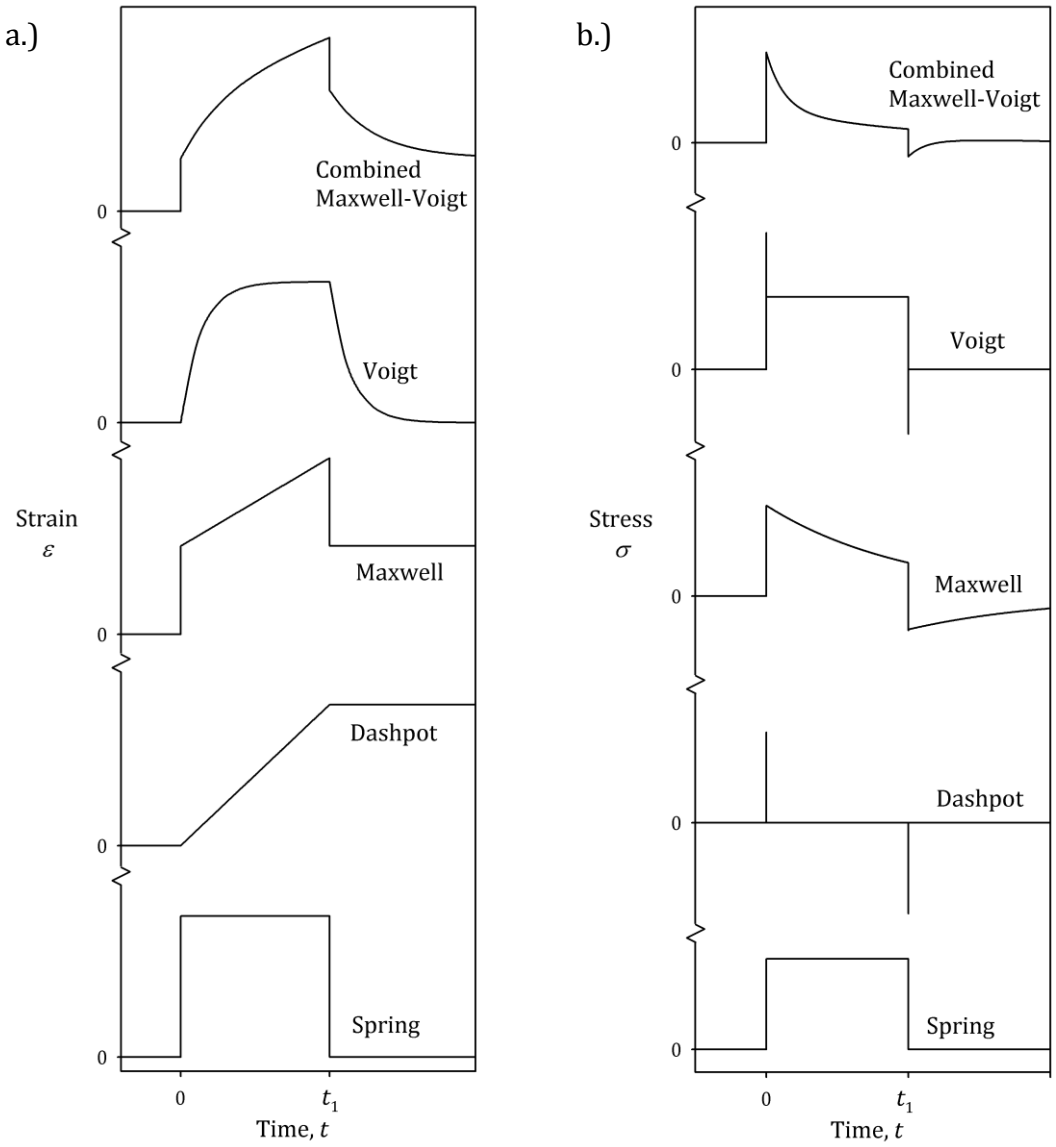

Figure 2.9. Qualitative response of spring and dashpot models to step changes in stress (a) and strain (b). In each case, the step change occurs from time $t = 0$ to $t = t_1$. In graph (b), vertical lines represent delta functions.

For the stress step change scenario, assuming an initial strain of zero, the analytical solution of Equations 2.21 and 2.22 is:

$$\varepsilon = \begin{cases} \frac{\sigma_0}{E_M} + \frac{\sigma_0 t}{\xi_M} + \frac{\sigma_0}{E_V}\left(1 - e^{-\left(\frac{t}{t_V}\right)}\right), & 0 \le t < t_1 \\ \frac{\sigma_0 t_1}{\xi_M} + \frac{\sigma_0}{E_V}\left(1 - e^{-\frac{t_1}{\tau_V}}\right) e^{-\left(\frac{t-t_1}{t_V}\right)}, & t \ge t_1 \end{cases} \tag{2.23}$$

where $t_V = \xi_V / E_V$.

A similar exponential decaying response is shown for the relaxation of the stress during an applied strain, ε_0, for the Maxwell model. In this case, the response is given by

$$\sigma = \varepsilon_0 E_M e^{-\left(\frac{t}{t_M}\right)} \tag{2.24}$$

with $t_M = \xi_M / E_M$.

Equations 2.17 through 2.24 provide a simplified mathematical view of viscoelastic fluids, using single variable mathematics. For most engineering applications, such as flow modeling, a tensor description is needed, such as the Oldroyd [*54*] or Geisekus [*55*,*56*] models. However, for the purpose of this dissertation, the spring and dashpot models serve as an efficient and intuitive tool, allowing us to obtain a quantitative understanding of relaxation and retardation times in polymers. These arise through the exponential relaxation terms in Equations 2.23 and 2.24. Particularly, the time constant t_V is referred to as the *retardation time*, and corresponds to the amount of time needed for chains to adjust their random coil dimensions under stress [*53*]. On the other hand, the time constant arising from the Maxwell element, t_M is called the

relaxation time, and relates to the time needed to relieve stress by chain slippage. Quantitatively, for each case, its particular mode is restored to 63% of its equilibrium condition after one time constant has passed, and reaches 95% by three time constants.

The relaxation and retardation times of polymers may be determined from experiments, though oscillatory perturbations are more useful than the conceptually simple step changes discussed above. Common approaches include dynamic mechanical analysis (DMA), torsional braid analysis (TBA), and thermal dynamic mechanical analysis (TDMA). Equivalent results can be obtained using electromagnetic perturbations, and dielectric relaxation spectroscopy (DRS) is another popular method. Here, we discuss the oscillatory methods in terms of a mechanical perturbation. In a typical forced oscillation experiment, a time-dependent shear stress is imposed according to:

$$\tau = \tau_0 \sin(\omega t) \tag{2.25}$$

where τ is the instantaneous shear stress, τ_0 is the maximum shear stress, and ω is the applied oscillation frequency. The strain response is measured, taking the general form:

$$\gamma = \gamma_0 \sin(\omega t - \delta) \tag{2.26}$$

Here, γ is the instantaneous shear strain, γ_0 is the maximum shear strain, and δ is the phase angle. For completely elastic solids, the strain will be in phase with the stress, and $\delta = 0$. For a completely viscous fluid, $\delta = 90°$. Because the instantaneous stress is not necessarily proportional to the instantaneous strain, it is useful to define the shear modulus in complex notation:

$$G^* = G' + iG'' \tag{2.27}$$

where the real component G' is the *storage modulus*, i is the unit imaginary number, and the imaginary component $G''$is the *loss modulus*.

Typical experimental sweeps show five regions of viscoelastic behavior in linear polymers, as shown in Figure 2.10. Starting from high frequencies and moving to low frequencies, the material begins by exhibiting a glassy response, then enters an apparent glass-rubber transition region, followed by the rubbery plateau, the rubbery flow region, and finally the melt flow region. In Figure 2.10, the storage modulus is plotted for each of these regions.

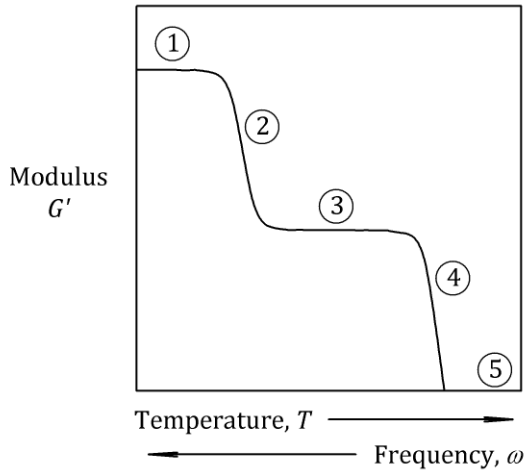

Figure 2.10. The five regions of viscoelastic behavior in linear amorphous polymers: 1.) Glassy state; 2.) Glass-rubber transition; 3.) Rubbery plateau; 4.) Rubber flow; 5.) Melt. Arrows on the horizontal axis indicate directions of increasing temperature and frequency of the applied perturbation.

In light of the above discussion, we see that polymeric materials such as PLA can have different relaxation times, depending on their state, and these characteristic relaxation times often very large. PLA under normal conditions can require several days, or even years if the temperature is below T_g, for its molecules to adjust to external or internal stresses. This has major consequences for applying atomistic simulation methods to PLA systems, since the temporal resolution of such methods is limited to tens or hundreds of nanoseconds. Fortunately, there is a well understood relationship in polymer physics that allows us to obtain useful information even from short timescale experiments. This is known as the *time-temperature superposition principle*. The concept of time-temperature superposition arose in Section 2.1.3, with the introduction of the WLF model (Equation 2.4). However, this concept is best illustrated when examining the results of dynamic experiments, such as DMA. In such a case, data obtained through a temperature sweep exhibits the same five region behavior as data obtained in the frequency sweep. This relationship is indicated in the horizontal axis labels in Figure 2.10. In effect, increasing the temperature is equivalent to reducing the frequency of an oscillating experiment, or increasing the observation time in a static experiment. Thus, from Equation 2.4, one can calculate the amount of temperature increase needed for a nanosecond scale observation to yield the same behavior as an experiment at ambient temperature performed over laboratory time scales. Figure 2.11 shows such a plot, using the universal WLF constants (refer to Section 2.1.3.1). In the plot, the reduced variables shift factor of Equation 2.4 was set to $A_T =$

$t_s/(10\ \text{seconds})$, where t_s is the time scale of a simulation. The results in Figure 2.11 indicate that a ten nanosecond simulation would require a temperature of about 120 °C for equivalence with a ten second lab experiment carried out at 60 °C.

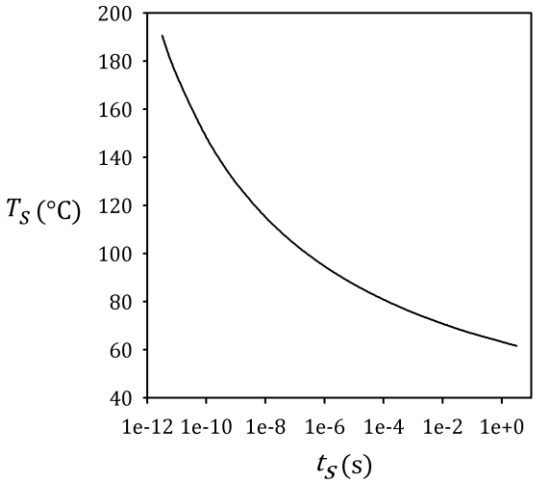

Figure 2.11. Time-temperature superposition as calculated by the WLF equation. The abscissa gives the temperature at which an experiment (or simulation) of duration t_s is expected to yield results equivalent to a ten second laboratory experiment at $60\ ^\circ\text{C}$. Universal WLF parameters used, with $T_0 = 60\ ^\circ\text{C}$.

The last peculiarity of polymer behavior to be discussed is the nonlinear relationship of the viscosity with the shear rate. For Newtonian fluids, the viscosity is independent of the flow field, while in our generalized Newtonian representation (Equation 2.14), η is allowed to be a function of $\dot{\boldsymbol{\gamma}}$. A common functional dependence for polymers is the power law model:

$$\eta = K_n \dot{\gamma}^{n-1} \tag{2.28}$$

where K_n is a constant, n is a real number, and $\dot{\gamma}$ is the magnitude of $\dot{\boldsymbol{\gamma}}$. For linear polymers, the viscosity is usually a decreasing function of the shear rate ($n < 1$), and this is referred to as shear-thinning or pseudoplasticity. Pseudoplastic materials pose a difficult problem for molecular simulation, since simulations are limited to very high shear rates due to their short time scales. As described in detail in Appendix B, most common simulation methods for estimating the viscosity are only applicable to the linear regime, and nonlinear responses are not easily simulated without more advanced techniques [*57*].

§ 2.1.8. Summary and Closing Remarks on Polymer Science

Before undertaking any modeling or simulation work, it is important to have a sound understanding of the physical concepts relevant to the system being modeled. In these sections, the highlighted concepts are those that are most important for modeling polymer behavior, and these concepts are employed throughout the rest of this dissertation. Section 2.1.1 dealt with the primary molecular structure of polymers, which will guide the creation of input structures used in the simulations of Chapters Four and Five.

Sections 2.1.2 through 2.1.4 discussed the different states of bulk polymers, including amorphous, glassy, and semicrystalline states. The characteristic ratio, C_∞, was introduced as a measure of amorphous chain dimensions, and the difficulties involved in

estimating C_∞ from dilute solution measurements were discussed. It was noted that the glass transition temperature, T_g, is dependent on the time scale of observation, and through free volume, kinetic, and thermodynamic theories we may estimate the effect that a decreasing observation time will have on T_g. In semicrystalline polymers, the observed melting point is also different than what one would simulate using conventional methods, and Thompson's rule provides means to estimate melting point depression.

In Sections 2.1.5 and 2.1.6, the interactions of polymers with small molecule penetrants were considered. Species solubility was defined, and the experimentally observed activation energy was related to the enthalpy of sorption according to the Clausius-Clapeyron equation. Solubility is known to be affected by glass transitions as well as semicrystallinity. The permeability was also defined in terms of the solubility and (Fickian) diffusion coefficient, though it was noted that PLA is known to facilitate non-Fickian diffusion at ambient temperatures.

Finally, in Section 2.1.7, the flow of polymer systems was discussed. The effect of molecular weight on the viscosity was presented, both for entangled and unentangled polymer chains. Relaxation and retardation times of polymers were discussed, and quantitatively described in terms of spring and dashpot models, as well as experimental (DMA) results. It was noted that relaxation times for PLA can be on the order of days or years, but that the WLF model provides a way to reconcile timescale issues in simulations via the time-temperature superposition principle. It was also noted that

polymers such as PLA have a nonlinear response to shear strain, and that conventional simulation methods for estimating the viscosity are not well-suited for such materials. The above information will be very important in the remaining chapters of this dissertation. In particular, Equation 2.4 will prove extremely useful in comparing experimental data to the simulation data presented here.

§ 2.2. Molecular Simulation Methods

The remainder of this dissertation is concerned with the details of developing molecular models capable of accurately simulating the behavior of PLA described above. In this work, we employ primarily two levels of theory in simulating PLA. First, as described in Section 2.2.1, are methods based on quantum mechanics. These methods are used extensively in Chapter Four of this work. The other level of theory we use, described in Section 2.2.2, is classical mechanics. Classical models are the focus of Chapter Five.

In selecting the methods used in Chapters Four and Five, we, in general, chose those which have been widely used and proven by the research community. We are aware that these methods are not without criticism, especially the quantum methods used here (see, for example reference [*58*]). Yet, in this work, we feel that their use is more than justified. In selecting any simulation method, there is a tradeoff between the method's accuracy and its computational cost. For the purpose of this work, the selected methods provide adequate accuracy while keeping the computational overhead relatively low. Yet, in the following discussion, we try to make note of some of

the newer methods which may provide different alternatives to those used here. These comments may be of use to new students and researchers in this field, and will give some idea of the directions in which the field might go in the near future.

§ 2.2.1. Computational Quantum Chemistry

In its simplest form, the basic problem of quantum computational chemistry is written

$$\hat{\mathcal{H}}\Psi = E\Psi \tag{2.29}$$

This is the familiar time-independent Schrödinger equation, where $\hat{\mathcal{H}}$ represents the Hamiltonian operator, Ψ is the wavefunction, and E is the total energy of the system (kinetic plus potential energy). The Schrödinger equation is one of the most fundamental relations in modern physics. It cannot be derived, but is accepted as an elementary law of nature due to the validity of its results. The Schrödinger equation might not look menacing as presented in Equation 2.29, but it is indeed very difficult to apply to real systems. Analytical solutions remain intractable for molecules of even modest size, and thus, all methods in use today suffer from one sort of inexactness or another. Practical methods must apply either simplifications to Equation 2.29 or assumptions about one or more of its terms.

§ 2.2.1.1. How the Schrödinger Equation Results in Quantum States

Though the Schrödinger equation is the cornerstone of quantum mechanics, it is not immediately apparent why Equation 2.29 results in a theory where properties such

as energy—classically thought of as continuous variables—are restricted to discrete values. In practice, solving the Schrödinger equation is complicated by the wave-like property of particles implied in Equation 2.29, which allows for multiple solutions for Ψ. For example, if an analytical solution exists for a particular problem, functional forms in the general solution will often involve trigonometric functions. These require discrete values for certain parameters (for example, the multiplicity of a cosine function) in order to satisfy the differential equation and boundary conditions. For a more specific example, consider the solution to the classic "particle in a box" problem, where the box is a cube with sides of length L:

$$\Psi(x,y,z) = \left(\frac{2}{L}\right)^{3/2} \sin\left(\frac{n_x \pi x}{L}\right) \sin\left(\frac{n_y \pi y}{L}\right) \sin\left(\frac{n_z \pi z}{L}\right) \tag{2.30}$$

Here, n_x, n_y, and n_z are independent but required to be integers. In such cases, multiple sets of these discrete parameters, or *quantum numbers* exist which are all valid solutions to the differential equation, and it is this feature that, mathematically, results in the quantum or discretized nature of the theory. In most cases, the value of the energy will change depending on the set of quantum numbers used, resulting in quantized energy levels. Thus, for numerical methods, measures must be taken to ensure that the desired solution (usually either the ground state or an ensemble average of all quantum states) is obtained.

§ 2.2.1.2. The Electronic Wave Function

The wavefunction, Ψ, in Equation 2.29 is an abstract concept at best. The usual physical interpretation, due to Born and Pauli, states that the product of Ψ with its complex conjugate Ψ^* is related to the probability of finding the system in a given state. Thus, when Ψ describes a single particle in three dimensions, the probability of finding the particle inside a volume V is found by integrating over the Cartesian space of V,

$$p(V) = \int_V \Psi^*\Psi \, dx \, dy \, dz = \int_V |\Psi|^2 \, dx \, dy \, dz \tag{2.31}$$

For a system of N particles, the wavefunction Ψ has $4N$ coordinates as independent variables (three Cartesian coordinates, $\mathbf{r}_i$, plus one spin coordinate, $m_{s,i}$, for each particle i). The large dimensionality in Ψ is perhaps the biggest obstacle in solving Equation 2.29 for realistic systems. For molecules, the dimensionality can be reduced by application of the *Born-Oppenheimer approximation*, in which the wavefunction of the electrons is assumed to be decoupled from the atomic nuclei. In such case, the positions of the nuclei can be considered parameters in the calculation rather than variables. Using the Born-Oppenheimer approximation, in what follows, we treat the system as a set of electrons interacting with "frozen" nuclei (e.g. the positions of the nuclei are fixed in space). Thus, the wavefunction of the system, Ψ, is interpreted as the *electronic wavefunction*, and the Hamiltonian $\widehat{\mathcal{H}}$ in equation 2.29 is the *electronic Hamiltonian*.

In solving the Schrödinger equation for molecules, it is common practice to assume the electronic wavefunction, Ψ, is composed of many *molecular orbitals*. A molecular orbital is a wavefunction which describes a single electron, and is in general a function of the electron's spatial coordinates and spin quantum number. Because of their explicit dependence on spin, these are often referred to as *spin orbitals*. There are certain restrictions imposed on the wavefunction, and thus, we must be mindful of these when the spin orbitals are arranged to form Ψ. These restrictions will be discussed below.

For the electronic wavefunction to be consistent with the postulates of quantum theory, it must satisfy two important principles. First is the *Pauli principle*, which states that the wavefunction for a system of electrons must be *exchange antisymmetric* [*59*]. That is, if two electrons, say j and k, exchange places in the electronic wavefunction, the value of the function must change sign. In mathematical terms,

$$\Psi(\mathbf{q}_1, \mathbf{q}_2, \cdots \mathbf{q}_j, \cdots \mathbf{q}_k, \cdots \mathbf{q}_N) = -\Psi(\mathbf{q}_1, \mathbf{q}_2, \cdots \mathbf{q}_k, \cdots \mathbf{q}_j, \cdots \mathbf{q}_N) \tag{2.32}$$

where $\mathbf{q}_i$ represents the spatial and spin coordinates of electron i. Pauli showed that this is true for particles of half-integral spin, using relativistic quantum field theory, and ample experimental evidence shows that electrons exhibit only antisymmetric exchange [*59*]. The next postulate regarding the wavefunction is the *Pauli exclusion principle*, which further states that no two electrons can occupy the same quantum state at the same time. That is, no two electrons can share the same spin orbital.

Slater showed that both the Pauli principle and the Pauli exclusion principle are upheld if the wavefunction is formed from a matrix determinant. For a system with n electrons occupying a set of spin orbitals $\{\chi_i\}_{i=1}^{n}$, the *Slater determinant* is given by [*60*]

$$\Psi(\mathbf{q}_1, \cdots \mathbf{q}_n) = \frac{1}{\sqrt{n!}} \begin{vmatrix} \chi_1(\mathbf{q}_1) & \chi_2(\mathbf{q}_1) & \chi_3(\mathbf{q}_1) & \cdots & \chi_n(\mathbf{q}_1) \\ \chi_1(\mathbf{q}_2) & \chi_2(\mathbf{q}_2) & \chi_3(\mathbf{q}_2) & \cdots & \chi_n(\mathbf{q}_2) \\ \chi_1(\mathbf{q}_3) & \chi_2(\mathbf{q}_3) & \chi_3(\mathbf{q}_3) & \cdots & \chi_n(\mathbf{q}_3) \\ \vdots & \vdots & \vdots & \ddots & \vdots \\ \chi_1(\mathbf{q}_n) & \chi_2(\mathbf{q}_n) & \chi_3(\mathbf{q}_n) & \cdots & \chi_n(\mathbf{q}_n) \end{vmatrix} \tag{2.33}$$

where the factor $1/\sqrt{n!}$ ensures that the wavefunction is normalized, if we require the spatial orbitals to form an *orthonormal set*. The condition of orthonormality is satisfied if

$$\int \chi_i{}^* \chi_j d\mathbf{q} = \delta_{ij} \tag{2.34}$$

for all such combinations of spin orbitals, where δ_{ij} is the Kronecker delta, and the integration is performed over all space. In constructing the Slater determinant in Equation 2.33, each row of the matrix corresponds to a single electron, while each column corresponds to a single spin orbital.

The Slater determinant satisfies the Pauli principle, since exchanging any two rows in a matrix reverses the sign of its determinant. The Pauli exclusion principle is also satisfied, since any matrix with two identical columns will have a determinant of zero. Thus, it is standard practice to use Equation 2.33 to describe the electronic wavefunction. Using this equation, the problem of solving for the wavefunction is

simplified into solving for the individual molecular orbitals. In the following section, we will discuss ways to represent the molecular orbitals.

Before proceeding to our discussion on representation of the molecular orbitals, we wish to note one more detail concerning the use of Slater determinants. While Equation 2.33 satisfies both the Pauli principle and the Pauli exclusion principle, representing the wavefunction as a single determinant does not capture one other important principle: *correlation* between the electrons. After introducing the concept of basis functions in the Section 2.2.1.3, we proceed with our discussion of solving for a single Slater determinant wavefunction (i.e., Equation 2.33) using Hartree-Fock theory in Section 2.2.1.4. The concept of electron correlation is then addressed in Section 2.2.1.5.

§ 2.2.1.3. Basis Functions

For realistic systems, such as molecules, analytical solutions such as Equation 2.30 cannot be obtained. In such a case, the electronic wavefunction can be estimated with numerical methods. Numerical approaches to solving Equation 2.29 typically employ the use of analytical *basis functions* to approximate the wavefunction. The collection of basis functions chosen for a particular solution is referred to as a *basis set*. An example of a basis set, familiar to engineers, is the set of sine and cosine functions that make up a Fourier series. In that case, any arbitrary function may be represented as a sum of individual sine and cosine terms, each term having a multiplicative coefficient that determines its contribution to the overall function. While it is possible to express any periodic function using a Fourier expansion, this is strictly true only if we have an

infinite number of sine and cosine terms (in this case, we say the basis set is *complete*). Inevitably, we must use an incomplete basis set in practice. Further, in non-periodic systems, other functions exist which are better suited than Fourier terms as basis functions for molecular orbital calculations.

Before defining basis functions to represent molecular orbitals, it is convenient to eliminate the dependence of the molecular orbitals on spin coordinates. To achieve this, each molecular orbital can be divided into the product of a *spatial orbital*, Ψ_i, which acts on an electron's position vector, and a *spin function*, written as one of α or β, which acts on the electron's spin coordinate. The spin functions are both Dirac delta functions, with α being zero for all values of the spin coordinate except ½ (*spin up*), and β being zero for all values but −½ (*spin down*). Thus, for closed-shell systems, a set of $2n$ spin orbitals can be written as

$$\{\chi_1, \chi_2, \chi_3, \chi_4, \cdots \chi_{2n-1}, \chi_{2n}\} = \{\Psi_1\alpha, \Psi_1\beta, \Psi_2\alpha, \Psi_2\beta, \cdots \Psi_n\alpha, \Psi_n\beta\} \qquad (2.35)$$

In this representation, each of the n spatial orbitals can be occupied by at most one spin up electron and one spin down electron.

To represent the spatial orbitals using basis functions, it is assumed that each one can be expressed as a linear combination of atomic orbitals (LCAO),

$$\Psi_i = \sum_j c_{ij}\Phi_j \qquad (2.36)$$

where the $\{\Phi_j\}$ terms are (spatial) atomic orbital functions, and, in this case, the basis set. The coefficients $\{c_{ij}\}$ in Equation 2.36 are the *basis set coefficients*. For a hydrogen-like atom, theory tells us that an individual electron's wavefunction has the general form of a decaying exponential function, centered about the atomic nucleus [*61*]. Thus, in the LCAO approach, we might expect the molecular orbitals to be reasonably close to decaying exponential functions centered on each atom,

$$\Phi_j \cong x^{l_j} y^{m_j} z^{n_j} e^{-\zeta_j r} \tag{2.37}$$

where l_j, m_j, and n_j characterize the symmetry of the orbital (e.g. an s, p, d, or f orbital), the Cartesian coordinates x, y and z (along with the radial distance r) are taken in reference to the nucleus about which the function is centered, and ζ_i ("zeta") is an adjustable parameter. Such functions are usually referred to as *Slater functions* or *Slater type orbitals* (STOs).

The form of the STO basis function on the right-hand side of Equation 2.37 is consistent with quantum theory for atoms. However, due to computational considerations, it is much more common to approximate the behavior of a Slater function with one or more Gaussian functions,

$$\eta_k = x^{l_k} y^{m_k} z^{n_k} e^{-\alpha_k r^2} \tag{2.38}$$

The Gaussian-type function (GTF), upon examination, is similar to the STO in Equation 2.37, except that in the GTF the radial distance is squared in the exponent. Again, the coefficient α_k is adjustable, while the exponents on the Cartesian coordinates

determine the symmetry of the function. Following Cook [*62*], we represent GTFs using the symbol η to distinguish it from a basis function Φ.

The reason for the popularity of Gaussian basis sets lies in the fact that the product of two Gaussian functions can be analytically resolved into one single Gaussian, even when the original two functions are not centered about the same point. In practice, as we will see in Section 2.2.1.4, this makes evaluation of certain integrals much faster for Gaussian functions than for Slater functions. Gaussian basis sets are extremely popular, as indicated by the name of the current industry standard computational chemistry software, Gaussian 03 [*63*].

Basis set specifications are well standardized in the computational chemistry community. Several common Gaussian-based basis set names follow the pattern STO-nG, which identifies a Slater-type orbital approximated by n Gaussian functions [*64*]. Each basis function (an approximate STO) is given as a sum of individual Gaussian functions,

$$\Phi_i = \sum_{k=1}^{n} d_{ik}\eta_{ik} \tag{2.39}$$

Generally the coefficients $\{d_{ik}\}$, as well as the exponential coefficients $\{\alpha_{ik}\}$ (from Equation 2.38) are fixed, depending on the type of atom on which the function is centered, and the type of shell the basis function represents. The basis set described by Equation 2.39 is usually called a *contracted* basis, referring to the fact that many GTFs are contracted into a single basis function. Conversely, one might say a single basis

function is *expanded* into several GTFs. Several contracted basis functions are shown in Figure 2.12, in comparison to the Slater function which they approximate.

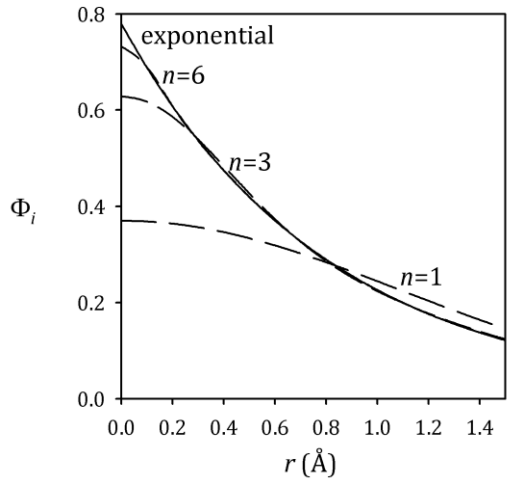

Figure 2.12. Gaussian approximations of a Slater-type orbital for hydrogen. The number n indicates the number of Gaussian functions used in the approximation. The Slater (exponential) function is shown for comparison.

Another popular class of Gaussian basis sets, developed by Pople and coworkers [*65-67*], are the so-called *split valence* basis sets. In these basis sets, the inner molecular orbitals are given a single basis function (as in the STO-nG basis sets), while each valence orbital is split into two shells, each with its own basis function. Some authors refer to split valence basis sets as *double zeta* basis sets (named from the exponent parameter in the STO, probably predating the GTF's rise in popularity), though opinions vary on how this term should be used [*68*,*69*].

The basic split valence basis sets are named in the pattern n-lmG, where n indicates the number of Gaussians used for the basis function of each core orbital, l is the number of Gaussians that make up the basis function of the first valence shell, and m is the number of Gaussians in the basis function of the second valence shell. For example, the 6-31G basis set has one six-Gaussian basis function for each inner orbital, and each valence orbital is divided into one three-Gaussian basis function and one single-Gaussian basis function. In this way, more flexibility is allowed in describing the valence electron shells, which are most affected by the chemical bonding of an atom.

Split valence basis sets usually, unless otherwise specified, include one $1s$ spatial orbital on H and He atoms. Since these are valence orbitals, they are split into two basis functions, $1s'$ and $1s''$. In turn, these orbitals are contraction shells consisting of one or more GTFs. Taking the 6-31G basis again as an example, we have an s' orbital made up of three GTFs and one s'' orbital made up of one GTF. Thus, in the 6-31G basis set, H and He each have one spatial orbital, two basis functions, and four GTFs. Atoms in the second row of the periodic table are assigned an inner $1s$ spatial orbital having one basis function of six GTFs, and the outer $2s$, $2p_x$, $2p_y$, and $2p_z$ orbitals are each divided into two basis functions: $2s'$ (3 GTFs), $2p_x{}'$ (3 GTFs), $2p_y{}'$ (3 GTFs), $2p_z{}'$ (3 GTFs), $2s''$ (1 GTF), $2p_x{}''$ (1 GTF), $2p_y{}''$ (1 GTF), $2p_z{}''$ (1 GTF). So, in the 6-31G basis, second row atoms have a total of five spatial orbitals, nine basis functions, and twenty-two GTFs.

In general, as the size of the basis set increases, the basis set's ability to approximate the true wavefunction is improved. This is the advantage of using a split-

valence basis set (such as 3-21G) over a regular contracted basis set (such as STO-3G). To further improve the accuracy, one could imagine using a triple zeta split-valence basis, such as the 6-311G basis (see [*70*]). However, above the double zeta level, the gains of further splitting the valence shells are often fairly small, since the added basis functions would have the same symmetry as those already in the double zeta basis set [*71*]. More flexibility is gained by considering orbitals with greater angular momentum quantum numbers, yielding new symmetries by which more complex electron distributions can be represented. This is especially important for molecules in which the electron clouds undergo some degree of polarization.

When polarized molecules are involved, accuracy may be gained by adding *polarization functions* to the "pure" split-valence basis sets. For example, a set of $3d$ orbitals might be added to second row elements, in which case an asterisk, or star (*) is appended to the basis set name. If the first-row elements also receive polarization functions (in this case it would be a set of $2p$ orbitals), two stars (**) are appended. Second-row polarization functions tend to improve geometries and relative energies calculated with the basis, while double-star polarized bases result in better treatment of hydrogen bonding interactions [*72*].

Calculations in Chapter Four of this dissertation use the 6-31G** basis set extensively. Table 2.1 lists the basis functions that make up this basis set, for the first two rows of the periodic table. Notice that there are six $3d$ orbitals added to the second row atoms, instead of the usual five presented in quantum theory. These are simply

linear combinations of the orbitals $3d_{xy}$, $3d_{x^2-y^2}$, $3d_{yz}$, $3d_{zx}$, $3d_{z^2}$, and the $3s$ orbital [*71*]. Thus, due to the use of the $3s$ orbital, the polarization functions impart an extra degree of flexibility in representing the spherically-symmetric portion of the orbitals. Also note in Table 2.1, that the added polarization functions are neither split nor contracted; they are each single Gaussians.

Table 2.1. Basis functions and primitive Gaussians in the 6-31G** basis set.

Elements	Spatial Orbitals	Contraction Shells	Gaussian Functions	Total Basis Functions	Total Gaussian Functions
$_1$H to $_2$He	$1s$	$1s''$	3	5	7
		$1s''$	1		
	$2p_x$	$2p_x$	1		
	$2p_x$	$2p_x$	1		
	$2p_x$	$2p_x$	1		
$_3$Li to $_{10}$Ne	$1s$	$1s$	6	15	28
	$2s$	$2s'$	3		
		$2s''$	1		
	$2p_x$	$2p_x{}'$	3		
		$2p_x{}''$	1		
	$2p_y$	$2p_y{}'$	3		
		$2p_y{}''$	1		
	$2p_z$	$2p_z{}'$	3		
		$2p_z{}''$	1		
	$3d_{xx}$	$3d_{xx}$	1		
	$3d_{yy}$	$3d_{yy}$	1		
	$3d_{zz}$	$3d_{zz}$	1		
	$3d_{xy}$	$3d_{xy}$	1		
	$3d_{yz}$	$3d_{yz}$	1		
	$3d_{zx}$	$3d_{zx}$	1		

There are many more basis sets in use for computational chemistry applications than we have discussed here, including those of Dunning and Huzinaga [*73*] and the correlation consistent basis sets [*74-76*]. Also, departures from the LCAO approach and Slater-type basis sets have been explored for use in computational chemistry; while such methods are not widely used, they have gained favor among some researchers. For example, plane wave basis functions have proven useful in studying periodic and crystalline systems [*77*,*78*], while wavelet-based methods provide means for definite systematic improvement of the wavefunction in the general case of three-dimensional systems [*79*].

§ 2.2.1.4. Hartree-Fock Theory and the Roothan-Hall Equations

In this section, we will demonstrate one of the standard equations used for obtaining a first approximation to the wavefunction in Equation 2.29. These are known as the Hartree-Fock (HF) equations. The HF equations are cast in a general form by making few assumptions about the wavefunction. After discussing the HF equations, we will invoke the LCAO assumption, and present the Roothan-Hall (RH) equations. The RH equations, combined with a proper basis set, allow the wavefunction and energy of a molecule to be estimated in the framework of HF theory. The HF/RH approach is used in Chapter Four for ab initio calculations of the electronic wavefunction of PLA conformers, prior to refinement with higher-level treatments. Thus, when interpreting the results of that chapter, it is important to have an understanding of how they are obtained.

The Hartree-Fock approach begins with multiplying Equation 2.29 by the wavefunction's complex conjugate, then integrating over all space, such that we may write

$$E = \frac{\int \Psi^* \widehat{\mathcal{H}} \Psi d\mathbf{q}}{\int \Psi^* \Psi d\mathbf{q}} \tag{2.40}$$

This relation is simplified if we require Ψ to be normalized, meaning $\int \Psi^* \Psi d\mathbf{q} = 1$. This is ensured by the normalization factor in Equation 2.33, if we require our wavefunction to be constructed from a single Slater determinant of orthonormal molecular orbitals. With this assumption, we can express Equation 2.40 in Dirac's "bra-ket" shorthand,

$$E = \langle \Psi | \widehat{\mathcal{H}} | \Psi \rangle \tag{2.41}$$

See Sections 1.1.4 and 1.2 in Szabo and Ostlund [*80*] for a thorough explanation of the Dirac notation. For a molecular system, having $2n$ electrons and m nuclei, the electronic Hamiltonian operator is given by

$$\widehat{\mathcal{H}} = -\sum_{i=1}^{2n} \frac{1}{2} \nabla_i^2 - \sum_{i=1}^{2n} \sum_{j=i+1}^{m} \frac{Z_j}{r_{ij}} + \sum_{i=1}^{2n} \sum_{k=i+1}^{2n} \frac{1}{r_{ik}} \tag{2.42}$$

In this form, all quantities are cast in *atomic units*, eliminating the need to include constants of nature (e.g., the permittivity of free space, Planck's constant) in Equation 2.42. For more information on atomic units, refer to Section 2.1.1 and Table 2.1 in Szabo and Ostlund [*80*].

The terms in Equation 2.42 represent the total kinetic and potential energy of the electrons in the system. Inside the first term, summed over all electrons $i = 1$ to $2n$, is the Laplacian operator, ∇^2, taken with respect to the Cartesian coordinates of electron i. In other words, $\nabla_i^2 = \frac{\partial^2}{\partial {x_i}^2} + \frac{\partial^2}{\partial {y_i}^2} + \frac{\partial^2}{\partial {z_i}^2}$. The remaining double sums are simply the pairwise potential interaction between the particles in the system. The middle sum gives the interaction between each electron i and each nucleus j, with Z_j being the electronic charge on the nucleus. The sum on the far right represents the repulsion of each electron with the others in the system. In each case, r_{pq} is the interparticle distance between particle p and particle q. Notice that, since we are using the Born-Oppenheimer approximation, we do not include the internuclear repulsions in the Hamiltonian; to obtain the total energy of the system, the internuclear repulsions must be added to Equation 2.41.

Substituting Equation 2.42 into Equation 2.41, we have

$$E = \sum_{i=1}^{2n} \langle \Psi | \hat{h}(i) | \Psi \rangle + \sum_{i=1}^{2n} \sum_{k=i+1}^{2n} \langle \Psi | \frac{1}{r_{ik}} | \Psi \rangle \tag{2.43}$$

where we've simplified the notation by defining a *one electron Hamiltonian* operator,

$$\hat{h}(i) = -\frac{1}{2}\nabla_i^2 - \sum_{j=i+1}^{m} \frac{Z_j}{r_{ij}} \tag{2.44}$$

Using the fact that we required the molecular orbitals to be orthonormal to each other in constructing the Slater determinant, it can be shown [*81-83*] that

$$E = \sum_{i=1}^{2n} \left[i|\hat{h}|i \right] + \frac{1}{2} \sum_{i=1}^{2n} \sum_{j=i+1}^{2n} \left([ii|jj] - [ij|ji] \right) \tag{2.45}$$

where the *chemists'* notation is used (as opposed to the *physicists'* notation; see reference [*84*] for the distinction) to define the *one-electron integrals*,

$$\left[i|\hat{h}|i \right] = \int \chi_i{}^*(\mathbf{q}_1) \hat{h}(1) \chi_i(\mathbf{q}_1) \, d\mathbf{q}_1 \tag{2.46}$$

and for the two-electron integrals, we have the *overlap*, or *Coulomb integrals*,

$$[ii|jj] = \int \int \chi_i{}^*(\mathbf{q}_1) \chi_i(\mathbf{q}_1) \frac{1}{r_{12}} \chi_j{}^*(\mathbf{q}_2) \chi_j(\mathbf{q}_2) \, d\mathbf{q}_1 \, d\mathbf{q}_2 \tag{2.47}$$

and the *exchange integrals*,

$$[ij|ji] = \int \int \chi_i{}^*(\mathbf{q}_1) \chi_j(\mathbf{q}_1) \frac{1}{r_{12}} \chi_j{}^*(\mathbf{q}_2) \chi_i(\mathbf{q}_2) \, d\mathbf{q}_1 \, d\mathbf{q}_2 \tag{2.48}$$

The Hartree-Fock equations follow from Equation 2.45, if the energy is minimized using *functional variation*. In other words, a stationary point in the energy may be found by varying the molecular orbitals $\{\chi_i\}$. This is done using the method of Lagrangian multipliers, the details of which are discussed in Section 3.2 of Szabo and Ostlund [*80*]. The Hartree-Fock equation for orbital i is given by

$$\hat{h}(1) \chi_i(\mathbf{q}_1) + \sum_{j \neq i} \left[\hat{\mathcal{J}}_j(1) \chi_i(\mathbf{q}_1) - \hat{\mathcal{K}}_j(1) \chi_i(\mathbf{q}_1) \right] = \varepsilon_i \chi_i(\mathbf{q}_1) \tag{2.49}$$

where ε_i is the energy for orbital χ_i. In writing Equation 2.49, we have used the *Coulomb operator*,

$$\hat{J}_j(1)\chi_i(\mathbf{q}_1) = \left[\int \frac{1}{r_{12}} \left|\chi_j(\mathbf{q}_2)\right|^2 d\mathbf{q}_2\right] \chi_i(\mathbf{q}_1) \tag{2.50}$$

and the *exchange operator*,

$$\hat{\mathcal{K}}_j(1)\chi_i(\mathbf{q}_1) = \left[\int \chi_j{}^*(\mathbf{q}_2) \frac{1}{r_{12}} \chi_j(\mathbf{q}_2)\, d\mathbf{q}_2\right] \chi_i(\mathbf{q}_1) \tag{2.51}$$

To draw an analogy with the Schrödinger equation (Equation 2.29), we use the *Fock operator*,

$$\hat{F}(1) = \hat{h}(1) + \sum_{j \neq i} \left[\hat{J}_j(1) - \hat{\mathcal{K}}_j(1)\right] \tag{2.52}$$

So, Equation 2.49 can be written

$$\hat{F}\Psi = \boldsymbol{\varepsilon}\Psi \tag{2.53}$$

with $\boldsymbol{\varepsilon}$ a diagonal matrix.

The Hartree-Fock Equations, given in Equation 2.53, apply in general for an electronic wavefunction that is a Slater determinant of orthonormal molecular orbitals. To solve this equation numerically, we must introduce a basis set as discussed in Section 2.2.1.3. The Roothan-Hall equations follow, by substituting Equation 2.36 for each of the spatial orbitals making up Ψ in Equation 2.53. The result is the system of equations

$$\mathbf{FC} = \mathbf{SC}\boldsymbol{\varepsilon} \tag{2.54}$$

where the matrices $\mathbf{F}$ and $\mathbf{S}$ represent the *Fock matrix*, the *overlap matrix*, respectively, and the $\mathbf{C}$ matrix contains the basis set coefficients. The matrices have as their elements

$$F_{ij} = \int \Phi_i(\mathbf{q}_1)\hat{\mathcal{F}}(1)\Phi_j(\mathbf{q}_1)\, d\mathbf{q}_1 \tag{2.55}$$

$$S_{ij} = \int \Phi_i(\mathbf{q}_1)\Phi_j(\mathbf{q}_1)\, d\mathbf{q}_1 \tag{2.56}$$

$$C_{ij} = c_{ji} \tag{2.57}$$

The RH equations can be solved self-consistently, and the HF method is often referred to as a *self-consistent field* (SCF) approach. First, the overlap and Fock matrices are calculated, using an initial guess for the basis set coefficients. Although the basis set coefficients do not appear in the Fock matrix elements of Equation 2.55, the Fock operator $\hat{\mathcal{F}}$ requires the molecular orbitals $\{\chi_i\}$ to be known, and therefore, the basis set coefficients are required to calculate $\mathbf{F}$. The Fock matrix is then diagonalized to find the orbital energies, giving a new set of basis set coefficients. This process is repeated until self-consistency is obtained, i.e., until the basis set coefficients show no change with further iteration. When examining the integrals in Equations 2.55 and 2.56, we explicitly see the advantage of using GTFs in the basis functions instead of exponential functions. In the case where Φ_i is not centered about the same atom as Φ_j, these integrals could only be evaluated numerically, e.g., using the trapezoid rule, when exponential functions are used; on the other hand, the product of two GTFs can be resolved into a single GTF, even when they are not centered about the same point in space. Therefore, when using Gaussian basis sets, the overlap integrals and parts of the Fock matrix integrals can be evaluated analytically.

§ 2.2.1.5. Post Hartree-Fock Calculations

In putting forth the Hartree-Fock equations (Equations 2.49 and 2.53), the electronic Hamiltonian operator was simplified so that the electron-electron repulsion terms were averaged out over the electron clouds of each electron. This is apparent in Equations 2.50 and 2.51. A more accurate treatment is gained by considering *correlation* between the electrons. Several methods exist for refining the Hartree-Fock wavefunction, which account for electron correlation. These are reviewed in Section 5.4 of Lewars [*85*], including the Møller-Plesset perturbation methods (MP2, MP3, etc.), configuration interaction (CI), multiconfigurational SCF (MCSCF), complete active-space SCF (CASSCF), coupled-cluster (CC), and quadratic configuration interaction (QCI) methods. In this dissertation, we use a more computationally tractable approach, density functional theory, which is discussed in the next section.

§ 2.2.1.6. Density Functional Theory

In recent decades, electron density functional theory (DFT) has been a popular approach to solving the Schrödinger equation for molecules. Actually, DFT methods aim to replace the Schrödinger equation with an equivalent form that acts on the total electron density rather than the wavefunction. While it has been proven by Hohenberg and Kohn that such an exact functional form exists [*86*], to date it has only been cast in approximate forms. For this reason, DFT is often not classified as a true *ab initio* method. In theory, casting the Schrödinger equation in a form that operates on the electron density, rather than the all-electron wavefunction, would reduce the

dimensionality of the problem from $4n$ electronic coordinates to only three spatial coordinates plus the spin coordinates. In current practice, a basis set of atomic orbitals is still needed, and thus, current DFT programs keep track of as many electronic coordinates as other ab initio methods. Still, the method is much faster than alternative post Hartree-Fock methods. Chapter 7 of Lewars gives a good overview of the DFT method [*85*].

§ 2.2.2. Classical Molecular Simulation

Given the complexity involved in *ab initio* calculations, most molecular level simulation methods employ a classical approach. In this way, the electronic degrees of freedom need not be considered, and the constituent atoms of a molecule may be treated as point particles. There are several very good textbooks on classical simulation methods, including Allen and Tildesley [*87*], Frenkel and Smit [*88*], and Haile [*89*]; the reader is referred to these texts for an in-depth review. Here, we touch on the important basic concepts as they apply to this dissertation, with mention of some of the more recent advances in the field. First, in Section 2.2.2.1, we present a discussion on the validity of the classical approximation. This is followed by a detailed discussion of classical potential energy functions in Section 2.2.2.2. In Sections 2.2.2.3 through 2.2.2.5, we describe the application of potential energy functions in molecular dynamics (MD) and Monte Carlo (MC) and hybrid methods. An additional simulation method, which applies only to polymers, is the rotational isomeric states (RIS) method, which is discussed in Section 2.2.2.6.

§ 2.2.2.1. The Classical Approximation

A classical treatment of the potential energy (as opposed to a quantized treatment) is valid for cases in which the discrete quantum mechanical energy states are spaced close together relative to the thermal fluctuations of the system. The usual interpretation of thermal fluctuations comes from the equipartition theorem of statistical mechanics, from which it follows that thermal fluctuations in a single degree of freedom are on the order of $k_B T$, where k_B is the Boltzmann constant and T is the system temperature.

In physics texts, an often cited illustration to compare the quantum and classical descriptions of a system is the one-dimensional harmonic oscillator. This is also chemically relevant, since it is an adequate description for the vibration of a chemical bond. Here, we present such a discussion, loosely following that of Steinbach [*90*]; see his article for a more in-depth treatment of the subject.

The quantum mechanical energy of a one-dimensional harmonic oscillator in a particular quantum state is

$$E_n = \left(n + \frac{1}{2}\right) hf \tag{2.58}$$

where n is a quantum number that defines the quantum state, and may take any value from 0 to infinity. The parameter h is Planck's constant, and f is the oscillator's characteristic vibration frequency. If the oscillator is coupled to a thermalized bath of

temperature T, its ensemble-averaged energy and heat capacity are given by the equations

$$\langle E \rangle_{quantum} = \frac{1}{Q} \sum_{n=0}^{\infty} E_n e^{-E_n/k_B T} \tag{2.59}$$

$$C_{V,quantum} = \frac{1}{k_B T^2} \left[\frac{1}{Q} \sum_{n=0}^{\infty} E_n^2 e^{-E_n/k_B T} - \langle E \rangle_{quantum}^2 \right] \tag{2.60}$$

where Q is the partition function,

$$Q = \sum_{n=0}^{\infty} e^{-E_n/k_B T} \tag{2.61}$$

If the same harmonic oscillator is treated classically, the corresponding values follow from equipartition,

$$\langle E \rangle_{classical} = \frac{1}{2} k_B T \tag{2.62}$$

$$C_{V,classical} = \frac{1}{2} k_B \tag{2.63}$$

These quantities are plotted for oscillators of various frequencies at room temperature in Figure 2.13.

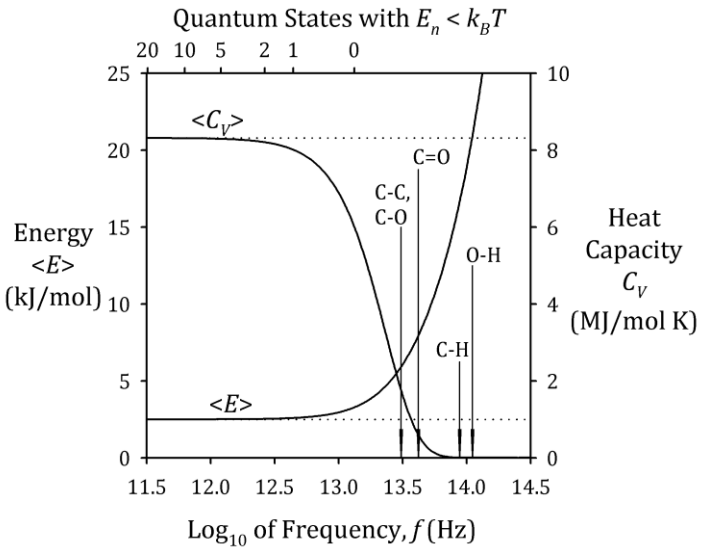

Figure 2.13. Isochoric heat capacity and ensemble averaged potential energy for various harmonic oscillators, thermalized at room temperature. Solid lines: quantum results; dotted lines: classical results. The stretching frequencies of several common chemical bonds, calculated with the OPLS force field [*91*,*92*], are indicated for reference. The secondary horizontal axis indicates the number of quantum states with energies below $k_B T$. Data calculated as described in the text, following Steinbach [*90*].

Note that, in the classical approximation, the energy and heat capacities are independent of the oscillator's natural vibrational frequency. When considering quantum effects, however, the vibrational frequency becomes important. Figure 2.13 shows that the classical approximation works quite well as long as there are multiple quantum states with energy less than $k_B T$. The classical approximation begins to break down for motions whose vibrational period is lower than 0.1 picosecond.

Unfortunately, most chemical bond stretching motions are just outside the range covered by the classical approximation. From Figure 2.13, we see that a classical approximation would allow more energy to be transferred to and from the bond than in the quantum description, due to the higher heat capacity of the classical oscillator. One way to combat this artifact is to prevent bond stretching altogether by using a constraint algorithm [*93*,*94*]. However, such a rigid treatment of bonds brings about its own deviations from the true quantum behavior, since even an oscillator in its ground state has vibratory motion. In practice, both treatments of bonds—rigid and spring-like—are frequently used, and for most applications either treatment will suffice. Other molecular motions, such as torsional motion about bonds and the translational motion of molecules are well within the valid range of the classical approximation; thus, a classical treatment of such motions is easily justified.

Once the premise of the classical approximation is accepted, there remains the problem of forming an accurate description of the system using classical equations. The basis of any classical simulation approach is the potential energy function, which governs how a molecular system behaves. This topic is discussed in the following section.

§ 2.2.2.2. Potential Energy Functions

Classical potential energy functions for molecules, or *force fields*, account for the quantum mechanical energy states of the electrons in the molecule, as a function of the

positions of atomic nuclei alone. Thus, for a molecular system with N atoms in three dimensions, the potential energy may be expressed as

$$\mathcal{V} = \mathcal{V}(\mathbf{r}^N) \tag{2.64}$$

where $\mathbf{r}^N$ is a vector with $3N$ components, corresponding to all Cartesian coordinates of the N atoms. That is, $\mathbf{r}^N = [\mathbf{r}_1\ \mathbf{r}_2 \cdots \mathbf{r}_N\ ] = [x_1\ y_1\ z_1\ x_2\ y_2\ z_2 \cdots x_N\ y_N\ z_N]$. Often, the $3N$-dimensional space in which $\mathbf{r}^N$ resides is called *configuration space* or *conformation space*, since the vector determines the conformations of all molecules in the system.

There are several popular force fields in use today, including CHARMM [*95*], AMBER [*96*], OPLS [*91*], and COMPASS [*97*]. Each force field differs in the types of mathematical functions used, but they almost invariably include one or more of the following terms: nonbonded interactions, such as dispersion (London) forces, atomic repulsion forces, and electrostatic forces; bonded (covalent) forces, such as bond stretching, angle bending, and torsional interactions; and cross terms, which correlate one or more of the previously mentioned interactions. In general, we can write the potential energy as

$$\begin{aligned}\mathcal{V} = &\sum_{\substack{nonbonded\\ i,j}} \left(\mathcal{V}_{ij}^{disp} + \mathcal{V}_{ij}^{rep}\right) + \sum_{\substack{charges\\ i,j}} \mathcal{V}_{ij}^{Coul} + \sum_{\substack{bonds\\ i,j}} \mathcal{V}_{ij}^{bond} \\ &+ \sum_{\substack{angles\\ i,j,k}} \mathcal{V}_{ijk}^{ang} + \sum_{\substack{torsions\\ i,j,k,l}} \mathcal{V}_{ijkl}^{tors} + \sum_{\substack{cross\\ terms\ i}} \mathcal{V}_{i}^{cross}\end{aligned} \tag{2.65}$$

In this section, we will give a brief overview of the typical mathematical functions used for these terms.

The most noted treatise on attractive intermolecular forces is probably that of London [*98*], where the interaction between two spherically symmetric, nonpolar molecules was considered. London used a simple model, but with the rigor of quantum mechanics, to calculate the potential due to dispersion, or the *induced dipole-induced dipole* effect. The phrase induced dipole-induced dipole is used because the molecules, normally nonpolar, incite dipoles in one another due to the alternating electric field produced by the zero-point movement of their electrons. The induced dipoles are also alternating, but are in phase with one another such that an attractive force results between the molecules. London considered two molecules, one whose electrons are in a quantum state k and another whose electrons are in quantum state ρ. The potential energy due to the dispersion effect is

$$\mathcal{V}_{\rho k}^{London} = -\frac{2}{3h(4\pi\epsilon_0)^2 {r_{\rho k}}^6} \sum_{\sigma} \sum_{l} \frac{{\mu_{kl}}^2 {\mu_{\rho\sigma}}^2}{f_{kl} + f_{\rho\sigma}} \tag{2.66}$$

where h is Planck's constant, ϵ_0 is the permittivity of free space, and $r_{\rho k}$ is the distance between the "Greek" molecule and the "Latin" molecule (London named the molecules based on the alphabets used in their subscripts). The first summation is over all states σ to which transitions are allowed from state ρ in the Greek molecule; likewise the inner sum is over states l to which transitions are allowed from state k in the Latin molecule. The term μ_{kl} is the transition dipole associated with excitation of the Latin molecule

from quantum state k to state l, and $\mu_{\rho\sigma}$ is defined in the same way for the Greek molecule. Similarly, the characteristic frequencies f_{kl} and $f_{\rho\sigma}$ are those associated with the said transitions.

For the purpose of classical simulation methods, the greatest importance of the London dispersion formula, Equation 2.66, is that the attractive potential falls off with the separation distance of the molecules to the sixth power ($\mathcal{V} \sim -1/r^6$). Another important point is that the model results in a purely additive potential. That is, the energy of three or more molecules is simply the sum of the interaction over all pairs. In the words of London [*98*],

> *If several molecules interact simultaneously with each other, one has to imagine that each molecule induces in each of the others a set of coordinated periodic dipoles, which are in constant phase relation with the corresponding inducing original dipoles. Every molecule is thus the seat of very many incoherently superposed sets of induced periodic dipoles caused by the different acting molecules. Each of these induced dipoles has always such an orientation that it is attracted by its corresponding generating dipole, whereas the other dipoles, which are not correlated by any phase relation, give rise to a periodic interaction only and, on an average over all possible phases, contribute nothing to the interaction energy. So one may imagine that the simultaneous*

interaction of many molecules can simply be built up as an additive superposition of single forces between pairs.

This is a fortunate result for classical simulation methods, since calculating three-body intermolecular interactions (not to mention higher orders) would be prohibitively expensive. For a system of N atoms, there are of order of N cubed ($O(N^3)$) three-body interactions, while only $O(N^2)$ pair interactions. Thus, in a system of several thousand atoms, any intermolecular potential that is not pairwise additive would be orders of magnitude more expensive to compute.

Though it is generally accepted that London's result shows the proper dependence of the potential with separation distance ($\mathcal{V} \sim -1/r^6$), there is not such an agreement on the proper form of the repulsive intermolecular interaction. The repulsive interaction comes into effect when molecules become so close that their electron clouds overlap and repel one another. Thus, it is a much shorter-range interaction than the dispersion force. Theory suggests the proper form of the potential is a decaying exponential function in separation distance, though most force fields use some type of power formula analogous to the dispersion ($\mathcal{V} \sim 1/r^n$). Casting the dispersion and repulsion forces in the same potential, a common mathematical form is attributed to Mie [*99*],

$$\mathcal{V}_{ij}^{Mie} = \frac{\varepsilon_{ij}(n^n m^m)^{1/(n-m)}}{n-m}\left[\left(\frac{\sigma_{ij}}{r_{ij}}\right)^n - \left(\frac{\sigma_{ij}}{r_{ij}}\right)^m\right] \tag{2.67}$$

This model takes the general shape shown in Figure 2.14, and the algebraic form allows the parameter ε_{ij} to be interpreted as the "well depth" of the potential, while the radius σ_{ij} is the distance at which the potential becomes positive (see Figure 2.14). Of course, for the attractive term to be consistent with London's theory, we have $m = 6$. The value of n varies in practice, usually taking values between nine and fourteen. A common choice is $n = 12$, which results in the well-known Lennard-Jones 12-6 potential,

$$\mathcal{V}_{ij}^{LJ} = 4\varepsilon_{ij}\left[\left(\frac{\sigma_{ij}}{r_{ij}}\right)^{12} - \left(\frac{\sigma}{r_{ij}}\right)^{6}\right] \tag{2.68}$$

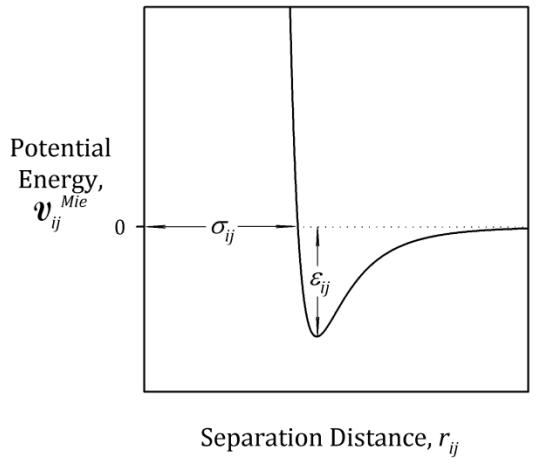

Figure 2.14. General shape of Mie's potential.

Equation 2.68 gives the intermolecular interaction between two spherical, noncharged, nonpolar molecules. Thus, it works quite well in modeling Argon and other monatomic systems. For more complex molecules, it may be applied to the individual

atoms in the molecule. Commonly, each atom in the system is assigned its own well depth and Lennard-Jones radius, and the parameters for pairs are calculated with some sort of mixing rule. Common mixing rules include the Lorentz-Berthelot rules used in AMBER [*100*] and CHARMM [*95*], prescribing a geometric mean for the well depths and an arithmetic mean for the radii [*101*],

$$\varepsilon_{ij} = \left(\varepsilon_i \varepsilon_j\right)^{1/2} \tag{2.69}$$

$$\sigma_{ij} = \frac{\sigma_i + \sigma_j}{2} \tag{2.70}$$

or, in other force fields such as OPLS [*91*], a geometric mean is used instead for the radii,

$$\sigma_{ij} = \left(\sigma_i \sigma_j\right)^{1/2} \tag{2.71}$$

While the Lennard-Jones potential accounts for the general repulsion and induced dipole–induced dipole attraction between atoms, it will not account for any interactions due to permanent charges, dipoles, or higher order multipoles in the molecule. For ions and molecules with permanent multipoles, the electrostatic forces may be calculated following Coulomb's law,

$$\mathcal{V}_{ij}^{Coul} = \frac{1}{4\pi\epsilon_0} \frac{q_i q_j}{r_{ij}} \tag{2.72}$$

where q_i and q_j are electrostatic point charges, which may be assigned in a way that reproduces the ionic charge or permanent multipoles of each molecule.

Commonly, the positions of the charges in Equation 2.72 are assumed constant and fixed at the atomic centers, yet this assumption is not necessary. For molecules with complex electrostatic interactions, better results may be obtained with other approaches. For example, many force fields developed for water make use of point charges assigned to locations away from the atom centers [*102*,*103*].

More sophisticated electrostatic models include the core-shell approach [*104*,*105*], which is most commonly applied to ions, and the fluctuating charge method [*106*,*107*], used for covalently bonded molecules. The core-shell model provides a means for the atoms to undergo polarization, by dividing an atom into a charged shell, and a core that may be neutral or carry a charge. The shell may be displaced spatially from the core, but the two are coupled with a restoring force (usually harmonic). To allow the use of a restoring force, some portion of the atomic mass must be artificially assigned to the charged shell; alternatively, the shell positions may be computed by minimizing the electrostatic energy of the system. In the fluctuating charge model, the point charges are fixed relative to the nuclei, either on the atomic centers, or on some well-defined point away from the atomic centers [*108*]. This model incorporates the concept of electronegativity of atoms, and allows partial electronic charges to migrate across covalent bonds as to minimize the overall electrostatic energy of the system. The method can be used in dynamic simulations by assigning a separate equation of motion to the charges with the extended Lagrangian approach, requiring fairly little additional computational overhead [*107*].

Bond stretching interactions for covalent bonds are most commonly treated as harmonic springs. The potential energy penalty associated with moving the bond from its equilibrium position, b_0, is then a quadratic function with some force constant, k_b,

$$\mathcal{V}_{ij}^{bond} = \frac{1}{2} k_b \left(r_{ij} - b_0\right)^2 \tag{2.73}$$

Higher-order bond potentials may be used to reproduce anharmonic behavior [*109*], finite extension [*110*], as well as more elaborate reactive potentials that allow creation and dissociation of bonds [*111*]. In other cases, as mentioned in Section 2.2.2.1, bonds may be constrained such that they have no vibratory motion at all [*93*,*94*].

Much like the stretching of covalent bonds, the bending motion of the angle between three adjacently bonded atoms can be treated with a harmonic potential,

$$\mathcal{V}_{ijk}^{angle} = k_\theta \left(\theta_{ijk} - \theta_0\right)^2 \tag{2.74}$$

In this dissertation, we refer to the angle θ_{ijk} between two bonds as a *valence angle*. Anharmonic bending interactions can be produced by adding an additional quadratic potential (such as that in Equation 2.73) to atoms i and k, as in the Urey-Bradley potential implemented in CHARMM [*95*].

The last interaction between bonded atoms we will discuss is torsional, or dihedral, rotation about a bond. A dihedral angle φ_{ijkl} is defined for four atoms i, j, k, and l, as the angle between the plane defined by atoms i, j, k, and the plane defined by atoms j, k, l. According to the IUPAC convention, the angle is computed such that a

trans arrangement of the atoms results in $\varphi_{ijkl} = 180°$. Several functional forms exist for torsional potentials, each with the condition that the potential is periodic with respect to the dihedral angle, with a period of 360 degrees. A common choice is based on the cosine function, sometimes referred to as a periodic dihedral,

$$\mathcal{V}_{ijkl}^{periodic} = k_{\varphi}\left(1 + \cos\left(n\varphi_{ijkl} - \varphi_0\right)\right) \tag{2.75}$$

where k_{φ} is the torsional force constant, n is the multiplicity (the number of peaks or valleys observed in the potential over one full rotation of the bond), and φ_0 is the phase shift. Other choices exist for the torsional interaction, such as the Ryckaert-Bellemans expansion used in GROMACS [*112*],

$$\mathcal{V}_{ijkl}^{RB} = \sum_{n=0}^{5} C_n\left[\cos\left(\varphi_{ijkl} - 180°\right)\right]^n \tag{2.76}$$

For more complicated torsional potentials, spline functions are often used based on tabulated values. Additionally, there is another type of dihedral potential in common use, referred to as *improper dihedral* force field terms. These can be defined by any four atoms, not necessarily those connected by three consecutive bonds. They are intended to keep certain chemical groups in a planar orientation (for example, aromatic rings, or carbonyl groups). In this work, the interaction potentials used for improper dihedral terms are the same as the periodic dihedral term shown in Equation 2.75.

The above interactions cover most of the relevant modes of molecular motion, though in real molecules, additional coupling may be observed between these modes.

For example, the stretching behavior of a bond might be affected by the bending of an adjacent angle, or a torsional barrier might also depend on the bonds and angles in its constituent atoms. Complex potential functions, such as COMPASS [*97*] and its predecessor CFF [*113*], use various cross terms to account for such interactions. This approach can improve agreement with vibrational modes (e.g., infrared spectroscopy data), and vibrational modes (e.g., microwave spectroscopy data). However, for other applications, such as estimating thermodynamic properties, the added computational expense of the additional terms (not to mention the effort required to properly parameterize the cross terms) does not always result in improved accuracy, especially when compared to other models where the quality of nonbonded interactions is good [*114*].

Once the form and parameters are chosen for the potential energy function, there are many methods available to simulate the behavior of chemical systems. In the following sections, we will describe two of the most popular methods, molecular dynamics (MD), and Monte Carlo (MC).

§ 2.2.2.3. Molecular Dynamics Simulations

The molecular dynamics (MD) method allows one to calculate how atoms move through space in time. From this information, it is relatively easy to calculate material properties, provided the trajectory covers an appropriate time scale for the relevant property. For example, by taking simple averages over time, one can obtain thermodynamic properties such as the internal energy, specific volume, temperature,

and pressure. In the molecular dynamics method, the equations of motion are integrated over time to obtain a trajectory of molecular motion.

For each atom in a molecular system, the equations of motion can be cast in the Hamiltonian form as

$$\dot{\mathbf{r}}_i = \frac{\partial \mathcal{H}}{\partial \mathbf{p}_i} \tag{2.77}$$

$$\dot{\mathbf{p}}_i = -\frac{\partial \mathcal{H}}{\partial \mathbf{r}_i} \tag{2.78}$$

where $\mathbf{r}_i$ is the Cartesian coordinates vector of atom i, $\mathbf{p}_i$ is the corresponding momentum vector, and overdots are used in the Newtonian fashion for time derivatives. The quantity $\mathcal{H}$ is the system Hamiltonian, which is simply the sum of the kinetic and potential energies,

$$\mathcal{H}(\mathbf{r}^N, \mathbf{p}^N) = \mathcal{K}(\mathbf{p}^N) + \mathcal{V}(\mathbf{r}^N) \tag{2.79}$$

where $\mathcal{V}(\mathbf{r}^N)$ is the force field energy and $\mathcal{K}(\mathbf{p}^N)$ takes the form

$$\mathcal{K}(\mathbf{p}^N) = \sum_{i=1}^{N} \left(\frac{1}{2m_i} \mathbf{p}_i{}^T \mathbf{p}_i \right) \tag{2.80}$$

in which $\mathbf{p}_i$ is represented as a column vector, and the superscript T indicates the transpose. For a system of N atoms, the Hamiltonian is a function of $6N$ coordinates (three velocity components and three momentum coordinates for each atom), the collection of which is often referred to as *phase space*.

As an alternative to the Hamiltonian form given in Equations 2.77 and 2.78, the equations of motion may also be cast in terms of the Lagrangian, using the Euler-Lagrange equation for the system

$$\frac{d}{dt}\left(\frac{\partial \mathcal{L}}{\partial \dot{\mathbf{r}}_i}\right) - \frac{\partial \mathcal{L}}{\partial \mathbf{r}_i} = 0 \tag{2.81}$$

where the Lagrangian, $\mathcal{L}$, is the kinetic energy minus the potential energy

$$\mathcal{L}(\mathbf{r}^N, \mathbf{p}^N) = \mathcal{K}(\mathbf{p}^N) - E(\mathbf{r}^N) \tag{2.82}$$

Taking the derivatives in Equation 2.81, we get the familiar form of Newton's second law,

$$\mathbf{f}_i = m_i \mathbf{a}_i \tag{2.83}$$

with the force on atom i given by $\mathbf{f}_i = \partial \mathcal{V} / \partial \mathbf{r}_i$ and the acceleration of atom i given by $\mathbf{a}_i = \ddot{\mathbf{r}}_i = \dot{\mathbf{p}}_i / m_i$. Similarly, it is not difficult to surmise Newton's second law, Equation 2.83, from the Hamiltonian form given by Equations 2.77 and 2.78 [*115*].

In a molecular dynamics simulation, Equation 2.83 is integrated numerically. This is typically done using finite difference schemes, including the Gear predictor-corrector schemes [*116*], the Verlet method and its variations [*117*,*118*], and so-called *leap-frog* schemes [*119*]. In each of these schemes, the equations of motion are used to advance the system over some time step Δt, and the method is repeated to obtain the trajectory of the system over time. Here, we will discuss the leap frog scheme as implemented in

GROMACS [*120*], since this is the main program used for molecular dynamics simulation in this dissertation.

The leap frog algorithm gets its name because of its similarity to the children's game. Atomic positions and forces are calculated at each time step, while the velocities are calculated at a time halfway between each step. The atomic velocities at time $t - \frac{\Delta t}{2}$ are advanced to time $t + \frac{\Delta t}{2}$ using the forces at time t, in a sense leaping over the positions at each time step. The positions are then advanced to the next time step $t + \Delta t$ using the velocities at the half time step, thus, leaping over the velocities. The equations are as follows

$$\dot{\mathbf{r}}_i\left(t + \frac{\Delta t}{2}\right) = \dot{\mathbf{r}}_i\left(t - \frac{\Delta t}{2}\right) + \frac{\mathbf{f}_i(t)}{m_i}\Delta t \tag{2.84}$$

$$\mathbf{r}_i(t + \Delta t) = \mathbf{r}_i(t) + \dot{\mathbf{r}}_i\left(t + \frac{\Delta t}{2}\right)\Delta t \tag{2.85}$$

This formulation is equivalent to the mathematics of the Verlet algorithm, but numerically sidesteps some of the error accumulation in the Verlet integrator due to calculation of small differences in large numbers [*121*].

The traditional equations of motion, described in Equations 2.77 through 2.83, apply to an isolated system at constant volume. In statistical mechanics, this is referred to as the *microcanonical* ensemble; often, it is identified simply by listing the constraints imposed on the system—that is, the number of atoms, volume, and total energy—as the NVE ensemble). Formulations exist for sampling other ensembles with the MD

approach, the most common ones being the *canonical*, or NVT ensemble, and the isothermal-isobaric, or NPT ensemble. In such formulations, the system is typically coupled to an artificial bath, or reservoir, which imparts fluctuations in momentum and/or volume as appropriate. In what follows, we describe a few of the commonly used MD methods for sampling the NVT ensemble and the NPT ensemble.

From statistical mechanics, we know that the temperature of a system in the NVE ensemble can be expressed as the ensemble average [*122*]:

$$T = \frac{2}{3(N - N_c)k_B}\langle \mathcal{K} \rangle \tag{2.86}$$

where N_c is the number of constraints imposed on the system, including any bond lengths or valence angles that are held fixed, and the removal of overall translational or rotational motion in the system. While the thermodynamic temperature, T, exists only in reference to the entire ensemble, it is convenient to think of an *instantaneous* or *kinetic temperature*,

$$\mathcal{T} = \frac{2\mathcal{K}}{3(N - N_c)k_B} \tag{2.87}$$

This quantity is defined such that its average over time (or its weighted average over all phase space) will be equal to the thermodynamic temperature. Thus, the goal of any temperature controlling method (or *thermostat*) should be to steer the long-time average of $\mathcal{T}$ towards the desired value of T. One sure way to do this would be to simply scale all particle velocities by the factor $(T/\mathcal{T})^{1/2}$ at each time step, thus, ensuring that

$\mathcal{T} = T$ for all time. Therefore, its long-time average would also result in the desired temperature. However, if one wants to properly sample the NVT ensemble, producing the relation $\langle \mathcal{T} \rangle = T$ alone is not sufficient to guarantee an adequate sampling of phase space. In fact, constraining the instantaneous temperature in this way results in dynamics that are far different than any real system at constant thermodynamic temperature [*123*]. For simulation at constant NVT, it is important that $\mathcal{T}$ be allowed to fluctuate in the same manner as it would in the canonical ensemble.

Berendsen and coworkers [*124*] suggested a refinement to the velocity rescaling approach outlined above. They imagined an external bath having temperature T, to which the system is coupled. Assuming a first-order relaxation process by which the system temperature is brought to that of the bath, the appropriate scaling factor, χ_T, would be

$$\chi_T = \left(1 + \frac{\Delta t}{\tau_{T,B}}\left(\frac{T}{\mathcal{T}} - 1\right)\right)^{1/2} \tag{2.88}$$

which allows some fluctuation of $\mathcal{T}$ about T with a predefined relaxation time constant $\tau_{T,B}$. This method still does not give true statistical sampling of the canonical ensemble, but is commonly used. It is effective in equilibration, and it often results in accurate averages of simple properties.

When a proper treatment of fluctuations in the NVT ensemble is needed (i.e., when derivative properties are being examined, such as the heat capacity), the method developed by Nosé [*125*] and extended by Hoover [*126*] will give a more proper phase

space distribution. A near-exact canonical phase space sampling can be achieved with this method for large systems in which the *ergodic hypothesis* applies (see Haile for a helpful discussion of ergodicity [*127*]). For small or stiff systems, however, the Nosé-Hoover method must be applied recursively to achieve proper sampling of the canonical phase space distribution [*128*].

Like the method of Berendsen et al. [*124*], the method devised by Nosé considers the system coupled to an external bath. However, in this scheme, the fluctuations in $\mathcal{T}$ are monitored in the bath as well as the system. Thus, the simulation has an added degree of freedom representing the kinetic temperature of the bath. Using the formulation of Hoover [*126*], the equations of motion are

$$\dot{\mathbf{r}}_i = \frac{\mathbf{p}_i}{m_i} \tag{2.89}$$

$$\dot{\mathbf{p}}_i = \mathbf{f}_i - \xi \mathbf{p}_i \tag{2.90}$$

with the friction coefficient, ξ, given by

$$\dot{\xi} = \frac{(N - N_c)k_B}{Q}(\mathcal{T} - T) \tag{2.91}$$

where Q is the *thermal inertia* of the bath. Being of the Berendsen camp, the programmers of GROMACS prefer to cast the bath in terms of the time period of oscillations in $\mathcal{T}$ [*129*], by defining

$$\tau_{T,NH} = 2\pi\sqrt{\frac{Q}{(N - N_c)T}} \tag{2.92}$$

This is a more convenient way of defining the bath, because a single value of $\tau_{T,NH}$ can be used for many system sizes, and the bath "mass" will automatically be scaled accordingly. Note that it is possible to cast the Berendsen thermostat in the form of Equations 2.89 and 2.90, but in that case the friction parameter is directly related to $\mathcal{T}$ instead of having dependence through a first-order differential equation such as Equation 2.91 [*130*]. In this sense, it is often said that the friction parameter in the Nosé-Hoover scheme follows its own equation of motion, whereas in the Berendsen scheme it is prescribed directly from the phase space vector.

Much like the techniques described above for controlling the temperature of an MD simulation, techniques also exist for controlling the system pressure. As in dealing with thermostats, it is useful to define an instantaneous property that relates to the pressure,

$$\boldsymbol{\mathcal{P}} = \frac{1}{V}\left(\sum_{i=1}^{N} m_i \dot{\mathbf{r}}_i \dot{\mathbf{r}}_i{}^T + \sum_{i=1}^{N}\sum_{j=i+1}^{N} \mathbf{r}_{ij}\mathbf{f}_{ij}{}^T\right) \tag{2.93}$$

from which the thermodynamic pressure may be calculated as $\boldsymbol{P} = \langle\boldsymbol{\mathcal{P}}\rangle$. In Equation 2.93, the volume is in general calculated from the determinant

$$V = |\mathbf{H}| \tag{2.94}$$

The box vector matrix $\mathbf{H}$ has as its columns the vectors $\mathbf{a}$, $\mathbf{b}$, and $\mathbf{c}$, each describing one edge of the simulation box. Using the box vector matrix, we can also define a set of scaled atomic coordinates $\mathbf{s}$, such that dimensional coordinates may be obtained by

$$\mathbf{r} = \mathbf{H}\mathbf{s} \tag{2.95}$$

That is, we multiply the scaled coordinates, $\mathbf{s}$, by the box vectors to obtain the dimensional Cartesian coordinates of the atoms.

Analogous to the Berendsen thermostat, the Berendsen pressure coupling method considers an external bath that dampens pressure fluctuations, with first-order kinetics [*124*]. At each time step, the bath causes a change in box vectors by the tensor

$$\boldsymbol{\chi}_P = \boldsymbol{\delta} - \frac{\Delta t}{3\tau_{P,B}}\kappa_T(\mathbf{P}_s - \boldsymbol{\mathcal{P}}) \tag{2.96}$$

where $\boldsymbol{\delta}$ is the Kroneker delta, κ_T is the (scalar) isothermal compressibility, $\mathbf{P}_s$ is the desired setpoint pressure tensor, and we have introduced the Berendsen pressure coupling time constant $\tau_{P,B}$, which is analogous to $\tau_{T,B}$. Equation 2.96 is applied at each time step such that the new box vectors are given by $\mathbf{H}(t + \Delta t) = \boldsymbol{\chi}_P\mathbf{H}(t)$. New atomic coordinates can then be calculated by 2.95.

For anisotropic materials, such as crystals, the compressibility in Equation 2.96 is not a scalar, but a rank three tensor, $\boldsymbol{\kappa}_T$. In such case, refer to the equations given in the *GROMACS User Manual* [*131*]. Note that the exact value of the compressibility need not be known, since this would only have the effect of altering the time constant $\tau_{P,B}$. Thus, the pressure in anisotropic materials may still be controlled using Equation 2.96, but the

actual relaxation times will vary for each component of $\boldsymbol{\mathcal{P}}$ [*124*]. Only when $\boldsymbol{\kappa}_T$ is accurately specified does the time constant $\tau_{P,B}$ actually correspond to the relaxation times observed in a simulation.

As was the case for temperature coupling, the assumptions in the Berendsen pressure coupling scheme allows the system to undergo damped fluctuations in the instantaneous pressure, while steering the thermodynamic pressure towards a prescribed value. Also like the Berendsen temperature coupling scheme, Berendsen pressure coupling does not result in proper sampling of phase space in any ensemble from statistical mechanics (i.e., the NPT ensemble). When such sampling is required, a better choice is the barostat developed by Parrinello and Rahman [*132*].

In the Parrinello-Rahman barostat, the equations of motion are augmented in a similar way to the equations used in the Nosé-Hoover thermostat. In this case, the box vector matrix becomes an added degree of freedom. The equations of motion for the Parrinello-Rahman barostat are best developed using the Lagrangian (Equation 2.82) with the appropriate Euler-Lagrange equation [*132*], which we show here for an isotropic setpoint pressure P_s. To do this, we add a term to the potential energy, due to the box size,

$$\mathcal{V}_{box} = P_s V = P_s |\boldsymbol{H}| \tag{2.97}$$

and a second term is added to the kinetic energy,

$$\mathcal{K}_{box} = \frac{1}{2} Q \mathrm{Tr}(\mathbf{H}^T \mathbf{H}) \tag{2.98}$$

where the Tr operator indicates the trace of a matrix, or the sum of its diagonal components. The Q term in Equation 2.98 is a fictitious *box mass*, analogous to the Q in Equation 2.91. Thus, the system Lagrangian takes the form $\mathcal{L} = \mathcal{K} + \mathcal{K}_{box} - \mathcal{V} - \mathcal{V}_{box}$. For our system, the Euler-Lagrange equation is given by Equation 2.81, with the additional relation for our new independent variable,

$$\frac{d}{dt}\left(\frac{\partial \mathcal{L}}{\partial \dot{\mathbf{H}}_i}\right) - \frac{\partial \mathcal{L}}{\partial \mathbf{H}_i} = 0 \tag{2.99}$$

Using the altered Lagrangian for the pressure coupling, the equations of motion are

$$m_i \ddot{\mathbf{s}} = \mathbf{H}^{-1}\mathbf{f} - m_i \mathbf{G}^{-1}\dot{\mathbf{G}}\dot{\mathbf{s}} \tag{2.100}$$

$$Q\ddot{\mathbf{H}} = (\boldsymbol{\mathcal{P}} - \mathbf{P}_s) V (\mathbf{H}^{-1})^T \tag{2.101}$$

where the matrix $\mathbf{G}$ is given by $\mathbf{G} = \mathbf{H}^T\mathbf{H}$ and we represent the isotropic setpoint pressure in its tensor form $\mathbf{P}_s$. Also, as in the Nosé-Hoover thermostat, the coupling strength may be specified independent of system size by redefining the mass parameter, Q, in terms of a time constant, $\tau_{P,PR}$. For details on defining $\tau_{P,PR}$, see the GROMACS User Manual [*131*].

§ 2.2.2.4. Monte Carlo Simulations

Monte Carlo (MC) methods arose in the 1940s as a computational approach to statistical sampling. Invention of the method is usually attributed to Stanislaw Ulam and

John von Neumann, both at Los Alamos National Labs, shortly after completion of the ENIAC electronic computer during World War II. The basic method involves the generation of random numbers which determine simulated events according to a prescribed statistical model. According to his account, Nicholas Metropolis suggested the name "Monte Carlo" to reflect the random aspect of the method, after the well-known casino in Monaco where Ulam's uncle often gambled [*133*].

While the Monte Carlo method was originally developed to study neutron scattering and fission processes in nuclear reactors, it is quite useful in molecular simulations. The algorithm is most commonly cast in the form devised by Metropolis [*134*]. The natural ensemble in Metropolis MC is the canonical (NVT) ensemble, governed by Boltzmann statistics. In the Metropolis MC method, a random configuration is generated for the system, and its energy is compared to the previously sampled configuration. The new configuration is accepted according to the probability

$$\rho = \min\left(1, e^{-(E-E_i)/k_BT}\right) \tag{2.102}$$

Thus, if the energy E of the new configuration is lower than the energy E_i of the last sampled configuration, the new configuration is accepted as the next sample. On the other hand, if $E > E_i$, the new configuration is accepted with a probability based on the exponential factor in Equation 2.102. If the new configuration is rejected, the last configuration i is counted again as the next sample. Formulations analogous to 2.102 are easily obtained for other ensembles [*135*].

§ 2.2.2.5. Hybrid Methods

In this dissertation, we make frequent use of a relatively new method which combines MD and MC methods, called replica exchange molecular dynamics (REMD). In the REMD method, a set of trajectories are sampled according to the molecular dynamics equations of motion for the ensemble of interest (usually NVT or NPT). These individual trajectories, or replicas, are usually set up to differ in the temperature and/or pressure of the simulation. At periodic intervals, Monte Carlo moves are attempted in which a pair of replicas are swapped; that is, the atomic coordinates of one replica are exchanged with the coordinates of another replica. Velocities are usually scaled upon swapping, depending on the particular formulation, such that the Monte Carlo probability of accepting the move depends only on the potential energies of the respective replicas.

Replica exchange methods are useful for equilibrating glassy systems, such as polymers, since they allow a single replica to overcome potential energy barriers that would otherwise trap it in a local state. The method is very similar to simulated annealing [*136*], in that thermal energy is added to the system to increase the probability of barrier crossings. However, unlike simulated annealing methods, the REMD framework results in statistically valid sampling at each temperature simulated, over the entire simulation time.

§ 2.2.2.6. Rotational Isomeric States (RIS)

Methods utilizing the principle of rotational isomeric states (RIS) were developed extensively in the 1960s by Flory and coworkers for the study of polymers. These methods consider different conformational isomers of a molecule, in which the rotational angle(s) about one or more bonds differ. These rotational isomers have unique energies that depend on the rotational angle of each bond, and by employing statistical averages of such states, the properties of long chain molecules can be deduced. In this section, we outline the RIS method for molecules with rigid bond lengths and valence angles, then extend the method for PLA-like molecules with the introduction of virtual bonds. For a more detailed description, see the text by Flory [*137*].

Consider the geometry shown in Figure 2.15, which depicts a portion of a polymer molecule. The atoms shown may correspond to, for example, the carbon atoms in a polyethylene chain. Centered about each atom i is a Cartesian coordinate system, such that its x-axis is collinear with the bond from atom i to atom $i-1$ (labeled simply as bond i). The y-axis of the coordinate system on i is taken to be in the plane of bonds $i-1$ and i, such that its projection onto x_{i-1} is positive. The z-axis is taken such that a right-handed coordinate system is defined by $x_i y_i z_i$. The bond lengths and valence angles are assumed to be rigid.

Using the RIS concept, we will calculate the unperturbed chain dimensions for a polymer of the type shown in Figure 2.15, with an arbitrary number of bonds. We do

this by performing multiple coordinate transformations on the vector representations of the bonds. In this way, all of the bond vectors may be expressed in a single coordinate system, and their sum may be taken to find the overall end-to-end distance of the chain.

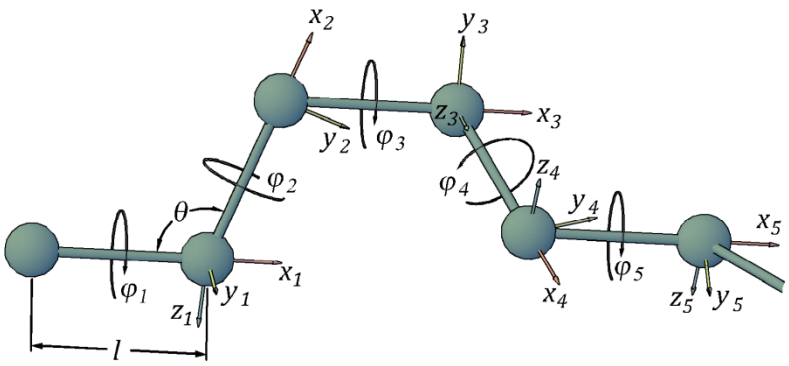

Figure 2.15. Geometry of a polymer segment having rigid bonds and angles. The bond length l and the valence angle θ are identical for each bond, while the dihedral angle φ_i is unique to bond i. Orientations of the y_1 and z_1 axes are arbitrary, with the value of φ_1 dependent on them; the remaining axes and dihedral angles are defined as discussed in the text.

We can express bond $i+1$ as a column vector in coordinate system $i+1$ as

$$\mathbf{b}_{i+1} = \begin{bmatrix} l \\ 0 \\ 0 \end{bmatrix} \tag{2.103}$$

where we have made use of the assumption that all bond lengths take the same value, l. If we are able to express $\mathbf{b}_{i+1}$ in coordinate system i, we can add the two vectors in a common frame of reference. This is done using rotation matrices. First, we rotate

coordinate system $i+1$ about its z-axis, by the angle θ_i. The rotation matrix corresponding to this operation is

$$\mathbf{R}_z(\theta_i) = \begin{bmatrix} \cos\theta_i & \sin\theta_i & 0 \\ -\sin\theta_i & \cos\theta_i & 0 \\ 0 & 0 & 1 \end{bmatrix} \tag{2.104}$$

Then, the coordinate system is rotated about its x-axis by the angle φ_i using the rotation matrix:

$$\mathbf{R}_x(\varphi_i) = \begin{bmatrix} 1 & 0 & 0 \\ 0 & \cos\varphi_i & \sin\varphi_i \\ 0 & -\sin\varphi_i & \cos\varphi_i \end{bmatrix} \tag{2.105}$$

By applying the above rotation matrices, any vector $\mathbf{v}$ in coordinate system $i+1$ may be represented as a vector $\mathbf{v}'$ in coordinate system i. It is useful to define a single transition matrix for this operation, such that

$$\mathbf{v}' = \mathbf{T}_i\mathbf{v} \tag{2.106}$$

where the transition matrix takes the form

$$\mathbf{T}_i = \mathbf{R}_x(\varphi_i)\mathbf{R}_z(\theta_i) = \begin{bmatrix} \cos\theta_i & \sin\theta_i & 0 \\ -\cos\varphi_i\sin\theta_i & \cos\varphi_i\cos\theta_i & -\sin\varphi_i \\ -\sin\varphi_i\sin\theta_i & \sin\varphi_i\cos\theta_i & \cos\varphi_i \end{bmatrix} \tag{2.107}$$

The same result could be arrived at, using the formula for Euler rotation, with the z-x-z convention and Euler angles $\alpha = \theta_i$, $\beta = \varphi_i$, and $\gamma = 0$.

With the transition matrix $\mathbf{T}_i$ defined for every bond i, we can go about calculating the end-to-end distance of a polymer having n bonds. We can express any bond vector $\mathbf{b}_j$ in the coordinate system of bond i, for $j > i$, as the matrix product:

$$\mathbf{T}_i\mathbf{T}_{i+1}\cdots\mathbf{T}_{j-1}\mathbf{b}_j = \left(\prod_{k=i}^{j-1}\mathbf{T}_k\right)\mathbf{b}_j \tag{2.108}$$

To find the end-to-end distance of the polymer chain, we take the sum of all bond vectors in the common coordinate system on bond 1:

$$\mathbf{r} = \mathbf{b}_1 + \sum_{i=2}^{n}\left(\prod_{j=1}^{i-1}\mathbf{T}_j\right)\mathbf{b}_i \tag{2.109}$$

We are interested in the magnitude of $\mathbf{r}$, the square of which is obtained from the scalar product. Using our column vector notation, the scalar product takes the form $\mathbf{r}^T\mathbf{r}$. Thus, we have

$$r^2 = \left[\mathbf{b}_1 + \sum_{i=2}^{n}\left(\prod_{j=1}^{i-1}\mathbf{T}_j\right)\mathbf{b}_i\right]^T\left[\mathbf{b}_1 + \sum_{i=2}^{n}\left(\prod_{j=1}^{i-1}\mathbf{T}_j\right)\mathbf{b}_i\right] \tag{2.110}$$

This formula can be simplified using a number of properties of matrices. We use the relations $(\mathbf{A}+\mathbf{B})^T = \mathbf{A}^T + \mathbf{B}^T$, $(\mathbf{AB})^T = \mathbf{B}^T\mathbf{A}^T$, and the fact that $\mathbf{v}^T\mathbf{w} = \mathbf{w}^T\mathbf{v}$ for any column vectors $\mathbf{v}$ and $\mathbf{w}$, to obtain

$$r^2 = {b_1}^2 + 2{\mathbf{b}_1}^T\sum_{i=2}^{n}\left(\prod_{j=1}^{i-1}\mathbf{T}_j\right)\mathbf{b}_i + \sum_{i=2}^{n}\sum_{j=2}^{n}{\mathbf{b}_i}^T\left(\prod_{k=1}^{i-1}\mathbf{T}_k\right)^T\left(\prod_{h=1}^{j-1}\mathbf{T}_h\right)\mathbf{b}_j \tag{2.111}$$

Taking the ensemble average, we obtain the average end-to-end distance:

$$\langle r^2 \rangle = l^2 + \mathbf{b}^T \left[2 \frac{\int e^{-E(\boldsymbol{\varphi})/k_B T} \sum_{i=2}^{n} \left(\prod_{j=1}^{i-1} \mathbf{T}_j \right) d\boldsymbol{\varphi}}{\int e^{-E(\boldsymbol{\varphi})/k_B T} \, d\boldsymbol{\varphi}} \right.$$
$$\left. + \frac{\int e^{-E(\boldsymbol{\varphi})/k_B T} \sum_{i=2}^{n} \sum_{j=2}^{n} \left(\prod_{k=1}^{i-1} \mathbf{T}_k \right)^T \left(\prod_{h=1}^{j-1} \mathbf{T}_h \right) d\boldsymbol{\varphi}}{\int e^{-E(\boldsymbol{\varphi})/k_B T} \, d\boldsymbol{\varphi}} \right] \mathbf{b} \tag{2.112}$$

where we have invoked Equation 2.103 and dropped the subscripts on the bond vectors. In this expression, E is the potential energy of the chain, k_B is the Boltzmann constant, and T is the temperature of interest. The vector $\boldsymbol{\varphi}$ has as its components all values of φ_i, for $i = 1$ to n.

Implicit in Equation 2.112 is the assumption that the energy of the polymer chain depends only on the rotational states of the bonds. We now make the additional assumption that the energy is separable for each bond; that is, the energy of the chain may be expressed as a sum of individual terms:

$$E(\boldsymbol{\varphi}) = E_1(\varphi_1) + E_2(\varphi_2) \cdots + E_n(\varphi_n) \tag{2.113}$$

Thus, Equation 2.112 may be rearranged into separate integrals. If we assume the energy attributed to each bond rotation has the same form (that is, if $E_1(\varphi) = E_2(\varphi)$, and so on), we can combine these separate integrals into the products of a single ensemble average:

$$\langle r^2 \rangle = l^2 + \mathbf{b}^T \left[2 \sum_{i=1}^{n-1} \langle \mathbf{T} \rangle^i + \sum_{i=1}^{n-1} \sum_{j=1}^{n-1} \langle \mathbf{T}^T \rangle^i \langle \mathbf{T} \rangle^j \right] \mathbf{b} \tag{2.114}$$

Note we have also redefined the summation indices. Now, making use of the fact that the rotation matrix $\mathbf{T}$ is orthogonal (that is, $\mathbf{T}^T = \mathbf{T}^{-1}$), we have

$$\langle r^2 \rangle = l^2 + \mathbf{b}^T \left[2 \sum_{i=1}^{n-1} \langle \mathbf{T} \rangle^i + \sum_{i=1}^{n-1} \sum_{j=1}^{n-1} \langle \mathbf{T} \rangle^{j-i} \right] \mathbf{b} \tag{2.115}$$

The $n-1$ diagonal elements in the double summation are simply identity matrices, and thus, may be grouped with the l^2 term. Further, the sum of upper off-diagonal elements is found to equal the sum of lower elements, if we recognize again that the transition matrix is orthogonal, and that the scalar product is commutative. Thus,

$$\langle r^2 \rangle = nl^2 + 2\mathbf{b}^T \sum_{i=0}^{n-1} \sum_{j=i+1}^{n-1} \langle \mathbf{T} \rangle^{j-i} \, \mathbf{b} \tag{2.116}$$

Here, we have also incorporated the single sum in Equation 2.115 into the double sum by adjusting the lower value of summation index i. Now, by a change of variables in the summation indices, we can express the double sum as a single sum:

$$\langle r^2 \rangle = nl^2 + 2\mathbf{b}^T \sum_{k=1}^{n-1} \sum_{h=1}^{n-k} \langle \mathbf{T} \rangle^k \, \mathbf{b} = \mathbf{b}^T \left[n + 2 \sum_{k=1}^{n-1} (n-k) \langle \mathbf{T} \rangle^k \right] \mathbf{b} \tag{2.117}$$

The sum in the brackets of Equation 2.117 is evaluated by considering the function $S_m = \sum_{k=1}^{n-1} k^m \alpha^k$ [*138*]. It can be shown that $S_{m+1} = dS_m/d \ln \alpha$. Expressing S_0 in terms of the infinite series, $\frac{\alpha}{1-\alpha} = \sum_{k=1}^{\infty} \alpha^k$, we have $S_0 = \sum_{k=1}^{\infty} \alpha^k - \alpha^{n-1} \sum_{k=1}^{\infty} \alpha^k =$

$\frac{\alpha-\alpha^n}{1-\alpha}$. Higher order sums can be obtained by differentiation of this result. Extending this result to matrix representations, and with some algebraic manipulations, we have

$$\langle r^2\rangle = \mathbf{b}^T[n(\mathbf{I}+\langle\mathbf{T}\rangle)(\mathbf{I}-\langle\mathbf{T}\rangle)^{-1} - 2\langle\mathbf{T}\rangle(\mathbf{I}-\langle\mathbf{T}\rangle^n)(\mathbf{I}-\langle\mathbf{T}\rangle)^{-2}]\mathbf{b} \qquad (2.118)$$

where $\mathbf{I}$ is the identity matrix of order 3. This allows us to calculate the characteristic ratio for a chain with n bonds as

$$C_n = \frac{\langle r^2\rangle}{nl^2} = \left\{(\mathbf{I}+\langle\mathbf{T}\rangle)(\mathbf{I}-\langle\mathbf{T}\rangle)^{-1} - \frac{2}{n}\langle\mathbf{T}\rangle(\mathbf{I}-\langle\mathbf{T}\rangle^n)(\mathbf{I}-\langle\mathbf{T}\rangle)^{-2}\right\}_{11} \qquad (2.119)$$

where we have used Equation 2.103, and the subscripts on the curly brackets indicate the 1,1 element of the matrix. Finally, Equation 2.119 may be extended to very large chains by taking the limit as $n \to \infty$,

$$C_n = \{(\mathbf{I}+\langle\mathbf{T}\rangle)(\mathbf{I}-\langle\mathbf{T}\rangle)^{-1}\}_{11} \qquad (2.120)$$

This is a useful relation to calculate the unperturbed chain dimensions of polymers having many backbone bonds with identical, independent torsional potentials. In what follows, we will show how the same relation may be used for more complicated molecules by defining *virtual bonds*.

The use of virtual bonds was developed under supervision of P.J. Flory, most notably by Brant and coworkers [*139*,*140*], to make the RIS problem more tractable for polypeptides and similar molecules. The method was necessary at that time because the computers available at the time were relatively slow. Brant et al. [*139*] showed that Equation 2.120 may be applicable for polypeptide-like molecules by defining imaginary

bonds that connect the α-carbons in the backbone of the polypeptide chain. This is illustrated in Figure 2.16.

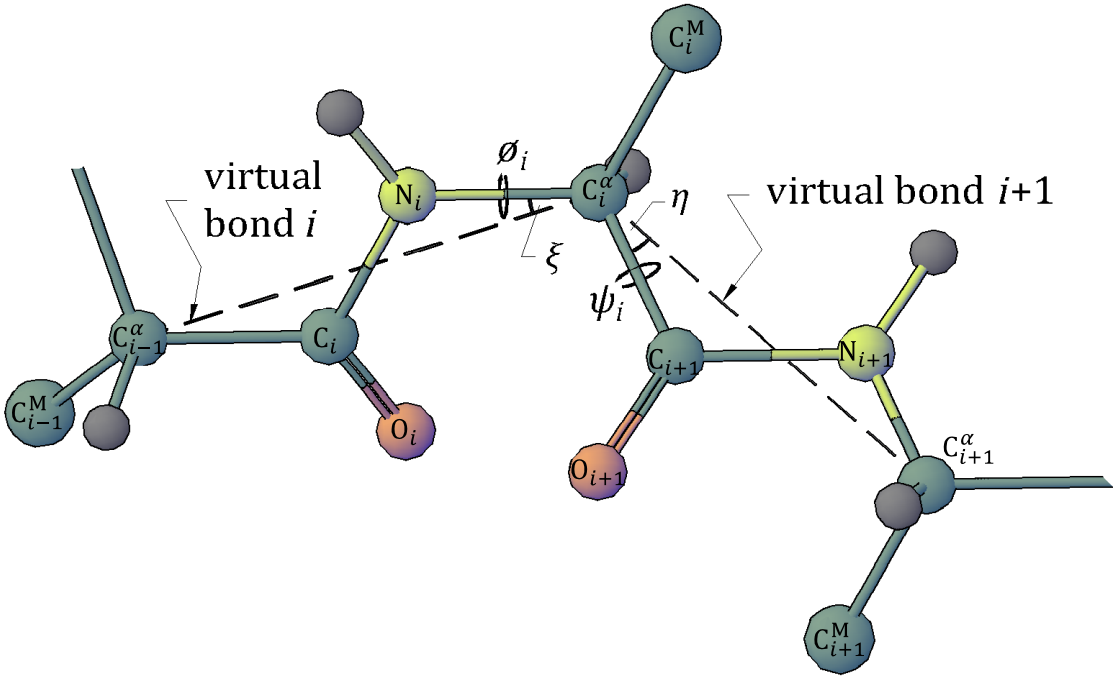

Figure 2.16. Virtual bonds defined between α-carbons in a polypeptide chain (polyalanine). Atom colors are: blue, carbon; red, oxygen; yellow, nitrogen; gray, hydrogen. Subscripts on atoms indicate the repeat unit, or residue, while superscripts on carbon atoms differentiate between alpha carbons (α), methyl carbons (M), and carbonyl carbons (no superscript). Methyl hydrogen atoms are omitted for simplicity.

Because the amide bond of a polypeptide is essentially rigid, and remains in the *trans* position, it is possible to change coordinates from virtual bond $i+1$ to virtual bond i using the following intermediate steps: 1.) Rotate the coordinate system from

virtual bond $i+1$ to that of the C_i^{α}-C_{i+1} bond; 2.) Rotate the coordinate system from the C_i^{α}-C_{i+1} bond to the N_i-C_i^{α} bond; 3.) Rotate the coordinate system from the N_i-C_i^{α} bond to virtual bond i. Referring to Figure 2.16 for the geometric parameters, the overall rotation matrix is given by the matrix product:

$$\mathbf{T}_i = \mathbf{T}(\phi_i, \psi_i) = \mathbf{R}_3(\xi)\mathbf{R}_2(\theta, \phi_i)\mathbf{R}_1(\eta, \psi_i) \tag{2.121}$$

with the valence angle θ defined between the real bonds as in Figure 2.15. The individual rotation matrices $\mathbf{R}_1$, $\mathbf{R}_2$, and $\mathbf{R}_3$, corresponding to the three steps discussed above, have the form

$$\mathbf{R}_1(\eta, \psi_i) = \begin{bmatrix} \cos\eta & -\sin\eta & 0 \\ -\sin\eta\cos\psi_i & -\cos\eta\cos\psi_i & \sin\psi_i \\ -\sin\eta\sin\psi_i & -\cos\eta\sin\psi_i & -\cos\psi_i \end{bmatrix} \tag{2.122}$$

$$\mathbf{R}_2(\theta, \phi_i) = \begin{bmatrix} \cos\theta & \sin\theta & 0 \\ -\sin\theta\cos\phi & \cos\theta\cos\phi & -\sin\phi \\ -\sin\theta\sin\phi & \cos\theta\sin\phi & \cos\phi \end{bmatrix} \tag{2.123}$$

$$\mathbf{R}_3(\xi) = \begin{bmatrix} \cos\xi & \sin\xi & 0 \\ -\sin\xi & \cos\xi & 0 \\ 0 & 0 & 1 \end{bmatrix} \tag{2.124}$$

If the angles η, θ, and ξ are assumed constant, $\mathbf{T}_i$ is a function of only ϕ_i and ψ_i. Further, if the potential energy contribution from each residue is assumed to be independent, the ensemble averages are again separable and Equation 2.120 applies. Thus, using the method of virtual bonds, the unperturbed chain dimensions (characteristic ratio) can be calculated quite easily for polypeptide-like molecules. This

method is also suitable for PLA [*140*], because of its similarity to polypeptides, and will be used in Chapter Four of this dissertation.

§ 2.3. Numerical Optimization Methods

In this dissertation, we make use of numerical optimization methods to achieve several ends. In molecular modeling, these methods can be applied to find minimum energy structures of a particular system. Also, in the process of developing the force field model for polylactide, we use optimization to explore the parameter space and minimize the error associated with a set of force field parameters. Most of the common optimization methods are iterative and gradient-based; that is, they use information based on the gradient of an objective function to determine the next (better) approximation to the optimum point. Gradient-based iterative optimization methods include steepest descent (SD), conjugate gradient (CG), and quasi-Newton (QN) methods. The SD method is the simplest implementation, in which each successive search direction is derived from gradient (first derivative) information alone. The full Hessian (the matrix of second partial derivatives) must be computed at each iteration for the CG method, though the algorithm can take far less iterations than SD, depending on the shape of the objective function. In QN methods, the Hessian is not calculated explicitly, but estimated from the gradient information stored from previous iterations. The bounded low memory Broyden-Fletcher-Goldfarb-Shanno (L-BFGS-B) algorithm is a particularly efficient example of a QN method which handled a bounded search space [*141*], and is used throughout this work.

CHAPTER THREE

REVIEW OF PRIOR WORK

In this chapter, we review several important works which were important precursors to this dissertation. Other than those in the dissertation of O'Brien [*142*], no openly published force field parameters have been developed specifically for α-polyesters, such as polylactide (PLA). Yet, there have been many theoretical, modeling, and simulation studies on PLA in which general purpose force fields or other models were used. The present chapter focuses on these studies. Additionally, some experimental work is included in the discussion where appropriate. The purpose of this chapter is to point out the varying levels of theory and simulation that have been applied to PLA, and how such prior art has influenced this work.

§ 3.1. Early Computational Work

Computational simulations of PLA were performed as early as the 1960s, by de Santis and Kovacs [*143*], and by Brant et al. [*140*]. These works focused on calculation of the structural properties of PLA, namely the unperturbed chain dimensions and the determination of the crystalline structure in conjunction with experimental diffraction or scattering patterns. These two studies continue to impact current work in the field, with the potential energy surface computed by Brant et al. used in numerous recent

studies [*144-147*], and the essential findings of de Santis and Kovacs remaining relevant to studying the crystalline phases of PLA [*45*,*144*,*148*].

In the paper by de Santis and Kovacs [*143*], the structure of poly lactic acid was studied using a pairwise additive van der Waals model. The authors recognized the similarity between the lactyl residue and its amino acid counterpart, alanine (see Figure 3.1), and thus, adopted the torsional angle convention and two dimensional map commonly encountered in the protein literature. The ω dihedral angle of PLA, as defined in Figure 3.1b, was assumed to be planar, which is also a valid assumption applied to proteins [*149*]. Thus, the primary degrees of freedom in a single residue reduce to the two remaining backbone torsions, labeled ϕ and ψ in Figure 3.1b. In the protein literature, the two dimensional (ϕ, ψ) subspace is often used as an indicator of secondary structure, and for example, a very common presentation of this information is the Ramachandran plot [*149*]. This convention is used in de Santis and Kovacs' crystal structure analysis of PLA. Fixed bond lengths and valence angles were assumed in the study, according to values derived from a previous X-ray analysis of dimethyl oxalate [*150*]. Tables 3.1 and 3.2 list these values, using nomenclature defined for each atom type in Figure 3.2.

The potential energy surface calculated by de Santis and Kovacs [*143*] is shown in Figure 3.3. The authors' model predicts two broad potential energy minima, located near $(\phi = -65°, \psi = -30°)$, and $(\phi = -65°, \psi = 150°)$, where the dihedral angles are given in the IUPAC convention and defined by the four-atom groups listed in Table

3.3. In the manuscript, these are referred to respectively as the R_α and δ helices, designating the right-handed α helix and the polyproline type II helix. This nomenclature is not to be confused with the designation of crystalline polymorphs of PLA, in which a conformation in the δ helix region of Figure 3.3 is referred to as the α polymorph. According to their van der Waals model, the α helix potential energy minimum is about 4 kJ/mol lower than the δ helix minimum; however, when crystalline packing was considered, it was found that accounting for intrachain dipole-dipole interactions caused destabilization of the α helix compared to the δ helix.

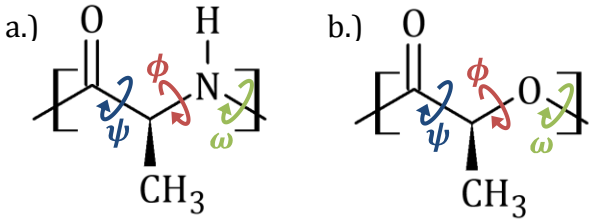

Figure 3.1. Structure of a.) the alanine residue, encountered in polypeptides; b.) the lactyl residue, which is the repeat unit in PLA. The structures are sufficiently similar that protein structure nomenclature may be used in reference to PLA. Skeletal dihedral angle conventions are shown, each of which are defined by four adjacent backbone atoms.

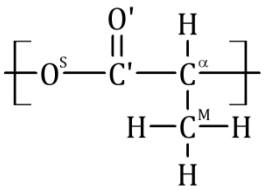

Figure 3.2. Atom types in the PLA repeat unit, as referred to in the text.

Table 3.1. Bond lengths used in structural analyses of PLA, listed by lead author.

Bond	Length (Å)				
	de Santis [*143*]	Brant [*140*]	Hoogsteen† [*144*]	Alemán [*148*]	Sasaki [*45*]
O^S–C'	1.31	1.34	1.310	1.310	1.31
C'–C^α	1.53	1.52	1.527	1.527	1.53
C'=O'	1.19	1.22	1.192	1.192	1.20
C^α–C^M	NL*	1.54	1.519	1.519	1.54
C^α–O^S	1.46	1.44	1.455	1.455	1.46
C^α–H	NL*	1.07	1.050	1.080	1.08

* Entries marked as NL were not listed in the manuscripts.

† Final values after refinement of the α polymorph (initial values taken from [*143*]).

Table 3.2. Valence angles used in structural analyses of PLA, listed by lead author.

Bond	Angle (degrees)				
	de Santis [*143*]	Brant [*140*]	Hoogsteen [*144*]	Alemán [*148*]	Sasaki [*45*]
O^S–C'–C^α	110	114	110	109.2	110
O^S–C'=O'	125	121	125	124.9	125
O'=C'–C^α	125	125	NL*	125.8	125
C'–C^α–C^M	NL*	NL*	NL*	109.5	109.5
C'–C^α–O^S	NL*	110	109.5	109.6	109.5
C^M–C^α–O^S	NL*	110	109.5	109.5	109.5
C^α–O^S–C'	118	113	118	118.3	118
C'–C^α–H	NL*	NL*	NL*	109.6	109.5
C^M–C^α–H	NL*	NL*	NL*	109.5	109.5

* Entries marked as NL were not listed in the manuscripts.

Table 3.3. Dihedral angle definitions in PLA. In each case, the dihedral angle is given by the angle between the planes ijk and jkl, following the IUPAC convention [*151*]. Refer to Figure 3.2 for atom names in the PLA repeat unit.

Dihedral	Atoms			
	i	j	k	l
ϕ	O^S	C'	C^α	O^S
ψ	C'	C^α	O^S	C'
ω	C^α	O^S	C'	C^α

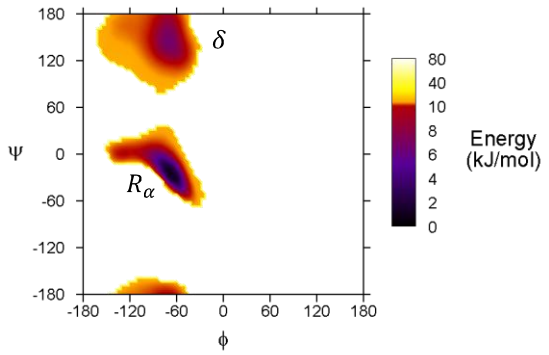

Figure 3.3. Potential energy surface from de Santis and Kovacs' van der Waals model; scaled from Figure 3 in reference [*143*]. White space in the plot denotes regions not shown in the original work. Two potential energy minima are apparent, which the authors designate as the R_α and δ helices following the protein convention. The δ helix forms the most stable crystalline polymorph of PLA, referred to as the α crystal structure in the remainder of this dissertation.

By examining the X-ray fiber diffraction pattern of PLA, de Santis and Kovacs found that the molecular conformation for the PLA α crystal structure was in the region of the δ helix, though the exact helical arrangement was reported as ten repeat units in three turns (denoted 10_3) as opposed to the polyproline type II helix which is 3_1 [*143*]. Additional weak meridional reflections were observed in the X-ray diffraction photograph, which are inconsistent with a pure 10_3 helix conformation, and the authors hypothesized that these were indicative of a "coiled coil" structure or configurational inversion [*143*].

Shortly after the work of de Santis and Kovacs, the conformational study by Brant et al. was published [*140*]. The focus of the manuscript was on the unperturbed chain dimensions (Section 2.1.2) of amorphous PLA rather than the crystal structure, yet similar computational methods were used as compared to de Santis and Kovacs. Again, all bonds and valence angles were considered rigid. Their values were taken from studies on methyl acetate and methyl formate [*152,153*]. Electrostatic interactions were included by the use of atom-centered point charges, which were assigned to approximate the dipole moment of methyl formate as measured by Curl [*152*]. Again, the authors recognized the similarity of PLA to proteins, and thus, the same dihedral angle nomenclature was used. Separate dihedral correction terms were used for ϕ and ψ, in the form of a single cosine function having a multiplicity of three. The ω dihedral angle was taken to be planar. Using this model, the authors constructed a potential energy surface for PLA as shown in Figure 3.4.

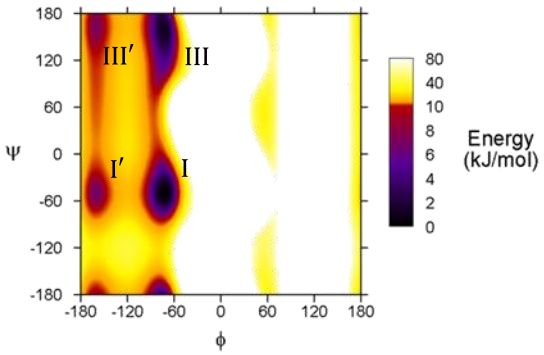

Figure 3.4. Potential energy surface calculated from the model of Brant et al. [*140*]. Four low energy minima were found, which the authors label as I, I', III, and III'. The lowest energy minimum was found to be III, though it was estimated to be only 0.33 kJ/mol lower in energy than I. Whitespace denotes regions greater than 80 kJ/mol in energy.

As shown in Figure 3.4, Brant et al. calculated that there should be four energetically accessible local energy minima on the (ϕ, ψ) potential energy surface [*140*], and this differs from the prediction of two broad minima by de Santis and Kovacs [*143*]. Following nomenclature from the authors' previous work on polypeptides, the minima were designated I, III, I' and III', taking IUPAC dihedral values of $(\phi = -73°, \psi = -46°)$, $(\phi = -73°, \psi = 158°)$, $(\phi = -160°, \psi = -50°)$, and $(\phi = -160°, \psi = 161°)$, respectively. A dividing ridge was predicted near $\phi = -120°$, which the authors found was due to steric interactions between the carbonyl unit and the α-hydrogen atom on adjacent residues. They go on to note that the same feature is less pronounced in the corresponding potential energy surface for polyalanine, due to the larger bond angle on its amide nitrogen atoms. This may also be the reason that the

ridge does not appear in de Santis and Kovacs' potential energy surface, since the corresponding angle in PLA (centered on the ester oxygen, O^S) was assumed to be 5° wider in their study than was assumed by Brant et al. (see Table 3.2). In Chapter Four, it will be shown that DFT calculations suggest the corresponding bond angle in PLA (centered on the ester oxygen atom) is sufficiently flexible to relieve the steric interaction, and no pronounced ridge is observed when the angle is left unconstrained.

The bulk of the paper by Brant et al. [*140*] focuses on RIS calculations on PLA. Assuming planarity in the ester moiety allowed the authors to define a single virtual bond for each residue, as discussed in Section 2.2.2.6. For PLA, the virtual bonds connect the α carbon atoms on adjacent residues as shown in Figure 3.5. The virtual bond convention allows the RIS method to be used for determining the characteristic ratio, with the transition matrix completely defined for each state by its values of ϕ, ψ, and the (constant) angles θ, η, and ξ.

For the purpose of RIS calculations on PLA, Brant et al. [*140*] estimated a probability distribution from their torsional potential energy surface using Boltzmann weights. With all remaining degrees of freedom being fixed in their model, the potential energy surface is truly a function of ϕ and ψ only, and thus, each point on their surface is entropically equivalent. More precisely, the prefactor on the Boltzmann weight was considered equal for all points in the (ϕ, ψ) plane. Note that, had the authors' model dealt with nonrigid bonds and angles, this assumption would be invalid. In such case, proper treatment would require a *free energy* surface to be constructed as a function of

ϕ and ψ, which would account for the reduction in degrees of freedom. This point will be relevant in Chapter Four of this work, where the bonds and valence angles are not constrained. In the model of Brant et al., however, the probabilities are completely determined by the potential energies, subject to their assumption of rigid bonds and valence angles.

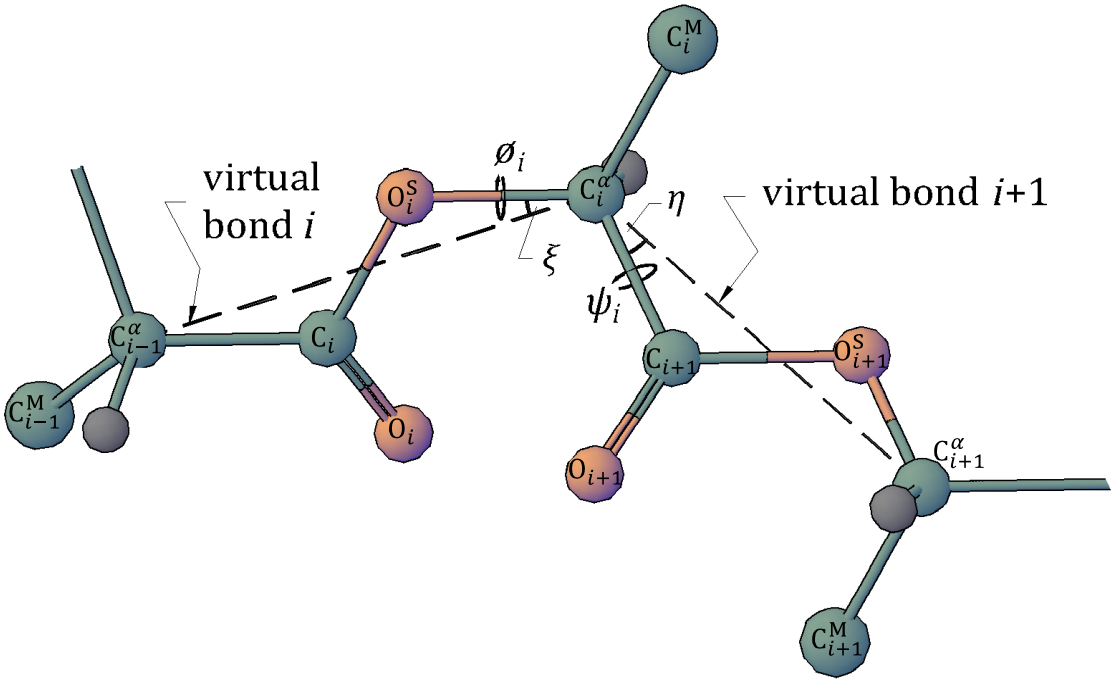

Figure 3.5. Virtual bonds and geometry parameters used in the study by Brant et al. [*140*]. Atom colors are: blue, carbon; red, oxygen; gray, hydrogen. Subscripts on atoms indicate repeat units; superscripts on carbon atoms differentiate between alpha carbons (α), methyl carbons (M), and carbonyl carbons (no superscript); superscripts on oxygen atoms differentiate between ester oxygens (S) and carbonyl oxygens (no superscript). Methyl hydrogen atoms are omitted for simplicity.

To simplify the RIS calculations, Brant et al. considered four distinct rotational isomeric states, rather than treating the potential energy surface as continuous. One state was assigned to each of the four local minima described above, and incorporated all surrounding points in the basin whose energies were within 3 kcal/mol of its local minimum. Thus, the total contribution to the partition function was determined for each state by summing the probabilities assigned to all points in its basin. Because the minima designated I and III are approximately 1.5 kcal/mol lower in energy than the minima designated by I' and III' (see Figure 3.4), they were found to account for 90% of the total partition function. Given this information, the authors also considered a two state model in terms of minima I and III only.

As we conclude the discussion of the paper by Brant, Tonelli, and Flory [*140*], note that in constructing their model, the authors made use of several unknown model parameters, which were adjusted to gain a better agreement with their experimental results [*154*]. In particular, the dielectric constant, ϵ, used for electrostatic interactions was shown to have a dramatic effect on the RIS calculations. It was found that increasing ϵ to a value between 3.0 and 4.0 produced agreement within their experimentally measured range of C_∞ values (4.3 to 5.2, on the basis of real bonds). Decreasing ϵ below 2.0 caused a drastic increase in C_∞, which presumably is due to the inability of the rigid valence angles in their model to relieve steric interactions. Thus, the authors ultimately set the dielectric constant to 3.0 in their calculations. The remaining unknown model parameters were the bond length between the α carbon C^α and the

methyl carbon C^M, and the heights of the cosine barrier correction terms for ϕ and ψ. According to the authors, varying these had relatively little effect on the characteristic ratio results. Ultimately, their work demonstrated for the first time that the bond rotational potential energy surface of PLA can be used directly in estimating the unperturbed chain dimensions of the polymer.

Though completed in the infancy of the digital age, the work of de Santis and Kovacs [*143*] and Brant et al. [*140*] proved that the methods of computational chemistry can be useful in examining the structural properties of polylactides. They also demonstrated the ease with which the methods and nomenclature from protein studies may be transferred to PLA. The main shortcoming of these studies is their assumption of rigid bond lengths and valence angles, the latter of which can have a dramatic and definite effect on the calculated potential energy surfaces. The best example of this is the value of the angle centered on O^S, which largely accounts for the difference in the four-minima potential energy surface of Brant et al. and the two-minima surface of de Santis and Kovacs.

It is recognized that many assumptions were necessary in these early works, presumably due to the speed of computer hardware available in the 1960s. In fact, the need for computational simplification is probably what incited these authors to devise some very astute methods for dealing with conformational predictions in PLA. Perhaps the best example of this is the assumption of planarity in the ester moiety, which along with some crafty geometry transformations, allowed Brant et al. [*140*] to greatly reduce

the computational burden of their problem through the definition of virtual bonds. In examining the same subject with modern computers, these assumptions need not be made. Further, more advanced theories and methods have become available to practitioners for estimating the potential energy.

Given the availability of improved methods and computer hardware, we are presently able to improve upon the work of Brant et al. [*140*] in Chapter Four, but using electron DFT methods instead of semi-empirical van der Waals models. We are able to do this without the need for assuming planarity in the ester moiety, or rigid bond lengths and valence angles. The elimination of these assumptions yields significantly different results from the earlier works!

§ 3.2. Recent Studies on PLA Structure

Several studies have been published over the past two decades which revisit structural calculations in PLA crystals, building upon the previously discussed works of de Santis and Kovacs [*143*], and Brant et al. [*140*]. The recent studies relied on the use of established molecular models, such as AMBER [*100*], and were able to examine interchain interactions to determine packing behaviors, in addition to the intrachain conformation as examined in the early studies [*140*,*143*]. In this section, we review several of these papers selected from the literature.

In 1990, Hoogsteen et al. carried out conformational calculations on PLA crystals [*144*]. The study pointed out the structural differences between the α polymorph considered by de Santis and Kovacs [*143*], and the β polymorph that was first

experimentally observed by Eling et al. [*155*]. Conformational energy calculations were used in conjunction with wide angle X-ray scattering (WAXS) experiments to determine structures for each of the polymorphs considered. In their structural calculations, the authors used a program developed by Zugenmaier and Sarko [*156*] for conformational and packing analyses of polysaccharide crystals. The program optimizes the geometry and packing in the crystalline unit cell by altering bond lengths, valence angles, and torsional angles, with the ester group assumed planar, i.e., $\omega = 180°$. The program confirmed the 10_3 helical form of the α polymorph described by de Santis and Kovacs [*143*], while predicting a 3_1 helix for the β polymorph. Box vectors were estimated to be $a = 10.6$ Å, $b = 6.10$ Å, and $c = 28.8$ Å. The potential energy calculations predicted that the intramolecular contributions to each structure were approximately equal, suggesting that interchain packing plays the dominant role in the stability of the α structure over the β polymorph.

The extra meridional reflections in the WAXS pattern of the α polymorph, first observed by de Santis and Kovacs [*143*] were also noted in the analysis of Hoogsteen et al. [*144*]. Again, these reflections suggest that the conformation is not a pure 10_3 helix. However, the authors dismissed de Santis and Kovacs' assertion that the additional reflections might be due to a coiled coil structure, noting that coiled coil structures usually result in meridional reflections whose layer line structures are offset from the pure helical layer lines. In PLA, the extra meridional reflections occur coincident with the second, fourth, sixth, seventh, eighth, and ninth layer lines, with those on even layer

lines having much greater intensity than reflections on odd layer lines. Further, the intensities of the extra reflections in general were only indicative of small deviations from the 10_3 helix.

A thorough study of the X-ray diffraction pattern of the α crystal structure of PLA was undertaken in 1995 by Kobayashi et al. [*44*], which confirmed the 10_3 helical conformation and atomic coordinates calculated by Hoogsteen et al. [*144*]. The authors' measurements also showed close agreement with the box dimensions proposed by Hoogsteen et al., with Kobayashi et al. reporting values of $a = 10.5$ Å, $b = 6.10$ Å, and $c = 28.8$ Å. In addition, the authors were able to refine the interchain packing structure, which was not attempted by Hoogsteen et al. No potential energy models were used in the study, which relied solely on the diffraction patterns for the placement of atoms. Two helical chains were considered in the unit cell, as shown in Figure 3.6. The position of chain II relative to chain I was varied, along with the setting angle θ—defined between the x-axis and a plane passing through the helical axis and the bottommost α-carbon of chain II (see Figure 3.6). Optimal values which reproduced the X-ray diffraction pattern were found to be $\Delta x = 0.543$, $\Delta y = 0.541$, $\Delta z = 0.021$, and $\theta = 2.46°$, with distances in fractional coordinates (i.e., each coordinate is the dimensional distance divided by the unit cell length in that direction). The value of the setting angle τ, defined similar to θ but for chain I (see Figure 3.6), was considered fixed according to the coordinates of Hoogsteen et al. [*144*].

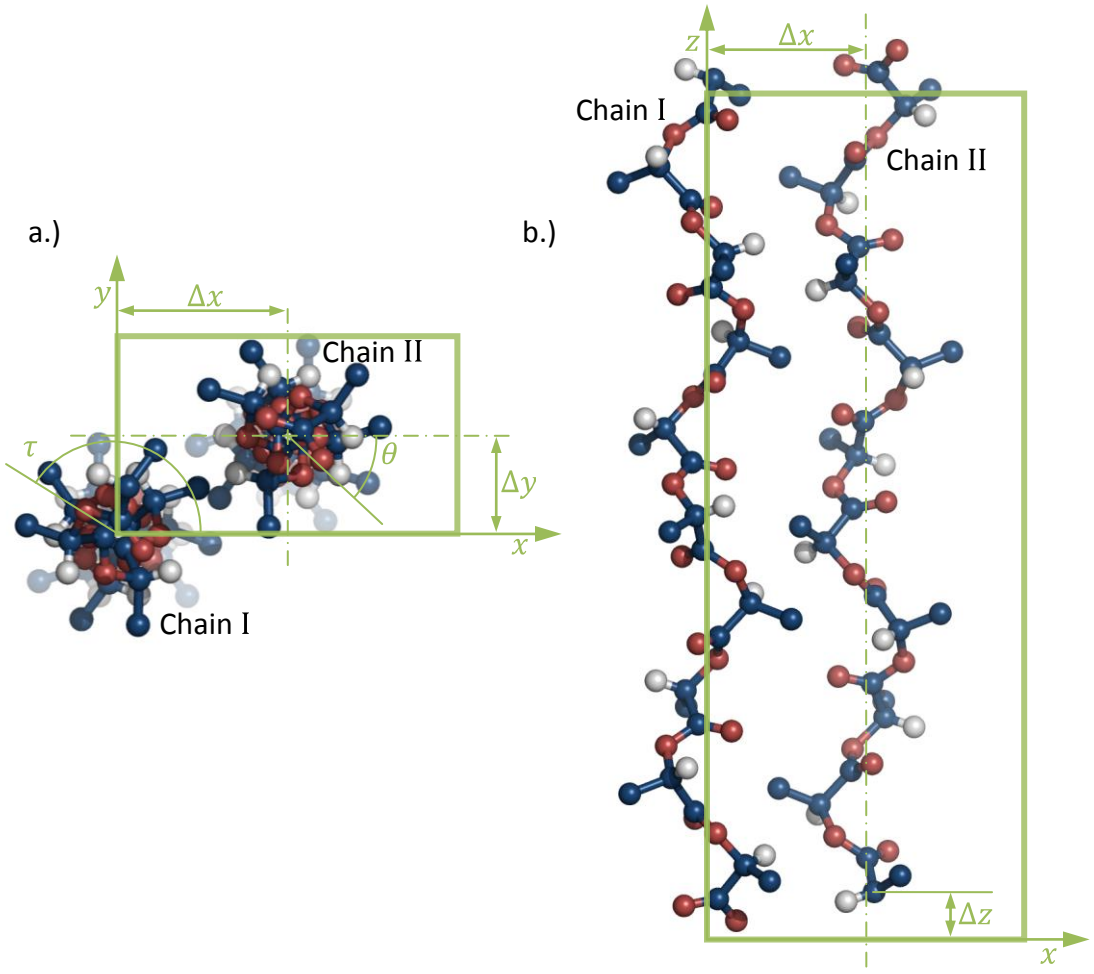

Figure 3.6. Packing of chains in the α crystalline form of PLA, as viewed along the helical axis (a) and from the side (b) of the unit cell. Coordinates taken from Alemán et al. [*148*]; origin arbitrarily placed so that the helical axis of chain I is coincident with the z axis; methyl hydrogens omitted for simplicity.

In 2001, Alemán, Lotz, and Puiggali used molecular mechanics calculations to further examine the α form of PLA [*148*]. The unit cell parameters and fractional coordinates of Hoogsteen et al. [*144*] were used as input to their PCSP (Prediction of the

Crystal Structure of Polymers) program [*157*]. The AMBER force field [*100*] was used with a united-atom representation of the methyl group (meaning the methyl group was approximated as a single atom). With the intrachain conformations fixed, the azimuthal displacement and setting angles of the chains relative to one another were varied. First, the value of τ was varied, considering only interactions of chain I with neighboring periodic images of itself. A value of $\tau = 150°$ was found to minimize the intermolecular energy between chains. Next, chains of type II were introduced into to the unit cell, and the values $\theta = -39°$ and $\Delta z = 0.11$ were found to minimize the total intermolecular energy (Δz in fractional coordinates). The parameters Δx and Δy were not considered as adjustable, as they were in the analysis of Kobayashi [*44*].

After estimating the optimal packing from potential energy methods, Alemán et al. accounted for symmetry considerations during a structural refinement step [*148*]. Two such space groups were considered, with $P2_12_12_1$ having a strict antiparallel arrangement of adjacent chains as indicated in Figure 3.6, and the $P222_1$ space group allowing a statistical arrangement of parallel and antiparallel chains. Diffraction patterns were estimated for varying values of τ, θ, and Δz, as defined in Figure 3.6, subject to the constraints of each particular space group. The best agreement with experimental results was achieved with the $P2_12_12_1$ space group, with $\tau = 138°$, $\theta = -30$ and $\Delta z = 0.18$ in fractional coordinates. This is in reasonable agreement with the authors' potential energy optimized structures, and thus, it was concluded that the proper space group is $P2_12_12_1$, with antiparallel chains.

Monte Carlo simulations were also performed by Alemán et al. [*148*], using the AMBER force field and fixed bond lengths. Averaged dihedral angles were in close agreement with the 10_3 helical coordinates of Hoogsteen et al. [*144*], though the a and b unit cell dimensions were underestimated in NPT simulations. A favorable result of the simulations is that the averaged setting angles and azimuthal displacement took values of $\tau = 149°$, $\theta = -30$ and $\Delta z = 0.18$, respectively, which is in agreement with their structural refinement results for the $P2_12_12_1$ space group. The Monte Carlo results also showed some degree of departure from the pure 10_3 helical conformation, which had previously been conjectured due to the observation of extra meridional reflections in the previously discussed studies [*44*,*143*,*144*]. In their conclusions, the authors note that the intermolecular interactions between chains will be different along the three unit cell axes, and this would most likely result in conformational deviations from the strict 10_3 helix used in their analysis.

In 2003, Sasaki and Asakura [*45*] analyzed the disorder in the PLA α polymorph using the linked atom full-matrix least squares method (LAFLS) [*158*], coupled with the Rietveld whole-fitting method [*159*]. Rather than assuming screw symmetry, as was done in previous studies, the LAFLS allows individual atomic positions to be optimized for agreement with the WAXD data. Results were examined with potential energy calculations using AMBER, following Alemán et al. [*148*]. The best fit structure was a 10_3 helix with $P2_12_12_1$ symmetry. The structure does not assume exact screw symmetry in the helices, which would be unreasonable in a rectangular unit cell. Therefore, the

authors refer to their structure as a "frustrated" 10_3 helix. Unit cell box vectors were found to be $a = 10.66$ Å, $b = 6.16$ Å, and $c = 28.88$ Å. The frustrated structure is shown in Figure 3.7, for comparison with the structure proposed in previous studies (Figure 3.6).

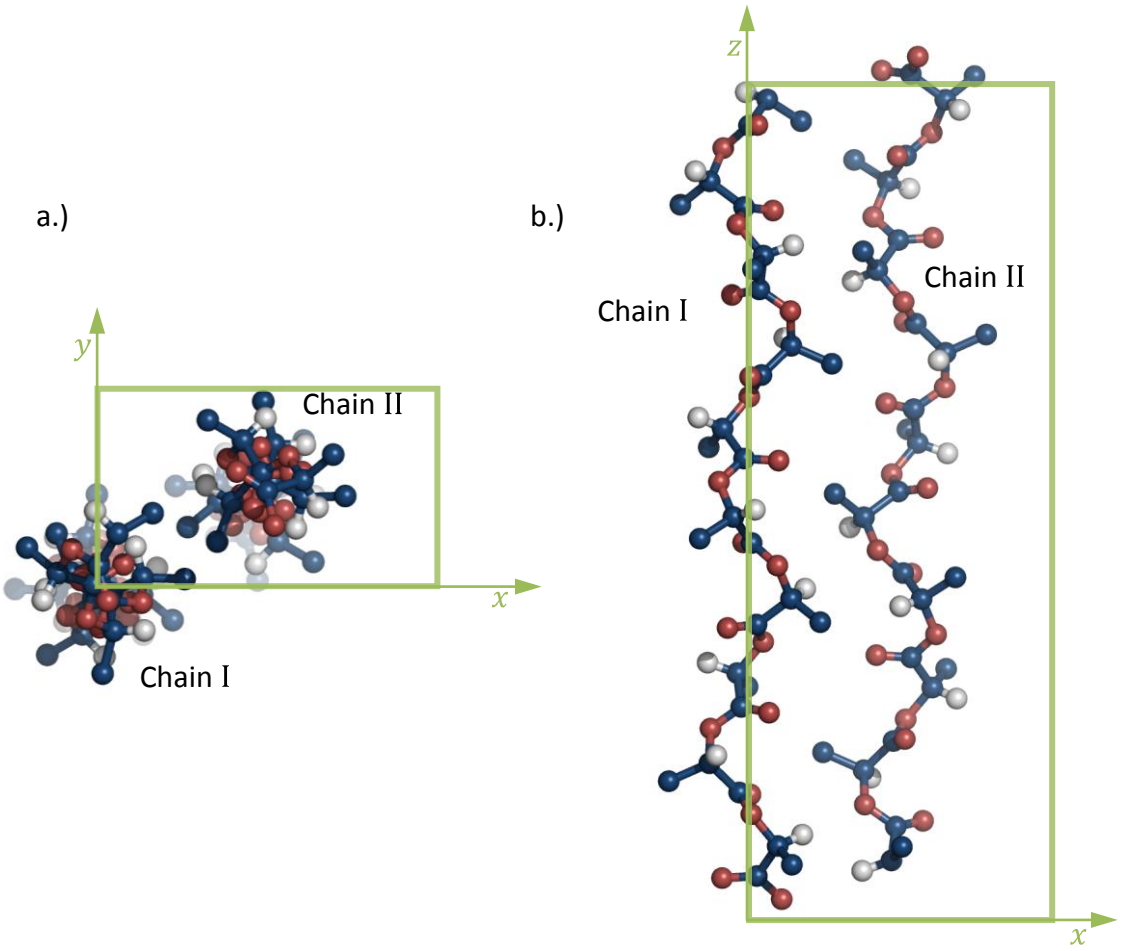

Figure 3.7. Unit cell for the α polymorph of PLA, as refined by Sasaki and Asakura [*45*]. Views shown are from the axial direction (a), and the side (b) of the unit cell.

From examining the crystal structures of Alemán et al. [*148*] and Sasaki and Asakura [*45*] in their axial views (Figures 3.6a and 3.7a), we see that the exact screw symmetry of the chains is disturbed in Sasaki and Asakura's refinement. The crystal structure conformations discussed in this section are summarized in Table 3.4, where we have compiled the dihedral values for each of the five residues making a half-turn of the helix. Sasaki and Asakura's frustrated helix [*45*] takes on unique dihedral values for each residue, whereas the previous studies assume exact screw-axis symmetry. On average, the studies are in fairly good agreement, though the individual residues in Sasaki's refinement show considerable deviations from the mean values of the dihedrals.

Table 3.4. Dihedral values in the α polymorph of PLA, listed by lead author.

Lead Author	Residue	ϕ	ψ	ω	Reference
Hoogsteen	all	-64.8	148.9	179.5	[*144*]
Alemán	all	-61.4	154.2	167.5	[*148*]
Sasaki	1	-66.0	163.9	167.3	[*45*]
	2	-63.0	154.5	165.0	
	3	-58.0	150.0	168.6	
	4	-65.8	158.7	178.1	
	5	-68.2	151.6	175.4	

§ 3.3. *Ab Initio* Studies on Aliphatic Esters

In a series of three papers, Mannfors and coworkers examined different types of polyesters using *ab initio* and DFT methods. These studies focused on bond rotations in esters with one carboxyl group [*160*], esters with two carboxyl groups [*161*], and esters with tartaric units [*162*]. The 6-31G* basis set was used with MP2, B3-LYP, and B-LYP methods to estimate the energetic barriers to bond rotation. These results were compared to force field calculations using the PCFF force field developed by Sun and coworkers [*163-166*]. It was found that the PCFF parameters poorly reproduce the *ab initio* and DFT energy barriers, and accordingly, new parameters were developed for PCFF. It was noted that, during rotation of bonds, the optimized values of bond lengths changed very little, whereas the valence angles and partial atomic charges showed considerable deviations. As pointed out in Section 3.1 of this dissertation, the flexibility of valence angles can have a pronounced effect on the energy landscape of PLA, evidenced by the difference in Figures 3.3 and 3.4.

In fitting the torsional parameters in the PCFF force field, Blomqvist et al. [*161*] considered energy profiles as a function of single bond rotations, rather than the multidimensional (ϕ, ψ) potential energy surfaces encountered in Figures 3.3 and 3.4. In fitting parameters for each bond rotation, the authors compared energies from structures optimized using the force field to structures optimized using *ab initio* or DFT methods. They emphasize that, when fitting to one-dimensional energy profiles in this

way, it is important to fix the values of dihedrals adjacent to the one being fit, in order to eliminate any variability due to the interdependence of the adjacent dihedral angles. After fitting the dihedral parameters in this way, it was shown that the minima on a (ϕ, ψ) type plot evaluated with the modified PCFF parameters correspond well with the minima found using *ab initio* and DFT methods.

§ 3.4. Force Field Development for Aliphatic Esters in General

In addition to the modified PCFF force field of Mannfors and coworkers [*160-162*], discussed in the previous section, there are several general purpose force fields which include parameters for esters. Here we discuss the development of ester parameters in the popular AMBER and OPLS force fields. While torsional potentials exist for the ester bonds in these force fields, they have not been parameterized for rotation about the C^{α}–O^{S} bond in α polyesters, such as PLA.

Ester parameters were implemented in the AMBER force field for use in simulating phospholipids, by Charifson, Hiskey, and Pedersen [*100*]. Bond stretching and angle bending parameters were obtained by fitting to Hartree Fock calculations (6-31G* basis) on methyl acetate. The torsional potential for rotation about the ester bond was adjusted for agreement with the experimental enthalpy difference between *cis* and *trans* states. The ester parameters were used in the study to build and simulate phospholipid monolayers in water.

Parameter development for simple esters in the all-atom OPLS force field was undertaken by Price, Ostrovsky, and Jorgensen [*167*]. The study considered Monte Carlo

simulations of five esters: methyl acetate, ethyl acetate, isopropyl acetate, methyl propionate, and methyl benzoate. Bond stretching and angle bending parameters were taken from the AMBER library previously discussed [*100*]. Torsional parameters were fit to HF/6-31G* calculations or experimental conformational data. Initially, van der Waals parameters were taken from standard OPLS atom types [*168*], and partial atomic charges were set according to HF/6-31G* calculations [*91*]. These parameters were subsequently refined to match the target liquid properties of the esters. Hydrogen-bonded complexes of the esters with water were examined, both with the force field and with HF/6-31G* calculations. The authors note that, to obtain correct solution densities, it is necessary to shorten the length of hydrogen bonding between the ester and water molecules. Liquid radial distribution functions, densities, and free energies of hydration were used as target data for refining the partial atomic charges. The Lennard-Jones parameters were not altered from their standard values, in keeping with previous OPLS parameterizations. However, it was noted that an increase in σ or decrease in ε for the carbons bonded to the alkoxy oxygen might be justified to reduce the densities.

§ 3.5. Force Field Development for Polylactides in Particular

An essential precursor to the developments presented here was the work of O'Brien [*142*]. The present dissertation builds upon O'Brien's dissertation, and offers some improvements over the methods used therein. In his dissertation, the potential energies for isolated rotation about single bonds were estimated for a lactic acid trimer at the B3LYP/6-31G** level. In addition, partial atomic charges were calculated using

the CHELPG method [*169*]. From these calculations, the PLAFF force field was developed for use in GROMACS [*170*], which gave excellent agreement with the crystalline structure of Sasaki and Asakura [*45*]. PLAFF is based on the OPLS force field [*92*], with newly parameterized partial atomic charges and skeletal dihedral terms. In addition, several other modifications were used that render PLAFF specifically applicable to PLA. This level of specialization in PLAFF precludes its parameters from being readily transferred to other polyesters.

One such modification of the original OPLS form, used in PLAFF [*142*], is that for each rotatable skeletal bond, only a single set of four atoms was selected as defining the dihedral interaction in the potential energy function. There are usually multiple four-atom sets that may define a dihedral, as illustrated in Figure 3.8. In the OPLS force field, and others, it is common that all four-atom interactions about a particular bond will have separate potential energy terms associated with them. In PLAFF, however, only one of these interactions is counted for each skeletal bond. This was done to simplify the fitting process, since it allows each backbone dihedral to be independently fit without complication. As an added benefit, leaving out these interactions decreases the number of dihedral terms per residue from nineteen interactions to twelve interactions, effectively reducing the computational burden for dihedral potentials by nearly 40%. However, in simulation of high molecular weight systems, the calculation of dihedral interactions typically occupies only a small portion of the total computational burden

(this is dominated by the calculation of nonbonded interactions), and the overall speed gained is typically only a few percent.

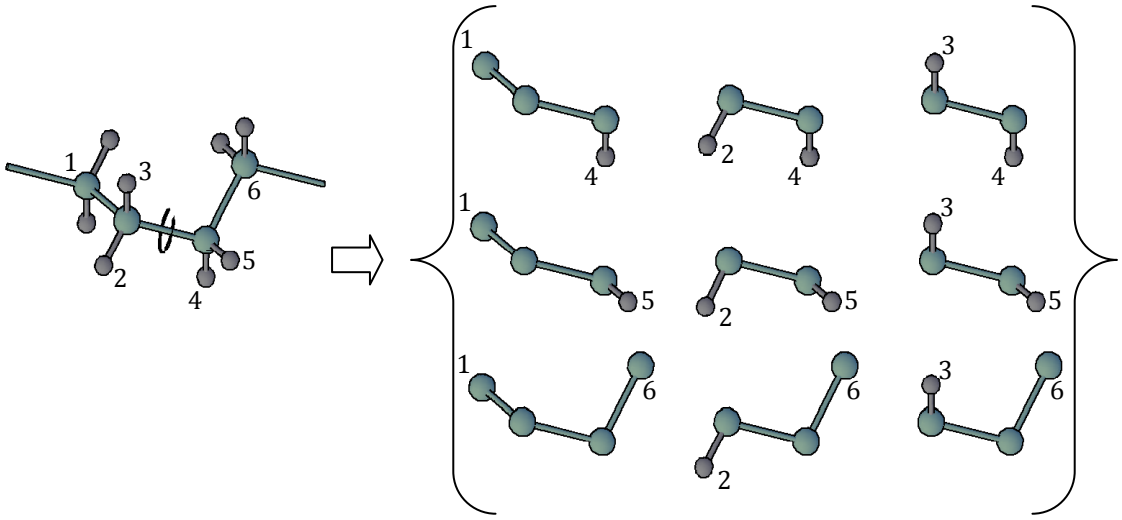

Figure 3.8. Example of several four-atom dihedral interactions defined on the same rotatable bond, indicated with the circular arrow on the molecule to the left. In PLAFF [*142*], only one of these interactions is included in the potential energy function for each main chain bond.

Another modification used in PLAFF is the elimination of 1-4 nonbonded interactions. In the original OPLS form, the van der Waals and electrostatic forces are scaled by a multiplicative factor of 0.5 for atoms separated by three bonds. In PLAFF, these interactions are omitted completely. Again, this modification was needed to facilitate fitting the dihedral interactions, since the 1-4 interactions caused excessive noise in the bond rotational energy profiles. We now believe this noise arises from the fact that geometry optimizations were not performed in PLAFF during the fitting

process. That is, in evaluating the PLAFF potential energy for each bond rotation, the DFT-minimized geometry was input directly into GROMACS and a single energy evaluation was performed. In Chapter Five of this dissertation, we show that sufficiently smooth potential energy surfaces may be calculated from force field models with 1-4 interactions by using constrained geometry optimizations. By allowing the remaining degrees of freedom to relax, especially valence angles, most of the noise observed by O'Brien can be eliminated. Since the 1-4 interactions affect all other dihedral parameters, and not just the skeletal dihedrals parameterized in PLAFF, it is preferable to include them in the force field.

The remaining sections in this dissertation follow much the same form as Dr. O'Brien's, consisting of DFT calculations (Chapter Four), and force field fitting (Chapter Five). While development of a set of dihedral parameters which are transferable to other polyesters was not a goal of this work, efforts were made to remain true to the original OPLS form. The essential differences between this work and Dr. O'Brien's are:

1) The aim of the current force field parameterization is to develop parameters which accurately describe both crystalline and amorphous PLA, rather than focusing on crystalline PLA alone. Attempting to fit both crystalline and amorphous properties with the same model demands a compromise; for this reason, the force field developed here offers only minor improvement over O'Brien's PLAFF in simulating the crystal structure, but provides a much more accurate description of the amorphous configurational statistics.

2) Self consistent reaction field (SCRF) models are used in the DFT calculations to account for the presence of a bulk condensed phase around the molecules.

3) DFT results are compared according to their performance in RIS calculations.

4) Potential energy surfaces are calculated with respect to a two dimensional (ϕ, ψ) parameter space, following de Santis and Kovacs [*143*] and Brant et al. [*140*], rather than considering rotation about isolated bonds.

5) In an attempt to more closely match the general OPLS form, all available four-atom dihedral parameters are included in the force field.

6) The 1-4 nonbonded interactions are scaled by 0.5 as in the original OPLS force field.

7) To accomplish items 5) and 6), it was necessary to include force field geometry optimizations prior to each parameter fitting iteration. This required development of additional software to coordinate the molecular mechanics minimizations and dihedral parameter optimizations.

§ 3.6. Force Field Based Studies on PLA

Following her parameterization of torsional terms in PCFF for polyesters [*160,161*], Blomqvist published two papers that apply the modified force field to polylactides. In the first paper [*171*], Blomqvist used the RIS Metropolis Monte Carlo (RMMC) method, developed by Honeycutt [*172*], to determine the unperturbed chain dimensions of polylactides of varying optical composition. RMMC employs simulation of single chains, much like conventional RIS calculations, yet it incorporates a force field

model to calculate conformational probabilities. This method is useful when statistical weight matrices are unknown for a polymer, and provides a more adequate treatment of the chain statistics when the relative free energies are not known for the rotational isomers.

Using the RMMC method, Blomqvist found that the characteristic ratio varies depending on the stereochemistry of PLA chains, as well as the methods used to calculate nonbonded interactions [*171*]. Particularly, the isotactic polylactide chains exhibited higher C_∞ values than the atactic and syndiotactic chains. On the basis of real bonds, calculated values were approximately 5.0 for the atactic and syndiotactic chains, and ranged from approximately 5.5 to 12 for PLLA. The variation in C_∞ for PLLA was observed with respect to changing the maximum number of bonded neighbors, which are considered in nonbonded calculations, by changing the Max_Bonds parameter in their software. Lower values of C_∞ were obtained when Max_Bonds was set to 4, while higher values were calculated when Max_Bonds was set to 9. Similar variations in Max_Bonds for the sydiotactic and atactic chains did not result in significant changes in C_∞. It should be noted that Blomqvist ran identical calculations with the unmodified PCFF parameters, and observed opposite trends with respect to tacticity. Using PCFF, the syndiotactic and atactic chains had higher C_∞ values than the isotactic chains. For isotactic PLLA, increasing the value of Max_Bonds resulted in a decrease in the value of C_∞. The characteristic ratios calculated from the unmodified PCFF parameters were in the range of 2.8 to 6.8.

A subsequent study by Blomqvist et al. simulated large, multichain, bulk amorphous polylactides and polyglycolic acids (PGAs) [*173*]. The modified PCFF parameters were again used for the polyesters [*160,161*], and the Amorphous Cell module of MSI's Insight II/Discover software (currently under Accelrys). The paper focuses on static properties of the amorphous polymers, and aimed to determine which properties influence the uptake of water in these polymers. Amorphous polymer systems were constructed using the method of Theodorou and Suter [*174,175*], followed by conjugate gradient energy minimization and an NVT simulated annealing molecular dynamics step at the experimental amorphous density of 1.25 g/mol. Five polymer chains with degree of polymerization 50 were used in each cell, and as in the previous study, several chain compositions were considered of differing optical purity. In addition, PGA/PLA copolymers were considered. After estimating solubility parameters and free volumes in the amorphous cells, the authors concluded that the cells with high PGA content are more likely to take on water, since the methyl side group in PLA sterically inhibits hydrophilic interactions with the main chain and carbonyl atoms.

Although not the primary focus of the paper, additional information was given in the study by Blomqvist et al. [*173*], which is relevant to this dissertation. A contour plot of the bond rotational potential energy surface was shown for their force field model. We have recreated this plot in Figure 3.9. This is valuable for comparison with the early work of de Santis and Kovacs [*143*] and Brant et al. [*140*]. We see that there are only two minima in the sterically accessible region, as predicted by de Santis and Kovacs (see

Figure 3.3); the four distinct minima predicted by Brant et al., shown in Figure 3.4, are not present. However, the relative energies of the two minima follow the opposite trend than predicted by de Santis and Kovacs.

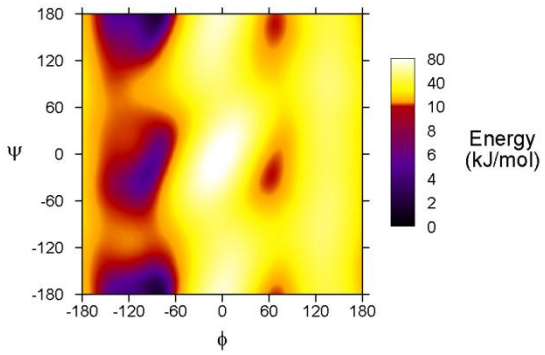

Figure 3.9. Bond rotational potential energy surface for PLA as calculated by Blomqvist [*173*].

In the paper by Entrialgo-Castaño et al. [*176*], the interaction of PLAs and PGAs with water was further examined with emphasis on hydrolytic degradation. Amorphous Cell studies were performed on PLA/PGA systems using Blomqvist's modified PCFF parameters [*160,161*], with particular focus on matching experimental degradation conditions. The authors confirmed Blomqvist's findings that the PGA polymers have more favorable interactions with water [*173*], and this was reinforced by the observation of increased swelling in water-loaded PGA during NPT molecular dynamics simulations as compared to PLA systems. Mean squared displacements (MSD) were also calculated during the simulations, and it was shown that the polymer chains exhibit

increased mobility upon swelling in water, and also that water molecules tend to travel in clusters while diffusing through the bulk polymers.

Another recent paper, by Karst and Yang [*177*], examined the hydrolytic degradation of PLLA/PDLA blends. The Amorphous Cell program, from Accelrys Inc., was used, with PCFF parameters as distributed in Materials Studio 3.0. Several blend compositions were considered, with each simulation cell containing 10 chains with degree of polymerization 50. It was shown that the potential energy of blended PLA stereoisomers reaches a minimum at the 50/50 blend composition, and after cleaving the chains in half, this causes a maximum in the potential energy difference ΔU due to bond breaking at the equimolar blend. The authors relate this energy difference to the equimolar blend's increased resistance to hydrolytic degradation, observed experimentally [*178*]. However, as the authors note in their introduction, this experimental trend may be due to the formation of the stable, close-packed stereocomplex crystallites.

§ 3.7. Summary

This concludes the review of pertinent literature on molecular modeling of PLA. In this chapter it was shown how the early studies of de Santis and Kovacs [*143*] and Brant et al. [*140*] demonstrated that the methods and nomenclature used in studying proteins are conveniently applied to polylactides. Crystallographic studies have revealed the polymorphism of PLA, with concurrence that the most common crystalline state (the α polymorph) is a 10_3 helix with a slightly frustrated packing [*45*,*144*,*148*]. The quantum

mechanics calculations of Blomqvist and coworkers were considered [*160-162*], and they have shown how such calculations might be used to improve the accuracy of a generalized force field, such as PCFF, for simulations of PLA. It was then pointed out that several of the popular force fields in wide use today (AMBER [*100*], OPLS [*91,167*], CHARMM [*95*]) could possibly benefit from the same type of parameterization, since they have not yet been tailored for α polyesters. This point was further demonstrated by O'Brien [*142*], who modified the OPLS force field to obtain PLAFF. This PLA-specific force field performs extremely well in simulation of the α polymorph of PLA, though the fitting methods used in PLAFF make it significantly less suitable for amorphous PLA than the crystalline phase. Finally, a number of application-based molecular modeling studies were discussed [*171,173,176,177*], which utilized Blomqvist's PCFF parameterization and focused primarily on the issue of water uptake. Each of the studies presented in this chapter will be important in the subsequent chapters of this dissertation, as they lay some important groundwork and will also be used for comparison and validation of our own data.

CHAPTER FOUR

ESTIMATION OF TORSIONAL POTENTIALS VIA ELECTRON DFT

§ 4.1. Introduction

For linear polymeric materials, most physical properties of interest are strongly influenced by the rotational energy landscapes of the chain molecules. Because of their size, molecular motion in polymers occurs primarily by reptation type movement that arises from the rotation of backbone bonds. Therefore, knowledge of the potential energy barriers to such rotations is indispensable for understanding the overall dynamics of polymer systems. On the other hand, the equilibrium thermodynamic properties of polymers are largely dictated by the relative position of minima on the bond rotational energy surface [*149*]. These observations dictate that understanding bond rotation behavior in polymers is essential in any attempt to model their properties, ranging from simple rotational isomeric states (RIS) calculations to complex molecular mechanics simulations.

While the potential energy surfaces of polymers have often been estimated using the methods of computational chemistry, studies are typically performed *in vacuo*, without taking into account the effects of interaction with the environment in which the polymer chain is immersed. Such 'gas phase' calculations have been applied with generally good success for parameterizing intramolecular interactions in classical force

field descriptions of large molecules, especially in cases where the assumed intermolecular parameters are of good quality [*92*]. As such, this approach will be used in Chapter Five to develop PLA-specific torsional parameters for use with the OPLS and CHARMM force fields. However, in other applications, such as RIS models, we assert that the energy landscape must be accurately estimated within the condensed environment to obtain meaningful results. Thus, after obtaining the needed *in vacuo* energy estimates, the remainder of this chapter focuses on how we might obtain and use condensed-phase energy estimates.

Using quantum theory to predict condensed-phase behavior of macromolecules has been a focus of computational chemists for some time. In the biomolecular field, the environment surrounding a macromolecule is often a liquid solvent (water), and continuum solvation models have been successfully applied in estimating potential energy barriers to bond rotation in protein chains [*179*]. For polymeric materials in the bulk, however, there is very little prior art on the subject. In the bulk, the environment encountered by a chain is markedly different from ordinary liquids due to the larger size and reduced mobility of the surrounding polymer chains. While low molecular weight solvents are able to undergo fast nuclear rearrangements in which their dipole moments align to produce favorable interactions with solute molecules, such rearrangements are greatly inhibited in polymers. Thus, efforts to successfully use conventional dielectric continuum models to describe the bulk amorphous polymer phase must take into account those factors unique to polymer systems. These include size effects on the first

'solvation' shell as well as the reduced entropy due to the incorporation of the solvating units into larger chains. In this chapter, we demonstrate for the first time how this might be achieved using a conventional solvation model developed for liquids, while illustrating some of the difficulties encountered in applying such a method to a polymer system.

To our knowledge, no quantum mechanical computations on the PLA family of molecules have been presented in the literature, though similar aliphatic polyesters have been examined *in vacuo* by Blomqvist and coworkers [*160,161*] and Korpelainen et al. [*162*]. Results of these works were later used by Blomqvist to calculate PLA-specific parameters for the Polymer Consistent Force Field (PCFF), a complex potential energy function used in molecular dynamics simulation of polymers. In Chapter Five, we will use our own electronic structure calculations to develop improved torsional potentials for use in the more conventional and widely used OPLS and CHARMM force fields.

In this chapter, computations were performed on model lactic acid oligomers, with particular attention given to the variation of molecular properties with rotational degrees of freedom. Given the structural similarity between the PLA repeat unit and α-amino acids (e.g., alanine), in this work we have adopted nomenclature commonly used in the protein literature. Thus, the principal rotational degrees of freedom within a single lactyl repeat unit are labeled in Figure 4.1 as ϕ, ψ, ω, and χ, each of which represents rotation about a single bond. Electron density functional theory (DFT) computations at the B3LYP/6-31G** level were performed on several oligomeric

surrogates of PLA, both *in vacuo* and within a simulated bulk phase. In each case, the potential energy landscapes were charted, and electrostatic charge densities were also estimated. Finally, as an example of the general applicability of this data, we present RIS calculations for the polymer, for comparison with experimental viscometric data. These results demonstrate the importance of accounting for the condensed phase environment of the molecules.

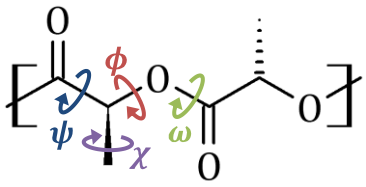

Figure 4.1 (L, L)-Lactide monomer showing the rotational modes present in a single L-lactyl unit. The primary dihedral angles, ϕ, ψ, and ω were defined in Section 3.1, with Figure 3.2 and Table 3.3.

It should also be noted that many of the RIS analyses of PLA in the current literature continue to rely on de Santis and Kovacs' van der Waals model in their 1968 publication [*143*], or the work published the following year by Brant et al., which included both van der Waals and electrostatic interactions [*140*]. While these results provide a relatively good qualitative description of the energy landscape for bond rotations, they have been shown to inadequately explain recent spectroscopic and viscometric data [*23,145,146,180*]. Given this discrepancy, and given the many advances

in computational methods over the past four decades, we feel it is time for the research community to adopt a more sophisticated theoretical model of bond rotation in PLA.

The fact that the potential energy surface for PLA calculated from Blomqvist's force field [*173*] differs remarkably from the early models of de Santis and Kovacs [*143*] and Brant et al. [*140*] further demonstrates the need to revisit the topic with a higher level of theory. Figure 4.2 illustrates that the four bond-rotational potential energy minima reported by Brant et al. are replaced by two broader basins in the more recent force field description of PLA by Blomqvist. This two-basin model is similar in topology to that predicted by de Santis and Kovacs, yet the relative energies of the two basins are opposite for Figures 4.2a and 4.2c. While the results shown in Figure 4.2c are not obtained *ab initio*, the methodology by which the force field description was parameterized (from high-level MP2 calculations on simple esters) make this the highest level of theory applied to calculating the potential energy surface of PLA to date.

We demonstrate in this chapter that both the topology and relative energies of Blomqvist's potential energy surface for bond rotations [*173*] are indeed similar to those achieved using direct electronic density functional theory (DFT) calculations. However, our studies demonstrate that subtle variations in the topology can significantly influence observable polymer behavior. Given this observation, and because our data represents the highest level of theory applied to calculating the bond rotational potential energy surface of PLA, we suggest that researchers use the DFT derived topology presented here in future conformational analyses of PLA.

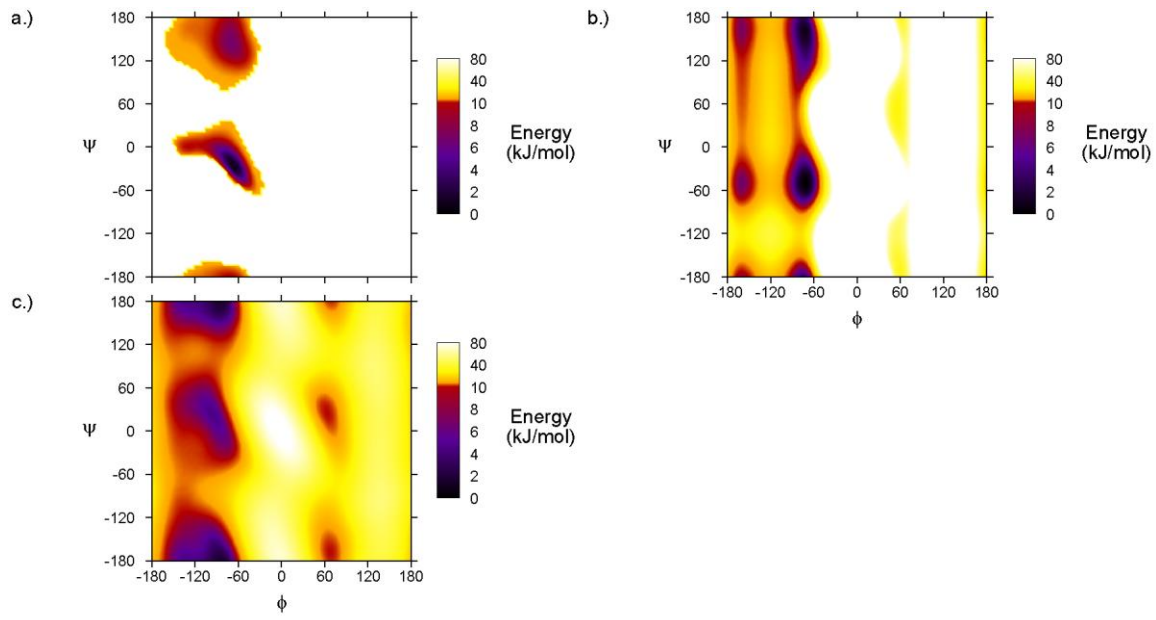

Figure 4.2 Potential energy surfaces for rotations about dihedrals ϕ and ψ, reconstructed from previous studies. a.) Scaled from Figure 3 in reference [*143*]; b.) Calculated using the method and parameters described in reference [*140*]. White regions are of higher energy than the scale shown; c.) Scaled from Figure 3 in [*173*].

§ 4.2. Methods

Except where noted otherwise, the quantum mechanical results detailed in this work are based upon DFT computations using Jaguar 4.2 software [*181*]. Initial computations on our system revealed that DFT results compared favorably with higher-level local Møller-Plesset second-order perturbation theory (LMP2) [*142*], as has been observed with many other organic systems [*182*]. Thus, the DFT method was chosen due to its greater computational efficiency.

§ 4.2.1. Partial Atomic Charges

The assignment of partial atomic charges to atoms has significance in developing classical force field descriptions of the molecule, and it also influences the quality of the self-consistent reaction field (SCRF) calculations discussed in Section 4.2.3. For all partial atomic charges reported in this work, the electrostatic potential (ESP) was fit to each atom center using a rectangular grid with 0.3-Å spacing, based on the observations of Sigfridsson [*183*]. The ESP was constrained to replicate the charge and molecular dipole, obtaining partial atomic point charges via the CHELPG method [*169*]. In estimating charges during SCRF calculations, the total charge and dipole moment were also replicated in the ESP fit, although Jaguar's default (spherical) grid spacing was used.

§ 4.2.2. Calculations *in vacuo*

Default settings for the B3LYP functional were used for the estimation of properties *in vacuo*, including the following terms: a Hartree-Fock exchange/Slater local exchange functional with Becke's non-local gradient correction [*184*], the Vosko-Wilk-Nusair local functional [*185*], and the Lee-Yang-Parr local and non-local functional [*186*]. The split-valence basis set 6-31G** was used in all calculations, which has been shown to perform well in estimating rotational energy barriers for many single and some conjugated bonds [*182*]. The commonly reported accuracy of this method is within approximately 2 kJ/mol for the calculation of relative conformational energies [*187*]. In this work, zero point energy corrections were not applied, as the calculated normal

mode vibrations are nearly equal for the different conformers studied and, thus, are not important when considering the relative energy difference between conformers.

§ 4.2.3. Calculations in the Bulk Amorphous Phase

Calculation of condensed phase properties via quantum methods has been discussed extensively in the literature, and for a comprehensive review the reader is directed to the papers of Tomasi and Persico [*188*] and Cramer and Truhlar [*189*]. In the present work, we utilize the self-consistent reaction field (SCRF) method as implemented in Jaguar version 4.2. In this method, the solute is considered to exist inside a cavity surrounded by a dielectric continuum (see Figure 4.3). The goal of this method is to estimate the free energy of solvation, corresponding to the energy needed to take a molecule from a fixed location in a gaseous phase and place it at another fixed location within a liquid [*190*].

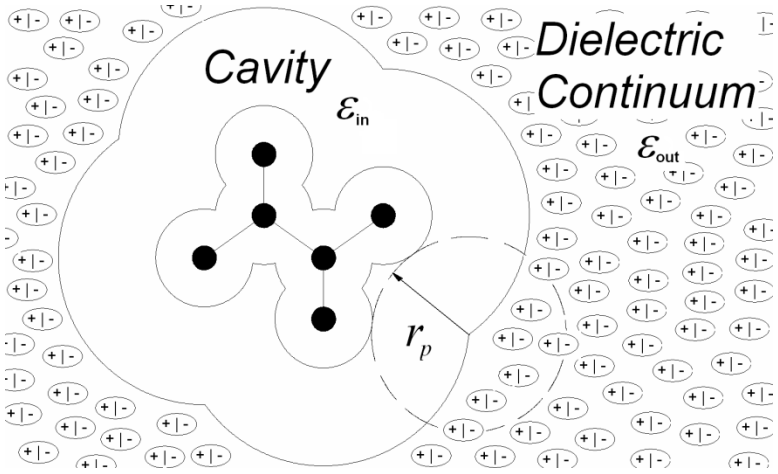

Figure 4.3. Representation of a molecule immersed in a dielectric continuum. The size of the cavity is dependent on the probe radius, r_p.

Jaguar's solvation model divides the Gibbs free energy of solvation into two terms,

$$\Delta G_{solv} = \Delta G_{el} + \Delta G_{np} \tag{4.1}$$

where ΔG_{el} is the energy difference due to the difference in the molecule's electronic wavefunctions within the continuum and *in vacuo*, and ΔG_{np} is the energy required to insert a noncharged, nonpolar molecule inside a cavity of the same size and shape as the solute cavity.

Jaguar's SCRF procedure estimates ΔG_{el} as follows. After estimating the partial atomic charges of all atoms in the solute molecule from the *in vacuo* DFT wavefunction, the Poisson-Boltzmann equation is solved using the PBF program (a finite-element solver developed by Cortis and Freisner [*191,192*]), yielding the charge distribution at the boundary surface between the dielectric continuum and the molecular cavity. Given this information, the electronic wavefunction is recalculated in the presence of the surface charges, and the process is repeated until the wavefunction and reaction field have converged. The principal adjustable parameters in this method are the internal dielectric constant within the cavity, ε_{in}, the dielectric constant of the continuum outside the cavity, ε_{out}, and the probe radius, r_p, defining the size of the molecular cavity (see [*192*]). Because the electronic wavefunction is solved explicitly for the molecule within the cavity, it is customary to use a value of $\varepsilon_{in} = 1.0$, and since the dielectric constant of PLA has been measured experimentally, we set $\varepsilon_{out} = 2.83$ for

PLA at room temperature [*193*]. However, the choice of a proper probe radius is not as obvious.

When the solvation effects of small molecules are of interest, the probe radius parameter has a meaningful definition, namely, one half the thickness of the first solvation shell surrounding the solute molecule. The first solvation shell itself is traditionally defined as the first layer of solvent molecules that surround and associate with the solute. Thus, its thickness is on the order of the solvent's molecular dimensions. In the case of small solvent molecules of approximately spherical geometry, r_p is easily estimated from knowledge of the size and packing of the solvent molecules [*194*].

$$r_p^3 = \frac{3m\Delta}{4\pi\rho} \tag{4.2}$$

Here, m represents the mass of a single solvent molecule, Δ is the packing density, and ρ is the (bulk) density of the solvent. Typical values of probe radii used for solvation calculations are between 1 and 3 Å. The approximation of spherical solvent geometries implicit in Equation 4.2 has been shown to work well in cases where all length dimensions of the solvent are of the same order of magnitude. However, for solvation of oligomers in a high molecular weight polymer matrix, relating the size of the first solvation shell to the solvent molecular dimensions is difficult since the length of a polymer chain can be orders of magnitude larger than its width.

Thus, when attempting to apply the SCRF method to amorphous phase polymers, we employ a broader definition of the first solvation shell. Rather than defining it as the first layer of molecules that associate with the solute, we consider the first solvation shell to be the first layer of solvating units to interact with the solute. In the case of polymers, these 'units' may be only small segments of the macromolecules, rather than entire polymer chains. In these terms, the first solvation shell certainly occupies less volume than even a single polymer chain, and therefore, a probe radius calculated by applying Equation 4.2 to the polymer molecules would vastly overestimate the size of the solvation shell.

As existing methods for calculating the solvent probe radius are inappropriate for solvent media consisting of oligomeric or polymeric species, one must identify other reasonable strategies for obtaining an appropriate probe radius. It is reasonable to imagine that the first solvation shell would be made up of a small number of chain repeating units, from one or more molecules, rather than being made up of entire chain molecules. Thus, one might expect that a reasonable value of the probe radius should be on the order of that for a lactyl unit ($CHCH_3OCO$), or about 2.28 Å (assuming the packing density is approximately 0.5). Alternatively, an estimate for the probe radius can be obtained using solvents with similar functionality and dielectric constant to PLA, such as diethyl carbonate. Using accepted packing densities for this solvent [*195*] and Equation 4.2, one calculates the probe radius to be 2.83 Å.

Another reasonable estimate of the probe radius may be arrived at by considering the polymer under Flory θ conditions (see Section 2.1.2). Because a polymer in solution at its θ condition has comparable interactions with itself and with its solvent, it may be reasonable to use parameters typical of a θ solvent to describe solvation within the bulk polymer. Based on interaction parameters derived from light-scattering experiments, it is estimated that dibutyl phthalate and dipropyl phthalate are θ solvents for pure isotactic PLA at approximately 80 °C and 0 °C, respectively [*28*]. Using Equation 4.2 for these solvents, probe radii are found to be approximately 9 and 11 Å, respectively. We note that such probe radii are well out of the range typically used in continuum solvation models. Further, though size effects are certainly at play within a polymer-solvent system, it is likely that energetic interactions play a greater role than size effects in determining the θ condition. This is evidenced, for example, in the widely-used Flory-Huggins theory [*196*]. While the relative sizes of polymer and solvent have a definite effect on thermodynamic properties of the system (i.e., phase equilibria), the θ condition is solely determined by the Flory-Huggins χ parameter—physically interpreted as a measure of the *energetic* interaction between polymer and solvent. Thus, relating the probe radius size to that of a θ solvent has relatively little justification from a theoretical standpoint.

All of the above estimates for probe radii vary widely, and *a priori* it was not obvious which method for calculating the probe radius was most appropriate. Thus, in this work we considered several probe radii within the range described above,

specifically between that of the lactyl unit (2.28 Å) and a θ-solvent for the polymer (approximately 10 Å). In practice, we found that the Poisson-Boltzmann solver failed to converge when using probe radii larger than 8 Å; therefore, this was the largest probe radius examined.

Additional difficulty in applying a solvation model to the PLA system is imparted by the fact that the creation of a cavity within the polymer would affect the conformation of neighboring intrachain units well outside the first solvation shell. The reorganization of the solvent phase is typically accounted for in the nonpolar cavity term given in Equation 4.1. For solvation in water, Jaguar estimates ΔG_{np} using an empirical correlation between solvent-accessible surface area (SASA) and the solvation energies of linear and branched nonpolar molecules (alkanes) in water [*197*]. However, empirical correlations for other solvent systems are not available, thus, ΔG_{np} was not automatically calculated by the simulation software. Because it is correlated with the SASA, one can conclude that this term does not significantly affect the topology of the conformational energy landscape so long as the SASA of the molecule of interest does not change significantly over the range of applicable conformations. Since the surface area of short PLA oligomers is only a weak function of oligomer conformation, the term simply shifts all computed energies by some (nearly) constant value and thus, can be neglected. Whereas, when absolute free energies are required, such as with the calculation of species solubility, the term should not be ignored. As the focus of this

paper is only on quantifying the relative energies associated with bond rotation, we have neglected the cavity term in reporting energy landscapes in the condensed phase.

§ 4.2.4. Exploring the Rotational Energy Landscape

Though there are four principal rotational degrees of freedom defined in Figure 4.1 for a single lactyl repeat unit (i.e., ϕ, ψ, ω, and χ), only those rotational degrees of freedom within the backbone of PLA chains, namely, the ϕ, ψ, and ω dihedral angles, are of importance for polymer modeling applications. Furthermore, as is common with proteins, the ω dihedral angle rarely deviated from a value corresponding to the minimum-energy *trans* state regardless of the values of the remaining degrees of freedom. This observation is easily explained by considering the partial π-bond character of the backbone ester bond. As will be shown in Section 4.3.2, initial DFT computations showed an extremely high energy barrier, with a negligible probability of barrier crossings under normal conditions, for rotation about this bond. Thus, following this initial investigation of ω, the parameter space explored in this work reduces mainly to that of the (ϕ, ψ) plane.

Rotational energy barriers about ω were computed starting from an initial configuration of a methyl terminated L-lactic acid trimer ($C_{11}H_{18}O_7$, molecule **1**, shown in Figure 4.4), in which the molecular geometry was set according to the WAXD-resolved coordinates of the α-form crystal structure proposed by Sasaki and Asakura [*45*]. To avoid bias due to the selection of the initial structure, thirty-five additional input structures were also used, in which the value of ω_1 was rotated in 10° increments. For

each of these thirty-six PLA trimer conformations, the molecule was initially subjected to unconstrained DFT energy minimization at the B3LYP/6-31G** level. During subsequent DFT minimizations, the value of ω_1 in the central repeat unit was constrained at assigned values, which varied between -180° and +180° via increments of 10°, yielding a total of 36 values for ω_1. In this work, all dihedral angles are defined along chain backbone atoms (the O^S, C', and C^α atom types as labeled in Figure 4.4) and follow the IUPAC convention [*151*]. Full rotation of the ester bond over 360° was necessary due to the asymmetric nature of lactic acid, which results from its chiral α-carbon. During this procedure, the optimized structure from a previous simulation served as the starting configuration for each new minimization, with ω_1 incremented by 10°. For each value of ω_1, the conformer yielding the lowest energy was selected as the most representative structure.

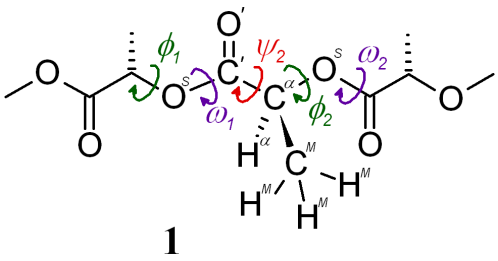

Figure 4.4. Methyl terminated L-lactic acid trimer used in determining rotational potentials. Dihedrals ϕ_2 and ψ_2 are the principle degrees of freedom studied.

To obtain an accurate representation of the rotational energy landscape in (ϕ, ψ) space, considerably more computational effort was expended so as to avoid any

bias of the DFT energy minimization results that might arise from the choice of initial trimer conformation at each grid point in (ϕ, ψ) space. Initially, the trimer structure was built using dihedral values from the experimentally resolved crystal structure [*45*]. From this conformation, the ϕ and ψ bonds of the central repeat unit (ϕ_2 and ψ_2) were each rotated at 30˚ increments, resulting in a total of 144 structures located in the (ϕ_2, ψ_2) plane. Each of these were subject to unconstrained energy minimization *in vacuo* at the B3LYP/6-31G** level. The 144 initial configurations settled each into one of seven unique stationary points, and Figure 4.5 shows the corresponding minimization paths projected onto the (ϕ_2, ψ_2) plane. Following this step, sequential grid searches were performed in the ϕ_2 and ψ_2 dimensions starting from each of the seven observed unconstrained energy minima.

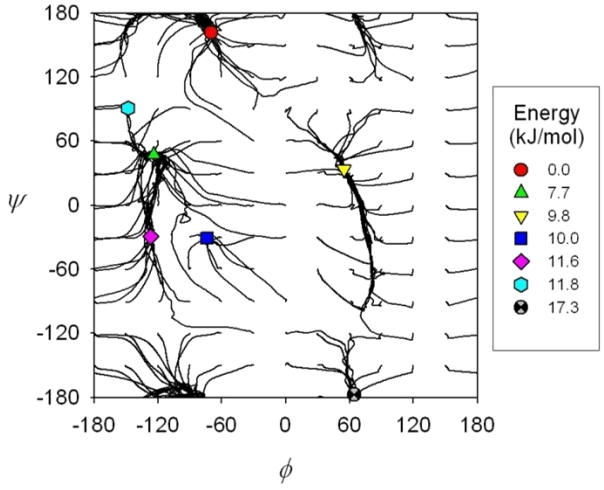

Figure 4.5. Trajectories for initial unconstrained minimizations in the gas phase. Points represent the seven unique stationary points identified from initial simulation studies. Reported energies are relative to the lowest-energy structure.

In each grid search, one of the seven stationary points described above was used as a starting structure for the development of a separate rotational energy surface, as described in the following paragraph. Subsequently, the lowest energy structures from the seven separate surfaces were combined to form a single representative minimum energy surface. The relative potential energy of trimer conformers was evaluated over the full rotational range in the (ϕ_2, ψ_2) parameter space using a diagonal square grid with a spacing of 10° on the hypotenuse (see Figure 4.6). The selected grid spacing yields 2592 different conformers, resulting in a large number of DFT simulations. However, it was found that the DFT energy minimizations converged more rapidly on the finer grid due to the quality of the initial structures. Thus, the chosen grid spacing gives a nearly optimal tradeoff between the number of DFT simulations and the number of geometry optimization steps required for each.

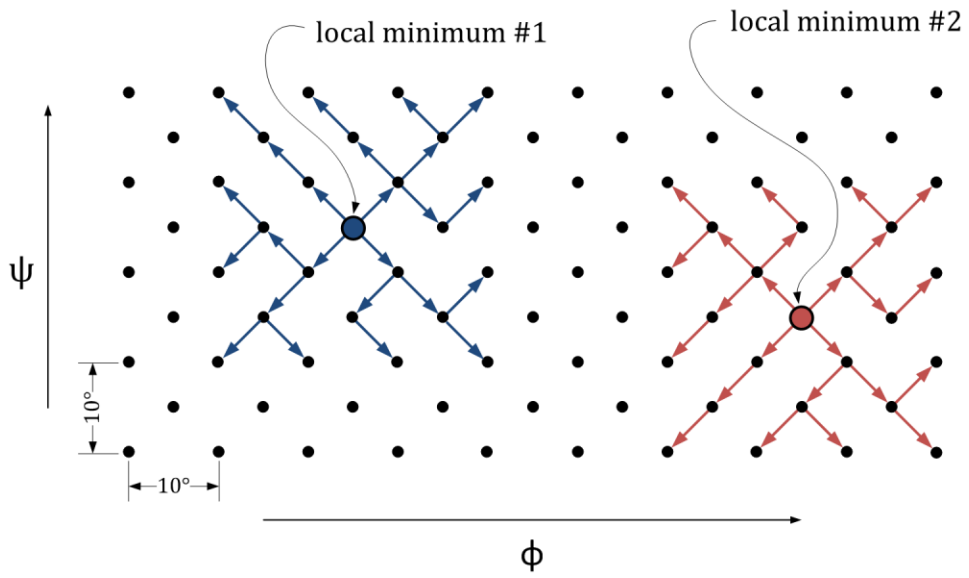

Figure 4.6. Schematic representation of the grid search procedure.

Each of the seven conformational energy surfaces described above was generated in a sequential pattern, with the first structure obtained by setting the ϕ_2 and ψ_2 values in the selected unconstrained minimum-energy conformer to those of the nearest grid point in (ϕ_2, ψ_2) space. This structure was subject to (ϕ_2, ψ_2)-constrained minimization, and upon completion of this simulation, bonds in the minimized trimer were rotated as needed to obtain the values of ϕ_2 and ψ_2 for each unminimized neighboring conformer (between 1 and 4) on the selected grid. Each new conformationally unique trimer was then optimized, again with both ϕ_2 and ψ_2 constrained to their new respective values. Subsequently, the process was continued by rotating and constraining ϕ_2 and ψ_2 to new neighboring points along the rotational energy surface, until constrained minimum energy structures were obtained at all grid points. Upon completion of these sequences, a representative minimum-energy surface was constructed by selecting the lowest energy at each grid point from the seven data sets. Since a proper averaging scheme would require more exhaustive sampling of phase space, we assume that the lowest energy structure dominates the partition function and is therefore most representative. The minimum-energy surface obtained in this way will be referred to as a *composite surface*, since it is constructed from several separate grid-search surfaces.

The entire grid search procedure, described in the preceding paragraphs and depicted in Figures 4.5 and 4.6, was repeated for each of the solvent probe radii investigated, with slight modification. The initial unconstrained minimizations, per

Figure 4.5, were performed starting from the 144 gas phase-minimized structures. Also, given the larger computational burden for the SCRF calculations, the grid searches, per Figure 4.6, were not taken to completion from each of the seven local minima starting structures. Rather, each grid-search energy surface was completed only near the local basin of the starting structure, refining the low-energy portion of the composite surface. The remaining (high energy) points were obtained by SCRF calculations on each of the gas phase composite surface structures without minimization. In cases where multiple grid-search surfaces overlapped at a grid point, the conformation with the lowest energy was selected for construction of the composite surface as described above. Thus, several composite potential energy surfaces were obtained in the (ϕ_2, ψ_2) space: one *in vacuo*, and one for each probe radius used in the solvent model (2.28, 2.83, 5.00 and 8.00 Å).

In an attempt to calculate atomic charges more representative of high molecular weight PLA chains, a series of *in vacuo* and SCRF DFT calculations were also performed on methyl terminated PLA chains containing 3 to 9 lactyl units. For these simulations, the PLA chain length was increased until the partial atomic charges of the central monomer unit did not vary with increases in oligomer length. For each chain, the crystal structure configuration was built and minimized as described previously, at the B3LYP/6-31G** level, *in vacuo* and using each of the probe radii examined for the SCRF method.

§ 4.2.5. Rotational Isomeric State (RIS) calculations

The RIS method was used to estimate unperturbed chain dimensions of amorphous PLA. In this work, two different RIS methods were utilized. In the first, we adopt the virtual bond definitions for PLA as originally laid out by Flory [*139*,*140*,*198*]. The characteristic ratio for this system can be obtained analytically by the relation [*199*]

$$C_{\infty,v} = \{(\mathbf{I} + \langle \mathbf{T} \rangle)(\mathbf{I} - \langle \mathbf{T} \rangle)^{-1}\}_{11} \tag{4.3}$$

where $\mathbf{I}$ is the identity matrix of order three, $\langle \mathbf{T} \rangle$ is the ensemble-averaged transition matrix, and the desired matrix element {1, 1} is given by the subscript. The subscript v indicates the basis of virtual bonds. For a particular geometry, the matrix $\mathbf{T}$ can be expressed as a product of three matrices, $\mathbf{T}^{\xi}\mathbf{T}^{\theta\phi}\mathbf{T}^{\eta\psi}$. The reader is referred to the previously cited works of Flory and coworkers for an in-depth explanation of the method, including definitions of the geometric parameters [*139*,*140*,*200*]. However, we note that the dihedral angle convention used in those references is opposite to the IUPAC convention used in this work. Thus, using the IUPAC convention for ϕ and ψ, the transition matrices are computed by:

$$\mathbf{T}^{\theta\phi} = \begin{bmatrix} \cos\theta & \sin\theta & 0 \\ -\sin\theta\cos\phi & \cos\theta\cos\phi & -\sin\phi \\ -\sin\theta\sin\phi & \cos\theta\sin\phi & \cos\phi \end{bmatrix} \tag{4.4}$$

and

$$\mathbf{T}^{\eta\psi} = \begin{bmatrix} \cos\eta & -\sin\eta & 0 \\ -\sin\eta\cos\psi & -\cos\eta\cos\psi & \sin\psi \\ -\sin\eta\sin\psi & -\cos\eta\sin\psi & -\cos\psi \end{bmatrix} \quad (4.5)$$

The matrix $\mathbf{T}^{\xi}$ remains the same as given by Flory. This method relies on the explicit assumption that ω remains constant at exactly 180° in each repeat unit, regardless of the value of ϕ and ψ. As discussed in the results section, the actual value of the ω dihedral deviates slightly from this value as to reduce other high-energy interactions within the molecule.

Due to the artificial constraint of ω at 180° in Flory's analytical method, we have employed a Monte Carlo method as a second approach to obtaining the amorphous statistics from the RIS model. With this method, the (ϕ, ψ) plane is sampled according to a Boltzmann distribution, and chains are constructed by reading the bond lengths, valence angles, and dihedral angles for the backbone atoms directly from the z-matrix output of our DFT calculations (all geometric parameters were taken from the central repeat unit of molecule **1**). While this method accounts for variations in molecular geometry, it is susceptible to statistical uncertainty due to incomplete sampling of phase space. In practice, several million Monte Carlo iterations were needed before converging on a meaningful estimate.

To allow for a more straightforward comparison of analytical and Monte Carlo RIS results to those reported in the literature, we calculated the characteristic ratio on the basis of real bonds,

$$C_\infty = C_{\infty,v}\frac{l_v^2}{n_{r/v}l^2} \tag{4.6}$$

where l_v is the average length of a virtual bond, $n_{r/v}$ is the number of real bonds per virtual bond, and l is the average length of a real bond. By definition, $n_{r/v}$ is 3 for PLA, and we use the average squared real bond length of 2.05 Å^2 as adopted by Dorgan [*23*]. For each SCRF probe radius, as well as for gas phase, the mean squared virtual bond length was calculated using a Boltzmann-weighted average over all structures in the appropriate composite rotational energy surface.

§ 4.2.6. Hardware

Most calculations were performed on a Beowulf cluster comprising 160 dual-cpu (997 MHz Pentium III) nodes running Linux kernel 2.6.8, though some of the less computationally intensive simulations were performed on single-cpu SGI O_2 platforms with R12k (270 MHz) processors and the Irix 6.0 operating system.

§ 4.3. Results and Discussion

§ 4.3.1. Comparison of DFT Results to Higher-level Theories

Here we briefly present a subset of the rotational barriers examined by Blomqvist et al. [*160*] to estimate the relative accuracies of DFT, LMP2, and MP2 levels of calculation for aliphatic polyesters, using the 6-31G** basis set in each case. The esters investigated by Blomqvist are shown in Figure 4.7. These are chemically similar to polylactide, and hence, we feel that the favorable comparisons of our results serve as

indicators of the performance of DFT compared to MP2 (and its local variation) in this application. Figure 4.8 reveals the rotational behavior of the carbon-oxygen bond in the ester linkage (dihedral τ_2) of molecule **2** calculated from DFT and LMP2 by O'Brien [*142*], comparing them to Blomqvist's MP2-level results. Because relative energy barriers are a primary focus in this work, the scale has been shifted such that the minimum energy conformation for each data set is assigned a value of zero kJ/mol, and all of the following figures use this convention. The three levels of theory are in close agreement, with a maximum disparity between DFT and MP2 occurring at the *cis* minimum with an energy difference of approximately 4 kJ/mol. Additionally, the height and position of the energy barrier were predicted by DFT to within 2.7 kJ/mol and less than 5°, respectively, when compared to MP2 results.

The DFT and MP2 results for rotation of torsional angle τ_3 in molecule **3** are shown in Figure 4.9. Due to the relatively small height of the energy barrier observed during rotation of this bond (approximately 4.5 kJ/mol compared to 62.5 kJ/mol for rotation about τ_2 in molecule **2**), the percentage difference between predicted relative energy maxima from DFT- and MP2-level simulations is increased. The absolute energies from DFT simulations are generally lower than those predicted using MP2 level theory, which was also observed in molecule **2**, though this is not presented in Figures 4.8 and 4.9 since the energies of each set have been shifted. DFT accurately predicts the overall shape of the rotational energy barrier, including the three energy minima and the position of the intervening transition points. The high-energy transition points resulting

from interaction between methyl groups and the carbonyl oxygen both peak at τ_3 values occur closer to their connecting gauche minimum than predicted by MP2.

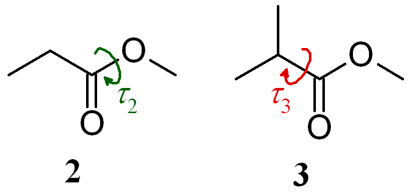

2 **3**

Figure 4.7. Dihedral angle conventions for molecules **2** and **3**, used for comparison with MP2 calculations of Blomqvist [*160*].

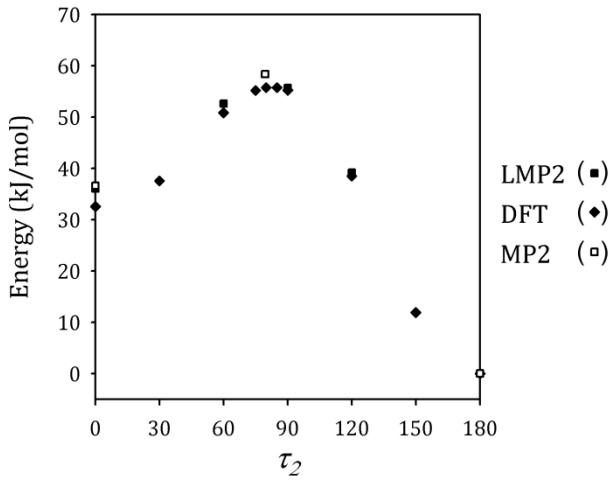

Figure 4.8. Bond rotational energy profile for the τ_2 dihedral for molecule **2**. ■: LMP2 and ♦: DFT [*142*], □: MP2 [*160*]. All data sets have been shifted so that the minimum at 180° has an energy of 0 kJ/mol. Only points of extrema, determined by energy minimization and eigenvector following, are shown for the MP2 results.

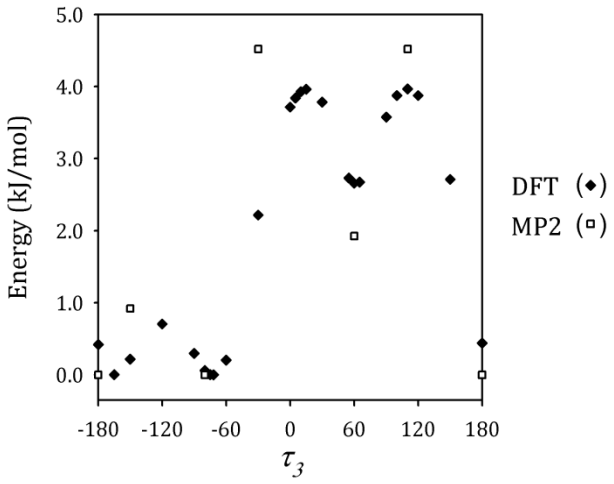

Figure 4.9. Bond rotational energy profile for the τ_3 dihedral of molecule **3**. ♦: DFT [*142*] and □: MP2 [*160*]. Only points of extrema, determined by energy minimization and eigenvector following, are shown from the MP2 results.

These results, and significant other work [*182*], illustrate that DFT-level calculations provide an acceptable level of accuracy for the investigation of the relative bond rotational barrier heights in aliphatic polyesters. In light of this, and due to the significantly reduced computational burden when employing DFT, the remaining results presented here have all been obtained using DFT at the B3LYP/6-31G** level.

§ 4.3.2. Rotations About ω

Changes in the DFT-calculated potential during rotation of ω_1 in molecule **1** are shown in Figure 4.10, along with the response of the adjacent backbone dihedrals. This energy barrier is nearly symmetric since the bond does not include the chiral α-carbon. However, unlike the corresponding energy barrier for rotation about τ_2 in molecule **2**,

the position of the *trans* energy minimum shows some deviation from 180° due to the chiral C^{α} atoms present on the ends of the ω_1 dihedral. The magnitude of the energy barrier along ω_1 is quite high (approximately 60 kJ/mol), which can be attributed to the significant double-bond character of the C'-O^S bond (as defined in Figure 4.4). It is easily seen from resonance structure arguments that charge transfer to the carbonyl oxygen causes the backbone oxygen atom to become more positively charged and sp^2 hybridized, while the carbonyl oxygen becomes more negatively charged and sp^3 hybridized [*201*]. It is this feature that is responsible for the overall size and shape of the curve, creating two distinct energy maxima at dihedral angles of approximately −90° and 80°, with the global energy minimum corresponding to the *trans* configuration. The height of the two rotational energy barriers relative to the energy minimum for the *trans* configuration supports our general observation that unconstrained ω angles rarely deviated from values outside the range 165 - 180°. We also see that the minimum-energy positions of the adjacent backbone dihedral angles ϕ_1 and ψ_2 do not deviate appreciably due to rotation of ω_1 within the *trans* energy basin, though considerable movement of ϕ_1 and ψ_2 is necessary to relieve high energy interactions in the secondary minimum. Given this information, it is anticipated that minimal error is introduced in rotational energy surface calculations that decouple the ϕ and ψ degrees of freedom from ω. Hence, the remainder of this work is focused on the principal rotational degrees of freedom ϕ and ψ. During exploration of the (ϕ, ψ) energy

landscape, we observed that the optimal value of all ω angles were indeed contained within the *trans* minimum energy conformation in both gas phase and SCRF calculations.

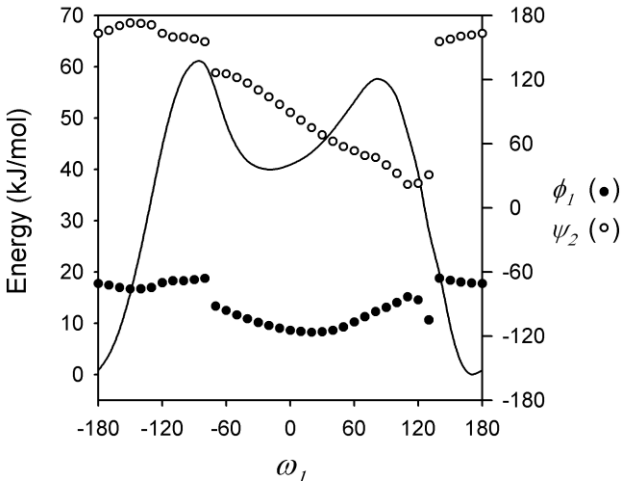

Figure 4.10. Bond rotational energy profile for dihedral ω_1 of molecule **1** (smooth curve, refer to the left-hand y-axis). At each increment of ω_1 rotation, the optimized values of ϕ_1 and ψ_2 are also shown (refer to the right-hand y-axis).

§ 4.3.3. Rotations about ϕ and ψ

Potential energy surfaces for rotations of molecule **1** about ϕ_2 and ψ_2 in the gas phase and using the SCRF method (with several different probe radii) are shown in Figure 4.11. In what follows, these dihedrals will be referred to simply as ϕ and ψ. In the SCRF calculations, the largest probe radius examined was 8.00 Å. This value is much higher than typical values used in solvation calculations, though slightly smaller than that estimated for a θ-solvent. As described in Section 4.2, considerable effort was exerted to find the global minimum structure at each of the constrained values of ϕ and

ψ, by obtaining multiple optimized structures at each point using different initial structures.

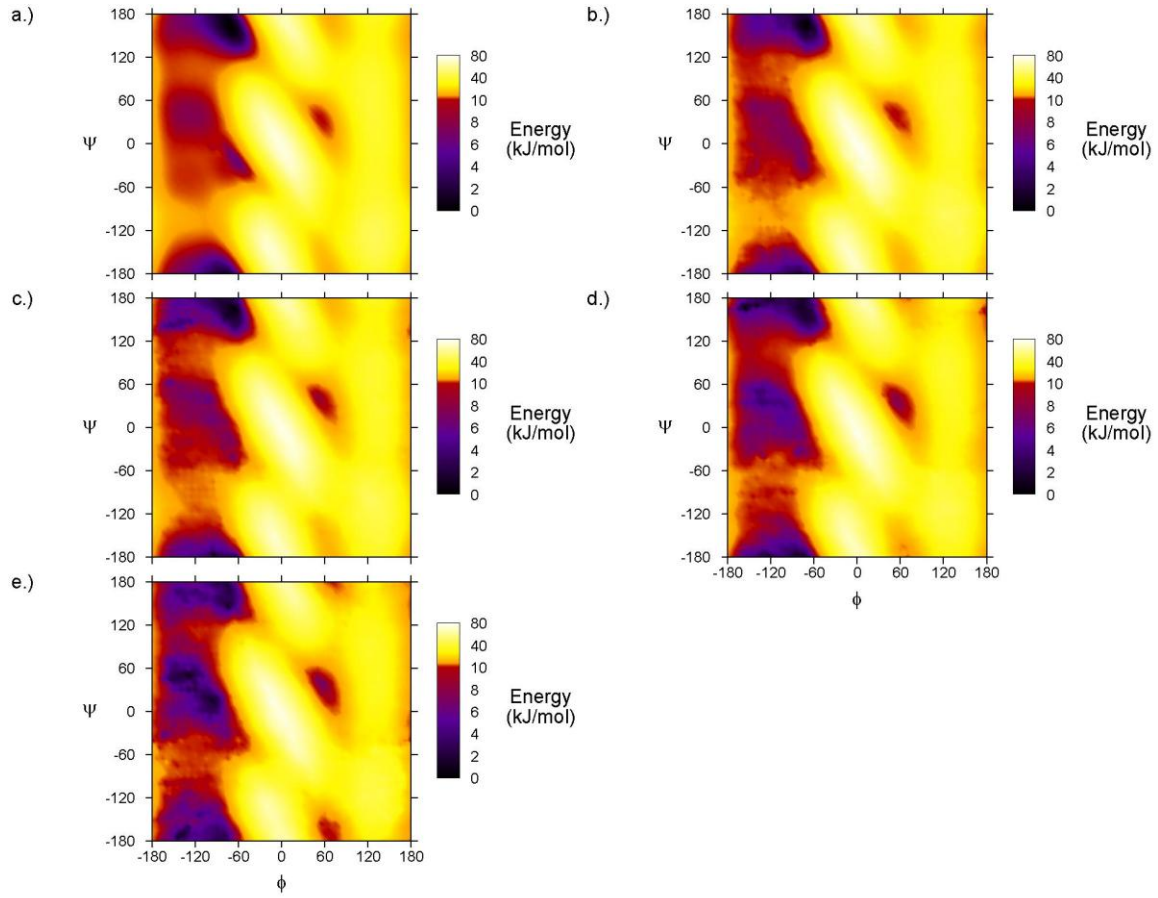

Figure 4.11. Bond rotational energy profiles for the ϕ_2 and ψ_2 dihedrals of molecule **1**. Plot (a) was obtained *in vacuo*. Plots (b) – (e) were obtained using the SCRF method using different solvent probe radii; b.) $r_p = 2.28$; c.) $r_p = 2.83$; d.) $r_p = 5.00$; e.) $r_p = 8.00$.

While it is not feasible to accurately determine how effectively the data points in Figure 4.11 represent the global minima for each grid point, the smoothness and

continuity of the gas phase bond rotational energy surface (Figure 4.11a) suggests that the data points are at least well-connected in conformational space as a result of the grid search. That is, the constrained energy minima do not show drastic or erratic changes in energy with respect to their neighbors on the grid. Should there exist lower-energy minima not encountered during the grid searches, chances are that one at least one adjacent grid point might find the basin and disrupt the continuity in the surface. On the other hand, this continuity is lost in the condensed phase surfaces (Figure 4.11b-e) as the SCRF probe radius is increased. We attribute some of this loss of precision to the difficulties involved in the SCRF method, especially the calculation of partial atomic charges, as well as construction of the finite element mesh that estimates the molecular cavity. These factors contribute further to the difficulty encountered in executing a normal optimization scheme effectively, and these details should be considered when examining the SCRF potential energy surfaces in addition to the (presumably small) error associated with the DFT method itself as discussed previously.

The overall shape of the gas phase potential energy surface presented in Figure 4.11a is markedly different than that of Brant et al. [*140*]. In that work, the potential energy surface is dominated by four distinct minima corresponding to structures having IUPAC (ϕ, ψ) values of $(-73, -46)$, $(-73, 158)$, $(-160, -50)$, and $(-160, 161)$. Here we denote these minimum energy conformers as g^-c, g^-t, *tc*, and *tt*, respectively, with g^- representing the negative *gauche* state, *c* the *cis* state, and *t* the *trans* state. The surface calculated in this work bears more similarity to that shown by Blomqvist [*173*], with

predominant energy minima corresponding to the g^-t, g^-c, g^+t, and g^+c conformers. In Brant's work, the *tt* and g^-t regions are separated by an energy barrier with respect to ϕ, as are the *tc* and g^-c regions. While in some of the continuum model results (particularly Figures 5.4c-e), a separate *tt* local minimum is observed, our calculations in general do not indicate the kind of energy barriers predicted by Brant.

We have reason to believe that the apparent energy barriers between the *tt* and g^-t regions, and between the *tc* and g^-c regions, are particularly affected by the treatment of the valence angle centered on the ester oxygen (O^S in Figure 4.4). In this work, this angle is allowed to bend considerably during geometry optimization, in effect relieving the high-energy interactions that cause the aforementioned energy barriers. Brant, on the other hand, treated this angle (and all others) as rigid; hence, the barriers are observed in Brant's treatment, and are not observed in this work.

In addition to the g^+t and g^+c conformers, which are not indicated in Brant's surface, in our work the g^-g^+ conformer also appears to be a minimum energy structure. However, for the *tc* and g^-g^+ structures, true minima were not found (only first order saddles with one negative Hessian eigenvalue). These stationary points on the energy surface are largely engulfed by the basin of the g^-c conformer, and in our analysis they are grouped with it accordingly.

The suitability of each potential energy surface shown in Figure 4.11 for describing bulk PLA can be best determined by examining features of the energy landscapes. The basin centered near $(\phi = -70°, \psi = 162°)$, referred to here as g^-t,

represents the minimum energy structure for all simulation conditions but the highest SCRF probe radius examined. The dihedral angles corresponding to the g^-t minimum closely resemble those derived from WAXD measurements for crystalline PLA ($\phi = -64.2°, \psi = 155.7$), when averaged over the 5 residues that compose the α-form proposed in [*45*]. The fact that the g^-c/g^-g^+ basin in the vicinity of $(-135°, 50°)$ is predicted to be lower in energy than g^-t when the SCRF probe radius is increased above 5.00 Å suggests that this value of r_p is too high, since one would expect the conformation of molecules in the crystal structure to correspond to the lowest energy state accessible to the molecule. However, it is important to recognize that the difference in energy between the g^-t and g^-c conformers is only 0.7 kJ/mol for SCRF simulations with $r_p = 8.00\,\text{Å}$, and this is within the error associated with these calculations. Thus, it is still conceivable that the composite surface with $r_p = 8.00\,\text{Å}$ may be correct. Also, previous theoretical works have reported the g^-c conformer as the global minimum in intramolecular potential, while simultaneously asserting that the g^-t conformer obtains the most stable crystalline packing when specific intermolecular interactions are considered [*143*]. These statements are not necessarily incongruous.

Interestingly, the minimum energy structure that lies closest to the WAXD structure in the (ϕ, ψ) plane results from calculations *in vacuo*. An exact congruency between the predicted and experimentally observed (via WAXD) minimum energy structures is not expected with the SCRF method, as the dielectric continuum model cannot readily reproduce the environment within a crystal. Specifically, the continuum

methods fail to capture the highly directional nature of the electric field that arises from immobile molecules at regular and fixed positions within the crystalline environment. The condensed phase energy calculated in this work is largely interpreted as an intramolecular potential, with the intermolecular interaction only accounted for in a smoothed or averaged sense. Thus, specific intermolecular interactions must also be accounted for when considering the crystalline form of the polymer. Therefore, to validate the suitability of the SCRF model in this application, it is much more suitable to use material properties of the disordered amorphous state than of the crystal.

§ 4.3.4. RIS calculations

Amorphous statistics were obtained using the RIS method as described in Section 4.2. Upon increasing the SCRF probe radius used in DFT simulations, the progressive stabilization of PLA conformations contained in the g^-c potential energy basin of the (ϕ, ψ) rotational energy surface has the effect of shortening the probable end-to-end distances of the polymer. Conversely, C_∞ becomes larger when chain statistics are dominated by conformations contained in the g^-t rotational energy basin, which correspond to those observed with the extended helical crystal structure of PLA. Figure 4.12 shows C_∞ as calculated by Flory's analytical approach, as well as the numerical Monte Carlo scheme. Though the temperature range shown in the figure extends partially into the glassy state of PLA, we assert here that RIS calculations are only valid above the glass transition temperature (T_g). Upon cooling below T_g, the rotational states become kinetically trapped, a phenomenon easily seen in Figure 11 of

Meaurio et al. [*180*]. Therefore, to estimate C_∞ of amorphous PLA at room temperature, the appropriate RIS calculation should be carried out at T_g, which can vary from 50 to 80 °C depending on molecular weight, enantiomeric purity, and moisture content [*9*].

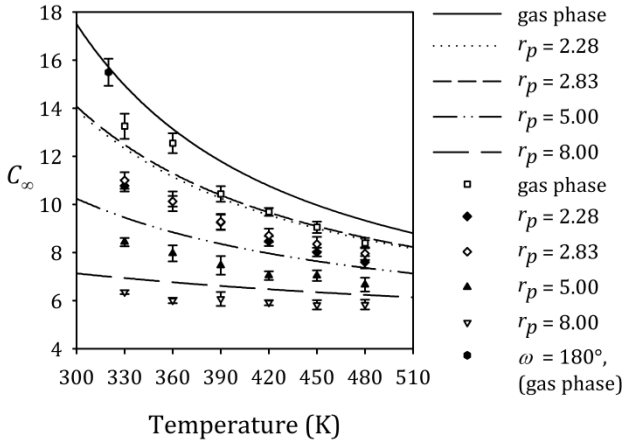

Figure 4.12. Calculated values of C_∞ from the (ϕ, ψ) potential energy surfaces computed in this work. Lines represent calculations based on Flory's analytical approach, while symbols represent results of the Monte Carlo approach. Data points were averaged over at least three separate Monte Carlo runs, each with one million sampled configurations. Error bars give the 95% confidence intervals. The data point at 320 K is shown to illustrate the effects of assuming the ester moiety is planar in the Monte Carlo method.

Though both methods use the same DFT potential energy surfaces to compute conformation probabilities, there is an obvious systematic difference in the calculated C_∞ values from Flory's analytical method and the numerical Monte Carlo approach. We

have concluded that this arises from the assumption that ω is a constant 180° for all structures in the Flory model. In the energy minimizations performed in this work, it is apparent that ω tends to lie closer to 172°, though deviations were observed especially in the high-energy states visited during the grid searches. Therefore, Flory's analytical method assumes the chain is stiffer than it actually is and thus, overestimates the value of C_∞. The Monte Carlo approach, though prone to the statistical uncertainties associated with incomplete sampling, accounts for deviations in the dihedral angle ω; therefore, it should yield a more accurate estimate of C_∞. As expected, Monte Carlo trials in which ω was set to a constant 180° resulted in values of C_∞ that were nearly equal to that calculated from Equation 4.3, reinforcing our assertion that the assumption of planarity in the ester moiety is responsible for the systematic difference shown in Figure 4.12. For illustration, one such value obtained at 320 K is shown in Figure 4.12.

In comparison with previous modeling studies, the values of C_∞ noted here are closer to the range reported by Blomqvist et al. [*171*]. On the basis of real bonds, Brant's reported value is 4.75 [*140*], which is outside of the range calculated here. In contrast, it was found in Blomqvist's study that, as more nonbonded interactions are incorporated between neighboring repeat units, C_∞ increases from 5.7 to 12.1. When considering the SCRF model in terms of interaction between nonbonded atoms, the presence of the dielectric continuum should shield such interactions. Therefore, the fact that the calculations *in vacuo* yielded the highest value of C_∞ is in accord with Blomqvist's

observations. However, when considering the different probe radii, the opposite trend is observed. As the probe radius is increased, the dielectric continuum should offer less shielding and therefore, increase the extent of intramolecular nonbonded interactions. As shown in Figure 4.12, though, this is accompanied by a decrease in C_∞ rather than the increase observed by Blomqvist. Similarly, it was anticipated that the larger probe radii should give results closer to the gas phase calculations, though this is clearly not the case for the RIS calculations. The same is observed in the shapes of the potential energy surfaces. Contrary to expectations, the smallest probe radius resembles the gas phase energies more than the larger probe radii. We note that this observation is true when considering the effect of the probe radius on the relative energies as plotted in Figure 4.11. The absolute energies, shown in Table 4.1 for the g^-t conformer, show the expected trend in which results approach those obtained *in vacuo* as the probe radius is increased. Still, the fact that the opposite trend applies to the relative energies is quite puzzling, and these results suggest that a solvation model more appropriate for polymeric systems should be developed.

Experimental values for C_∞ vary widely in the literature. A recent publication by Dorgan [*23*] asserts persuasively that the true value is likely close to 6.5, based on intrinsic viscosity data in several different solvents and extensive statistical analysis. Given this value, our data suggest that the large probe radius of 8.00 Å best describes the bulk state of PLA. As previously stated, this value is vastly larger than that encountered in conventional SCRF calculations, while being close to that of a θ-solvent.

The argument that the most suitable SCRF probe radius for modeling amorphous polymers should be on the order of the size of a θ-solvent is not only convenient to apply in practice, but also has an intuitive interpretation that fits nicely within the framework of the SCRF method and some fundamental concepts of polymer science. While Dorgan's estimate is most recent, another very commonly encountered estimate of C_∞ is that of Joziasse [*202*], which puts the value at approximately 11.7. This value is more closely reproduced by probe radii on the order of the lactyl unit's size, and thus, would suggest that the proper probe radius is on the order of the chain repeating unit rather than the θ-solvent. However, accepting either of these assertions as a general rule would require more testing on different polymer systems, and establishing such a trend would require additional comparison with experimental observations.

Table 4.1. Absolute energies of the lowest energy g^-t minima found during unconstrained minimization of molecule **1**.

Solvation Treatment	ϕ (degrees)	ψ (degrees)	Energy (hartrees)
r_p = 2.28 Å	-79.6	169.6	-206467.4
r_p = 2.83 Å	-77.1	167.2	-206465.3
r_p = 5.00 Å	-79.5	167.3	-206460.6
r_p = 8.00 Å	-76.6	163.1	-206455.6
in vacuo	-70.1	161.3	-206396.4

§ 4.3.5. Molecular Geometries

A comparison of bond lengths for the global minimum energy structures from DFT gas phase and SCRF calculations with those commonly adopted in wide-angle X-ray diffraction (WAXD) and scattering (WAXS) analyses [*45*,*143*,*144*] is shown in Table 4.2. The bond lengths and angles predicted by all DFT simulations in this work exhibited minimal deviation from the widely accepted values. Furthermore, the incorporation of solvation effects had negligible effect on calculated bond lengths, and very little (less than 2%) deviation was observed during the bond rotations studied. An important feature captured in all of our DFT simulations is the difference between the two carbon-oxygen bonds formed by the ester oxygen atom. The ester linkage O^S-C' is predicted to be approximately 0.1 Å shorter than the remaining carbon-oxygen single bond C^{α}-O^S, reinforcing the already well-documented evidence of resonance effects within the ester moiety and the partial double bond character exhibited in the ester bond. A 2% elongation was observed for the ester bond length when overcoming the energy barriers associated with rotation of ω, which also coincided with a contraction of the carbonyl double bond. This effect can also be attributed to resonance interactions, with the loss of sp^2 character in O' and a gain of sp^2 character in O^S during highly nonplanar conformations.

Table 4.2. Comparison of standard accepted bond lengths in PLA with those of DFT energy minimized structures in this work. Reference values were originally adopted by de Santis and Kovacs [*143*] and subsequently used by Hoogsteen et al. [*144*] and Sasaki and Asakura [*45*]. Data from this work are representative of both gas phase and SCRF calculations. Refer to Figure 4.4 for atom labels.

Bond	Length (Å)	
	Reference [*45*,*143*,*144*]	This Work
O^S-C'	1.31	1.35
C'-C^α	1.53	1.53
C'=O'	1.20	1.21
C^α-C^M	1.54	1.53
C^α-O^S	1.46	1.44
C^α-H^α	1.08	1.09

A similar survey of accepted values for the valence angles in PLA is shown in Table 4.3. As in Table 4.2, the accepted values reported in Table 4.3 are those used in recent X-ray studies on PLA [*45*,*143*,*144*]. It should be noted that these values were actually transferred from studies of simpler esters [*150,152,153*], rather than determined specifically for PLA. The optimized value of valence angles was more greatly affected by the SCRF calculation, unlike the bond lengths reported above. However, no discernable trend was observed with respect to the probe radii examined.

Table 4.3. Comparison of standard accepted values for valence angles in PLA with those from gas phase and SCRF energy minimized structures in this work. Reference values are the set of angles originally adopted by de Santis and Kovacs [*143*] and subsequently used by Hoogsteen et al. [*144*] and Sasaki and Asakura [*45*]. Refer to Figure 4.4 for atom labels.

Angle	Angle Measure (degrees)					
	Reference	Gas Phase	$r_p = 2.28$	$r_p = 2.83$	$r_p = 5.00$	$r_p = 8.00$
O^S-C'-C^α	110.0	109.7	109.9	109.9	109.7	109.9
O^S-C'=O'	125.0	124.7	124.8	124.7	124.9	124.8
O'=C'-C^α	125.0	125.7	125.3	125.4	125.4	125.3
C'-C^α-C^M	109.5	110.7	111.5	110.9	111.2	110.8
C'-C^α-O^S	109.5	109.4	108.6	109.1	109.0	109.2
C^M-C^α-O^S	109.5	107.4	107.5	107.3	107.4	107.3
C^α-O^S-C'	118.0	115.7	117.0	116.6	116.7	116.6
C'-C^α-H^α	109.5	108.2	108.3	108.5	108.4	108.5
C^M-C^α-H^α	109.5	111.6	111.4	111.4	111.4	111.5

Also in contrast to the bond lengths, a number of the bond angles experienced significant distortion during rotation of the dihedral angles. This information may be important when developing dihedral-angle cross terms in a force field description of PLA, and for this reason we have included much of the data in the Supporting Information files of the previously published version of this work [*203*]. During rotation of bonds, it was noted that, while the three angles composing the ester moiety showed large individual variation, overall planarity of the moiety was maintained for any given conformation. For example, even though the O^S-C'-C^α angle adopts values over a range

greater than 10° during the rotation of ω, the sum of the three angles having the carbonyl carbon at their vertex never deviates from 360° (i.e., a planar conformation) by more than 1.5°. Deviation of this sum was even smaller during exploration of the (ϕ, ψ) rotational energy landscape.

Dihedral angles for the lowest energy conformer in the $g^{-}t$ basin for each composite surface are shown in Table 4.4. As mentioned previously, the gas phase results lie closest to the experimentally resolved crystal structure proposed by Sasaki and Asakura [*45*]. Of the SCRF composite surfaces, the probe radius of 8.00 lies closest to the WAXD structure, though it should be emphasized that at this probe radius the $g^{-}c$ energy minimum is predicted to be slightly lower in energy than the $g^{-}t$ conformer. Another feature of interest is that none of the DFT calculations, whether in the SCRF continuum model or *in vacuo*, yielded minimum-energy values of ϕ that were in the range of those resolved from the WAXD experiments. The minimum energy value of the ω dihedral, which exhibits the highest energy barrier to rotation, lies within the range of experimental results, while the dihedral exhibiting the next highest rotational energy penalty, ψ, was predicted to have minimum energy values within or just outside the experimental range.

Table 4.4. Comparison of dihedral angles from the crystal structure proposed from WAXD results by Sasaki and Asakura [*45*], and those from energy minimized structures in this work. The WAXD values are the minimum and maximum values of the 5 residues in the proposed α-form crystal.

Dihedral	Angle Measure (degrees)					
	WAXD	Gas Phase	$r_p = 2.28$	$r_p = 2.83$	$r_p = 5.00$	$r_p = 8.00$
ϕ	-68.2 to -58.0	-70.4	-80.9	-78.1	-80.1	-76.6
ψ	150.0 to 163.9	162.2	172.1	164.8	168.4	164.4
ω	165.0 to 178.1	173.0	172.5	175.0	173.3	173.5

§ 4.3.6. Partial Atomic Charges

Table 4.5 shows that the CHELPG partial atomic charges for atoms in the energy minimized central monomer of molecule **1** (see Figure 4.4), which were obtained from *in vacuo* DFT simulations as well as simulations employing the reaction field approximation. Reported charges are taken as a Boltzmann-weighted average over all conformations on the appropriate composite energy surface in Figure 4.11, with Boltzmann weights evaluated at 60 °C (approximately T_g). The back-polarization of the molecule in response to the reaction field has the effect of strengthening the carbonyl dipole, though the charges of the other atoms remain largely unchanged.

Table 4.5. Partial atomic charges for each atom in the central repeating unit of molecule 1, taken as a Boltzmann-weighted average over all conformations on the appropriate composite energy surface. Refer to Figure 4.4 for atom labels.

Atom	SCRF Probe Radius, r_p (Å)				Gas Phase
	2.28	2.83	5.00	8.00	
C'	0.636	0.636	0.631	0.620	0.613
O'	-0.512	-0.512	-0.509	-0.515	-0.478
C^{α}	0.373	0.371	0.373	0.376	0.370
O^{S}	-0.478	-0.476	-0.469	-0.431	-0.471
H^{α}	0.032	0.031	0.029	0.022	0.024
C^{M}	-0.424	-0.425	-0.419	-0.403	-0.424
H^{M}	0.126	0.126	0.124	0.119	0.123

To examine the effect of chain length on our calculations, Table 4.6 shows the CHELPG charges of the central repeat unit for gas phase energy–minimized conformations of lactic acid oligomers having three, five, seven, and nine repeat units. The values listed in the first column, for the molecule with three repeat units, are essentially the data as listed in Table 4.5, with the difference being that Table 4.6 reports charges for the minimum energy structures, whereas the charges in Table 4.5 are Boltzmann weighted average values. At low molecular weights, the charges show significant variation with size of the oligomer, while at higher molecular weights the addition of repeat units has negligible effect. Therefore, we feel it can be assumed that charges taken from the central repeat unit in the nonamer are representative of the electrostatic potential within the bulk of a high-molecular weight PLA chain. These

results demonstrate the level of approximation involved in modeling the bond rotations of a polymer using a small oligomer; the electronic structure of the central repeat unit is definitely affected by chain length.

Table 4.6. Variation in partial atomic charges as a function of PLA oligomer length using the DFT/CHELPG method. Refer to Figure 4.4 for atom labels.

Atom	Number of Repeating Units			
	3	5	7	9
C'	0.624	0.550	0.583	0.561
O'	-0.478	-0.469	-0.480	-0.474
C^{α}	0.380	0.485	0.450	0.480
O^{S}	-0.499	-0.520	-0.506	-0.523
H^{α}	0.024	0.009	0.020	0.013
C^{M}	-0.423	-0.461	-0.452	-0.454
H^{M}	0.124	0.133	0.132	0.131

§ 4.4. Conclusion

While often neglected in DFT calculations for polymeric materials, we have shown that a treatment of the condensed phase reaction field surrounding a polymer molecule can have a dramatic effect on electronic structure calculations. These effects would likely be more significant for polymers with higher dielectric constants than PLA. However, most solvation models for use in *ab initio* calculations are not well suited for describing a polymeric solvent phase, and in particular we have shown the difficulties involved in selecting a suitable solvent probe radius parameter for use in Jaguar's SCRF

method. We have demonstrated that accounting for the reaction field improves agreement with recent viscometric data, when compared to conventional DFT calculations *in vacuo*, or to previous theoretical work. Nonetheless, we believe that improved models are needed when considering the reaction field created by an amorphous polymer phase or polymer melt.

In the following chapter, the gas phase data presented here will be used in parameterization of classical potential energy functions, which are more amenable to computations on larger systems. We chose to use the gas phase data in constructing the classical model for several reasons. Use of a Poisson-Boltzmann solver to model the dielectric continuum in the classical model would have introduced a large degree of nonlinearity during the parameter optimization, and given the concerns pointed out in this chapter regarding proper selection of a probe radius for polymers, we felt that such a complication would be unwarranted. Therefore, it was decided that the best course of action was to construct the classical model to reproduce the gas phase energies reported in this chapter.

In addition to providing the energetic data needed for construction of a classical model, the series of DFT simulations performed during the assessment of the dihedral barriers also provided an extensive and varied source of molecular geometries. This allows for examination of the conformational dependence of the valence properties and partial atomic charge assignments. Thus, our QM studies of lactic acid oligomers

(especially the three-repeat-unit segment) provide a much greater depth of understanding of the behavior of this important polymer system.

§ 4.5. Supplemental Files

Electronic files are available in the previously published version of this work [*203*]. Molecular geometries in Cartesian coordinates are included, in electronic form, for all structures reported in Figures 4.10 and 4.11, along with the energies and partial atomic charges calculated for each conformer. Molecular geometries, energies, and the number of associated negative frequencies are included for unconstrained energy minimized structures reported in Figure 4.5 and Table 4.6.

CHAPTER FIVE

FITTING THE TORSIONAL POTENTIALS IN CLASSICAL MODELS

§ 5.1. Introduction

In this chapter, we use the electronic structure calculation results from Chapter Four to improve the accuracy of classical models in simulating PLA. The ability of a classical force field to effectively model a real chemical system is dictated by two factors: the appropriateness of its mathematical form, and the accuracy of its various parameters. Both of these determine how the interatomic interactions of the system are modeled. The mathematical form is largely fixed for any given force field, as it defines the set of equations used to calculate the energy of the system and the forces on individual atoms. Within these equations, however, are a set of parameters which may be assigned numerical values. Thus, parameters are the means by which a force field's accuracy may be tuned to describe various molecular systems. For more information on force field models, and classical molecular simulation in general, refer to Section 2.2.2.

The CHARMM [*95*] and OPLS [*91*] force fields have been widely used for simulating organic molecules, by and large with good success. However, neither force field has been parameterized specifically for the dihedral angles present in α-polyesters, such as polylactide (PLA). Specifically, dihedral parameters for the O^S-C-C^α-O^S, C-C^α-O^S-C,

and C^{α}-O^{S}-C-C^{α} motifs, all of which are unique to α-polyesters, are not found in the parameter databases for such force fields. However, the models do include some general parameters that are suggested for use in cases where specific parameters are unknown. Because the approach of the authors was focused on creating force fields that are generally transferrable, or portable, to a wide range of molecules, they provide parameters for the general case of rotation about these bonds, represented by *X*-C-C^{α}-*Y*, *X*-C^{α}-O^{S}-*Y*, and *X*-O^{S}-C-*Y*, where *X* and *Y* may be any atom type. Such parameters are sometimes referred to as *wildcards*. In this chapter, we show that use of the wildcard parameters for α-polyesters results in poor performance in modeling PLA.

An additional concern with using a portable force field, such as OPLS or CHARMM, in polymer modeling applications is that such force fields were not developed with high molecular weight polymers in mind (barring, of course, polypeptides—which were a primary focus in CHARMM and OPLS. The availability of these force fields, along with AMBER [*100*], has been a major factor in the growing success that molecular modeling has enjoyed in the biomolecular field). For non-peptide molecules, most of the target data to which these force fields were fit was derived from a host of experiments involving small molecular compounds rather than large polymer molecules

In this chapter, we develop a classical force field model specifically suited for polylactides, based on the OPLS and CHARMM forms. The present force field follows the work of O'Brien [*142*], in which the PLAFF model was developed and validated extensively for crystalline PLA. We demonstrate that the new model, PLAFF2, is better

suited for modeling the amorphous dihedral angle distributions in PLA, and that it retains the accuracy of PLAFF in simulating the crystalline phase. We believe that these parameters will be of value to the biological science community, in that the resulting model retains consistency with the protein and amino acid parameters of OPLS and CHARMM. Further, with the growing interest in using renewable polymers for commodity packaging applications, this model will likely be of use to the materials science community in exploring new PLA-based materials. The PLAFF and PLAFF2 parameters represent the first non-commercial molecular models validated for PLA. As such, we hope this work will allow a larger number of researchers to study the material through simulation than was previously feasible.

§ 5.2. Methods

The fitting procedure used in this work is shown schematically in Figure 5.1. The procedure begins with assembling target data and providing an initial guess for the force field parameters. As a first step, the torsional parameters are adjusted using a least-squares fit to the DFT data presented in Chapter Four. Next, once the least-squares method has converged in a self-consistent manner, the model is tested against experimental crystal structure data for PLA. Dihedral parameters are then adjusted accordingly, until reasonable agreement is obtained with the experimental box vectors and dihedral angles of crystalline PLA. Following this step, the model is used to simulate the polymer in its melt state. The volume expansivity, β, is estimated from these simulations and compared with experimental dilatometric measurements. In some

cases, an adjustment of the relative energies between the g^-c and g^-t energy minima can affect a change in β, by establishing a different temperature dependence of the polymer's rotational isomeric states (RIS). However, if a more drastic change is required, the nonbonded parameters are adjusted for those atom types that are unique to α-polyesters, until the density and volume expansivity are near experimental values. After such adjustments, the entire fitting procedure must be repeated to ensure the agreement with DFT and crystal structure data is maintained. Finally, the model is used in quench simulations, where the polymer is rapidly cooled from the melt state into the glassy state. Using the WLF equation presented in Section 2.1.3, the resulting glass transition temperature, T_g, may be compared to experimental measurements. The energy barriers are then adjusted for rotation about each main chain dihedral angle until agreement is reached with experimental T_g values. Each of these steps will be discussed in greater detail in the following sections.

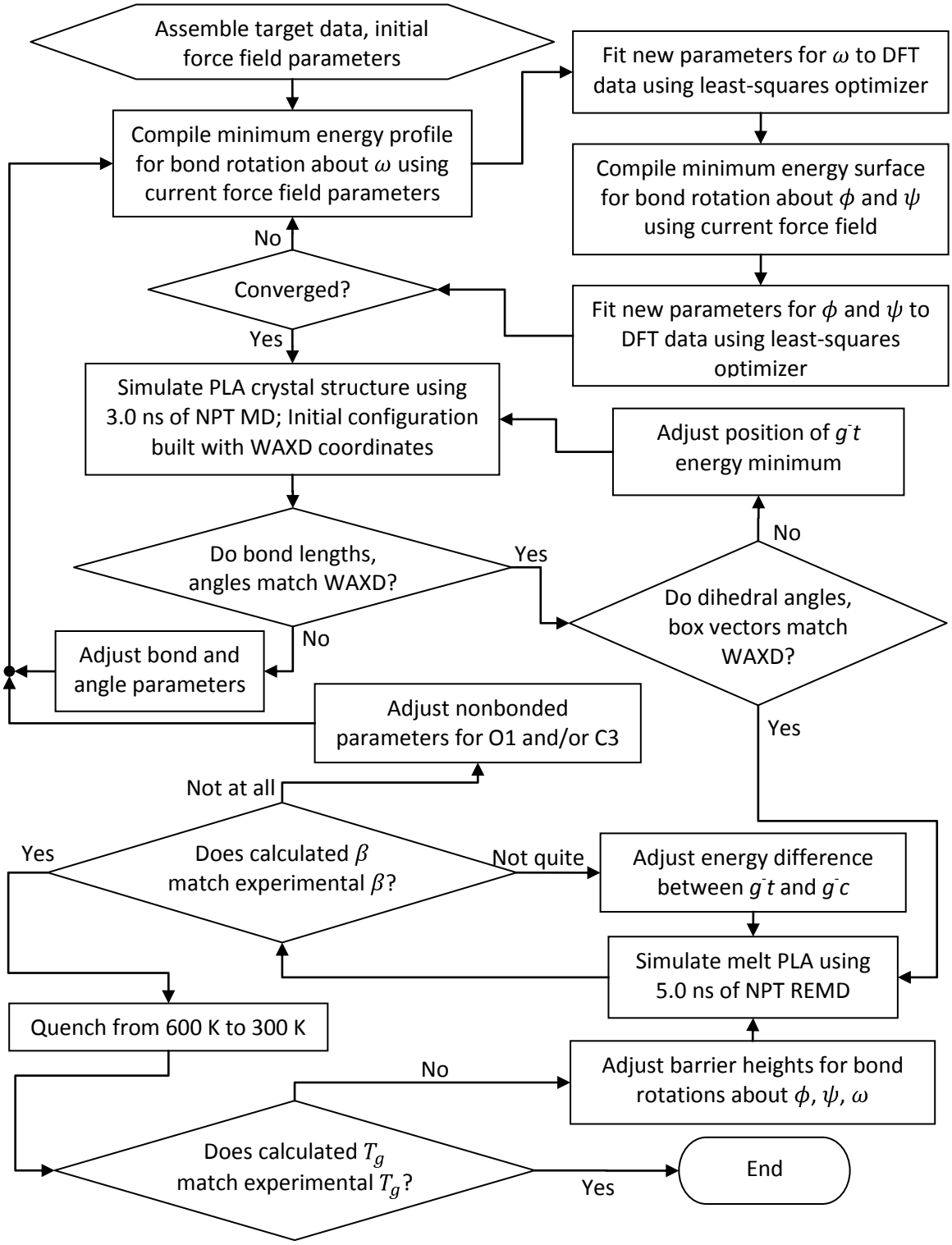

Figure 5.1. Flow diagram showing the procedure for fitting PLA force field parameters.

§ 5.2.1. Initial Force Field Parameters

We considered two force fields as a first approximation during parameter fitting: The Optimized Potential for Liquid Simulations (OPLS) and the force field from the Chemistry at Harvard Molecular Mechanics (CHARMM) package. The OPLS parameters for electrostatic, van der Waals (Lennard-Jones), bond stretching, angle bending, and dihedral interactions were taken from the OPLS-AA parameter files as distributed with GROMACS version 4.0.3. For the CHARMM force field, these parameters were taken from the CHARMM27 protein-lipid parameter files distributed with CHARMM version c32b2. Atoms in the PLA repeat unit were given numeric names as shown in Figure 5.2, and assigned atom types as in Table 5.1. Partial atomic charges were unaltered in each force field, with the exception of main-chain atoms and the carbonyl oxygen, which were adjusted slightly to achieve charge neutrality in the lactyl residue. The needed CHARMM27 parameters for PLA were ported into GROMACS. Upon using these parameters, GROMACS energy evaluations were within six significant digits of those from the CHARMM program, when compared term by term, and this was taken as proof that the CHARMM parameters were successfully transferred into GROMACS. All further molecular mechanics calculations were performed in GROMACS version 4.0.3 or version 3.3.3, depending on the type of simulation. The GROMACS software was chosen due to its higher computational efficiency, as compared to CHARMM.

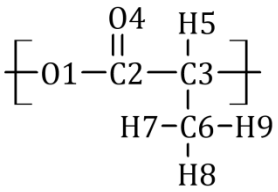

Figure 5.2. Molecular structure of the PLA repeat unit (lactyl residue). To facilitate discussion in the text, each atom in the repeat unit was given a unique name by assigning numeric suffix to its atomic symbol.

Table 5.1. Atom types assigned to the PLA repeat unit from the OPLS and CHARMM27 force fields. Refer to Figure 5.2 for the naming of atoms.

Atom Name	OPLS Number	OPLS Type	CHARMM27 Number	CHARMM27 Type
O1	467	OS	163	OSL
C2	465	C_2	120	CL
C3	491	CT	121	CTL1
O4	466	O_2	160	OBL
H5	282	HC	105	HAL1
C6	135	CT	123	CTL3
H7, H8, H9	140	HC	107	HAL3

In the fitting procedure, three dihedral interactions were adjusted to achieve better agreement with the bond rotational potential energy surfaces calculated from DFT. These correspond to the backbone dihedrals labeled as ϕ, ψ, and ω (see Figure 4.1). Because the GROMACS software package was used for evaluating the force field model, the initial torsional potentials were represented by a six-term Ryckaert-Bellemans cosine expansion,

$$\mathcal{V}_{RB}(\tau) = \sum_{n=0}^{5} C_n \left[\cos(\tau - 180°)\right]^n \tag{5.1}$$

where τ represents the dihedral angle according to the IUPAC convention, and the set of coefficients $\{C_n\}$ determine the shape of the potential. This potential is symmetric about $\tau = 0°$, and can be adapted to describe most of the dihedral functions used in molecular mechanics. For example, consider the OPLS form for dihedral parameters, which is a Fourier series truncated at four terms. It is possible to analytically transform such a series into a Ryckaert-Bellemans expansion, using trigonometric identities. For cases in which analytical conversion is not possible, the potential can be fit numerically. Most of the widely used all-atom force fields have, as required by their portable nature, symmetric dihedral functions defined separately over each of the four-atom dihedral angles in a rotatable bond. In other cases, such as united atom models or force fields that are not designed for portability to other arbitrary molecules, symmetric functions may not suffice.

When asymmetric dihedral interactions are desired, GROMACS provides two options. The first option is the periodic style function. The potential due to a single periodic function on a dihedral τ in GROMACS is given by

$$\mathcal{V}_{PER}(\tau) = k_\tau[1 + \cos(n\tau - \tau_0)] \tag{5.2}$$

where the force constant, k_τ, gives the amplitude of the periodic function, and n is the multiplicity. The phase shift, τ_0, is what allows the periodic function to represent

potentials that are asymmetric with respect to $\tau = 0°$. This is the style of the dihedral energy terms implemented in CHARMM, though in that force field the phase shift is usually set to $0°$ or $180°$ to render the functions symmetric. For complicated functions, multiple periodic terms can be assigned to a dihedral angle, similar to a truncated Fourier series. Note, however, that assigning multiple functions with the same multiplicity, n, is redundant because the sum of any two cosine functions having equal periods can be expressed as a single cosine.

Another way to represent asymmetric dihedral interactions is the tabulated dihedral function, available in GROMACS version 4.0 and later. In this representation, the dihedral interaction potential and its derivative are listed in a table, over a set of regularly spaced dihedral values. The potential and its derivative can then be calculated for intermediate dihedral values using cubic spline interpolation. Such dihedral functions allow considerably more freedom in shaping the energy profiles for each dihedral, at relatively low computational expense. For this reason, in fitting dihedral energy functions for PLA, we performed all manipulations to the dihedral energy terms using tabulated functions. However, some simulations required features available only in GROMACS major release 3, and for these simulations the tabulated functions were expressed as the sum of twelve periodic terms using a least-squares fit to the tabulated data.

§ 5.2.2. Target Data

In selecting the target data, which we wish our model to reproduce, we had several criteria. One criterion was that the model should be consistent with results from higher-level molecular simulation methods, such as the DFT results presented in Chapter Four. In addition, we aimed to be consistent with experimental results. Because PLA is often used in its semicrystalline form, we desired a model that could reproduce the properties of both the crystalline and amorphous states of the material. Conformational data for the crystalline form of PLA was used, as well as kinetic and thermodynamic data for the amorphous polymer.

§ 5.2.2.1. DFT Data

The DFT data from which the target potential energy values were taken was first presented in Figures 4.10 and 4.11a. The first plot, reproduced in Figure 5.3, shows the potential energy barriers encountered during rotation of ω, while the second, in Figure 5.4, shows the potential energy landscape as a function of ϕ and ψ. In each case, many geometry optimizations were performed for each value of the independent variable(s), using different initial geometries. Only the lowest energy structure found at each value of ω in Figure 5.3, or (ϕ, ψ) in Figure 5.4, was included in the plots. Thus, the target data represents two sets of minimum energy structures, each evaluated over a range of its own particular independent variable(s). In general, we refer to data sets such as those depicted in Figures 5.3 and 5.4 as *minimum energy surfaces*. All DFT calculations

were performed at the B3LYP/6-31G** level of theory. These figures were described in greater detail in Chapter Four.

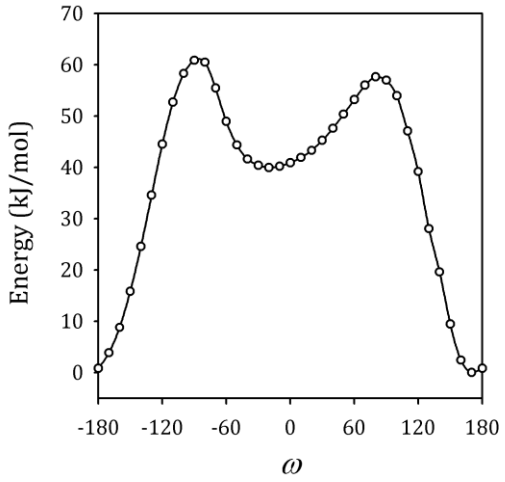

Figure 5.3. DFT potential energy profile for rotation about ω. Calculations performed on a PLA trimer *in vacuo*; see Chapter Four for a detailed description.

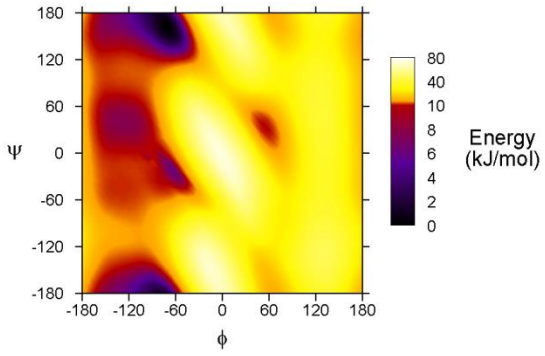

Figure 5.4. DFT potential energy surface, with ϕ and ψ as independent variables. Calculations performed on a PLA trimer *in vacuo*; see Chapter Four for a detailed description.

§ 5.2.2.2. Crystal Structure Data

Several studies on the PLA crystal structure appear in the literature, as discussed in Section 3.2. We have chosen to use the structural coordinates from Sasaki and Asakura [*45*] as our target data, because the authors' work represents the most detailed analysis of the structure to date. As discussed in Section 3.2, their use of the linked atom full-matrix least squares (LAFLS) method [*158*] and the Rietveld whole-fitting method [*159*], allowed for the positions of individual atoms in the unit cell to be determined with greater accuracy. The authors derived the α-form of the crystal structure from WAXD data, resulting in a frustrated 10_3 helix. The unit cell parameters from that study are: $a = 10.66$ Å, $b = 6.16$ Å, and $c = 28.88$ Å.

§ 5.2.2.3. Thermodynamic Data for Amorphous/Melt PLA

While fitting our model to the crystal structure of PLA ensures that the most stable conformation and packing of the molecules is reproduced, we also desired to reproduce the packing behavior of the amorphous phase. The specific volume of the polymer is a thermodynamic parameter that is measurable and easily simulated for the melt state of the polymer. We have selected the data from Sato et al. [*204*], where the specific volumes of polylactide samples were measured at various temperatures and pressure by metal bellows dilatometry. The values measured by heating PLA samples at 1 bar are plotted in Figure 5.5. While the data covers a wide range of temperatures, the data points we are interested in are those above the melting temperature, T_m. It can be seen in Figure 5.5 that a dramatic change in volume occurs upon heating above T_m,

which is attributed to the change in volume that occurs when the crystallites become amorphous.

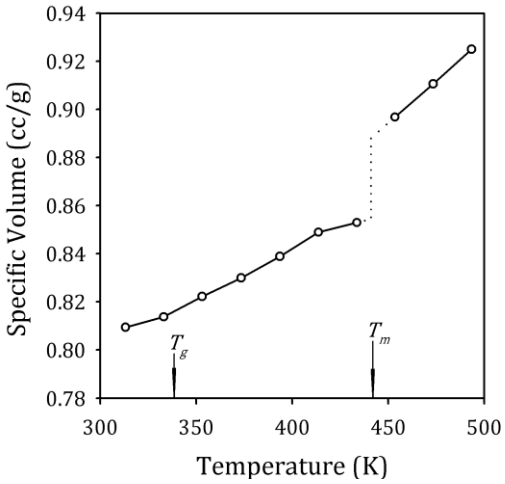

Figure 5.5. Target volume-temperature data at 1 bar, taken from Sato et al. [*204*]. Arrows indicate the authors' estimate of the glass transition temperature, T_g, and the melting temperature, T_m, taken from separate calorimetry data.

In practice, we use molecular simulation to study the melt phase of polymers at temperatures higher than those shown in Figure 5.5, utilizing the time-temperature superposition principle discussed in Sections 2.1.7 and illustrated in Figure 2.11. Thus, we look at the volume expansivity (Equation 5.5) to facilitate a comparison. From the data in Figure 5.5, an expansivity of $\beta = 7.8(10^{-4})\ K^{-1}$ is calculated for the melt state.

§ 5.2.2.4. Kinetic Data for Chain Motion: T_g

Thus far, our set of target data has covered energetic criteria in the form of DFT data, structural data in the form of WAXD-derived unit cell coordinates, and

thermodynamic data in the form of the dilatometric measurements on PLA melts. What is lacking is some type of dynamic property, which would quantify how well our model reproduces the time-dependent behavior of the material. Reproducing the correct dynamic behavior of PLA will improve the accuracy of our model in predicting transport properties, such as diffusivity and viscosity. In this work, we have chosen the glass transition temperature, T_g, as a dynamic parameter to add to our target data. As discussed in Section 2.1.3, the glass transition in polymers is caused by kinetic trapping of bond rotation within the polymer chains. It is generally accepted that barriers to bond rotation play a dominant role in determining material properties of polymers. Therefore, a model that accurately reproduces the glass transition temperature of PLA would likely do well in simulating other dynamic properties of the material.

The value of the PLA glass transition is dependent on the method used to measure it, and has been reported to vary widely with moisture content [*9*]. Common reported values of T_g for PLA are in the range of 327 to 345 K (see Table 5.2), which were obtained using differential scanning calorimetry (DSC) and dielectric relaxation spectroscopy (DRS). The value reported by Auras was measured after extensive drying of the PLA samples [*9*]. Since water is known to have a plasticizing effect on the material, it follows that this estimate is at the high end of the reported range of T_g values. Hence, we believe that a T_g in the vicinity of 70 °C is appropriate for dry PLA.

Table 5.2. Some reported values of the glass transition temperature of PLA.

Lead Author	Method	Rate	T_g (K)	Reference
Dorgan	DSC	10 °C/min	331.6	[*205*]
Sato	DSC	--	337	[*204*]
Auras	DSC	10 °C/min	344.6	[*9*]
Joziasse	DSC	10 °C/min	336	[*202*]
Kanchanasopa	DRS	$\tau = 100$ s	327	[*193*]

§ 5.2.3. Fitting Procedure using DFT Target Data

When examining the bond rotational modes in the force field model, we used an approach paralleling that which was used in examining the bond rotations with DFT. In obtaining the DFT target data in Figures 5.3 and 5.4, care was taken to obtain a set of energies as a function of a small number of independent variables, namely, ϕ, ψ, and ω. To accomplish this, all other degrees of freedom were allowed to relax such that they minimize the molecule's energy. Thus, in trying to reproduce the DFT data with our classical force field model, the objective of our fitting procedure for the torsional potentials can be stated as follows: Find the set of dihedral interaction parameters that will produce force field-derived minimum energy surfaces with the least deviation from the DFT minimum energy surfaces.

There is an important distinction between the above statement, and the methods used in various previous works. That is, we do not expect our force field model to give exact correspondence to the DFT energies in the molecule's entire configuration

space. Rather, we desire correspondence only for the independent variables selected (either ω, or ϕ and ψ) *after all other degrees of freedom have been relaxed* according to the characteristics of the particular model. This approach was taken as a means to separate contributions from the dihedral interactions and those from other force field terms, such as bond stretching or angle bending. It is clearly shown in the work of O'Brien that bond lengths and valence angles vary widely during rotation of the PLA bonds [*142*]. Thus, if the DFT-optimized geometries were input directly into the force field model, such deviations in the bond lengths and valence angles would result in substantial contributions from the bond and angle force field terms.

Calculating minimum energy surfaces with the force field model adds a high level of nonlinearity to the fitting procedure. Each time the dihedral parameters are adjusted, the molecular conformations making up the force field's minimum energy surface also change. Because the geometries of these constrained energy minima cannot be obtained analytically, numerical geometry optimization must be performed each time the force field parameters are changed. Thus, obtaining the optimal torsional potentials according to this prescription requires an iterative scheme, and we employ a Picard iteration step for this purpose. Before proceeding, we will make a brief digression to discuss how Picard iteration works.

§ 5.2.3.1. Picard Iteration

Picard iteration is a type of *fixed point iteration* which can be used for nonlinear functions. Simply put, a *fixed point* of an operator $\boldsymbol{F}$ is any point $\boldsymbol{x}$ that is unaffected by

the application of $\boldsymbol{F}$. That is, $\boldsymbol{x} = \boldsymbol{F}(\boldsymbol{x})$. In such a case, when searching for a fixed point of $\boldsymbol{F}$, one may apply an initial guess $\boldsymbol{x}_k$ and obtain successive approximations to the fixed point by $\boldsymbol{x}_{k+1} = \boldsymbol{F}(\boldsymbol{x}_k)$. Picard iteration also appears as a technique for solving ordinary differential equations (ODEs), where successive approximations are obtained by linearizing the ODE. When the fixed point is reached, the successive iterations become unaffected by linearization of the ODE. In this work, the method is applied to fitting force field parameters self-consistently.

Since the optimal set of torsional parameters should be unaffected by further optimization attempts, the solution to our problem is considered a fixed point. As in solving ODEs, a linearizing step is useful. In our method, this occurs after compiling the minimum energy surface. In each fitting iteration, the minimum energy conformers are found using the current guess for the torsional potentials. Subsequently, these conformations are used, along with the DFT target data, to obtain a new set of corrected torsional potentials with a gradient-based least squares approach. During the least squares optimization step, the minimum energy conformations are assumed to be unaffected by the manipulation of the torsional parameters. This is obviously an approximation, since the minimum energy molecular geometries depend on the shape of the potential energy function. However, not refining the molecular conformations during parameter optimization allows us to decouple the molecular mechanics steps from the parameter optimization steps.

The procedure begins with fitting self-consistently to the DFT data, starting with the dihedral having the largest potential energy barriers. Thus, the ω interaction is fit to DFT data first, followed by a simultaneous fit of the ϕ and ψ potentials. A weighted least-squares approach is used, with the DFT-calculated rotational energy profile as the target data. After each of these parameter optimization steps, the force field minimum energy surface is reevaluated using the most current dihedral parameters. This process is repeated until reasonable convergence is achieved with respect to the dihedral parameters and the minimum energy surfaces. While a more detailed discussion of the least-squares optimization program is relegated to Appendix C, there are a few items which warrant discussion here before we describe the remaining steps in Figure 5.1.

§ 5.2.3.2. Bounded Optimization

Perhaps the most important detail of the DFT-fitting procedure is that we employ a *bounded* minimization package (L-BFGS-B) for the parameter optimization steps to avoid drastically changing the minimum energy surface. Initial trials with the unbounded L-BFGS solver resulted in divergent behavior in the Picard iterations, due to large movements in the torsional parameter space between geometry optimizations. As previously discussed, the minimum energy surface of the force field model is itself dependent on the torsional potentials, and nonlinearly so. Thus, venturing too far in parameter space during the least squares step will move the system out of the local linear regime where our self-consistent iteration scheme is stable. It was found that suitable stability was achieved by limiting the change in energy at each tabulated point

to 10 kJ/mol for fitting the ω dihedral, and 5 kJ/mol for fitting ϕ and ψ. Because these limits gave satisfactory performance, no attempt was made at further tuning the fitting procedure with respect to them.

§ 5.2.3.3. Weighting of Data Points

Another important detail of our fitting procedure is the way in which data points are weighted in the least-squares parameter fit. Since molecular systems, at temperatures of practical interest, tend to reside primarily in the low-energy regions of phase space, it is far more important for a model to achieve accuracy in these regions than in the high-energy parts of phase space. This is recognized in the literature, and an approach commonly taken is to weight the data points according to Boltzmann statistics, calculated from the target potential energies at some relevant temperature. While this appropriately biases the fit towards low-energy regions, we encountered noticeable problems during our attempts to apply a purely Boltzmann weight in the fit.

When applied to parameter fitting, Boltzmann weighting factors allow large errors to occur in the fitted model for high-energy conformations, while allowing for higher accuracy in the low-energy conformations. This seems desirable, and is the motivation behind using a Boltzmann weighting scheme in the first place. Indeed, when a conformation has a relative energy of 50 kJ/mol compared to the ground state, it makes little difference if the model predicts an energy of 50 kJ/mol or 100 kJ/mol; the probability of accessing such a state is negligible at reasonable temperatures. On the other hand, an error of 4 or 5 kJ/mol in lower energy conformations can have

deleterious effects on simulation outcomes. The difficulty in applying smaller weighting factors to the high energy regions is that *least-squares fitting schemes do not distinguish between positive and negative deviations*. Using the example above, if the 50 kJ/mol conformation was predicted by the model to have an energy of 0 kJ/mol (the same error but opposite sign), the model would inappropriately open up regions of conformation space that should physically be very difficult to access. While it might be possible to incorporate some weighting scheme that is based on, say, the lowest potential energy between the target and model predictions, this would introduce larger nonlinearities to an already nonlinear problem. Our method was to define an energy cutoff, above which the weights are uniform. Specifically, we define the weight as

$$W_i = \max\left(e^{-E_{i,DFT}/k_BT}, 0.01\right) \tag{5.3}$$

Where $E_{i,DFT}$ is the target DFT energy of data point i, k_B is the Boltzmann constant, and we set T equal to 298 K.

§ 5.2.4. Refinement using Crystal Structure Data

The above procedure allows us to obtain force field parameters in agreement with DFT-calculated energies, after which the resulting parameters must be further refined to reproduce experimental measurements of material properties. While the DFT data provides a good idea of what the potential energy surface should look like, reproducing the DFT bond rotation profiles alone is not necessarily sufficient to accurately describe the physics of the molecular system. This is due to two main factors.

First, much of the force field model's behavior depends on other parameters not adjusted here, and second, the DFT data itself is not without error. Commonly accepted error estimates of B3LYP/6-31G** energy calculations are on the order of 2 kJ/mol, and authors are now finding that estimate to be optimistic [*58*]. As seen from the RIS calculations in Chapter Four, even changes of this order of magnitude in the bond rotational energy landscape can have a marked effect on the bulk properties of polymers. Thus, using the fit to DFT data as a starting point, the torsional parameters were further adjusted to assure reproduction of the experimental crystal conformation.

Returning to our discussion of Figure 5.1, it is shown that after sufficient convergence is obtained in fitting to DFT data, the crystal structure of PLA is examined with the force field parameters. In these simulations, the crystalline unit cell was built according to the WAXD resolved structure of Sasaki and Asakura [*45*]. The system is simulated for 3.0 ns in the NPT ensemble, whereby the box dimensions are allowed to adjust to their equilibrium values. Anisotropic pressure coupling was applied with the Berendsen algorithm, such that each box length was adjusted independently. The Nose-Hoover thermostat was used to simulate the system at 300 K. A cut-off of 1.0 nm was used for van der Waals interactions, while the electrostatics were treated with the Particle-Mesh Ewald (PME) method.

After simulating the PLA crystal structure with a given parameter set, the ability of the force field to reproduce the structural properties is examined. While our focus is on obtaining accurate dihedral angles, obtaining these in the crystal structure is difficult

without first having accurate bond lengths and valence angles. Therefore, before examining the dihedral values from the simulations, we must make any necessary corrections to the bond and angle force field parameters. This is done in much the same way as fitting the dihedral parameters to DFT data, and the Picard iterations used to obtain our final set of bond and angle parameters are outlined in detail in Appendix D.

Once the prerequisite of accurate valence geometries is achieved, the dihedral angles (ϕ, ψ, and ω) and box vectors are examined over the final 1.0 ns of dynamics of a crystal structure simulation, and their values are compared to those reported in the experimental literature. Should the simulations be inconsistent with the experimental data, the position of the g^-t energy minimum is adjusted with respect to ϕ and ψ, as is the position of the *trans* energy minimum for ω. The position of the energy minimum was altered using the script `adjustDih.py`, which is provided in the supplemental electronic files of this dissertation. Put briefly, the script examines the total energy to bond rotation using the current force field, then constructs a target potential energy surface by shifting the position of the g^-t minimum by some prescribed amount, subtracts the current dihedral energy contribution, and then refits the dihedral potentials for rotation about ϕ and ψ to match the target potential energy surface. This process is repeated until the experimental dihedral values are accurately reproduced.

§ 5.2.5. Refinement using Melt Phase Target Data

Once adequate agreement with the crystalline unit cell was obtained, simulations were carried out on amorphous PLA using isothermal-isobaric replica

exchange molecular dynamics (NPT-REMD) as implemented in GROMACS. The replica exchange method allows for fast equilibration of simulation cells, while providing valid thermodynamic averages over a wide range of temperatures and/or pressures.

In our implementation, each replica is comprised of three chains, each containing five hundred repeat units (refer to Figure 5.2), and two lactide molecules. The chain length was chosen to be greater than the experimental entanglement length, which is approximately 125 repeat units. Lactide molecules were included since there is always a small percentage of residual lactide monomer in a real polylactide sample, and these have a plasticizing effect on the material. With two lactide molecules per simulation cell, our simulated PLA system contains 0.26% residual lactide on a weight basis; the specific amount of lactide present in an industrially produced PLA resin is usually less than one percent [*18*], and 0.2 to 0.3 weight percent is common [*206*].

In the NPT-REMD simulations, each replica was assigned a pressure of 1 bar using the Berendsen scheme, while the temperature was set with the Nose-Hoover thermostat. As suggested in the literature [*207*,*208*], temperatures were assigned in a geometric progression, according to the formula

$$T_i = T_0 \left(\frac{T_{n-1}}{T_0} \right)^{i/n-1}, \quad i = 0, 1, \ldots, n-1 \tag{5.4}$$

where all temperatures are in Kelvin, n is the number of replicas, T_0 is the lowest temperature used, and T_{n-1} is the highest temperature used. The value of T_{n-1} was adjusted until an average exchange acceptance rate of approximately 20% was reached.

While more elaborate schemes exist to determine the optimal temperature spacing, most authors agree that an acceptance rate of 20% gives optimal sampling of most molecular systems [*208-210*].

Four separate NPT-REMD runs were performed with unique input configurations, which were initially generated using the Amorphous Cell module in Accelrys' Materials Studio version 4.0. The PCFF force field was used in the Amorphous Cell construction. Each of the first NPT-REMD runs were carried out for a total of 6.0 ns of dynamics, after which, the volumes remained relatively constant over time. This appeared sufficient time for the system to shed any influence of the PCFF force field, as indicated by relatively unchanging time averages of the system energy, box vectors, and dihedral angle distributions. Thus, results following 6.0 ns of equilibration time were taken to be indicative of our OPLS-based parameters alone. For later simulation runs, where only minor adjustments were made to the force field, the initial structures were taken from the final structures of these first (6.0 ns) simulations. This allowed the systems to equilibrate faster, since the bias from the PCFF force field had already been removed. Such systems usually equilibrated in one to two nanoseconds. Hence, these runs were performed over 3.0 ns of simulated time, with the last 1.0 ns used to accumulate property averages. As in the crystal structure simulations, a cutoff of 1.0 nm was used for van der Waals forces, and the PME method was used for electrostatic interactions.

In each replica exchange simulation, the average volume is calculated for the melt state as a function of temperature. From this, the volume expansivity can be estimated graphically from the relation

$$\beta = \frac{1}{v}\left(\frac{\partial v}{\partial T}\right)_P \tag{5.5}$$

where v is the specific volume of the system. Since each replica has the same pressure, a plot can be constructed of $\ln v$ versus T, and β can be estimated from its slope. This is compared to experimental measurements of the expansivity of PLA. If satisfactory agreement is not obtained, this indicates that the nonbonded parameters may need further adjustment.

When it was necessary to alter the nonbonded parameters, the atom types for the ester oxygen and α-carbon were chosen for adjustment. These atom types were selected because they are the most likely to deviate from the behavior of normal esters, and no such atom types exist in OPLS for α-polyesters. By examining the pairwise interactions for the atoms in our model (see Appendix E), we can adjust the nonbonded parameters in a way that gives the desired change in thermal expansion. Note that, when adjustment of these atoms' nonbonded parameters is necessary, the dihedral angles must again be readjusted to preserve agreement with the crystal structure.

§ 5.2.6. Refinement using Glass Transition Target Data

Thus far, in selecting target data for our model, we have considered energetic data from DFT calculations, geometric data from crystal structure WAXD studies, and

thermodynamic data in the form of the thermal expansion coefficient. What is missing is a parameter that describes the time-dependent or kinetic behavior of PLA. Perhaps the most important kinetic parameter that applies to polymers is the glass transition temperature, and we select this as our final target data for the model. The glass transition temperature, T_g, is commonly interpreted for polymers as the temperature below which bond rotations are kinetically trapped. That is, it is the temperature below which torsional energy barriers are crossed at rates much longer than the time scale on which the polymer is observed. As such, the value of T_g for PLA is influenced by the height of the energy barrier between the various rotational isomeric states.

Many studies have appeared in the literature examining the glass transition temperature via molecular dynamics [*211-213*], though relatively few papers address the temporal dependence of the observed glass transition temperature (e.g., references [*214*,*215*]). It is well known, experimentally, that the glass transition will be observed at higher temperatures when a polymer specimen is cooled at a faster rate [*19*]. As discussed in Section 2.1.3.2, this behavior is described very well, over the range of experimental time scales, by the WLF equation [*38*]. The quenching rates accessible to molecular dynamics simulations, however, can differ from experimental cooling rates by fourteen orders of magnitude or more. The validity of the WLF equation over such wide a temporal range has been explored only recently through molecular simulation. Soldera and Metatla applied the WLF equation to molecular dynamics simulations of the

glass transition [*215*], in which they simulated dilatometric experiments at various cooling rates for a wide range of glass-forming polymers.

While the authors' focus was on comparing the glass transition temperatures observed in their simulations to those observed experimentally, Soldera and Metatla [*215*] applied the WLF equation by fitting the parameters $C_1 = B/f_0$ and $C_2 = f_0/\alpha_f$ in Equation 2.4, to find the values which give the best agreement between their simulation data and the experimentally observed T_g for each polymer they studied. These parameters, in turn, were compared to those fit to experimental dilatometric measurements for the polymers to examine agreement of the models with experiment. Because many authors contend that the WLF parameters should be universal for all linear polymers [*40*,*41*], when the reference temperature and time variable are taken at the glass transition observed in the lab (at a cooling rate of 10 K/min), in this work we take a slightly different approach than that described by Soldera and Metatla. By using the universal parameters, there is no need to intermingle the experimental and simulation results (which is undesirable, because it assumes that the model and experiment behave in the same way—indeed, this is the very hypothesis we wish to test!). Furthermore, in the present method, the only remaining adjustable parameter is the reference temperature, T_0. If universality of the WLF equation is valid, T_0 is simply interpreted as the lab-scale glass transition temperature. Thus, by using the universal WLF constants, we may compare the glass transition temperature simulated our model to those observed experimentally at lab-scale quench rates. Additionally, the question

as to the validity of the universal parameters, which is the subject of ongoing debate, can be examined by assessing how well the WLF equation fits the simulation data.

In this work, the glass transition temperature of PLA was estimated from our force field model by quenching the amorphous conformations from the NPT-REMD simulations, using a replica at 604.5 K as the starting structure. Simulation conditions, including time steps, treatment of electrostatics and van der Waals forces, and temperature and pressure coupling time constants, were identical to those used in each of the NPT-REMD replicas, except that the setpoint of the Nose-Hoover thermostat was varied linearly with simulation time over the entire run. Each run lasted until a temperature of 300 K was reached. For each of the four NPT-REMD simulations, six separate quench runs were performed, with quench rates of 15 K/ns, 30 K/ns, 60 K/ns, 150 K/ns, 300 K/ns, and 600 K/ns. The glass transition temperature was estimated for each run by fitting a straight line to a plot of $\ln v$ versus T, using all data points below 400 K. A second straight line was drawn through the melt data taken from the NPT-REMD runs, for temperatures above 500 K; these were assumed to be well equilibrated, because the simulations were run long enough that the higher temperature replicas maintained stable volumes over time (see Section 5.2.5). The intersection of the two lines was taken as T_g. Such estimates were then averaged for each quench rate, and then a least-squares fit was performed using the WLF model (Equation 2.4) with T_0 as the adjustable parameter. The reference quench rate was taken to be 10 K/min (normal lab conditions for measuring T_g), and the universal WLF constants were used ($B/f_0 =$

40.16 and $f_0/\alpha_f = 51.6$) during the fit. In our method, we have opted to simulate high-molecular weight polymers directly, as to avoid correcting our glass transition temperature estimates with the Fox-Flory equation (see references [*35*,*36*]).

§ 5.3. Results and Discussion

In implementing the iterative procedure described in Figure 5.1, very many sets of force field parameters were examined in this study. Thus, discussion of each particular model would be impractical. Here, we discuss the important results from seven different force fields, ranging from the unaltered CHARMM and OPLS force fields, to our intermediate parameter sets derived from those force fields, and from the first generation PLAFF force field of O'Brien, to the latest version of our PLA force field, PLAFF2. Abbreviations for these different force fields are summarized in Table 5.3 for ease of reference. The intermediate parameter sets were selected at various points during the fitting process. These include the models obtained directly after a least-squares fit to the DFT potential energies, referred to as the OPLS' and CHARMM' models. These models demonstrate that fitting to the DFT energies alone is not sufficient to reproduce experimental data, and further adjustment was required as described in Figure 5.1. The OPLS'' model shows results in which the parameters have been further adjusted to match the bond lengths and valence angles reported in crystal structure studies of PLA, and in which the nonbonded parameters were adjusted by trial-and-error to better match the melt density and volumetric expansivity of PLA.

Table 5.3. Description of the various classical models discussed in the text.

Name	Description
OPLS	The OPLS force field as developed by Jorgensen and coworkers [*91,167*] (all-atom version, also known as OPLS-AA)
CHARMM	The CHARMM force field as developed by Brooks and coworkers [*95*]
OPLS'	OPLS, with backbone torsional potentials refit to DFT data
CHARMM'	CHARMM, with backbone torsional potentials refit to DFT data
OPLS''	OPLS, with CHARMM nonbonded parameters substituted for O1 and C3; selected bond stretching and angle bending terms refit to DFT (see Appendix D), and backbone torsional potentials refit to DFT data
PLAFF	The PLA force field developed by O'Brien [*142*] (all-atom version, also known as PLAFF-AA)
PLAFF2	The PLA force field developed in this work; the model is OPLS'', with backbone torsional parameters further adjusted to reproduce crystal structure data and to improve agreement with the experimental glass transition temperature of PLA

§ 5.3.1. Comparison of the Classical Models to DFT Data

Minimum energy surfaces for bond rotation about ϕ and ψ are shown in Figure 5.6, calculated using the various models described in Table 5.3. The figure also shows the DFT potential energy surface for comparison. While we do not expect the optimum force field to be in complete agreement with DFT data, we desire the overall shape and location of relative minima/maxima to coincide with the DFT results. Thus, as shown in Figure 5.6b, the first generation PLAFF force field raises some concern, due to the presence of a low-energy local minimum in the vicinity of $(\phi, \psi) = (30, -150)$ that does not appear in the DFT potential energy surface. Additionally, the $g^{-}c$ minimum is predicted by PLAFF to be much less probable than predicted by DFT.

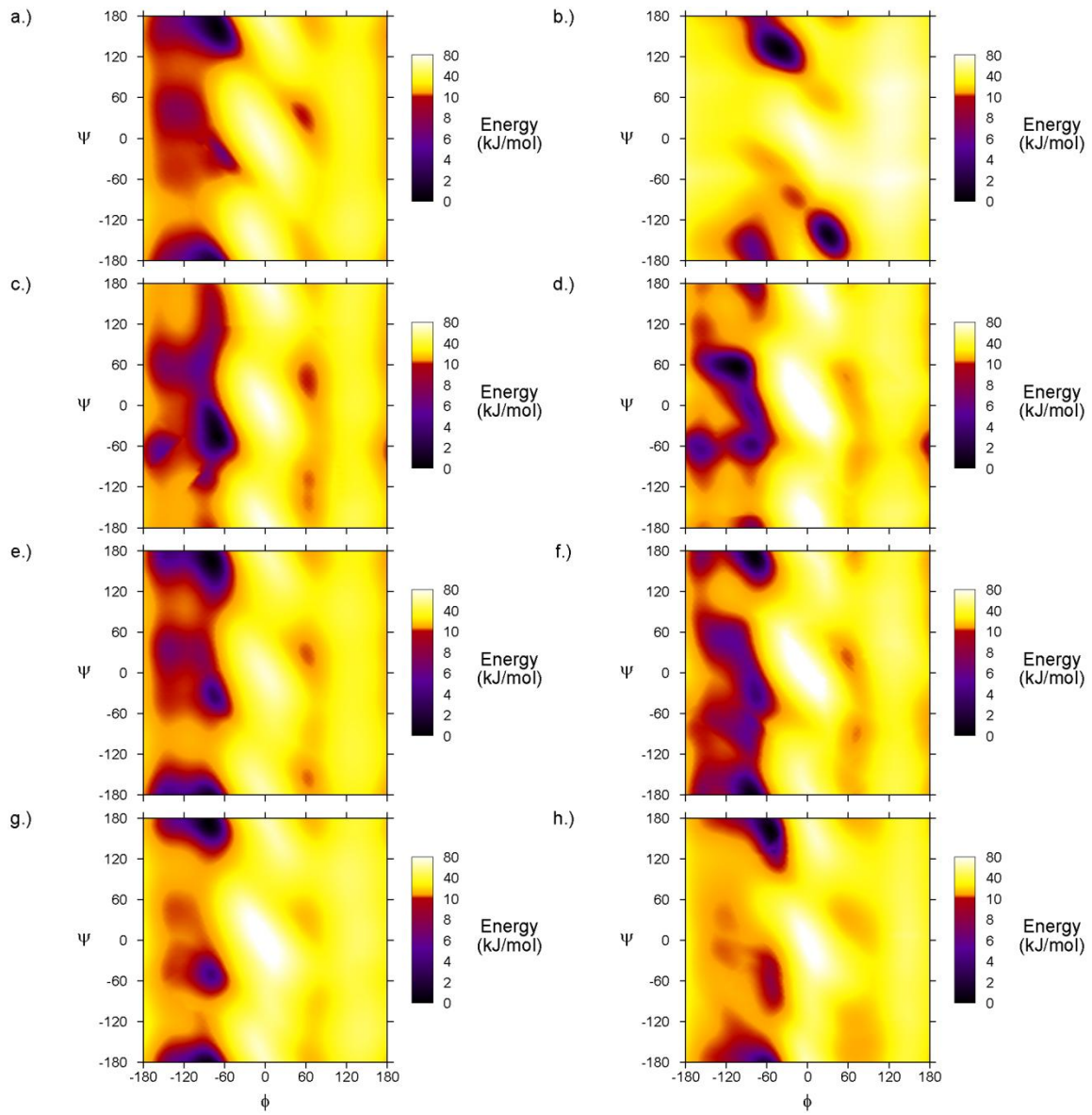

Figure 5.6. Bond rotational energy profiles for the ϕ_2 and ψ_2 dihedrals of molecule **1** (shown in Figure 4.4), calculated from a.) B3LYP/6-31G**; b.) PLAFF [*142*]; c.) OPLS [*91*]; d.) CHARMM [*95*]; e.) OPLS'; f.) CHARMM'; g.) OPLS''; h.) PLAFF2. Refer to Table 5.3 for a description of the models.

The presence of the extra minimum in Figure 5.6b is of primary concern for applications of PLAFF involving amorphous phases of PLA, in which case the entire dihedral space may be accessed by the simulated polymer chains according to the energetics of the force field model. Thus, due to the presence of the extra low-energy local minimum, the PLAFF model would open up regions of dihedral angle space that should be physically unlikely according to DFT calculations.

While the non-physical local minimum is a striking feature of Figure 5.6b, it is also obvious from the figure that O'Brien was very successful in fitting the potential energy surface in the vicinity of the global minimum (in the $g^{-}t$ position, to use the nomenclature introduced in Section 4.3.3). This is evidenced in the remarkable performance of PLAFF in simulating crystalline PLA [*142*], and therefore, we feel that the original PLAFF is still well-suited in modeling the crystalline phase of PLA.

As discussed in Section 2.1.4, PLA most commonly exists in semicrystalline form. While there are certainly relevant and interesting physical phenomena in which the crystalline phase of PLA plays a dominant role (for example, it is well known that PLA plastic devices undergo stress-induced crystallization at their surfaces; hence, surface interactions are well modeled by considering crystalline PLA alone [*216*]), the majority of bulk material properties of polymers are dictated by the behavior of the amorphous phase and the interstitial amorphous-crystalline regions. Phenomena such as crystallization from the melt phase, gas diffusion, melt viscosity, and the glass transition depend on an accurate treatment of the amorphous configuration distributions of a

polymer (see Chapter Two for a discussion of these properties). For this reason, we have seen fit to modify PLAFF such that it may be used equally well in simulations of crystalline and/or amorphous phase PLA. We refer to the resulting force field, described in Table 5.3, as PLAFF2.

In addition to the OPLS model, used by O'Brien as a starting point for development of PLAFF, in this work we considered CHARMM as a candidate for borrowing force field parameters to develop PLAFF2. Potential energy surfaces for these force fields are shown in Figures 5.6c and 5.6d, both of which lack adequate representation of the global $g^{-}t$ minimum predicted by DFT. This observation helps to explain the superior performance of PLAFF in the crystalline phase as compared with OPLS and CHARMM, and suggests that OPLS and CHARMM should not be used for crystalline or amorphous phase simulations without first correcting the backbone torsional potentials.

Figures 5.6e and 5.6f show the results of performing a least-squares fitting procedure to alter the torsional potentials, as described in Section 5.2.3, while leaving all other interaction parameters in the model unchanged. These figures demonstrate that there are limitations inherent in each model, preventing a perfect fit to the desired potential energy surface. For example, the CHARMM' potential energy surface in Figure 5.6f still shows remnants of the local minima, situated in the negative ψ region between the $g^{-}c$ and $g^{-}t$ energy minima of the CHARMM model in Figure 5.6d. Without use of more sophisticated potential energy functions, e.g., the CMAP dihedral-dihedral cross

terms available in recent versions of the CHARMM program [*217*], accurately reproducing the entire two-dimensional potential energy surface of Figure 5.6a is highly dependent on the other interactions within the model, such as the bond stretching and angle bending parameters.

We have mentioned, in Sections 3.1 and 4.3.3, that the stiffness of the valence angle centered about O1 can bring about energy barriers with respect to ϕ, between the *tt* and $g^{-}t$ regions, and between the *tc* and $g^{-}c$ regions of (ϕ,ψ) dihedral space. When examining the average valence angles during simulation of the crystal structure, shown in Table 5.5, we see that the CHARMM-based models impose a more acute angle between the C3-O1-C2 atoms than do any of the other models considered here. Because of the shorter reference angle (see Appendix D) assigned to this interaction when compared to OPLS, and the added Urey-Bradley type interaction included in CHARMM, the C3-O1-C2 linkage is less able to flex outward. This results in the bond rotational energy barrier shown along $\phi \approx -60^{\circ}$ in Figure 5.6d, and remnants of this result are still evident in Figure 5.6f. For this reason, we feel the OPLS model is generally more conducive to constructing the proper configuration distribution in (ϕ,ψ) dihedral space, as indicated by the good overall fit of Figure 5.6e in comparison with the DFT target data in Figure 5.6a.

§ 5.3.2. Comparison of the Classical Models to Crystal Structure Data

Results from crystal structure simulations using each of the models are shown in Tables 5.4, 5.5, and 5.6, and in Figure 5.7. Details of these simulations were described in

Section 5.2.4. In each case, the simulations results are compared to reference values from the experimentally resolved crystal structure(s). We wish to emphasize that the referenced values for bond lengths in Table 5.4 and the angles in Table 5.5 were not measured directly in the experimental work, but they are *assumed* as part of the analysis of the X-ray diffraction data. The actual values used by Sasaki and Asakura date back to a study performed in the 1950s on dimethyl oxalate [*150*], a small ester with similar, but not identical, chemical structure to PLA. As seen in Table 5.5, many of the angles in the original study were assumed to be exactly tetrahedral (at 109.5°) during the analysis. The DFT-derived values referenced in Tables 5.4 and 5.5, on the other hand, are calculated in the gas phase for a small molecular analog of PLA, molecule **1** in Figure 4.4. While it is not unreasonable to assume these values would be similar for a long polymer chain in the crystalline phase, it should be pointed out that the DFT data may include some effects due to the small size of molecule **1** compared to high molecular weight PLA.

We believe the most reliable experimental data available for the crystal structure is in fact the unit cell dimensions presented in Table 5.6. The crystalline density and box vectors can be measured directly, with very few assumptions involved in the experimental analysis. For this reason, we have given priority to matching the data in Table 5.6, when adjusting our models to match the crystal structure of PLA.

Table 5.4. Bond lengths (Å), averaged from crystal structure simulations of PLLA at 300 K; refer to Table 5.3 for a description of the models. Fluctuations are listed, as a single standard deviation, for PLAFF2; these are generally representative of the fluctuation in all simulations. Bond lengths from the most recent crystal structure analysis [*45*], and from DFT energy minimization of a PLLA trimer are shown, for comparison with the classical simulations. The recommended model, PLAFF2, is emphasized in bold.

Bond†	OPLS	CHARMM	OPLS'	CHARMM'	OPLS''	PLAFF [*142*]	**PLAFF2**	Sasaki [*45*]	DFT‡
O1-C2	1.35	1.34	1.35	1.33	1.36*	1.34	**1.37* ± 0.04**	1.31	1.35
C2-C3	1.54	1.56	1.54	1.56	1.53*	1.52	**1.54* ± 0.03**	1.53	1.53
C2-O4	1.23	1.22	1.23	1.22	1.21*	1.21	**1.21* ± 0.02**	1.21	1.21
C3-H5	1.09	1.12	1.09	1.12	1.10	1.08	**1.10 ± 0.03**	1.08	1.09
C3-C6	1.54	1.55	1.54	1.55	1.53*	1.53	**1.53* ± 0.03**	1.53	1.53
C3-O1	1.43	1.45	1.43	1.44	1.44	1.44	**1.44 ± 0.03**	1.44	1.43
C6-H7	1.09	1.11	1.09	1.11	1.09*	1.08	**1.09 ± 0.03**	1.08	1.09

* The stretching parameters for these bonds were adjusted from their default values (see Appendix D)

† Refer to Figure 5.2 for atom names in the lactyl residue

‡ Gas phase B3-LYP/6-31G** optimized bond lengths for molecule **1**, shown in Figure 4.4.

Table 5.5. Valence angles (degrees), from simulations of crystalline PLLA at 300 K; refer to Table 5.3 for a description of the models. Fluctuations are listed, as a single standard deviation, for PLAFF2; these are representative of the fluctuations in all simulations. Angle values from crystal structure analysis [*45*], and from DFT energy minimization of a PLLA trimer are shown at the far right, for comparison with the classical simulations. The recommended model, PLAFF2, is emphasized in bold.

Angle†	OPLS	CHARMM	OPLS'	CHARMM'	OPLS''	PLAFF [*142*]	**PLAFF2**	Sasaki [*45*]	DFT‡
C3-O1-C2	120.5	115.4	120.2	115.7	116.6*	121.1	**117.5* ± 2.8**	118.0	115.8
O1-C2-C3	112.2	109.7	112.4	109.8	110.0*	112.0	**110.3* ± 2.7**	110.0	109.7
O1-C2-O4	125.3	124.5	125.2	124.8	123.6	124.6	**123.6 ± 2.5**	125.0	124.7
C3-C2-O4	122.1	125.5	122.2	124.9	126.1*	121.2	**125.8* ± 2.7**	125.0	125.6
C2-C3-H5	107.9	107.0	107.6	104.6	108.8	108.7	**108.1 ± 4.4**	109.5	108.3
C2-C3-C6	110.5	111.0	110.8	112.4	111.1	111.4	**110.6 ± 3.3**	109.5	110.5
C2-C3-O1	112.7	112.5	112.3	111.7	110.3*	111.2	**113.1* ± 3.9**	109.5	109.5
H5-C3-C6	108.3	107.4	108.4	108.2	108.1	110.0	**108.0 ± 4.4**	109.5	111.6
H5-C3-O1	109.4	111.6	109.9	112.0	111.1	NL	**108.6 ± 4.6**	109.5	109.6
C6-C3-O1	107.5	107.0	107.5	107.6	107.1	107.6	**107.8 ± 3.7**	109.5	107.3
C3-C6-H7	111.2	110.6	111.2	111.0	111.4	110.0	**111.3 ± 4.5**	109.5	109.9
H7-C6-H8	111.2	110.7	111.2	110.9	111.2	107.8	**111.2 ± 4.4**	109.5	109.9

* The stretching parameters for these angles were adjusted from their default values (see Appendix D)

† Refer to Figure 5.2 for atom names in the lactyl residue

‡ Gas phase B3-LYP/6-31G** optimized valence angle for molecule **1**, shown in Figure 4.4.

Table 5.6. Box dimensions from published studies, and from crystal structure simulations of PLLA at 300 K; refer to Table 5.3 for a description of the models. Differences are calculated with respect to the most recent experimental study (Sasaki and Asakura [*45*]). The recommended model, PLAFF2, is emphasized in bold.

	a (Å)	diff (%)	b (Å)	diff (%)	c (Å)	diff (%)	density (g/cc)	diff (%)
Sasaki [*45*]	10.66	--	6.16	--	28.88	--	1.261	--
Alemán [*148*]	9.66	-9	5.80	-5	29.01	1	1.472	16.7
Hoogsteen [*144*]	10.60	-1	6.10	-1	28.80	0	1.285	1.8
de Santis [*143*]	10.70	0	6.45	5	27.80	-4	1.247	-1.2
OPLS	10.46	-1.9	6.05	-1.8	31.14	7.8	1.214	-3.8
CHARMM	10.72	0.6	5.97	-3.1	31.47	9.0	1.188	-5.8
OPLS'	10.51	-1.4	5.97	-3.1	31.36	8.6	1.216	-3.6
CHARMM'	8.78	-17.6	6.03	-2.1	34.67	20.0	1.303	3.3
OPLS''	10.54	-1.1	6.08	-1.3	30.85	6.8	1.210	-4.1
PLAFF2	**10.59**	**-0.7**	**6.25**	**1.5**	**29.74**	**3.0**	**1.215**	**-3.7**

Figure 5.7 shows the dihedral angle distributions during simulation of crystalline PLA. In each model, five different histograms are accumulated for each backbone dihedral, ω, ϕ, and ψ, shown in Figure 4.1. These separate histograms were measured for each of the five unique residues in the frustrated helical structure predicted by Sasaki and Asakura [*45*] (see Section 3.2). In each model, it is evident that these five residues take on different dihedral values, according to their orientation inside the unit cell. This supports the existence of a frustrated structure, and suggests a helix with perfect screw symmetry is not possible under the crystalline packing conditions of PLA.

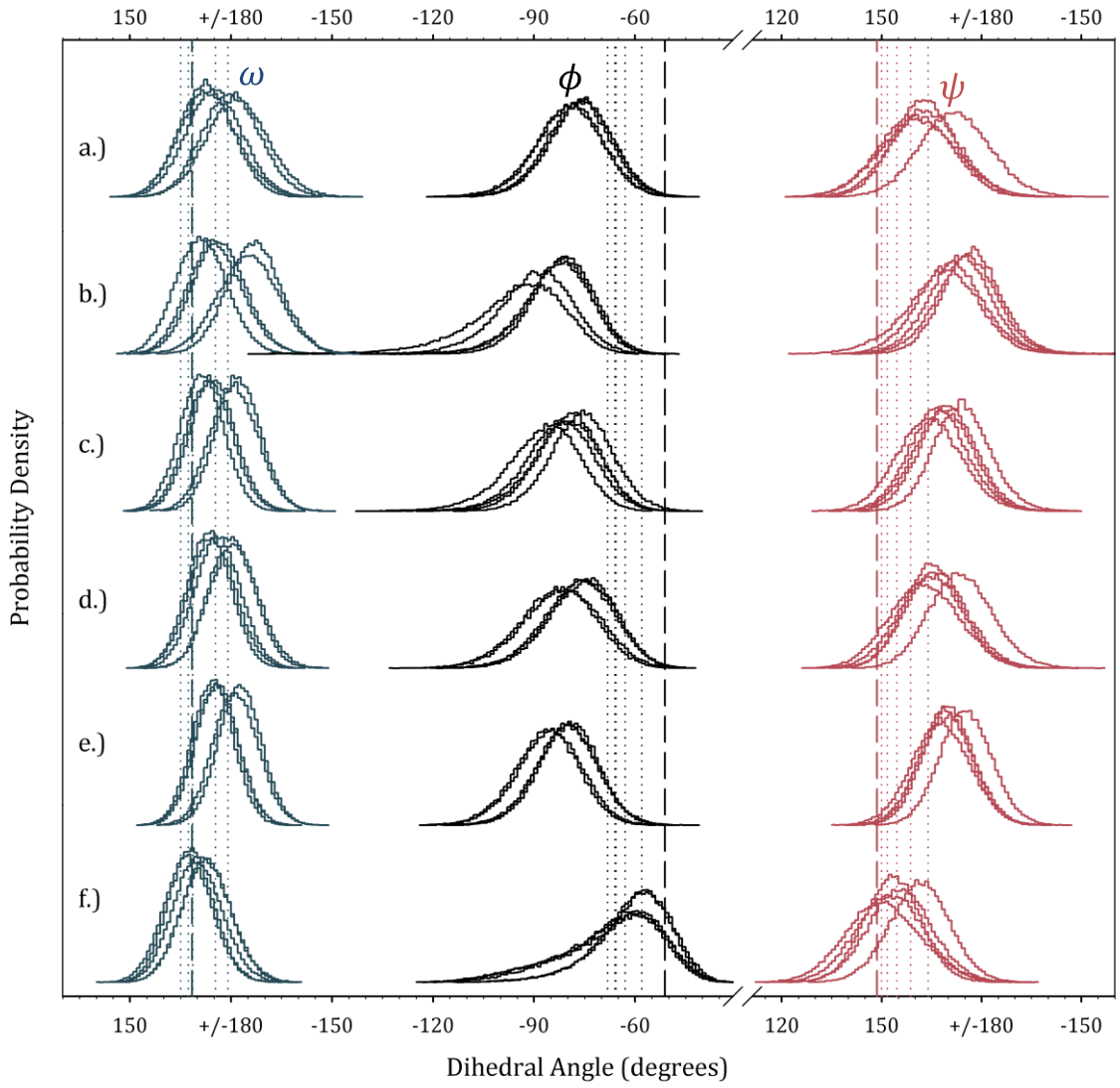

Figure 5.7. Dihedral angle distributions for crystalline PLLA at 300 K, simulated with a.) OPLS [*91*]; b.) CHARMM [*95*]; c.) OPLS'; d.) CHARMM'; e.) OPLS''; f.) PLAFF2. Refer to Table 5.3 for a description of the models. Vertical dotted lines: values from the WAXD crystal structure analysis of Sasaki and Asakura [*45*]; vertical dashed lines: averaged values from the PLAFF simulations performed by O'Brien [*142*].

From Figures 5.7a and 5.7b, it is apparent that the OPLS and CHARMM models do not predict the same dihedral angle distribution as suggested by the WAXD results [*45*]. A more surprising result was that refitting the torsional potentials to DFT data had very little effect on the dihedral angle distributions in the crystalline phase, as evident in Figures 5.7c and 5.7d. Ultimately, in our attempts to improve the agreement with the experimentally-resolved dihedral angles, we found that additional adjustments were necessary. First, we found it essential to improve agreement with the experimental unit cell box vectors. In addition to being the most directly-measured parameters in the WAXD analysis, the unit cell dimensions impose constraints on the set of dihedral angles that are probable, given that the crystal structure must be periodic with respect to those dimensions. Further, the set of bond lengths and angles played a vital role in achieving agreement with the crystal structure, as these impose the same sort of constraints on the dihedral angles when a periodic cell is used.

It can be seen in Tables 5.4 and 5.5 that the adjustments to bonded parameters used in the OPLS'' and PLAFF2 models, as outlined in Appendix D, generally resulted in bond lengths and valence angles that are closer to the values used in the WAXD analysis of Sasaki and Asakura [*45*]. There are two noted exceptions, which are the O1-C2 bond and the C2-C3-O1 angle, where adjustment of the stretching parameters only worsened the agreement with the standard accepted values. In both cases, we have chosen to continue using the altered stretching parameters, for several reasons. First, we emphasize again that the bond lengths and valence angles used by Sasaki and Asakura

[*45*], as well as those used in other crystal structure analyses [*143*,*144*,*148*], are values that are *assumed* rather than measured. In altering the valence parameters in Appendix D, we used molecular geometries optimized at the DFT level as the target data, rather than fitting directly to the values reported in the experimental study. While there are certain misgivings in the research community regarding the level of theory used in the geometry optimization [*58*], it is generally expected to give reasonable molecular geometries [*218*]. Second, as also noted earlier, the unit cell dimensions reported by Sasaki and Asakura [*45*] are directly determined from their measured diffraction patterns, without making a large number of assumptions. As shown in Table 5.6, the unit cell dimensions are reproduced quite well by PLAFF2, even with the lengthened O1-C2 bond and the broadened C2-C3-O1 angle. Given these results, we saw it unnecessary to reinstate the OPLS stretching parameters in our model, though this action may certainly be justified.

Once the bonded interactions were adjusted and more closely matched those used in the WAXD analysis of Sasaki and Asakura [*45*], adjustment of the dihedral angles in the crystalline structure was relatively simple; in practice, we found that all of the backbone dihedral angle distributions could be shifted towards the WAXD values, by altering the potential with respect to the ϕ dihedral angle alone. A simple shift in the position of the global minimum was required, as depicted in Figure 5.8.

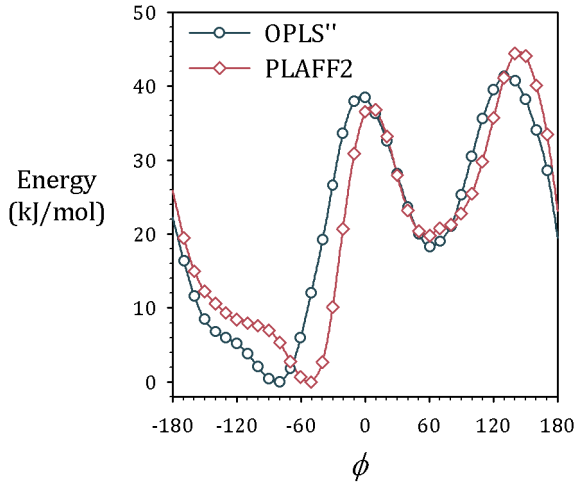

Figure 5.8. Adjustment of the torsional potential for the ϕ dihedral angle, which resulted in improvement of the dihedral angle distributions in crystalline simulations. The total energy of molecule **1** is plotted during rotation about ϕ.

In developing the PLAFF2 model, one of our stated goals was to obtain a force field that is suitable for modeling PLA in its amorphous state. Simultaneously, we wished to retain the model's accuracy in simulating crystalline PLA, which was a hallmark of O'Brien's original PLAFF [*142*]. We believe the results presented thus far demonstrate that PLAFF2 does indeed accurately predict the crystalline structure of PLA. In addition, Figure 5.6h shows the improvement in the topography of the PLAFF2 bond rotational energy landscape, when compared to PLAFF, and suggests that the new model is more likely to have the correct dihedral angle distribution in the melt and amorphous state. In what follows, we show that PLAFF2 is also better suited for simulating PLA in its no

crystalline form, up to high temperatures when compared to the other models discussed here.

§ 5.3.3. Comparison of the Classical Models to Melt Phase Dilatometric Data

When examining the models' performance in high temperature simulations, we found that the OPLS model under predicts the specific volume of PLA in the melt phase. This is shown in Figure 5.9, using results from the NPT-REMD simulations described in Section 5.2.5. CHARMM, on the other hand, tends to overestimate the specific volume. Results from the OPLS-based force fields generally reproduced the volume expansivity of PLA, as shown in Table 5.7, whereas the CHARMM-based models tended to have higher expansivities than indicated in the experimental results of Sato et al. [*204*]. It was found that substituting one or more of the nonbonded parameters from CHARMM helped to increase the specific volume in the melt, without increasing the expansivity above the desired range. Following this observation, in the PLAFF2 force field, CHARMM nonbonded parameters are used for the O1 and C3 atoms. While still slightly lower than the experimental measurements, the melt volumes predicted by PLAFF2 are noticeably closer to the experiment than either OPLS or CHARMM; this result supports our assertion that the model may be used equally well in simulating the melt and/or crystalline states of PLA.

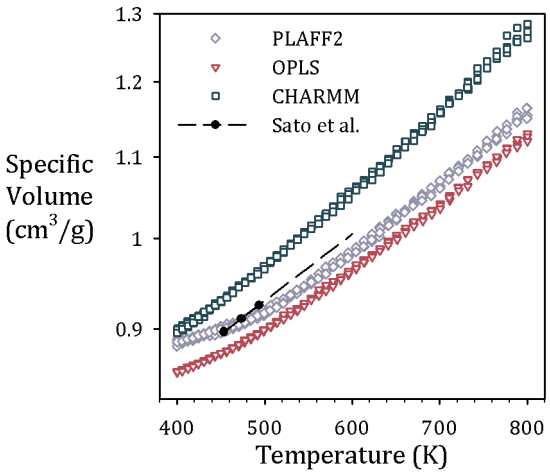

Figure 5.9. Melt phase densities of PLA, plotted from four separate NPT-REMD simulations for each of the CHARMM, OPLS, and PLAFF2 models. The melt phase experimental measurements of Sato et al. [*204*] are included for comparison, and extrapolated towards the higher simulation temperatures.

Table 5.7. Volume expansivities estimated for melt phase PLA. Values are calculated from the simulation results shown in Figure 5.9, by a linear regression (on a log scale plot) of the data points above 550 K. An estimate using the experimental data of Sato et al. is included for comparison. Listed errors are 95% confidence intervals for each slope.

	$\beta \times 10^4$ (K^{-1})
OPLS	7.74 ± 0.07
CHARMM	9.5 ± 0.1
PLAFF2	8.08 ± 0.08
Sato et al. [*204*]	7.8 ± 0.4

§ 5.3.4. Comparison of the Classical Models to Glass Transition Data

The last material property we used in constructing the PLAFF2 set of parameters was the PLA glass transition temperature, T_g. The method for determining T_g from simulation results was described in Section 5.2.6. Figure 5.10 gives an example of the specific volume intersection method, at two different quench rates, using the OPLS force field. The results depicted in the figure are generally representative of all intersection plots constructed during this work; the faster quenching rates consistently gave intersection points that are higher up on the melt volumetric curve. Figure 5.11 demonstrates the extrapolation involved in applying the intersection plots to estimate the glass transition for laboratory scale quench rates.

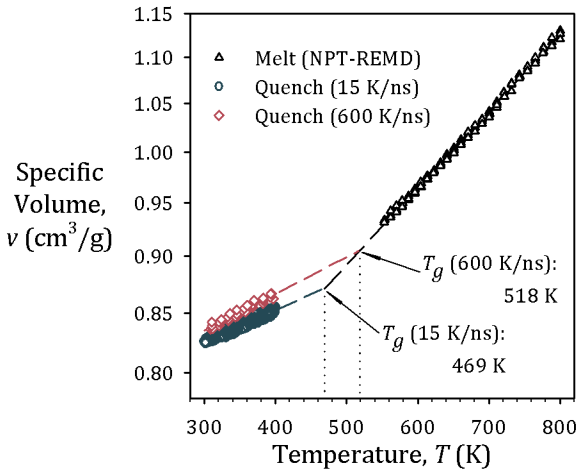

Figure 5.10. Specific volume–temperature (v-T) plot used to determine the glass transition in the OPLS model, using two different quench rates. Linear fits (on log scale) were used to determine the intersection points.

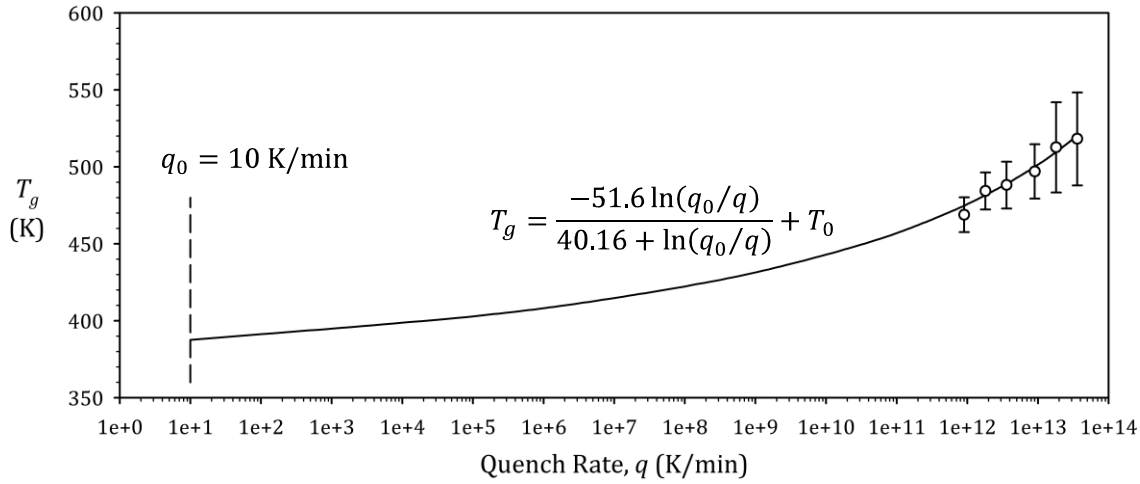

Figure 5.11. WLF plot for extrapolating glass transition temperatures, observed from simulation results, to realistic (laboratory scale) quench rates. Log scale used for quench rate. These particular results are from the OPLS model. Universal WLF constants are used, with a lab scale quench rate of $q_0 = 10\ \mathrm{K/min}$. Error bars are propagated from 95% confidence intervals on the slopes and intercepts of the melt and glassy v-T plots (see Figure 5.10). Here, the expected glass transition temperature is $T_0 = 388\ \mathrm{K}$ for the quench rate q_0.

One striking feature of Figure 5.11 is how closely the data points match the slope of the WLF curve. In fitting Equation 2.4 to the data points in the figure, we have only used one adjustable parameter, the lab scale glass transition temperature T_0. Manipulating this parameter has only the effect of shifting the curve in Figure 5.11 in the vertical direction. The slope of the curve at each point is governed solely by the WLF parameters B/f_0 and f_0/a_f, which we have set to the universal WLF parameters for linear polymers (see section 2.1.3.1). The glass transition temperatures observed in the

simulations follow quite closely the quench rate dependence predicted by the WLF equation. We found this feature to be typical for nearly all WLF plots constructed in this work, regardless of the force field model. In most cases, as in Figure 5.11, the data points lie much closer to the WLF curve than would be expected from our error propagation estimates.

We wish to note that, because the WLF equation is most often used to relate time scales that differ over relatively few orders of magnitude, we initially apprehensive towards applying the WLF equation to the extrapolation of glass transition temperatures. We know of only one study that employs the equation over time scales that differ by as many orders of magnitude as those presented here, and in that case the universal parameters were not used [*215*]. As shown in that article, the slope of the WLF curve changes significantly when examined over such a large span of timescales. To illustrate this point when presenting the data in Figure 5.11, we chose to plot the fully extrapolated curve, rather than simply showing the quality of fit over our simulation data range.

Due to the level of extrapolation involved in applying the WLF equation to our simulation data, it was uncertain whether the dependence of the observed glass transitions in our simulations could be approximated by the WLF equation and the universal constants. In fact, the results were much better than we expected, and this is perhaps evidence of the validity of the WLF theory, as well as the assumption that the universal constants apply for all linear polymers. It would certainly be interesting to

examine the dependence of T_g on the quench rate using molecular dynamics for a broad range of linear polymers, such as those considered in Soldera and Metatla's study [*215*], and compare the results to the slope of the universal WLF form. Such a study would determine whether the behavior in Figure 5.11 is indicative of all linear polymers, or if such results are unique to the models studied here for PLA. Further, it would contribute to the literature a much-needed discussion on the issue of relating the glass transition observed from molecular dynamics simulation to that observed during experiments with realistic time scales.

A survey of the glass transition temperatures for some of the models discussed in this chapter is presented in Table 5.8. Not all models were tested for the glass transition temperature; following our procedure laid out in Figure 5.1, we required that our models performed accurately in both the crystalline and melt states before attempting to examine the glass transition temperature. Thus, the OPLS' and CHARMM' models were not examined with glass transition simulations, as they did not meet the prerequisites in simulating the crystal structure; similarly, PLAFF was not used because it is believed to give inadequate dihedral angle distributions. We made three exceptions, for demonstration purposes. We chose to estimate T_g using OPLS, CHARMM, and OPLS'', despite each of their accuracies being deemed insufficient during simulation of the crystal structure, because these results give some idea of how the glass transition temperature was affected by changes made early on in the fitting procedure.

Table 5.8. Glass transition temperatures calculated from the various models explored in this work. A previous study, using PLAFF [*219*], and experimental results for dry PLA [*9*] are also included for reference.

	T_g (K)
OPLS	388 ± 14
CHARMM	367 ± 15
OPLS''	403 ± 12
PLAFF2	**386 ± 11**
PLAFF [*219*]	408†
Auras [*9*]	344

† Extrapolated to infinite molecular weight limit; not corrected for quench rate dependence

All estimates of T_g shown in Table 5.8 are higher than the experimentally observed glass transition temperature, with the CHARMM force field being the closest to the experimental value. It is also apparent in Table 5.8 that the modification of the torsional and other potentials from the OPLS to the OPLS'' model resulted in a worsening of the T_g estimate using OPLS''. It is obvious that, in adjusting the nonbonded and valence interactions in OPLS to obtain the OPLS'' model, we affected the barrier height of bond rotation about the ψ dihedral angle. In the PLAFF2 model, we were able to remove this artifact. Although we were not able to bring the glass transition temperature to within the range observed experimentally, we reduced T_g to below the OPLS value through judicious manipulation of the ψ torsional potential.

To manipulate the glass transition temperature of PLA predicted by our model, it was necessary to lower the energy barriers to rotation about the ψ dihedral angle.

Figure 5.12 shows two attempts at lowering the glass transition, proving that the energy barrier heights correlate well with the glass transition temperature. Unfortunately, additional lowering of the energy barriers became difficult without drastically changing the shape of the dihedral energy profile. As shown in Figure 5.13, the maxima and minima in the total energy do not necessarily coincide with the positions of the maxima and minima in the torsional potential. This fact makes adjustment of the individual barriers difficult, since in some cases the barriers exist largely due to interactions other than the torsional potential. Thus, the barrier height depicted in Figure 5.12 for PLAFF2 was essentially the lowest attainable with that model while retaining the general shape of the DFT potential energy surface.

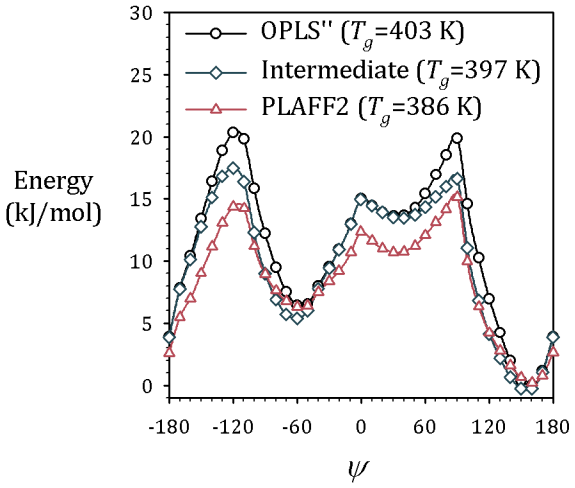

Figure 5.12. Lowering of the energy barrier to rotation about psi. Values plotted are the total energy of molecule **1** during rotation about ψ.

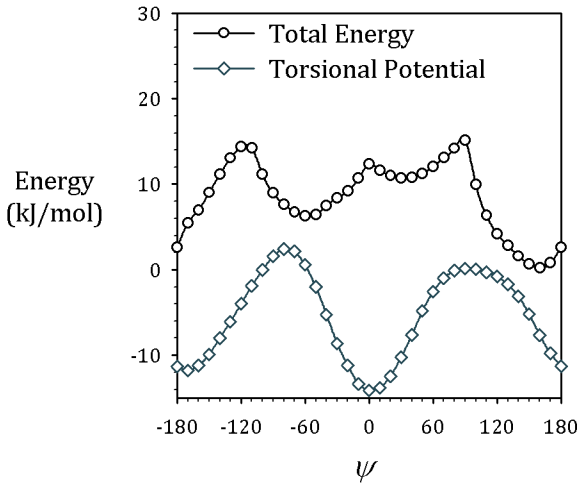

Figure 5.13. Total potential energy, and contribution from the ψ dihedral potential in PLAFF2.

While we did not simulate the glass transition using PLAFF, in compiling Table 5.8, we have included one such study that appeared in the literature [*219*]. This study, by Zhang et al., examined the glass transition temperature of PLA using relatively small chain lengths (10, 20, and 30 repeat units). The authors then extrapolated their results to higher molecular weights using the Fox-Flory equation (described in [*35*,*36*]). The value of T_g presented in Table 5.8 is the authors' estimate in the infinite molecular weight limit. Note that, although the glass transition temperature listed for PLAFF is the highest in Table 5.8, had the authors corrected their estimate to account for the effect of quench rate, the number would be drastically lower—most likely below the experimental value of T_g.

We have several comments regarding the findings published by Zhang et al. [*219*]. First, let us state that we are somewhat curious as to how the authors arrived at their figures. It seems that each of their quench simulations were performed only once for each system size, using a single starting configuration (although, to their credit, they did prepare several structures using energy minimization, choosing the lowest energy system for use in the quench simulation). In several of the authors' v-T plots, when determining the slope of their curves, the linear fits were made using only two data points; the two highest temperature data points were omitted from the melt curve fit. Given these details, it is somewhat remarkable that the authors' Fox-Flory plot gives a regression coefficient of "larger than 0.99." In doing some preliminary work regarding glass transition simulations, we were unable to recreate such a plot by following the authors' procedure, even after performing multiple quench simulations. We believe their method could benefit from additional (larger) system sizes and multiple simulations using different starting structures. In general, we found that it is preferable to perform such simulations on high-molecular weight systems rather than extrapolating using the Fox-Flory relation.

Despite our misgivings about the authors' procedure in estimating the glass transition temperature of PLA from O'Brien's PLAFF model, the results of Zhang et al. [*219*] are in fact quite plausible. As mentioned above, it is likely that the WLF-corrected value of T_g based on their results is below that of the experimental results, and well below any of the simulated results presented here. We recommend not using PLAFF in

amorphous simulations, due to its incorrect description of the relative energies of bond rotational isomers, as discussed with regards to Figure 5.6b. However, this does not preclude the model from having a T_g within the experimental region. Especially, when one considers the effect of the model's omission of 1-4 bonded neighbor interactions, PLAFF chains would likely have a higher degree of flexibility than those described by PLAFF2.

§ 5.4. Conclusion

In this chapter we have presented our work in developing an updated model for atomistic simulation of polylactide (PLA). The model, PLAFF2, was shown to perform well in the crystalline state of PLA, and additionally in the amorphous state. This model is an update to the previous version by O'Brien [*142*], in which we have improved the ability of the model to describe the proper dihedral angle distributions in the amorphous states of PLA. Based on the results of this chapter, we recommend the use of the PLAFF2 model under most circumstances.

While the inability of PLAFF2 to reproduce the experimental glass transition temperature is perhaps the largest shortcoming of this work, we emphasize that the model is likely to work very well in the majority of other conditions that are important in materials science applications. Rubbery configurations can likely be obtained with PLAFF2 in the vicinity of 450 K, provided a slow enough quench rate is used. Lower temperature rubbery configurations may even be possible with prolonged application of

the REMD protocol. This temperature range is well suited for crystallization studies, and we see no reason why PLAFF2 wouldn't perform well in such an application. We have proven that the melt simulations of PLA using PLAFF2 follow closely the experimentally observed volumetric expansion with respect to temperature. We would expect that PLAFF2 would also be suitable in measuring other melt properties of the material, such as shear or elongational viscosity. Due to the accuracy of PLAFF2 in simulating the pure crystalline form, the model should work equally as well as PLAFF in simulating various surface interactions with the polymer. A small number of applications do exist for PLA in which T_g happens to play an important role. For example, the high glass transition temperature predicted by PLAFF2 would probably preclude the use of the model in situations where plasticization effects are important, such as anomalous diffusion of vapors within the polymer. We feel that, keeping these limitations in mind, any judicious practitioner of molecular modeling should be able to successfully identify the many applications in which PLAFF2 is likely to excel.

§ 5.5. Supporting Information

In addition to the detailed information on parameter fitting presented in Appendices D, E, and C, we provide complete input files for the PLAFF2 force field in the supplemental electronic files of this dissertation, for use in the GROMACS molecular dynamics package. Fully equilibrated melt configurations are also provided.

CHAPTER SIX

CONCLUSION AND RECOMMENDATIONS

This chapter concludes the work of this dissertation. Here, we provide a brief summary of the entire work, revisiting the main achievements therein. In addition, we offer several recommendations for future work in this area, indicating the portions of the present work that could be improved. As a final note, we comment on the likely future of our research field in general, and how the work presented in this dissertation might fit into that framework.

§ 6.1. Summary

In this dissertation, we have presented a detailed atomistic study of polylactide (PLA), with special emphasis on the energy landscape due to rotation of its bonds. In Chapter Two of this dissertation, we provided ample background information to explain why the energetics of bond rotations are so important for polymers, such as PLA. This review of the literature was continued in Chapter Three, where we discussed many of the important research efforts to date which specifically examined the atomistic structure and energy landscape of PLA. In the remainder of the dissertation, we borrowed from this knowledge base when appropriate, while offering several improvements and updates to it.

Chapter Four focused on the calculation of the bond rotational energy landscape of PLA, using electron density functional theory (DFT). Though such methods have become standard protocol for force field development, we pointed out the major assumptions involved in applying gas phase electronic structure data to the development of models intended for use in condensed phase simulations. The results in Chapter Four demonstrate that accounting for the condensed phase environment surrounding a molecule can have a dramatic effect when estimating the relative energies of the molecule's conformational isomers. This was shown to be an important factor when applying the rotational isomeric states (RIS) concept to PLA. However, we found that the conventional dielectric continuum models, originally developed for simple liquids, are not well-suited for application to polymer systems. Further work in the area of condensed phase model development, specifically for use in modeling polymeric media, is strongly encouraged.

While we emphasize the need for force field development protocols using condensed phase quantum mechanical models, given the current state of the technology, we chose to develop the improved version of our classical force field for PLA, presented in Chapter Five, using the conventional method. That is, we began by fitting the force field's potential energy using the gas phase calculations on PLA presented in Chapter Four, and subsequently made adjustments to improve the model's performance in simulating the condensed (crystalline and amorphous) phases of PLA. In this way, we were able to obtain an updated version of O'Brien's PLA force field (PLAFF).

This new force field, which we call PLAFF2, was shown to retain the accuracy of PLAFF in simulating the crystalline phase of PLA, while obtaining a more realistic conformational distribution in amorphous polymer or melt. We were able to obtain good agreement with experimental data using PLAFF2, especially the crystalline structure and density, and the amorphous melt densities as a function of temperature.

Also in Chapter Five, we presented a method for interpreting the glass transition temperature observed in a molecular dynamics (MD) simulation, in direct comparison to the glass transition temperature expected under laboratory conditions. We required a sophisticated way of extrapolating the results of an MD simulation to real-world conditions, and developed such a method in the framework of the Williams-Landel-Ferry (WLF) theory. By adopting the universal WLF constants for linear polymers, we were able to compare our simulation results directly to experimental measurements of the glass transition temperature. The results obtained from our models suggest that the universal constants, and the WLF theory itself, work quite well in relating time scales that differ by up to twelve orders of magnitude. We believe this to be a major contribution to the ongoing debate as to the existence of such universal parameters.

§ 6.2. Recommendations

The PLAFF2 model presented in this work provides excellent performance in simulating amorphous and crystalline PLA; yet, during its development, we identified several areas that would benefit from further study and development. Specifically, the following parts in this work show room for improvement:

- ***Development of new methods for modeling the condensed phase environment of an amorphous polymer during electronic structure calculations:*** Currently, to our knowledge, no such method has been devised to deal with very long chain-like molecules. A good starting point for such model development is the work of Geisen et al. [*220*], which considered such a model for n-hexadecane using a multiscale continuum approach. Traditionally, the best benchmark data for such a model involves measuring the species solubilities and/or free energy of solvation, for a wide range of molecules submersed in the condensed phase media. From a practitioner's point of view, any successful implementation of a continuum model should involve a simple prescription for its key adjustable parameters, in terms of simple measurable properties of the polymer, akin to the conventional relation for the probe radius in Equation 4.2. Such measurable properties might include the dielectric constant, molecular weight, density, viscosity, and theta conditions for the polymer. Additionally, it might be worthwhile to explore a combined molecular mechanics–quantum mechanics (MM/QM) method in which the solvating media is modeled explicitly using point charges or a similar scheme.
- ***Reexamination of the characteristic ratio for PLA:*** One difficulty in assessing the amorphous phase properties of PLA was the lack of consensus in the literature regarding the unperturbed chain dimensions for the amorphous polymer. While the rigor of the authors' statistical analysis is quite convincing, the most recent

measurements by Dorgan et al. [*23*] are quite different from previously published studies, e.g., reference [*202*]. The characteristic ratio is a critical parameter in analyzing the configuration distribution in polymer chains, and for this reason, agreement within the experimental community as to its proper value would be extremely helpful in validating molecular models of PLA

- ***Development of standard protocols for estimating the glass transition temperature from molecular dynamics simulations:*** While we believe the method presented here, based on the WLF equation, to be thoroughly acceptable in relating simulation data to laboratory measurements, it is evident from Figure 5.11 that the method involves a great deal of extrapolation. Generally, our results show that the glass transition temperature varies with quench rate with the same slope as predicted by WLF theory. This observation suggests that the WLF theory may be applied, using the universal constants for linear chains, in simulating a wide range of polymers. We suggest a study in which this hypothesis is tested, comparing the observed cooling rate dependence of T_g to the WLF/universal constants model.
- ***Further adjustment of the PLAFF2 model to more accurately describe vitrification:*** Because PLAFF2 over predicts the glass transition temperature, it may not be suitable for use in some applications. Further improvements may be possible by adjusting additional parameters, other than the dihedral energies. For example, the nonbonded parameters are likely to have a direct effect on the

glass-forming ability of the polymer, especially the parameters for the side chain (methyl) groups in PLA. While we manipulated the nonbonded parameters to some extent, such parameters were not the focus of this study. Finding a set of parameters that produces an accurate T_g, while maintaining the accuracy in the other parameters considered in this work, is likely to be a very time consuming task. Often, the nonbonded parameters are determined using phase equilibria data for the molecule of interest, yet this approach is often not feasible for polymers.

§ 6.3. Suggested Applications of PLAFF2

Force field development is a long and arduous task, and this is especially true for polymer systems. Although the focus of this work was on the development of the PLAFF2 model rather than its application, the many long periods of waiting for computer simulations to complete during parameter adjustment has offered us the opportunity to research, in some detail, many of the methods that would be used in applying the PLAFF2 model to engineering problems. Any researcher interested in applying our model would be well advised to read through the second chapter of this dissertation, especially the polymer science material in Section 2.1. In addition, we summarize some of our reading in Appendices B and A. Here, we list several areas where PLAFF2 might be applied, with our comments and thoughts about how each might best be implemented.

- ***Crystallization:*** A thorough reading of the studies of Kuppa and Rutledge [*47*] would be a valuable starting point for examining the interlamellar structure of PLA. Though the authors studied isotactic polypropylene, the crystalline structure adopted by that molecule is helical, similar to the PLA crystal structure. Therefore, the Monte Carlo method developed by the authors may be transferred quite naturally to the study of PLA.
- ***Diffusion:*** For diffusion phenomena at higher temperatures, i.e., in rubbery PLA, the linear response methods outlined in Appendix B should work well. For accurate application of these methods, a relation is needed for the chemical potential of the diffusing species as a function of concentration. This relation can be obtained using the methods outlined in Appendix A. For diffusion of molecules through glassy PLA, which is relevant for refrigerated and on-the-shelf food packaging applications, the transition state theory is perhaps the best feasible method for determining diffusion coefficients. Greenfield has published several extensive papers on this subject [*51*,*221*]. As noted in Section 5.4, one should be careful to observe whether anomalous diffusion effects are to occur, as the higher glass transition temperature of the PLAFF2 model may be problematic with regards to the plasticization effect.
- ***Viscosity:*** Linear response methods are outlined in Appendix B, for estimating the viscosity from molecular dynamics simulations. It should be noted that these methods are only applicable in the zero-shear limit; they are not suited for

examining behaviors such as shear-thinning, which is important in polymer processing. The transient time correlation function (TTCF) methods, on the other hand, are reportedly suitable for capturing nonlinear effects. The review paper of Todd and Daivis [*57*] gives a very good introduction to this topic. Because small relaxation times are preferable when applying TTCF analysis, we suggest starting with high temperature simulations and gradually reducing the temperature until the TTCF method no longer converges.

§ 6.4. The Future of Molecular Modeling

Though this section will surely become dated shortly after being written, we take this opportunity to reflect candidly on what an exciting time this is to be involved in molecular modeling. Developments of newer, cleverer algorithms are constantly extending our capabilities, while new designs for computing hardware continue to make yesterday's state-of-the-art obsolete. It is both saddening and thrilling to think, that the type of server known as our University's flagship supercomputer on the first day I entered the campus, today finds its best use as a beverage cooler [*222*].

Recently, perhaps the most promising technologies to emerge in the field of molecular modeling have been application specific integrated chip (ASIC) designs, such as the MDGRAPE project [*223*,*224*] and ANTON [*225*,*226*]. These technologies embed simulation algorithms directly into a computer's processing chip, in parallel, rather than relying on software to coordinate processing tasks in sequence. If the authors' projections are correct, their prototype of the ANTON molecular dynamics machine will

perform *three orders of magnitude* faster than today's best conventional (non-ASIC) supercomputers, such as IBM's Blue Gene/L. What is quite amazing about ANTON is that it will achieve its thousand fold performance increase using only 512 processors, compared to the over 130,000 Blue Gene/L processors in use at Lawrence Livermore labs. This increase in performance is phenomenal compared to the conventional Moore's Law scaling, which predicts speedup due to improvements in chip manufacturing processes (specifically, transistor number densities) alone.

Note that, up until the end of 2008, the Blue Gene/L system at Lawrence Livermore was purported as the fastest supercomputer in the world, though in 2006 researchers at Japan's RIKEN institute had already surpassed its molecular dynamics performance by a factor of two, with their MDGRAPE-3 architecture. Further, this was done using less than 5,000 of their ASIC processors (four percent of the number of processors in Blue Gene/L), which also lends credence to the seemingly wild assertions of the ANTON developers in forecasting such high performance with their small network of only 512 ASICs. Unfortunately the RIKEN MDGRAPE-3 system does not even show up on the TOP500 list, which is the computing community's standard indicator of supercomputer performance. The reason for its exclusion is that the application-specific design of MDGRAPE-3 precludes it from running LINPACK, the benchmark application required for TOP500. This is just an indicator of the drastic paradigm change that ASIC technology is bringing about; we must totally rethink how supercomputer performance is defined.

These developments discussed in this section indicate that, in the near future, it will likely be possible to simulate bulk polymers over time scales long enough to capture the full complexity of polymer behavior. This would allow modelers to directly simulate realistic polymer systems without relying on semi-empirical theories to extrapolate to lab conditions. This invites the prospect of truly high-throughput screening studies on a large number of chemical variations for biodegradable polymers, as described in Chapter One. These advances, in our estimation, make the development and parameterization of molecular models—such as the PLAFF2 model presented in this work—extremely valuable, so that the research community may take advantage of the improved hardware technology as soon as it becomes available.

APPENDICES

APPENDIX A

METHODS FOR CALCULATING THE CHEMICAL POTENTIAL

The chemical potential is commonly used in calculating solubilities, phase equilibria, and reaction equilibria. Present techniques for obtaining the chemical potential via molecular simulation incorporate one or more of the following: free energy perturbation methods, distribution-histogram methods, thermodynamic integration, and use of expanded ensembles. These methods are described in detail and quantitatively compared by Kofke and Cummings [*227*]. In general, the chemical potential is calculated as the difference in free energy between a system of N particles and a system of $(N-1)$ particles. In mathematical expressions to follow, these will be referred to as systems 1 and 0, respectively.

Equation A.1 gives Widom's test particle insertion method [*228*], which is widely used for obtaining the chemical potential but is not well suited for dense systems of large molecules.

$$e^{-\mu^{res}} = \langle e^{-(U_1 - U_0)} \rangle_0 \tag{A.1}$$

In this notation, μ^{res} is the dimensionless residual chemical potential, i.e., the residual chemical potential multiplied by $\beta = 1/kT$. The quantities U_1 and U_0 are the dimensionless potential energy functions for system 1 and system 0, respectively, and the angular brackets indicate a canonical ensemble average in system 0. Both U_1 and U_0

are in general functions of all $3N$ coordinates of configuration space, although in this case U_0 will be independent of the 3 coordinates of the N^{th} particle since it does not interact in system 0.

An inverse to Widom's formula was proposed by Shing and Gubbins [*229*], commonly referred to as a test particle removal or deletion scheme,

$$e^{+\mu^{res}} = \langle e^{+(U_1 - U_0)} \rangle_1 \tag{A.2}$$

The derivation of this expression is as rigorously true as Widom's formulation, but the deletion scheme generally gives poor results when implemented in a simulation. The insertion and deletion methods differ in respect to the ensemble on which the sampling is performed; with insertion, the sampling is performed on the $(N-1)$-particle system, whereas the N-particle system is sampled in the deletion scheme. The difficulty with the deletion scheme lies in the fact that the term accumulated in the ensemble average of Equation A.2 is largest for configurations that have the lowest probability of being sampled. Specifically, for configurations such that U_1 is large relative to U_0, the quantity of interest grows exponentially with U_1, while the probability of sampling these configurations decreases exponentially. Therefore, to accurately evaluate the ensemble average with a Monte Carlo or molecular dynamics method it is important to adequately sample regions of configuration space that have extraordinarily low Boltzmann factors. This of course demands an extraordinarily long simulation time using conventional methods.

The deficiency in Equation A.2 demonstrates the importance of examining the behavior of the function to be averaged at the tail of the probability distribution. A similar examination of Equation A.1 will show that the Widom method is not as prone to this kind of systematic error. However, the Widom method fails at high densities because for these systems there is only a small region of configuration space in which both U_1 and $U_0$are sufficiently small to contribute to the ensemble average. Thus, for dense systems Widom's method also requires long simulation times to properly sample these few configurations important to evaluating the ensemble average. In other words, the problem is now to adequately sample a small region within the bulk of the probability distribution instead of trying to sample the vast amount of configurations at the tail of the distribution.

The acceptance ratio method devised by Bennett [*230*] provides a means of combining results from simulations performed on both systems 1 and 0, and it achieves greater accuracy under dense conditions. The acceptance ratio formula can be written

$$e^{-\mu^{res}} = \frac{\langle e^{-(U_1 - U_W)} \rangle_0}{\langle e^{-(U_W - U_0)} \rangle_1} \tag{A.3}$$

Here, U_W is an arbitrary potential, which we will refer to as the weighting potential function. Although this may be any function of the particle coordinates, Bennett suggested the following form of U_W which minimizes the expected variance in the right-hand side of Equation A.3:

$$U_W = U_0 - \ln\left[\frac{Z_1 n_0}{Z_0 n_1} + e^{-(U_1 - U_0)}\right] \tag{A.4}$$

In this notation Z_1 and Z_0 are configuration integrals for systems 1 and 0, while n_1 and n_0 are the number of configurations sampled from each system. Bennett found that the optimal value for the ratio of n_1 and n_0 is approximately unity in most cases. The ratio of configuration integrals is of course not known during the simulation (the ratio is in fact equal to the left-hand side of Equation A.3), and evaluating the ensemble averages will require iterative methods as discussed by Bennett. Note that Equations A.1 and A.2 can be seen as special cases of Bennett's acceptance ratio formula given the proper choice of the potential function U_W. Boulougouris et al. suggested an alternative to the deletion scheme [*231*], which can also be derived from the acceptance ratio formula:

$$e^{-\mu^{res}} = \frac{\langle e^{-\Phi} \rangle_0}{\langle e^{-\Phi} e^{+(U_1 - U_0)} \rangle_1} \tag{A.5}$$

Here, Φ is a hard-core potential for the test particle of arbitrary size, with the optimal size being determined in the equilibration portion of a simulation. Hence, the numerator on the right-hand side of Equation A.5 is simply the fraction of volume that would be accessible to a hard-core test particle inserted in the $(N-1)$-system. The denominator is similar to the right-hand side of Equation A.2. However, it lacks the undesirable dependence on poorly sampled configurations to evaluate its average, since the first exponential term in the brackets will cause the value at the tail of the distribution to be zero (for configurations in which the test particle overlaps another) or approximately

zero (for configurations where both U_1 and U_0 are very large) instead of increasing unboundedly as in Equation A.2.

Another, less widely used formula was suggested by Torrie and Valleau [*232*], in which the free energy difference is obtained from a single simulation. In this case, the simulation is performed on the system in which the arbitrary potential function acts, and the chemical potential is given by

$$e^{-\mu^{res}} = \frac{\langle e^{-(U_1 - U_W)} \rangle_W}{\langle e^{+(U_W - U_0)} \rangle_W} \tag{A.6}$$

Again, Equations A.1 and A.2 can be obtained as special cases. Effective use of this method requires careful construction of the potential function. At least one of the ensemble averages in Equation A.6 will likely be susceptible to the same systematic error as the particle deletion formula given by Equation A.2. The weighting potential function U_W is usually chosen to exhibit behavior between U_0 and U_1, in which case the numerator of Equation A.6 will be analogous to Widom insertion, while the denominator will be analogous to the deletion method. Therefore, the behavior at the tails of the probability distributions should be considered before using a given potential function. Han [*233*] suggested the following form of U_W, which was derived to minimize the variance in the left-hand side of Equation A.6:

$$U_W = U_0 - \frac{1}{2} \ln \left[1 - \left(\frac{Z_0}{Z_1} e^{-(U_1 - U_0)} \right)^2 \right] \tag{A.7}$$

As in Equation A.4, the ratio of configuration integrals appears, which can be estimated before the simulation or, alternatively, adjusted during simulation to achieve consistency. However, when using Monte Carlo techniques, adjusting this parameter during a simulation may result in disrupting the Markov process and undermining assumptions based on Markov behavior [*227*]. In theory, Equation A.6 is valid for any potential function, so when implementing Equation A.7 the value specified for the ratio of configuration integrals need not be exact.

In practice, it is often easier to implement a free energy perturbation in conjunction with a distribution-histogram method. In this type of method, histograms are collected during the simulations to approximate p_1 and p_0, the probability densities of a configuration occurring with a given potential difference $(\mathcal{V}_1 - \mathcal{V}_0)$ in system 1 and system 0, respectively. Bennett describes an overlapping distribution method based on the following identity and normalization constraints [*230*]:

$$\frac{p_1(\Delta\mathcal{V})}{p_0(\Delta\mathcal{V})} = \frac{\langle\delta(\mathcal{V}_1 - \mathcal{V}_0 - \Delta\mathcal{V})\rangle_1}{\langle\delta(\mathcal{V}_1 - \mathcal{V}_0 - \Delta\mathcal{V})\rangle_0} \tag{A.8}$$

$$\int_{-\infty}^{\infty} p_1(\Delta\mathcal{V})\, d\Delta\mathcal{V} = \int_{-\infty}^{\infty} p_0(\Delta\mathcal{V})\, d\Delta\mathcal{V} = 1 \tag{A.9}$$

Here, $p_1(\Delta\mathcal{V})$ and $p_0(\Delta\mathcal{V})$ are the probability densities for finding configurations with potential energy difference $\Delta\mathcal{V} = \mathcal{V}_1 - \mathcal{V}_0$ in system 1 and system 0, respectively. Frenkel provides a useful illustration similar to that of Figure A.1 to explain the idea behind Bennett's overlapping distribution method [*234*]. Knowing that the chemical

potential may be obtained from the ratio of configuration integrals Z_0/Z_1, imagine the set of all roads represents Z_0 and the set of all train tracks represents Z_1. The roads and tracks overlap each other at level crossings. If the level crossings account for 1% of the total area of train tracks and for 0.1% of the total area of roads, then the roads must have ten times more area than the tracks. Of course the relation for Z_0/Z_1 depends also on the criteria for overlapping configurations, i.e., on the value of $\Delta\mathcal{V}$ as seen in Equation A.8. Therefore, the analogy is consistent only when $\Delta\mathcal{V}$ is zero.

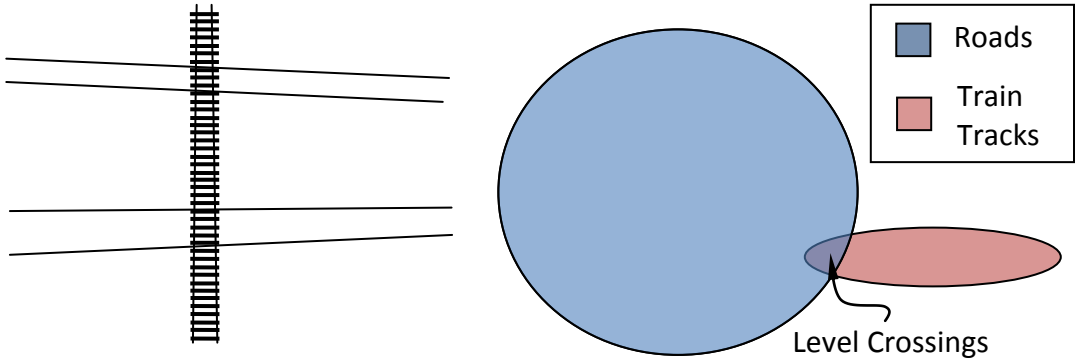

Figure A.1. Adaptation of Frenkel's illustration [*234*] with corresponding Venn diagram to demonstrate Bennett's overlapping distribution method.

For systems where $\mathcal{V}_1$ and $\mathcal{V}_0$ are similar, the histograms collected during a simulation to approximate $p_1(\Delta\mathcal{V})$ and $p_0(\Delta\mathcal{V})$will likely overlap for certain values of $\Delta\mathcal{V}$, and the free energy difference is easily determined. However, the chemical potential may be extracted from the histograms even when they do not overlap, since

the functions are not independent, as shown in Equations A.8 and A.9. The method is similar to interpolation and often gives reliable results.

Torrie and Valleau describe an alternative method based on the umbrella sampling technique [*232*]. The chemical potential can be written in the following form:

$$e^{-\mu^{res}} = \int_{-\infty}^{\infty} p_0(\Delta\mathcal{V})\, e^{-\Delta\mathcal{V}} d\Delta\mathcal{V} \tag{A.10}$$

Therefore, if the form of $p_0(\Delta\mathcal{V})$ is known with accuracy, it can be integrated to obtain the chemical potential. In practice, ordinary Boltzmann-weighted sampling of the $(N-1)$-particle system is not adequate to result in a well-defined distribution. If a weighting potential can be found such that a broad and uniform probability distribution p_W results, then the probability distribution p_0 can be obtained, and subsequently the chemical potential, from the following transformation:

$$p_0(\Delta\mathcal{V}) = p_W(\Delta\mathcal{V}) \frac{e^{\mathcal{V}_W - \mathcal{V}_0}}{\langle e^{\mathcal{V}_W - \mathcal{V}_0} \rangle_W} \tag{A.11}$$

This concludes our survey of methods for estimating the chemical potential from molecular simulation. For estimating the chemical potential of small molecule penetrants in polymer systems, the Widom method is likely to give satisfactory results. These results can be verified with one of the more sophisticated techniques, such as Bennett's acceptance ratio method, the overlapping distribution method, umbrella sampling, or the umbrella distribution method. In any case, the particle deletion scheme should be avoided.

APPENDIX B

LINEAR RESPONSE THEORY

Non-equilibrium thermodynamics provides a foundation for studying transport properties of systems via molecular level simulation. A detailed discussion of this topic can be found in the texts by Fitts [*235*] and de Groot and Mazur [*236*]. This appendix gives two examples of how linear response theory, a key component of non-equilibrium thermodynamics, can be used to study the transport properties of molecular systems.

Derivation of a transport coefficient using linear response theory follows a particularly simple approach. First, the measured variable of interest is defined according to microscopic variables. Then, a small perturbation is considered, which is chosen by considering the driving force for the transport phenomenon. It is assumed that the perturbation is small enough that a first-order approximation of the measured variable's response is valid—that is, the response is considered linear with a slope given by a phenomenological coefficient. Through the use of ensemble averages, the phenomenological coefficient can be estimated by considering the equilibrium value and perturbed response of the measured variable.

In Section B.1, the binary diffusion coefficient is derived from linear response theory. For this case, the measured variable of interest is the mass flux of a particular species, while the perturbation is an imposed chemical potential gradient. Then, in

section B.2, an expression for the viscosity is developed by considering the velocity gradient brought about by a perturbation in shear stress.

§ B.1. Calculating the Binary Diffusion Coefficient in the NPT Ensemble

It is engineering practice to define the diffusion coefficient according to Fick's first law (shown for a binary system),

$$\mathbf{j}_A = -\rho D_{AB} \boldsymbol{\nabla} w_A \tag{B.1}$$

where $\mathbf{j}_A$ is the diffusive mass flux of component A relative to the local center-of-mass velocity, D_{AB} is the diffusion coefficient for component A in component B, ρ is the total mass concentration, w_A is the mass fraction of component A, and $\boldsymbol{\nabla}$ is the gradient operator. This relation is readily applied to real systems where the concentration of the diffusing species can be estimated.

Calculation of diffusion based on Equation B.1 is convenient in practice for most engineering applications. However, when considering the phenomenon from a theoretical standpoint, the driving force for diffusion is more properly a gradient in *chemical potential*, not concentration. For a binary isotropic system, non-equilibrium thermodynamic arguments show that the linear-regime response of the mass flux to a chemical potential gradient is given as

$$\mathbf{j}_A = -\frac{1}{w_B}\frac{L_{AA}}{T}\boldsymbol{\nabla}\mu_A \tag{B.2}$$

where we define μ_A as the mass-based chemical potential of component A, L_{AA} is the phenomenological coefficient giving the contribution from the chemical potential gradient of A to the flux response of A, and T is the temperature of the system.

We now endeavor to relate the macroscopic concept given in Equation B.2 to quantities that are observable in a typical molecular dynamics (MD) simulation. Although the chemical potential gradient is a thermodynamic driving force which acts in an *averaged out* sense, it is generally accepted that the response of a system to a thermodynamic driving force is the same as that for a mechanical force applied on the system. The static response due to a mechanical field is easily obtained from linear response theory, and the general framework for such a derivation can be found in most modern texts on statistical mechanics. For completeness, we present a short derivation here. First, we define the instantaneous diffusive mass flux of species A in terms of microscopic variables

$$\boldsymbol{j}_A = \frac{m_A}{V}\sum_{i=1}^{N_A}\left(\dot{\mathbf{r}}_i - \dot{\mathbf{r}}_{ref}\right) \tag{B.3}$$

Here, m_A is the mass of a single A-particle, V is the system volume, $\dot{\mathbf{r}}_i$ is the center-of-mass velocity of particle i, $\dot{\mathbf{r}}_{ref}$ is the velocity of the frame of reference, and the sum runs over all A-particles. The macroscopic mass flux $\mathbf{j}_A$ is found from the time average or ensemble average of $\boldsymbol{j}_A$, from which it is easily seen that the expectation value of $\boldsymbol{j}_A$ at equilibrium will be zero when $\dot{\mathbf{r}}_{ref}$ is chosen as the mass-averaged velocity.

Now consider an isothermal-isobaric ensemble of N particles at temperature T and pressure P governed by the Hamiltonian $\mathcal{H}_0(r_N, p_N, V)$ at equilibrium, where r_N represents the position vectors for all N particles, p_N represents their momenta, and V is the box vector for the system. We have included dependence on the box vector to show that periodic boundary conditions may be enforced. Now consider the Hamiltonian when the system is perturbed by a small constant mechanical force F acting on all A-particles,

$$\mathcal{H}_1 = \mathcal{H}_0 - \mathbf{F} \cdot \mathbf{R}_A \tag{B.4}$$

where $\mathbf{R}_A$ is the sum of the positions of all A-particles with respect to the frame of reference,

$$\mathbf{R}_A = \sum_{i=1}^{N_A} \left(\mathbf{r}_i - \mathbf{r}_{ref}\right) \tag{B.5}$$

Now we take the ensemble average of $\boldsymbol{j}_A$ in the perturbed system, after allowing it to evolve over a time t from the phase point at which the average is accumulated

$$\langle \boldsymbol{j}_A(t) \rangle_1 = \frac{\int d\boldsymbol{\Gamma}\, e^{-\beta(\mathcal{H}_0 - \mathbf{F}\cdot\mathbf{R}_A + PV)} \boldsymbol{j}_A(t)}{\int d\boldsymbol{\Gamma}\, e^{-\beta(\mathcal{H}_0 - \mathbf{F}\cdot\mathbf{R}_A + PV)}} \tag{B.6}$$

such that $\boldsymbol{\Gamma}$ is the phase space vector $[\mathbf{r}^N\ \dot{\mathbf{r}}^N\ V]$ for the system. If we are considering an isotropic system in three dimensions, the phenomenological coefficient may be found by taking one-third of the trace of the response of $\langle \boldsymbol{j}_A(t) \rangle_1$. Since we are considering

small perturbations, we take the limit as the perturbing force goes to zero. The long time limit must also be imposed to obtain the steady-state response, giving the relation

$$\frac{L_{AA}}{T} = \lim_{\substack{\mathbf{F}\to\mathbf{0} \\ t\to\infty}} \frac{1}{3} \boldsymbol{\nabla}_{\mathbf{F}} \cdot \langle \boldsymbol{j}_A(t) \rangle_1 \tag{B.7}$$

Here, the subscript on the del operator indicates that the gradient is taken with respect to the components of $\mathbf{F}$. Performing these operations on Equation B.6, we have the following equation.

$$\begin{aligned} \boldsymbol{\nabla}_{\mathbf{F}} \cdot \langle \boldsymbol{j}_A(t) \rangle_1 = & \frac{\int d\boldsymbol{\Gamma}\, e^{-\beta(\mathcal{H}_0 - \mathbf{F}\cdot\mathbf{R}_A + PV)} (-\beta \mathbf{R}_A) \cdot \boldsymbol{j}_A(t)}{\int d\boldsymbol{\Gamma}\, e^{-\beta(\mathcal{H}_0 - \mathbf{F}\cdot\mathbf{R}_A + PV)}} \\ & + \frac{\left[\int d\boldsymbol{\Gamma}\, e^{-\beta(\mathcal{H}_0 - \mathbf{F}\cdot\mathbf{R}_A + PV)} (-\beta \mathbf{R}_A)\right] \cdot \left[\int d\boldsymbol{\Gamma}\, e^{-\beta(\mathcal{H}_0 - \mathbf{F}\cdot\mathbf{R}_A + PV)} \boldsymbol{j}_A(t)\right]}{\left[\int d\boldsymbol{\Gamma}\, e^{-\beta(\mathcal{H}_0 - \mathbf{F}\cdot\mathbf{R}_A + PV)}\right]^2} \end{aligned} \tag{B.8}$$

Taking the limits, and recognizing the definition of the NPT ensemble average,

$$\frac{L_{AA}}{T} = \lim_{t\to\infty} \frac{\beta}{3} \left[\langle \mathbf{R}_A \cdot \boldsymbol{j}_A(t) \rangle_0 - \langle \mathbf{R}_A \rangle_0 \cdot \langle \boldsymbol{j}_A(t) \rangle_0 \right] \tag{B.9}$$

The last term in the brackets of equation B.9 vanishes, since the expectation value of $\boldsymbol{j}_A$ at equilibrium is zero when the frame of reference is selected as the mass-averaged velocity. The remaining terms on the right-hand side may be evaluated using

$$\langle \mathbf{R}_A \cdot \boldsymbol{j}_A(t) \rangle_0 = \langle \int_t^0 dt'\, \dot{\mathbf{R}}_A(t') \cdot \boldsymbol{j}_A(t) \rangle_0 = m_A \int_t^0 dt' \, \langle \frac{\dot{\mathbf{R}}_A(t') \cdot \dot{\mathbf{R}}_A(t)}{V(t)} \rangle_0 \tag{B.10}$$

Changing the variable of integration to $t = t' - t$, we may write B.10 as

$$\langle \mathbf{R}_A \cdot \boldsymbol{j}_A(t) \rangle_0 = m_A \int_0^t d\tau \, \langle \frac{\dot{\mathbf{R}}_A(t-\tau) \cdot \dot{\mathbf{R}}_A(t)}{V(t)} \rangle_0 \tag{B.11}$$

and, because the ensemble average is impervious to a time shift we have

$$\langle \mathbf{R}_A \cdot \boldsymbol{j}_A(t) \rangle_0 = m_A \int_0^t d\tau \, \langle \frac{\dot{\mathbf{R}}_A(-\tau) \cdot \dot{\mathbf{R}}_A(0)}{V(0)} \rangle_0 \tag{B.12}$$

Making use of the fact that the ensemble average in B.12 is an even function of time, we may write

$$\langle \mathbf{R}_A \cdot \boldsymbol{j}_A(t) \rangle_0 = m_A \int_0^t d\tau \, \langle \frac{\dot{\mathbf{R}}_A(\tau) \cdot \dot{\mathbf{R}}_A(0)}{V(0)} \rangle_0 \tag{B.13}$$

Finally, using equation B.13 with B.9, we have the relation

$$L_{AA} = \frac{m_A}{3k_B} \int_0^\infty d\tau \, \langle \frac{\dot{\mathbf{R}}_A(\tau) \cdot \dot{\mathbf{R}}_A(0)}{V(0)} \rangle_0 \tag{B.14}$$

where k_B is the Boltzmann constant (the B subscript should not be confused with component B in our system). Equation B.14 is what is known as a Green-Kubo relation; that is, if casts the phenomenological coefficient in terms of the long-time integral of an autocorrelation function. This has the equivalent Einstein formulation

$$L_{AA} = \lim_{t \to \infty} \frac{m_A}{6k_B t} \langle \frac{\mathbf{R}_A(t) - \mathbf{R}_A(0)}{V(0)} \rangle_0 \tag{B.15}$$

When applying the above formulations in a molecular dynamic simulation, note that they are valid only when V is not affected by the equations of motion for the system. Proper evaluation of the ensemble averages in Equations B.14 and B.15 would

require sampling of initial phase points according to the isothermal-isobaric ensemble, then performing dynamic simulations in an appropriate isochoric ensemble. It has been shown that autocorrelation functions, like steady-state averages, are unaffected when a proper temperature coupling method is used (e.g., the Nosé-Hoover thermostat) in the large-system limit, and are unaffected by the thermostat coupling strength [*237*]. Therefore, it is permissible to use canonical ensemble molecular dynamics methods in evaluating Equation B.14, provided that the set of initial phase points are represented of the NPT ensemble.

§ B.2. Calculating the Viscosity in the NPT Ensemble

A variety of methods exist for determining the shear viscosity from molecular dynamics. The methods fall into one of two categories: equilibrium and non-equilibrium methods. In equilibrium methods, the MD simulation is carried out in the absence of external forces, whereas non-equilibrium methods impose some net force on the system. Each method has its advantages and disadvantages; equilibrium methods are easily applied using conventional simulation software, but often require more computation time than non-equilibrium methods. Non-equilibrium methods, on the other hand, require software to be specifically developed for the particular method.

Using a similar derivation as in Section B.1, the equilibrium relation for the zero shear viscosity is given by linear response theory as

$$\eta_0 = \frac{V}{k_B T} \int_0^t \langle \mathcal{P}_{\alpha\beta}(0) \mathcal{P}_{\alpha\beta}(t) \rangle \, dt \tag{B.16}$$

where $\mathcal{P}$ represents the pressure tensor, and the subscripts denote a particular off-diagonal component (α and β may each take on values of x, y, or z). As in Equation B.14, Equation B.16 is a Green-Kubo relation, involving the integral of an autocorrelation function. The equivalent Einstein form is

$$\eta_0 = \lim_{\mathrm{t}\to\infty} \frac{V}{2tk_B T} \langle \Big(\mathcal{Q}_{\alpha\beta}(\mathrm{t}) - \mathcal{Q}_{\alpha\beta}(0) \Big)^2 \rangle \tag{B.17}$$

where $\mathcal{Q}_{\alpha\beta} = \frac{1}{V} \sum_i \ \mathrm{r}_{i\alpha} \mathrm{p}_{i\beta}$.

Non-equilibrium molecular dynamics (NEMD) methods for estimating the viscosity are reviewed by Todd and Daivis [*57*]. The most common method in recent years has been the SLLOD method [*238,239*], whose name is meant to indicate the method's use of the transposed Doll's tensor (the Doll's tensor, in turn was named by W. G. Hoover; because it involves a product of positions and momenta—in Hoover's notation qp—the method evoked thoughts of the "Kewpie" dolls popular in the early and mid-twentieth century [*240,241*]). The SLLOD equations of motion are non-Hamiltonian, and may be written as

$$\dot{\mathbf{r}}_i = \frac{\mathbf{p}_i}{m_i} + \mathbf{r}_i \cdot \nabla \mathbf{v} \tag{B.18}$$

$$\dot{\mathbf{p}}_i = \mathbf{f}_i - \mathbf{p}_i \cdot \nabla \mathbf{v} \tag{B.19}$$

where $\nabla \mathbf{v}$ is the imposed velocity gradient. The SLLOD equations of motion should be used with appropriate boundary conditions, such as those proposed by Lees and Edwards [*242*]. Once a trajectory is obtained with the SLLOD equations, the stress normal to the velocity gradient can be calculated and the effective viscosity obtained.

The major shortcoming of using NEMD methods, such as SLLOD, for estimating the viscosity is that they are limited to very high shear rates. For example, consider a reasonably-sized simulation box, say 10 nm on each side, with flow in the x-direction and a velocity gradient with respect to the y axis. To adequately observe the effect of shear rate on the stress tensor, the box should undergo deformation on the order of the box length. Thus, in a reasonable simulation time, say 10 ns, the box would deform 10 nm in the x direction per every 10 nm in the y direction. The corresponding shear rate is 10^8 s^{-1}, which is orders of magnitude higher than the shear rates encountered in high-shear processes, such as fiber spinning. This causes complications in the case of polymers, since they exhibit a nonlinear response to shear flow.

In simple molecular systems, it has been demonstrated that the low-shear response of a fluid can be successfully extrapolated from NEMD according to nonlinear response theory, with the use of the transient time correlation function (TTCF) analysis [*243-245*]. These methods work generally well when the relaxation times of the system are small, though we know of no studies published which report their performance on slow-relaxing systems such as polymers.

APPENDIX C

LEAST SQUARES FITTING PROCEDURE FOR TORSIONAL POTENTIALS

§ C.1. Introduction

In this appendix, the least squares method used in the **`torsfit`** program is discussed. The overall fitting procedure involves the repeated application of this method in a prescribed order, as discussed in Chapter Five. Here, the least squares objective function and its derivatives are developed, followed by the relevant source code for the **`torsfit`** program. First, we begin with an elementary discussion of the least squares method itself.

The least squares method can be applied as a fitting technique for both linear and nonlinear *model functions*. In this method, the term model function is defined as the function that is supposed to explain a trend in a given data set. The model function takes as its arguments the independent variables in the data set, as well as one or more adjustable parameters. For example, when fitting two dimensional data, say $\{x_i, y_i\}$, to a linear function, $f = mx + b$, the model function f depends on the independent variable x as well as the parameters m and b. The essence of the least squares method is to find the point in parameter space that results in a minimum of the sum of squared deviations, between the data set's dependent variables, and the corresponding values

as predicted by the model function. For the example case of a linear model function, we can define the sum of squares as our *objective function* to be minimized,

$$F = \sum_i [y_i - f(x_i, m, b)]^2 \tag{C.1}$$

The objective function is constructed to measure the inaccuracy of our model function, so finding the set of model parameters that result in the highest accuracy amounts to finding the model parameters that drive the objective function to a minimum. Thus, the solution to our problem is to find the values of m and b that minimize F. Of course, in this commonly encountered linear least squares problem, analytical solutions are easily obtained due to the simplicity of the model function (see any textbook on statistics and regression). However, in most cases where f is nonlinear, the objective function must be minimized using numerical methods. One method particularly well-suited for nonlinear least squares optimization is the Marquardt-Levenberg algorithm. This is implemented in many readily-available mathematics and data analysis packages. However, in the case of fitting the torsional potentials for PLA, as described in Chapter Five, the overall fitting procedure was sufficiently complex that a customized, command-line driven least squares optimization program was needed. In addition, analytic gradients were available for the objective function, and thus, other optimization methods could be used which have better performance than Marquardt-Levenburg. In the **`torsfit`** program, the bounded quasi-Newton L-BFGS-B routine was used [*141*].

§ C.2. Objective function for fitting dihedral parameters

The objective function is a weighted sum of squared differences between the DFT energy and the force field energy for each of the N_{dat} data points on the minimum energy surface:

$$F = \frac{\sum_{i=1}^{N_{dat}} W_i (\Delta V_i)^2}{\sum_{i=1}^{N_{dat}} W_i} \tag{C.2}$$

Here W_i is the weighting factor for data point i on the minimum energy surface, the collection of which need not be normalized. The difference ΔV_i in Equation C.2 is taken between V_i^{FF}, the potential energy of the conformer associated with data point i as calculated with the current force field parameters (though the geometry of the conformer is determined by energy minimization using the *initial* force field parameters; see Chapter Five), and the DFT calculated energy of data point i, V_i^{DFT}. To separate the contributions of the dihedral parameters used in the least squares optimization from the other remaining force field parameters, the initial force field energy, V_i^{FF0} is calculated for each data point before running the least squares procedure. The contribution from the initial values of the dihedral parameters V_i^{DIH0} is also determined before optimization, so that the force field energy may be calculated during optimization as

$$V_i^{FF} = V_i^{FF0} - V_i^{DIH0} + V_i^{DIH} - K \tag{C.3}$$

where V_i^{DIH} is the dihedral term contribution using the current guess of dihedral parameters. The additive shift constant, K, appears in Equation C.3 to alleviate errors brought about by the arbitrary definition of a reference state in each model. Thus, the objective function has the form

$$F = \frac{1}{Q}\sum_{i=1}^{N_{dat}} W_i\left[\left(V_i^{FF0} - V_i^{DIH0} + V_i^{DIH} - K\right) - V_i^{DFT}\right]^2 \tag{C.4}$$

where Q is defined as the normalization constant or the sum of weights for the DFT data points.

The individual contributions to the dihedral term V_i^{DIH} depends on the number of dihedral types that are fit during the optimization, N_{dih}, and the number of repeat units in the molecule, N_{rep} (assuming each dihedral type occurs only once per repeat unit). Further, each type j, of the N_{dih} dihedral types, may have an arbitrary number of periodic functions, $N_{per,j}$, associated with it in addition to its Ryckaert-Bellemans expansion. Thus, using the Ryckaert-Bellemans and periodic energy functions, we have

$$V_i^{DIH} = \sum_{j=1}^{N_{dih}}\sum_{k=1}^{N_{rep}}\left[\sum_{n=0}^{5} C_{n,j}\left(\cos\left(\tau_{k,j,i} - 180°\right)\right)^n + \sum_{p=1}^{N_{per,j}} k_{p,j}\left(1 + \cos\left(n_{p,j}\tau_{k,j,i} - \varphi_{p,j}\right)\right)\right] \tag{C.5}$$

where the independent variable $\tau_{k,j,i}$ is the value in degrees of the dihedral angle of type j in repeat unit k in conformer i, as defined by the IUPAC convention. Equation C.5

also presents the parameter space coordinates used in the optimization: the Ryckaert-Bellemans coefficients $\{C_{n,j}\}$, of which there are $5N_{dih}$ that will be adjusted, and the periodic amplitudes $\{k_{p,j}\}$ and phase shifts $\{\varphi_{p,j}\}$, for each of which there are $\sum_{j=1}^{N_{dih}} N_{per,j}$. The set of zero-order Ryckaert-Bellemans coefficients $\{C_{0,j}\}$ will be eliminated, as discussed when considering the shift constant K. There are also $\sum_{j=1}^{N_{dih}} N_{per,j}$ periodic multiplicities, $\{n_{p,j}\}$, but since these are by definition integers, they cannot be used in gradient-based optimization. A brute-force approach is taken to optimize the multiplicities, where the optimization is run for all permutations of combinations of $\{n_{p,j}\}$, and the permutation resulting in the lowest value of F is selected as the optimum set. Multiplicities are only considered such that $0 < n_{p,j} \leq 3$ for all p and j.

A few words are warranted regarding the use of multiple periodic terms per dihedral. Care should be taken that only one periodic function is used for each multiplicity. This is because the sum of two or more cosine functions of differing amplitude and phase can be expressed analytically as one single cosine function with one amplitude and phase, provided the multiplicities of the original functions are equal. Similarly, if one were to use more than one Ryckaert-Bellemans series, their sum would collapse to a single series.

As previously mentioned, the reference values in relation to which the DFT and force-field energies are computed are trivial; that is, each set of energies may be shifted

up or down by an additive constant and still yield the same behavior in terms of the forces (energy derivatives). Thus, the dependence of the objective function on the arbitrary 'shift' degrees of freedom must be accounted for when fitting the remaining parameters. To this end, the additive constant K is selected such that the objective function is minimized with respect to it. Finding the point where F is stationary with respect to K, we have

$$\frac{\partial F}{\partial K} = 0 = -\frac{1}{Q}\sum_{i=1}^{N_{dih}} 2W_i\left[\left(V_i^{FF0} - V_i^{DIH0} + V_i^{DIH} - K\right) - V_i^{DFT}\right] \tag{C.6}$$

This is readily solved for K:

$$K = \frac{1}{Q}\sum_{i=1}^{N_{dih}} W_i\left[\left(V_i^{FF0} - V_i^{DIH0} + V_i^{DIH}\right) - V_i^{DFT}\right] \tag{C.7}$$

Equation C.7 would also follow by direct comparison with the intercept term in an ordinary linear least squares fit.

Another set of additive constants, $\{C_{0,j}\}$, is contained in the Ryckaert-Bellemans dihedral terms. These will not be used as fitting parameters, and for convenience those degrees of freedom are eliminated by setting them equal to

$$C_{0,j} = \sum_{n=1}^{5} C_{n,j} \tag{C.8}$$

such that the Ryckart-Bellemans potential for any dihedral type is zero at the *trans* position. Thus, equations C.7 and C.8 account for the linear "shift" degrees of freedom,

and the objective function depends solely on the $5N_{dih} + 2\sum_{j=1}^{N_{dih}} N_{per}$ parameters previously mentioned.

For use in the L-BFGS-B optimization scheme, partial derivatives of the objective function are required for every parameter space variable. These may be obtained in closed form as follows:

$$\begin{aligned}\frac{\partial F}{\partial C_{n,j}} &= \frac{1}{Q}\sum_{i=1}^{N_{dat}} 2W_i\Delta V_i \frac{\partial(\Delta V_i)}{\partial C_{n,j}} = \frac{1}{Q}\sum_{i=1}^{N_{dat}} 2W_i\Delta V_i\left[\frac{\partial V_i^{DIH}}{\partial C_{n,j}} - \frac{\partial K}{\partial C_{n,j}}\right] \\ &= \frac{2}{Q}\sum_{i=1}^{N_{dat}} W_i\Delta V_i \sum_{k=1}^{N_{rep}}\left[\left(-\cos\left(\tau_{k,j,i}\right)\right)^n - \frac{1}{Q}\sum_{l=1}^{N_{dat}} W_l\left(-\cos\left(\tau_{k,j,i}\right)\right)^n\right]\end{aligned} \tag{C.9}$$

$$\begin{aligned}\frac{\partial F}{\partial k_{p,j}} &= \frac{1}{Q}\sum_{i=1}^{N_{dat}} 2W_i\Delta V_i \frac{\partial(\Delta V_i)}{\partial k_{p,j}} = \frac{1}{Q}\sum_{i=1}^{N_{dat}} 2W_i\Delta V_i\left[\frac{\partial V_i^{DIH}}{\partial k_{p,j}} - \frac{\partial K}{\partial k_{p,j}}\right] \\ &= \frac{2}{Q}\sum_{i=1}^{N_{dat}} W_i\Delta V_i \sum_{k=1}^{N_{rep}}\left[1 + \cos\left(n_{p,j}\tau_{k,j,i} - \varphi_{p.j}\right)\right. \\ &\qquad \left. - \frac{1}{Q}\sum_{l=1}^{N_{dat}} W_l\left[1 + \cos\left(n_{p,j}\tau_{k,j,i} - \varphi_{p.j}\right)\right]\right]\end{aligned} \tag{C.10}$$

$$\frac{\partial F}{\partial \varphi_{p,j}} = \frac{1}{Q}\sum_{i=1}^{N_{dat}} 2W_i \Delta V_i \frac{\partial(\Delta V_i)}{\partial \varphi_{p,j}} = \frac{1}{Q}\sum_{i=1}^{N_{dat}} 2W_i \Delta V_i \left[\frac{\partial V_i^{DIH}}{\partial \varphi_{p,j}} - \frac{\partial K}{\partial \varphi_{p,j}}\right]$$

$$= \frac{2}{Q}\frac{180^\circ}{\pi}\sum_{i=1}^{N_{dat}} W_i \Delta V_i \sum_{k=1}^{N_{rep}} \left[k_{p,j}\sin\left(n_{p,j}\tau_{k,j,i} - \varphi_{p.j}\right)\right. \tag{C.11}$$

$$\left. - \frac{1}{Q}\sum_{l=1}^{N_{dat}} W_l\, k_{p,j}\sin\left(n_{p,j}\tau_{k,j,i} - \varphi_{p.j}\right)\right]$$

where in Equation C.9 we have used the identity $\cos(\theta - 180^\circ) = -\cos\theta$. These equations give us all the information needed to implement the least squares fitting method using the L-BFGS-B routine.

§ C.3. The `torsfit` program

Given the objective function and derivatives above, the L-BFGS-B minimization subroutine by Zhu, Byrd, Nocedal [*141*] was used for building a customized torsional parameter fitting program. The program is called **`torsfit`** and reads a data file containing entries of V_i^{DFT}, V_i^{FF0}, and $\{\tau_{k,j,i}\}$, as well as the starting point in parameter space. The format of the data file is free within each line (numbers must only be space delimited), but the sequence of lines must follow Table C.1, below. The optimization is performed with the bounded quasi-Newton algorithm L-BFGS-B, which approximates the Hessian based on information from the first partial derivatives in previous cycles. In each cycle, the direction of search is calculated based on the current Hessian approximation, and a line search minimization is performed in that direction. The quality

of the Hessian approximation is dictated by the variable `msav`, which is the number of previous iterations used to approximate the Hessian. For `msav` = 0, the algorithm collapses to a normal steepest-descent approach. Here, the value of `msav` is set in the subroutine **`lbfgsb`**, to the number of variables used in the minimization.

Table C.1. Input file format for the **`torsfit`** program. The indices take on the following values: $1 \leq i \leq N_{dat}$, $1 \leq j \leq N_{dih}$, $1 \leq k \leq N_{rep}$, $1 \leq p \leq N_{per,j}$

Line Number(s)	Contents	Data type
1	Comment line	--
2	N_{dat}, N_{rep}, N_{dih}	Integers
3	Comment line	--
4	Dihedral type names (one entry for each of the N_{dih} dihedral types)	Strings
5	Comment line	--
6	$\{N_{per,j}\}$ (one entry for each of the N_{dih} dihedral types)	Integers
7	Comment line	--
$7 + i$	V_i^{DFT} (kJ/mol), V_i^{FF0} (kJ/mol), then $\{\tau_{k,j,i}\}$ (degrees); N_{dih} dihedrals are listed for the first repeat unit ($k = 1$), then the second ($k = 2$), up to the last repeat unit ($k = N_{rep}$)	Floating point numbers
$8 + N_{dat} + \sum_{l=1}^{j-1} 3(1 + N_{per,l})$	Comment line	--
$9 + N_{dat} + \sum_{l=1}^{j-1} 3(1 + N_{per,l})$	Comment line	--
$10 + N_{dat} + \sum_{l=1}^{j-1} 3(1 + N_{per,l})$	$\{C_{n,j}\}$, the initial Ryckaert-Bellemans coefficients for dihedral type j (six entries, each in kJ/mol)	Floating point numbers
$11 + N_{dat} + \sum_{l=1}^{j-1} 3(1 + N_{per,l}) + 3(p-1)$	Comment line	--
$12 + N_{dat} + \sum_{l=1}^{j-1} 3(1 + N_{per,l}) + 3(p-1)$	Comment line	--
$13 + N_{dat} + \sum_{l=1}^{j-1} 3(1 + N_{per,l}) + 3(p-1)$	$\varphi_{p,j}$ (degrees), $k_{p,j}$ (kJ/mol), and $n_{p,j}$, the initial parameters for periodic function p on dihedral type j	Floating point numbers
$8 + N_{dat} + \sum_{l=1}^{N_{dih}} 3(1 + N_{per,l})$	Comment line	--

§ C.3.1. Sample input file for `torsfit`: omega_iter1.in

(Lines are numbered for reference only; they are not to be included in input file)

```
1  ;   Ndat    Nrep    Ndih
2        36       3       1
3  ;  dihname[1]
4           omega
5  ;     Nper[1]
6               1
7  ;V_DFT (kJ/mol) V_FF0 (kJ/mol)      omega1      omega2      omega3
8         0.790300      11.173000   -170.7585   -179.9844    166.5158
9         3.833900       8.944000   -170.8069   -170.1868    171.0353
10        8.770100       7.873000   -171.9195   -160.2049    176.1213
11       15.808200       8.059000   -174.0536   -150.5471   -179.6658
12       24.569900       9.464000   -174.9620   -140.6584   -177.5504
13       34.528800      12.063000   -174.9224   -130.5526   -177.3356
14       44.500000      14.193000    178.8335   -120.2675    162.5098
15       52.680200      23.250000   -173.8713   -109.9647   -176.8401
16       58.271400      22.129000   -173.6212   -100.2017   -177.0388
17       60.845200      21.978000   -174.5788    -90.5989   -175.2948
18       60.469900      22.865000   -173.9894    -79.9453   -172.9118
19       55.416700      23.112000   -178.8751    -70.1091    166.9887
20       48.954400      27.191000    179.1873    -60.6246    167.1560
21       44.329900      31.186000    175.4477    -50.0836    171.0984
22       41.587100      34.926000    174.4455    -40.1222    173.1416
23       40.356100      38.523000    175.4813    -30.0233    175.6322
24       39.927500      42.075000    178.5670    -20.5551    179.8300
25       40.169400      45.560000   -179.3643    -10.2225   -177.8172
26       40.883200      48.494000   -178.6184     -0.0342   -177.7098
27       41.888900      50.362000   -179.3548      9.8307   -179.2221
28       43.284200      50.883000    179.1763     19.5590    178.6291
29       45.236600      50.196000    177.2680     30.4551    177.5258
30       47.592700      45.117000   -177.7031     39.4457    175.4268
31       50.344600      38.647000   -177.2099     49.9227    175.6840
32       53.170200      32.023000   -176.2950     60.2218    175.9246
33       55.994400      25.954000   -175.2282     70.2849    175.1986
34       57.600100      21.588000   -174.5079     79.9251    175.8257
35       56.960900      19.124000   -174.0542     90.5636    164.7294
36       53.920500      18.957000   -174.7594     99.3718    166.4566
37       47.082200      16.843000   -176.9538    110.2125    166.8924
38       39.149500      13.384000   -175.0573    119.9512   -177.7566
39       28.018500       5.683000   -174.5654    130.1365    179.7031
40       19.591600       0.988000   -172.1621    140.4101    175.9609
41        9.412600       0.000000   -169.1299    150.1607    172.5153
```

```
        2.405800       2.500000   -167.7875    159.9187    168.6268
        0.000000       6.749000   -170.9635    170.1889    165.5192
; Ryckaert-Bellemans parameters for omega
;         C0        C1        C2        C3        C4        C5
      2.87441   0.58158   2.09200  -5.54799   0.00000   0.00000
; Periodic Dihedral parameters for omega
;       phi0      kphi         n
            0         0         1
; Shift constant K =    0.00000
```

§ C.3.2. Sample output files from `torsfit`

File `omega_iter1.out`

```
; Ryckaert-Bellemans parameters for omega
;       C0        C1        C2        C3        C4        C5
    50.00696  -10.52518  -36.97481   48.16037   -5.59111  -45.07623
; Periodic Dihedral parameters for omega
;       phi0      kphi         n
   -40.81554    2.96508    3
; Shift constant K =   18.43635
```

File `omega_iter1.out.fit`

```
#    V_DFT     V_FF0    V_DIH0     V_FF1    V_DIH1    omega1
     0.790    11.173     0.468     2.143     9.875   -179.98
     3.834     8.944     0.464     1.223    11.179   -170.19
     8.770     7.873     0.796     6.340    17.699   -160.20
    15.808     8.059     1.368    15.098    26.843   -150.55
    24.570     9.464     2.066    25.432    36.470   -140.66
    34.529    12.063     2.671    34.638    43.682   -130.55
    44.500    14.193     3.510    45.753    53.506   -120.27
    52.680    23.250     3.181    53.164    51.532   -109.96
    58.271    22.129     3.101    54.194    53.602   -100.20
    60.845    21.978     2.973    55.635    55.067    -90.60
    60.470    22.865     3.021    57.475    56.067    -79.95
    55.417    23.112     3.435    54.287    53.047    -70.11
    48.954    27.191     4.037    52.052    47.334    -60.62
    44.330    31.186     5.007    45.702    37.959    -50.08
    41.587    34.926     6.273    41.134    30.918    -40.12
    40.356    38.523     7.611    38.101    25.625    -30.02
    39.928    42.075     8.722    38.052    23.136    -20.56
```

```
 40.169    45.560     9.625    40.291    22.792   -10.22
 40.883    48.494     9.946    42.247    22.135    -0.03
 41.889    50.362     9.641    42.871    20.587     9.83
 43.284    50.883     8.830    43.271    19.655    19.56
 45.237    50.196     7.506    45.696    21.442    30.46
 47.593    45.117     6.275    46.937    26.531    39.45
 50.345    38.647     4.895    50.118    34.803    49.92
 53.170    32.023     3.836    54.092    44.341    60.22
 55.994    25.954     3.212    56.844    52.538    70.28
 57.600    21.588     2.952    57.237    57.037    79.93
 56.961    19.124     3.345    60.821    63.479    90.56
 53.920    18.957     3.369    57.441    60.290    99.37
 47.082    16.843     3.413    50.472    55.478   110.21
 39.150    13.384     3.049    39.988    48.090   119.95
 28.018     5.683     2.686    26.142    41.581   130.14
 19.592     0.988     2.165    14.719    34.332   140.41
  9.413     0.000     1.641     7.211    27.288   150.16
  2.406     2.500     1.159     3.133    20.228   159.92
  0.000     6.749     0.679     0.083    12.449   170.19
```

§ C.4. The `torsfit` source code

The source code for **`torsfit`** primarily consists of the files `torsfit.f` and `fgvalue.f`. All other files needed for compiling are taken from the Tinker version 4.2 source code. This code is available in the electronic supplemental information of this dissertation. It may be compiled from Fortran 77 compiler using the supplied makefiles.

File `torsfit.f`

```
c
c     ##############################################################
c     ##                                                          ##
c     ##  program torsfit    -- Fit torsional parameters using   ##
c     ##                        GROMACS dihedral functions        ##
c     ##                                                          ##
c     ##############################################################
c
c
      program torsfit
      implicit none
      include 'torsdata.i'
      include 'iounit.i'
```

```
      include 'math.i'
      character*120 filenm
      character*1 ext
      character*240 string,text,mults(maxdih)
      character*4 mult
      integer ifile,ifit,freeunit,mlen
      integer Nperm,perm,i,div,com
      integer bestnp(maxdih,maxper),Nparms
      integer trimtext,leng,next
      real*8 parms((5+2*maxper)*maxdih),bestparms((5+2*maxper)*maxdih)
      real*8 F,minF,grdmin,ncalls
      real*8 iC0(maxdih),iCn(maxdih,5)
      real*8 ipp(maxdih,maxper),ikp(maxdih,maxper),inp(maxdih,maxper)
      real*8 fgvalue
      external fgvalue
      external optsave
      external writefit
c
c     set input/output units
c
      input=5
      iout=6
c
c     Open data file
c
      call getarg(1,filenm)
      leng = trimtext (filenm)
      ifile=freeunit()
      open(unit=ifile,file=filenm(1:leng),status='old')
c
c     Skip this header line
c
      read(ifile,*)
c
c     Read parameters
c
      read(ifile,*) Ndat,Nrep,Ndih
c
c     Skip this header line
c
      read(ifile,*)
c
c     Read names of dihedrals
c
      next=1
      read(ifile,10) string
10    format(a240)
      do dih=1,Ndih
        call gettext(string,text,next)
        read(text,*) dihname(dih)
      end do
c
c     Skip this header line
c
      read(ifile,*)
c
c     Read number of periodic functions
c
      next=1
      read(ifile,20) string
20    format(a240)
```

```
      do dih=1,Ndih
        call gettext(string,text,next)
        read(text,*) Nper(dih)
      end do
c
c     Skip this header line
c
      read(ifile,*)
c
c     Read the Ndat data points
c
      do dat=1,Ndat
        next=1
        read(ifile,30) string
30      format(a240)
        call gettext(string,text,next)
        read(text,*) V_DFT(dat)
        call gettext(string,text,next)
        read(text,*) V_FF0(dat)
        do rep=1,Nrep
          do dih=1,Ndih
            call gettext(string,text,next)
            read(text,*) dihs(dat,rep,dih)
          end do
        end do
      end do
c
c     Read initial parameters
c
      do dih=1,Ndih
c
c       Read the Ryckaert-Bellemans Parameters
c
        read(ifile,*)        !Skip this header line
        read(ifile,*)        !Skip this header line too
        read(ifile,*) iC0(dih),iCn(dih,1),iCn(dih,2),
     &                iCn(dih,3),iCn(dih,4),iCn(dih,5)
c
c       Read the periodic dihedral parameters
c
        do per=1,Nper(dih)
          read(ifile,*)        !Skip this header line
          read(ifile,*)        !Skip this header line too
          read(ifile,*) ipp(dih,per),ikp(dih,per),np(dih,per)
        end do
      end do
      close(unit=ifile)
c
c     Calculate dihedral interactions from initial parameters
c
      do dat=1,Ndat
        V_DIH0(dat)=0.0d0
        do rep=1,Nrep
          do dih=1,Ndih
            V_DIH0(dat)=V_DIH0(dat)+iC0(dih)
            do n=1,5
              V_DIH0(dat)=V_DIH0(dat)+iCn(dih,n)*
     &                    (cos((dihs(dat,rep,dih)-180.0d0)/radian))**n
            end do
            do per=1,Nper(dih)
              V_DIH0(dat)=V_DIH0(dat)+ikp(dih,per)*(1+cos((inp(dih,per)
```

```
     &                        *dihs(dat,rep,dih)-ipp(dih,per))/radian))
            end do
          end do
        end do
      end do
c
c     List all permutations of periodic multiplicity parameters
c
      Ncom(0)=1
      Ncom(1)=3
      combs(1,1,1)=1
      combs(1,2,1)=2
      combs(1,3,1)=3
      Ncom(2)=3
      combs(2,1,1)=1
      combs(2,1,2)=2
      combs(2,2,1)=1
      combs(2,2,2)=3
      combs(2,3,1)=2
      combs(2,3,2)=3
      Ncom(3)=1
      combs(3,1,1)=1
      combs(3,1,2)=2
      combs(3,1,3)=3
      Nperm=1
      do dih=1,Ndih
        if (Nper(dih) .ne. 0) then
          Nperm=Nperm*Ncom(Nper(dih))
        end if
      end do
c
c     Increment the multiplicity of the periodic terms and run
c     minimizations
c
      minF=-1.0d0
      do perm=1,Nperm !21,21
        write(iout,*) 'Minimizing for periodic multiplicities:'
        div=1.0d0
        do dih=Ndih,1,-1
          write(mults(dih),40) dihname(dih)
40        format(a8,': ')
          mlen=10
          com=1+mod(int((perm-1)/div),Ncom(Nper(dih)))
          div=div*Ncom(Nper(dih))
          do per=1,Nper(dih)
            np(dih,per)=combs(Nper(dih),com,per)
            write(mult,50) np(dih,per)
50          format(i4)
            mults(dih)=mults(dih)(1:mlen)//mult
            mlen=mlen+4
          end do
          write(iout,*) mults(dih)(1:mlen)
        end do
c
c       Store the parameters to the parameter array
c
        i=0
        do dih=1,Ndih
          do n=1,5
            i=i+1
            parms(i)=iCn(dih,n)
```

```
            end do
            do per=1,Nper(dih)
              i=i+1
              parms(i)=ipp(dih,per)
              i=i+1
              parms(i)=ikp(dih,per)
            end do
          end do
c
c         Run the minimization
c
          Nparms=i                ! Set the # of fitting parameters
          grdmin=0.0005d0         ! Set the convergence criteria
          call lbfgs(Nparms,parms,F,grdmin,fgvalue,optsave)
          if (F.lt.minF .or. minF.eq.-1.0d0) then
            write(iout,*)'F < Fmin for:'
            minF=F
            do dih=1,Ndih
              write(iout,*) mults(dih)(1:mlen)
              do per=1,Nper(dih)
                bestnp(dih,per)=np(dih,per)
              end do
            end do
            do i=1,Nparms
              bestparms(i)=parms(i)
            end do
            bestK=K
          endif

        end do
        do dih=1,Ndih
          do per=1,Nper(dih)
            np(dih,per)=bestnp(dih,per)
          end do
        end do
c
c       Open optimization output file
c
        call getarg(2,filenm)
        leng = trimtext (filenm)
        iopt=freeunit()
        open(unit=iopt,file=filenm(1:leng),status='new')
        call optsave(0,minF,bestparms)
        close(unit=iopt)
c
c       Open the file to write the final fit
c
        ifit=freeunit()
        open(unit=ifit,file=filenm(1:leng)//'.fit',status='new')
        call writefit(ifit,bestparms)
        close(unit=ifit)

        end
```

File fgvalue.f

```
c
c
c     ################################################################
c     ##                                                            ##
c     ##  function fgvalue  -- find value and gradient of           ##
c     ##                          the objective function            ##
c     ##                                                            ##
c     ################################################################
c
c
c
      function fgvalue (parms,g)
      implicit none
      include 'torsdata.i'
      include 'math.i'
      integer i,j,idih,Nparms
      real*8 parms((5+2*maxper)*maxdih)
      real*8 k_Boltz,T
      real*8 dKdCn(maxdih,5),dKdkp(maxdih,maxper),dKdpp(maxdih,maxper)
      real*8 dfdCn(maxdih,5),dfdkp(maxdih,maxper),dfdpp(maxdih,maxper)
      real*8 Q,DV(maxdat),ang
      real*8 fgvalue,f,g((5+2*maxper)*maxdih)
c
c     Constants & parameters
c
      k_Boltz=0.008314   ! kJ/mol K
      T=298.15           ! K
c
c     Set values of Ryckaert-Bellemans and periodic parameters
c
      i=0
      do dih=1,Ndih
        C0(dih)=0.0d0
        do n=1,5
          i=i+1
          Cn(dih,n)=parms(i)
          C0(dih)=C0(dih)-Cn(dih,n)
        end do
        do per=1,Nper(dih)
          i=i+1
          pp(dih,per)=parms(i)
          i=i+1
          kp(dih,per)=parms(i)
        end do
      end do
      Nparms=i
c
c     Compute sums for the normalization factor Q,
c     K and its derivatives
c
      do dih=1,Ndih
        do n=1,5
          dKdCn(dih,n)=0.0d0
        end do
        do per=1,Nper(dih)
          dKdkp(dih,per)=0.0d0
          dKdpp(dih,per)=0.0d0
        end do
```

```
      end do
      K=0.0d0
      Q=0.0d0
      do dat=1,Ndat
c
c       Compute Boltzmann weight
c
        W(dat)=exp(-V_DFT(dat)/(k_Boltz*T))
        if (W(dat).lt.0.1) then
          W(dat)=0.1
        end if
c
c       Terms independent of dihedral angles
c
        DV(dat)=V_FF0(dat)-V_DIH0(dat)-V_DFT(dat)
c
c       Dihedral interactions
c
        do dih=1,Ndih
          do rep=1,Nrep
c
c           Ryckaert-Bellemans terms
c
            DV(dat)=DV(dat)+C0(dih)
            do n=1,5
              DV(dat)=DV(dat)
     &          +Cn(dih,n)*(cos((dihs(dat,rep,dih)-180.0d0)/radian))**n
            end do
c
c           Periodic terms
c
            do per=1,Nper(dih)
              DV(dat)=DV(dat)
     &          +kp(dih,per)*(1.0d0+cos((np(dih,per)*dihs(dat,rep,dih)
     &          -pp(dih,per))/radian))
            end do
          end do
        end do
c
c       Accumulate shift & normalization constants
c
        K=K+W(dat)*(DV(dat))
        Q=Q+W(dat)
c
c       Shift constant derivatives
c
        do dih=1,Ndih
          do rep=1,Nrep
            do n=1,5
              dKdCn(dih,n)=dKdCn(dih,n)
     &                +W(dat)*(cos((dihs(dat,rep,dih)-
180.0d0)/radian))**n
            end do
            do per=1,Nper(dih)
              dKdkp(dih,per)=dKdkp(dih,per)+W(dat)*(1.0d0+cos(
     &                (np(dih,per)*dihs(dat,rep,dih)-
pp(dih,per))/radian))
              dKdpp(dih,per)=dKdpp(dih,per)+W(dat)*kp(dih,per)*sin(
     &                (np(dih,per)*dihs(dat,rep,dih)-pp(dih,per))/radian)
            end do
          end do
```

```
          end do
        end do
        K=K/Q
        do dih=1,Ndih
          do n=1,5
            dKdCn(dih,n)=dKdCn(dih,n)/Q
          end do
          do per=1,Nper(dih)
            dKdkp(dih,per)=dKdkp(dih,per)/Q
            dKdpp(dih,per)=dKdpp(dih,per)/Q
          end do
        end do
c
c       Now evaluate the objective function and its derivatives
c
        f=0.0d0
        do dih=1,Ndih
          do n=1,5
            dfdCn(dih,n)=0.0d0
          end do
          do per=1,Nper(dih)
            dfdpp(dih,per)=0.0d0
            dfdkp(dih,per)=0.0d0
          end do
        end do
        do dat=1,Ndat
          DV(dat)=DV(dat)-K
          f=f+W(dat)*(DV(dat))**2
          do rep=1,Nrep
            do dih=1,Ndih
              do n=1,5
                dfdCn(dih,n)=dfdCn(dih,n)+2*W(dat)*DV(dat)*((cos(
     &             (dihs(dat,rep,dih)-180.0d0)/radian))**n-dKdCn(dih,n))
              end do
              do per=1,Nper(dih)
                dfdpp(dih,per)=dfdpp(dih,per)+2*W(dat)*DV(dat)*
     &              (kp(dih,per)*sin((np(dih,per)*dihs(dat,rep,dih)
     &              -pp(dih,per))/radian)-dKdpp(dih,per))
                dfdkp(dih,per)=dfdkp(dih,per)+2*W(dat)*DV(dat)*
     &              (1.0d0+cos((np(dih,per)*dihs(dat,rep,dih)
     &              -pp(dih,per))/radian)-dKdkp(dih,per))
              end do
            end do
          end do
        end do
c
c       For the derivative wrt pp, multiply by 180/pi
c
        do dih=1,Ndih
          do per=1,Nper(dih)
            dfdpp(dih,per)=dfdpp(dih,per)/radian
          end do
        end do
c
c       Normalize the function and its derivatives
c
        fgvalue=f/Q
        i=0
        do dih=1,Ndih
          do n=1,5
            i=i+1
```

```
      g(i)=dfdCn(dih,n)/Q
    end do
    do per=1,Nper(dih)
      i=i+1
      g(i)=dfdpp(dih,per)/Q
      i=i+1
      g(i)=dfdkp(dih,per)/Q
    end do
  end do

  return

  end
```

APPENDIX D

ADJUSTMENTS TO BOND AND ANGLE PARAMETERS

This appendix outlines the adjustments made to the bond and angle parameters in PLAFF2. The set of bonds and angles shown here were selected because they deviated from the values in the crystal structure analysis, as well as the equilibrium positions predicted by DFT. The DFT calculations, plotted in the following figures, were carried out at the B3-LYP/6-31G** level using the PLA molecule in Figure 4.4. Similar to the fitting procedure for the dihedral energy parameters described in Chapter Five, constrained geometry optimizations were used to obtain the DFT energy, and again for the force field energy prior to each force field parameter adjustment.

DFT methods are generally known to give accurate geometries, while they are less accurate at predicting vibrational frequencies [*246*]. For this reason, each of the following interactions were fit to DFT data by adjusting the geometric parameters (the b_0 parameter for bonds, and the θ_0 parameter for angles) only; the force constants (k_b and k_θ) were unaltered from their original OPLS values. In this way, we deviate as little as possible from the OPLS model. Fitting each bond or angle interaction requires the use of Picard iteration, much like that described in fitting dihedral potentials in Section 5.2.3.1. For each of the nine bonds and angles shown below, a total of ten Picard iterations was sufficient achieve self-consistent convergence.

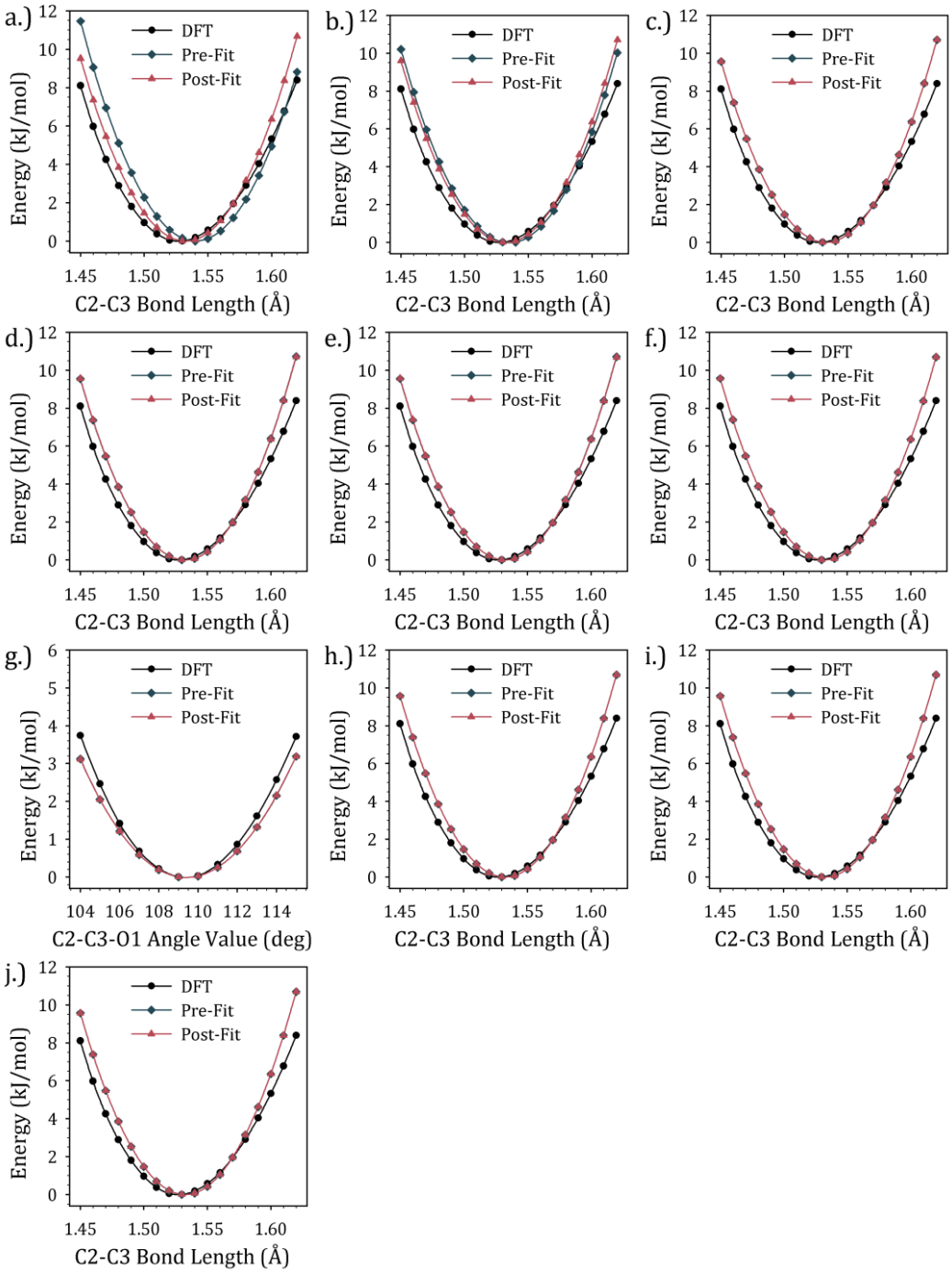

Figure D.1. Bond stretching energies for C2-C3 as defined in Figure 5.2. Plots a-j show the energy before and after each of ten Picard iterations.

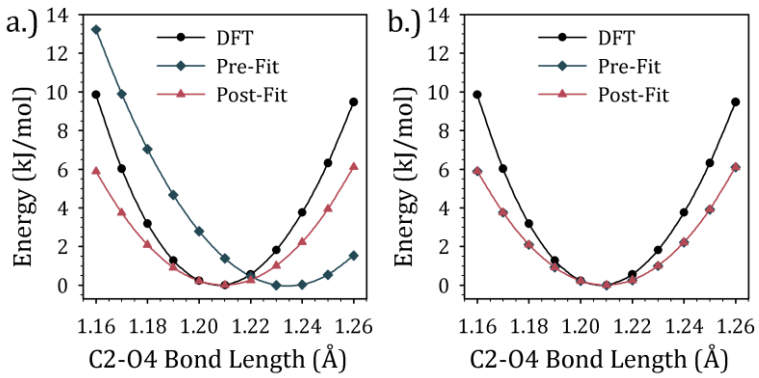

Figure D.2. Bond stretching for C2-O4. a.) first Picard iteration; b.) tenth iteration.

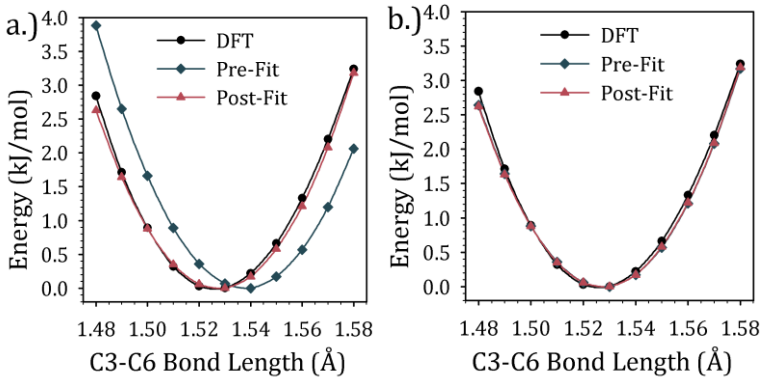

Figure D.3. Bond stretching for C2-O4. a.) first Picard iteration; b.) tenth iteration.

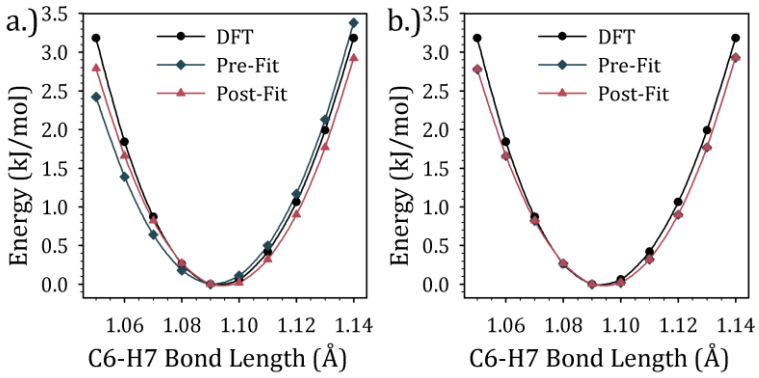

Figure D.4. Bond stretching for C2-O4. a.) first Picard iteration; b.) tenth iteration.

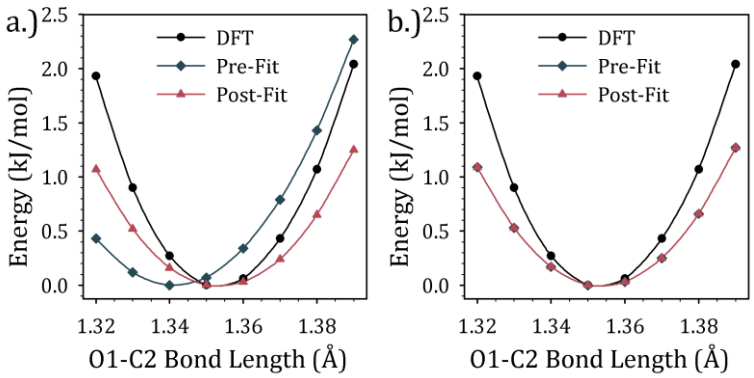

Figure D.5. Bond stretching for C2-O4. a.) first Picard iteration; b.) tenth iteration.

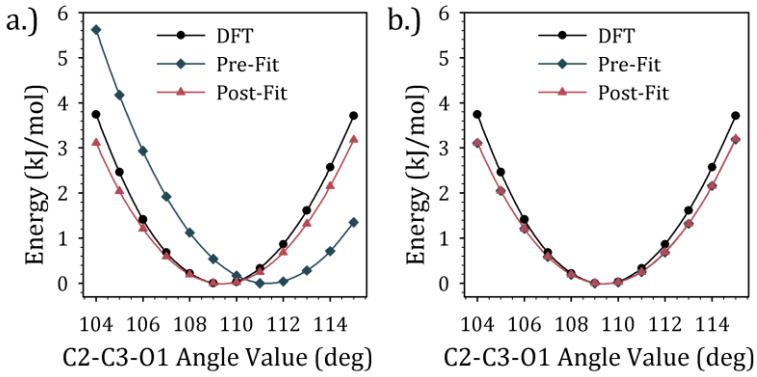

Figure D.6. Angle bending for C2-C3-O1. a.) first Picard iteration b.) tenth iteration.

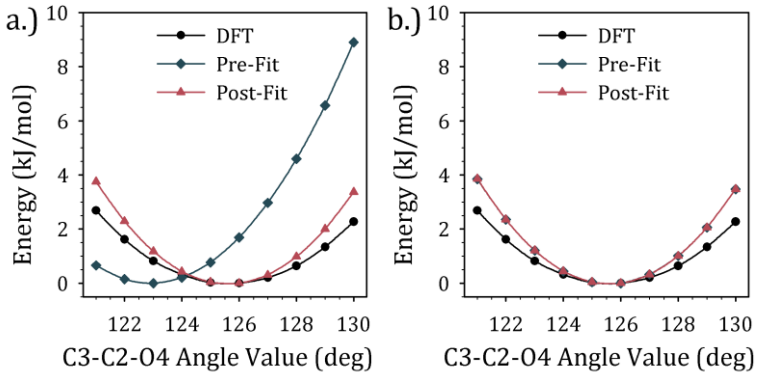

Figure D.7. Angle bending for C2-C3-O1. a.) first Picard iteration b.) tenth iteration.

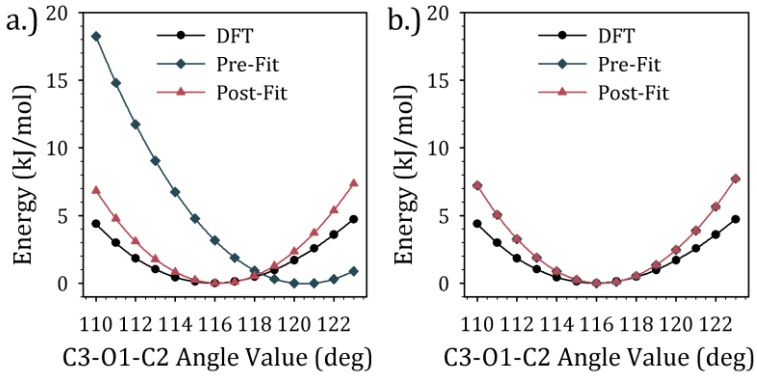

Figure D.8. Angle bending for C2-C3-O1. a.) first Picard iteration b.) tenth iteration.

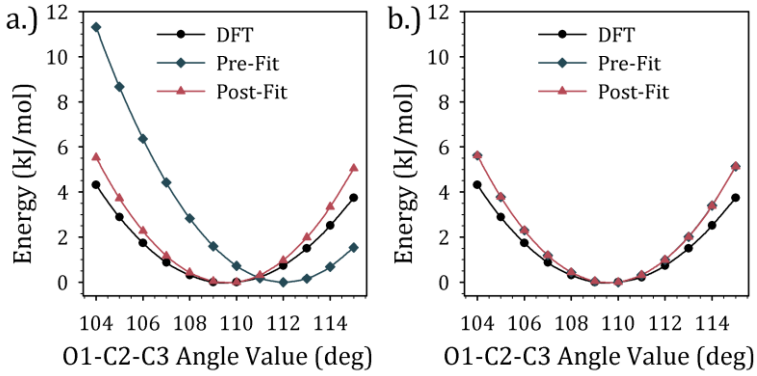

Figure D.9. Angle bending for C2-C3-O1. a.) first Picard iteration b.) tenth iteration.

Table D.1. Bond stretching parameters for the bonds adjusted in Figures D.1 through D.5. Force constants from OPLS were used in this work; initial bond lengths are from OPLS, and reported values for this work are after 10 Picard iterations. CHARMM parameters are shown for comparison.

	This Work	OPLS		CHARMM	
Bond	b_0 (Å)	b_0 (Å)	k_b (kJ/mol nm^2)	b_0 (Å)	k_b (kJ/mol nm^2)
C2-C3	1.5109	1.5136	265265.6	1.522	167360
C2-O4	1.2017	1.2290	476976.0	1.220	627600
C3-C6	1.5178	1.5290	224262.4	1.538	186190
C6-H7	1.0929	1.0900	284512.0	1.111	269450
O1-C2	1.3217	1.3270	179075.2	1.334	125520

Table D.2. Angle bending parameters for the angles adjusted in Figures D.6 through D.9. Force constants from OPLS were used in this work; initial angle values are from OPLS, and reported values for this work are after 10 Picard iterations. CHARMM harmonic angle parameters are shown for comparison.

	This Work	OPLS		CHARMM	
Angle	θ_0 (deg)	θ_0 (deg)	k_θ (kJ/mol rad^2)	θ_0 (deg)	k_θ (kJ/mol rad^2)
C2-C3-O1	105.58	109.50	418.400	111.14	633.4576
C3-C2-O4	128.90	120.40	669.440	125.00	585.7600*
C3-O1-C2	108.84	116.90	694.544	109.60	334.7200*
O1-C2-C3	113.04	111.40	677.808	109.00	460.2400*

*These angle types have additional Urey-Bradley interactions

APPENDIX E

PAIR INTERACTIONS IN THE OPLS AND CHARMM FORCE FIELDS

The figures in this appendix show the pairwise interactions between atoms in the PLA repeat unit (Figure 5.2), as calculated with the OPLS and CHARMM atom types assigned in Table 5.1. These plots were used to ascertain which atom types might be altered in terms of their nonbonded parameters. In each figure, the total nonbonded energy (Coulomb + van der Waals) is plotted for the atom pair. For those pairs with attractive electrostatic interaction, the separation length at the nonbonded energy minimum is indicated.

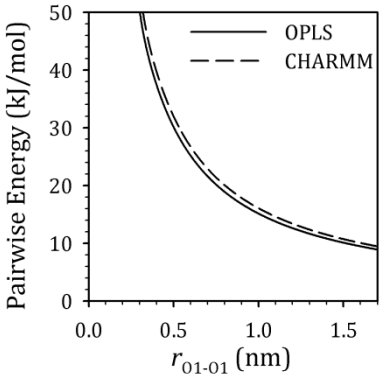

Figure E.1. Total nonbonded interaction energy for a pair of O1 atoms.

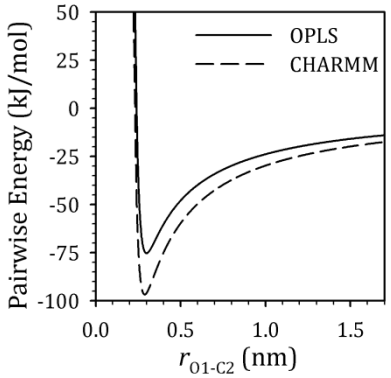

Figure E.2. Total nonbonded interaction energy for atoms O1 and C2.

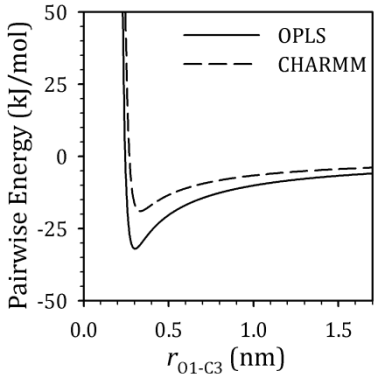

Figure E.3. Total nonbonded interaction energy for atoms O1 and C3.

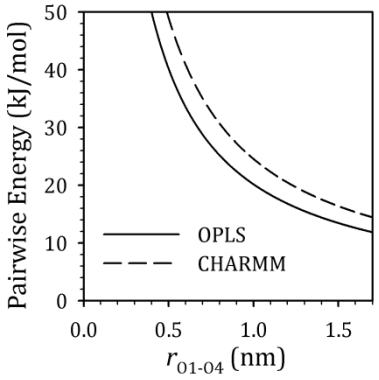

Figure E.4. Total nonbonded interaction energy for atoms O1 and O4.

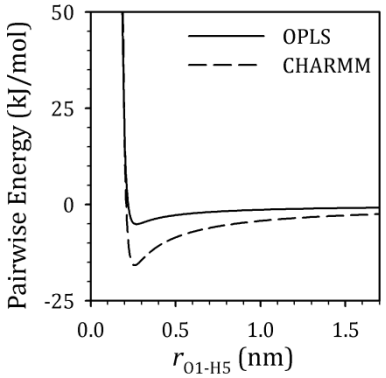

Figure E.5. Total nonbonded interaction energy for atoms O1 and H5.

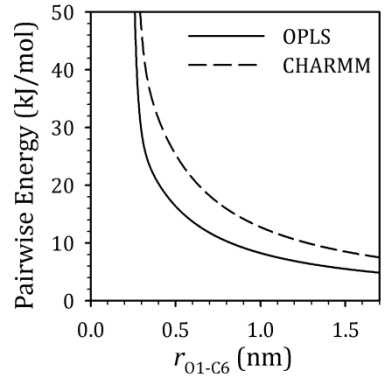

Figure E.6. Total nonbonded interaction energy for atoms O1 and C6.

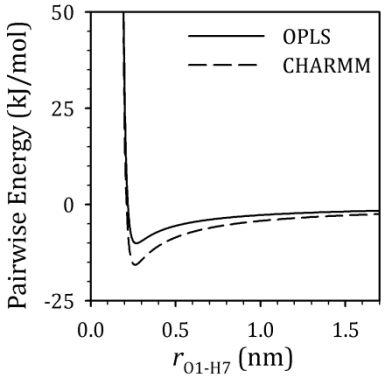

Figure E.7. Total nonbonded interaction energy for atoms O1 and H7.

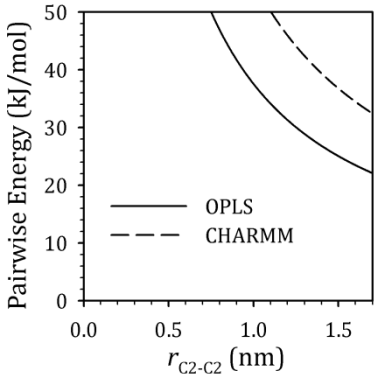

Figure E.8. Total nonbonded interaction energy for a pair of C2 atoms.

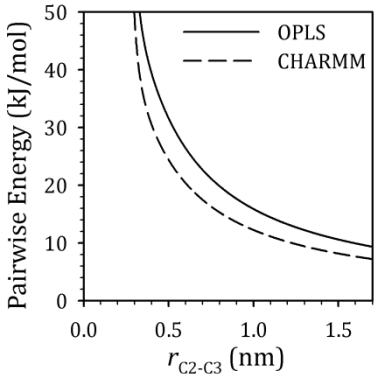

Figure E.9. Total nonbonded interaction energy for atoms C2 and C3.

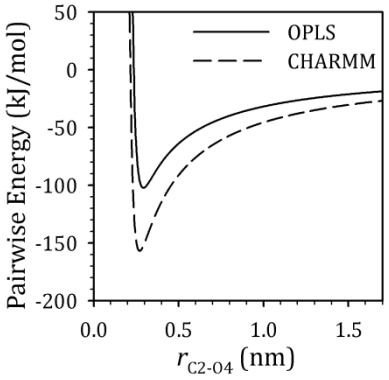

Figure E.10. Total nonbonded interaction energy for atoms C2 and O4.

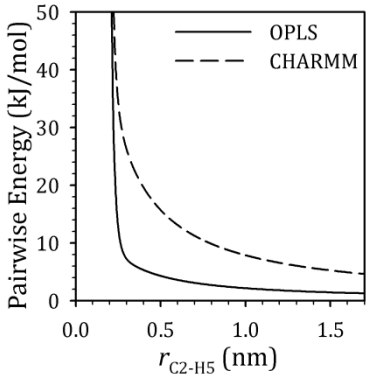

Figure E.11. Total nonbonded interaction energy for atoms C2 and H5.

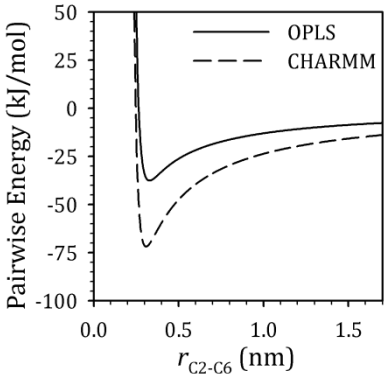

Figure E.12. Total nonbonded interaction energy for atoms C2 and C6.

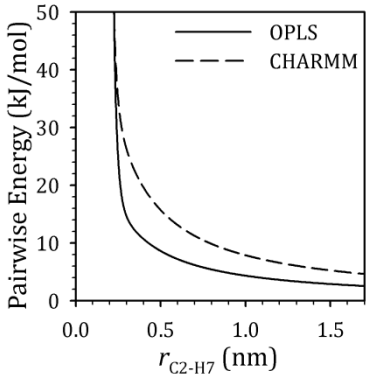

Figure E.13. Total nonbonded interaction energy for atoms C2 and H7.

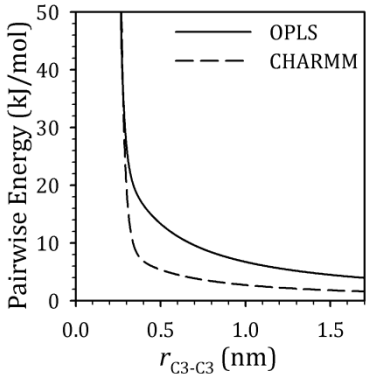

Figure E.14. Total nonbonded interaction energy for a pair of C3 atoms.

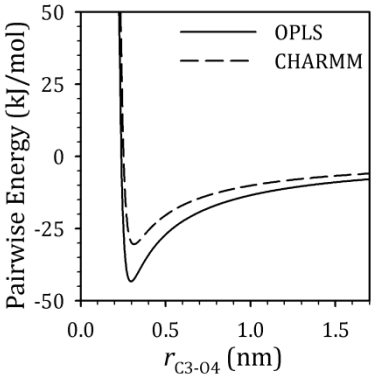

Figure E.15. Total nonbonded interaction energy for atoms C3 and O4.

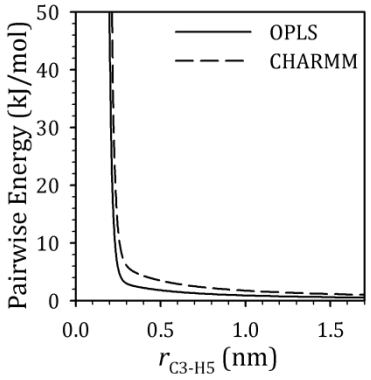

Figure E.16. Total nonbonded interaction energy for atoms C3 and H5.

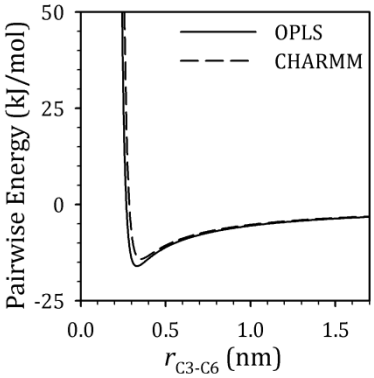

Figure E.17. Total nonbonded interaction energy for atoms C3 and C6.

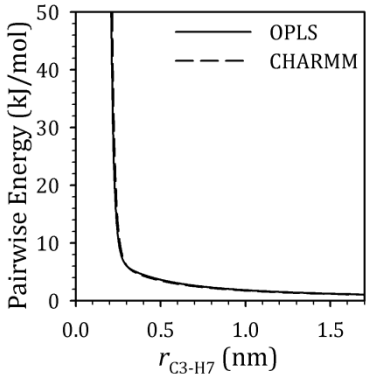

Figure E.18. Total nonbonded interaction energy for atoms C3 and H7.

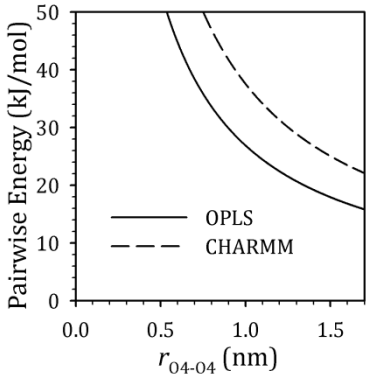

Figure E.19. Total nonbonded interaction energy for a pair of O4 atoms.

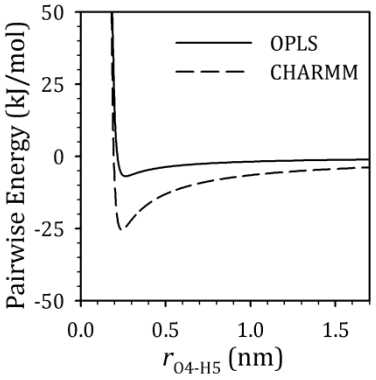

Figure E.20. Total nonbonded interaction energy for atoms O4 and H5.

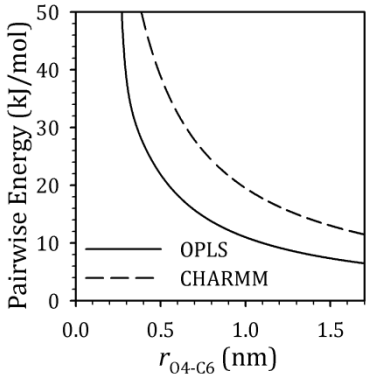

Figure E.21. Total nonbonded interaction energy for atoms O4 and C6.

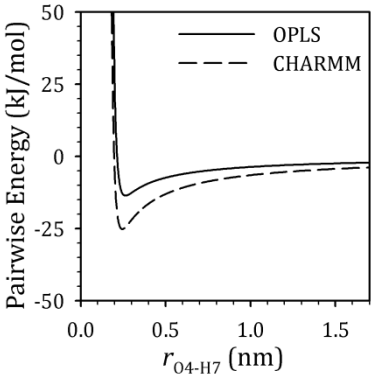

Figure E.22. Total nonbonded interaction energy for atoms O4 and H7.

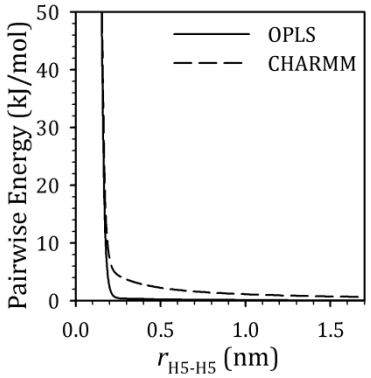

Figure E.23. Total nonbonded interaction energy for a pair of H5 atoms.

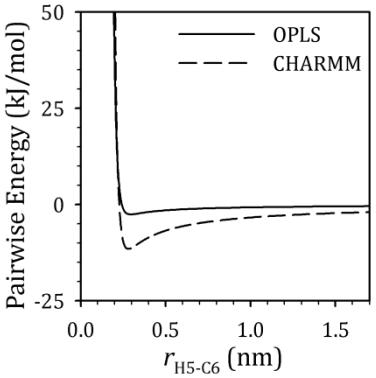

Figure E.24. Total nonbonded interaction energy for atoms H5 and C6.

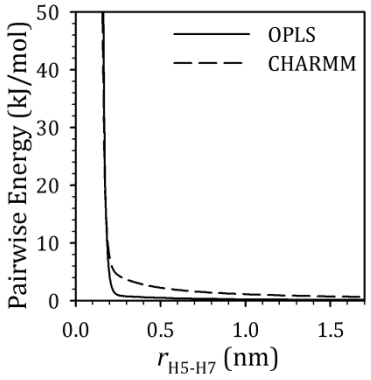

Figure E.25. Total nonbonded interaction energy for atoms H5 and H7.

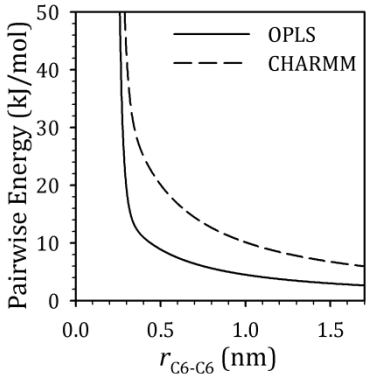

Figure E.26. Total nonbonded interaction energy for a pair of C6 atoms.

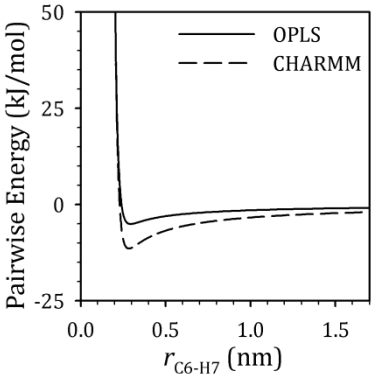

Figure E.27. Total nonbonded interaction energy for atoms C6 and H7.

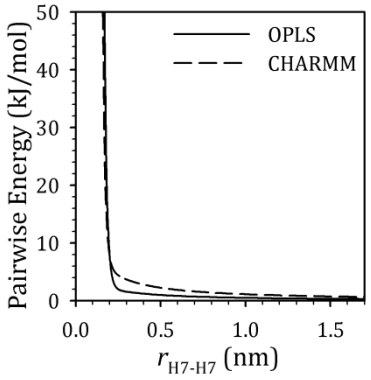

Figure E.28. Total nonbonded interaction energy for a pair of H7 atoms.

APPENDIX F

SCRIPTS AND SMALL PROGRAMS

Various scripts used for automating data acquisition and analysis in this work are included as part of the electronic media that accompanies this dissertation. While these are not documented in full, the interested reader may consult the README file for a working description of each program. The files are in a .tar.gz archive, which may be extracted on a Linux computer by placing the file in the current working directory and issuing the command:

```
> tar –xvzf ./McAlileyDissertation_Supplemental.tar.gz
```

APPENDIX G

BUILDING A LINUX CLUSTER

Most of the computational results in this dissertation were obtained using clusters of commodity processors running the Linux operating system. This is an economical way to increase computing speed with readily-available components, and is currently one of the most common paradigms in scientific computing. In this chapter, we briefly describe how to set up a Linux cluster using PCs and Ethernet. The cluster hardware, shown schematically in Figure G.1, consists of:

- A head node, to which users may login remotely
- Several compute nodes, which run computational tasks
- A fileserver, to store common data files
- A network switch (usually Ethernet), to relay network traffic
- Network (Ethernet) cables, to connect the hardware together

In this configuration, the head node is required to have two Ethernet interfaces: one for communicating with compute nodes and the fileserver (labeled eth0), and one for communicating with the internet (eth1). All other nodes are required to have one network interface. The network switch, to which all nodes are connected, should only be configured for basic switching capabilities. All routing is handled by the head node.

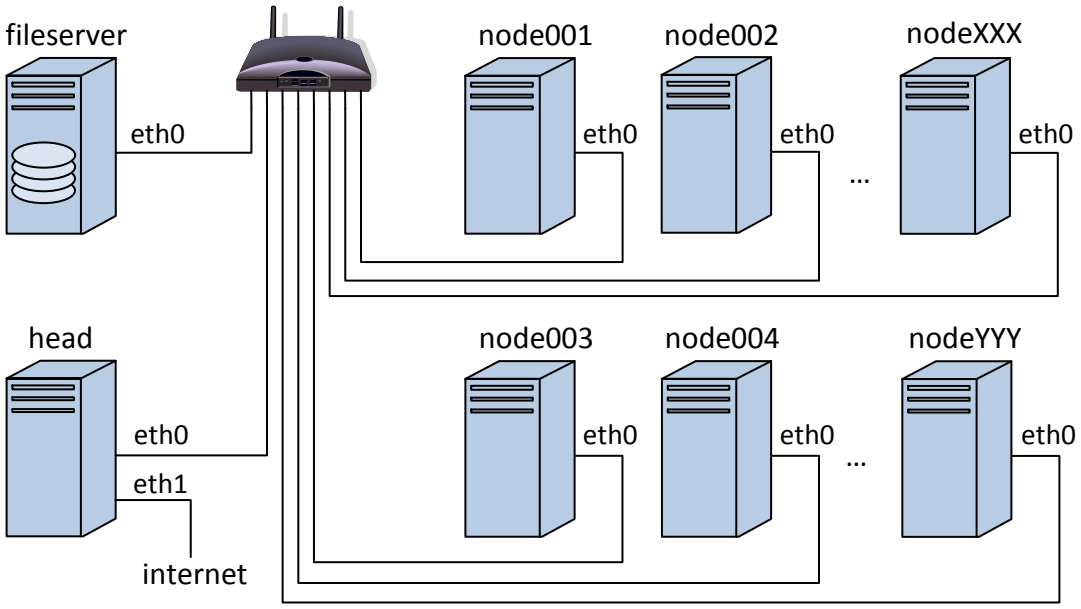

Figure G.1. Hardware layout in a typical Linux cluster. Lines connecting the components are physical network cables.

There are many software packages which must be installed and configured on each node to operate the cluster, including:

- A Linux operating system, such as Centos, Debian, Fedora, Ubuntu, Red Hat, or, SUSE.
- The Dynamic Host Configuration Protocol (DHCP), for assigning network addresses
- BIND, a version of the Domain Name System (DNS), for domain name resolution
- The Network Information Service (NIS), for managing passwords globally

- Remote Shell (RSH) or Secure Shell (SSH) protocols for logging in to each node remotely
- The Network File System (NFS) protocol, for accessing files from multiple nodes
- The Network Time Protocol (NTP), for synchronizing system clocks
- An iptables-based firewall, for blocking unwanted network requests
- Torque, a freely distributed version of the Portable Batch System (PBS), for assigning compute tasks to nodes
- MPICH, a freely distributed version of the Message Passing Interface (MPI), for compiling and running parallel software

Other software may also be needed. The specific configuration of each of these software packages is dependent on the Linux distribution chosen. Each distribution will have different locations for the various files and binaries, and will have different software versions for each component. Therefore, in this chapter we give a brief overview of what needs to be configured on each node in the cluster, without specific details of how to do it. There are many books and websites that discuss these topics in detail. The books by Frisch [*247*], Liu and Albitz [*248*], and Stern, Eisler, and Labiaga [*249*] are excellent resources.

§ G.1. Linux

The choice of a Linux distribution will affect many aspects of cluster operation. In general, no one distribution is much better than the others for cluster applications; they all have their strengths and weaknesses. The decision should be based on the experience level of the system administrator, the features needed, and your organization's operating budget. For those new to Linux, we strongly recommend obtaining a supported operating system such as Red Hat Enterprise Linux (RHEL) or SUSE. Though you will have to buy a subscription to support services, it will likely save you time and headaches by giving you access to expert help. Of the free operating systems, Ubuntu is probably the most user-friendly version of Linux available today. Users with some Linux experience, who require the absolute latest versions of software and libraries, should consider the latest Fedora Core distribution. There is a trade-off, however, when going with a "bleeding edge" distribution, such as Fedora Core. You are likely to encounter many more bugs with newer software, and also you must vigilantly update the software to prevent security vulnerabilities. More stable alternatives, such as Debian and CentOS (CentOS is based on RHEL but without the Red Hat branding) require less updates and are less likely to cause mischief due to bugs.

Linux should be loaded on each node in the cluster. With most distributions, installation media can be downloaded and transferred to a CD, DVD, or USB disk. Installation is usually as simple as booting with the installation media and answering several questions on the computer screen. Most of the process will be automated, but

after installing, it is worth checking that appropriate kernel packages were loaded. One should especially check that SMP kernel modules are present, in the case when each node has multiple processors.

After installation of the operating system, most Linux distributions come with a package manager for installing, removing, or modifying software. For proprietary distributions, such as RHEL and SUSE, the user is required to authenticate the computer before the package manager can be used; for free distributions, such as CentOS or Debian, all that is required is an internet connection. Package managers can have a graphical user interface (GUI), such as Synaptic (Ubuntu), or be command-line driven, such as apt-get/aptitude (Debian), and yum (CentOS/RHEL). Some operating systems even allow multiple package managers to be used.

For all of the software services discussed in this appendix, the system administrator should verify that the services (often in the form of background processes, or *daemons*) are started automatically when the system boots. This avoids having to manually start the processes every time the cluster is rebooted. On most Linux systems, there is a list of boot scripts in the /etc/init.d/ directory. The directories named /etc/rc.X.d/, in turn, contain many symbolic links to the boot scripts, indicating whether the individual script should be used in the run level indicated by X.

§ G.2. Dynamic Host Configuration Protocol (DHCP)

The DHCP service is responsible for assigning unique *network addresses* (commonly, *internet protocol* or simply *ip* addresses), which distinguish each computer

in the system. For local networks, the network addresses are usually numbers in the form 192.168.x.y, where the numbers x and y between dots are in the range 0 to 255. These ip addresses can be reassigned as needed by the DHCP server. Each hardware interface, on the other hand, has a unique number assigned to it by the manufacturer. It is a string of six hexadecimal numbers called the *hardware address* or *MAC address*.

Networks that are managed by DHCP are much easier to maintain than networks in which ip addresses are manually assigned to individual machines. In the DHCP system, each host sends a request over the network to obtain a *lease* on an ip address. The DHCP server grants this lease for a set period of time, after which the host must renew the lease. Depending on the configuration, the server may choose a new ip address or assign the same one to the host. For clustering, it is best to configure the server to always assign each host the same ip address, which is usually done by adding a list of hardware addresses in the server's DHCP file. Consult the documentation provided in your specific DHCP implementation to learn how to do this.

Some network switches include a DHCP server, which may be the easiest solution for many people. However, there are numerous reasons why it may be preferable to have the DHCP server run from one of the Linux-based hosts in the cluster. For a cluster as shown in Figure G.1, it is best to choose the head node or the file server as the DHCP server. If the head node is chosen to handle DHCP requests, make sure that it handles the requests through the eth0 network interface, since the other interface is not connected to the cluster's local network.

§ G.3. Domain Name System (DNS)

The DNS utility included in most Linux distributions is BIND. DNS allows you to match human-readable names, such as *head.mycluster* or *fileserver.mycluster*, with the ip addresses of specific hosts. In Figure G.1, the head node is probably the best choice to be used as the DNS server. It should be configured to resolve the host names of all nodes on the local network, and to relay DNS requests for names outside the local network to its internet DNS server. In this case, it is assumed that the head node also routes traffic requests from the local hosts to the internet. This is usually set up with the route command. See Frisch for more information on configuring routing [*247*], and, as always, consult the documentation supplied with your particular Linux distribution. DNS is discussed in depth by Liu and Albitz [*248*].

§ G.4. Network Information Service (NIS)

All user accounts and groups active on the cluster nodes can be handled globally using NIS. This prevents having to create the same user account multiple times on every node, and keeps users from having to change their passwords individually on each node. In the cluster setup shown in Figure G.1, it is probably best to use the fileserver as the NIS master. Access to the fileserver is not needed by normal users, and can be prevented by properly configuring SSH and RSH, and the firewall. This presents a security advantage, since any potential attackers would have to hack through an additional firewall to manipulate the NIS settings. Refer to Stern et al. for details on

setting up NIS [*249*]. Note that, on most systems, users should use the 'yppasswd' command to change their passwords on the head node instead of the usual 'passwd' command. Likewise, 'ypchsh' and 'ypchfn' should be used to change the user's login shell and full name on the system (these commands are prefixed with 'yp' because the original name of NIS was Yellow Pages; this was later changed due to copyright infringement).

§ G.5. Remote Shell (RSH) and Secure Shell (SSH)

Though RSH is still in use, many administrators prefer to use the encrypted SSH protocol for security purposes. This should be considered depending on the security level desired. For a small cluster with only a few users, RSH can be used without a problem. Both protocols can be setup to allow login to the compute nodes without prompting for passwords. With SSH, it is worthwhile to learn to setup SSH keys for security purposes. Passwordless logins are usually needed if the cluster is to be used in batch mode, as is commonly the case. When the batch job scheduler permits a job to run on the compute nodes, the user is not around to type in a password.

§ G.6. Network File System (NFS)

Networked storage is a convenient way to access files in a global location from all nodes on the network. In this way, each compute node can read or write to the same disk, as if it were a disk attached directly to the node. In our example cluster, Figure G.1,

we have a dedicated node that acts as the file server. This node allows all other nodes in the cluster to access specified file locations through network requests.

Typically, the file server is outfitted with a large amount of disk storage, which is easily implemented as a redundant array of independent disks (RAID). There are several RAID levels, including fully redundant (RAID0), and parity bit schemes (e.g., RAID5). Parity bit schemes are currently popular as only one disk in the array is redundant. This maximizes the storage capacity, and still protects data if any one disk were to fail.

If intensive reading or writing is needed on the network storage, the network interface and switch should be sized appropriately for the network traffic. Also, the disks themselves, and the hardware interface to the disk array, must also be fast enough to handle the desired read/write speeds. For read/write intensive programs, it is often better to read from and write to a *scratch* directory, which physically exists on the compute node. At the end of the program, necessary results can be copied to network storage and the scratch files deleted.

NFS is relatively easy to set up. On the file server, a configuration file is edited to specify what location(s) on the file server should be shared. Then, on each other node in the cluster, a mount point is defined (usually in the /etc/fstab file), and an NFS option is specified for the mount point. Consult the documentation provided with your version of NFS, or see the book by Stern et al. [*249*] for details.

§ G.7. Network Time Protocol (NTP)

It is important that the system clocks on all compute nodes be synchronized, especially when NFS file resources are being used. Every file has a time stamp, giving the date at which it was modified. If the system clocks are not synchronized between nodes, it is possible that a node will request an NFS file that has a time stamp that appears to be in the future, relative to the requesting node's system time. This is not allowed and will result in an error on most systems. There are various other examples of how unsynchronized system clocks can cause trouble in a cluster.

The NTP daemon periodically checks with a *time server*, then adjusts the local system time to match. The protocol accounts for latency in the network communication when adjusting the time, since there is always some lag between the time at which the time server receives an NTP request and the time at which the local host receives the time transmitted by the server. Thus, the less network latency between the time server and the local host, the more accurate the synchronization. Most workstation computers connect to time servers over the internet (e.g., at pool.ntp.org), but for clusters it is preferable to define a time server on the local network to reduce latency. In our example cluster (Figure G.1), the time server role can be equally met by the head node or the file server. The NTP server software should be installed on the selected host, and all other nodes on the network should have the NTP client software installed. For the client nodes, the time server is usually specified in a configuration file. Consult the NTP documentation on how to set up the server and hosts.

§ G.8. Firewall

A good firewall will limit access to your cluster and increase the security of the network. Processes send network requests using a *transport layer* protocol, such as UDP or TCP. These use numbered *ports* to specify connections between computers. Using a firewall program, such as iptables, it is possible to deny access to specific ports based on the credentials of the request. In this way, one can prevent logins to certain nodes (e.g., the file server) by unwanted users and block a multitude of other attacks.

§ G.9. Batch Scheduler

Most clusters are used in *batch mode*, where users log into the head node, specify that they want to run a program on a certain number of nodes, and then the system schedules the job to run as soon as the resources become available. This optimizes use of the cluster, since jobs may be run around the clock instead of only during peak times of the day. A popular batch system is the Portable Batch System, or PBS. This began as an open source project, and eventually evolved into the proprietary software PBSPro. Currently, another popular PBS-based alternative is *Torque*, offered free of charge by Cluster Resources, Inc. (www.clusterresources.com).

The components of Torque include the job scheduler daemon, pbs_server, and the client daemon, pbs_mom. The Torque server should be the node from which users will submit jobs. In the case of Figure G.1, the head node is the server. The server is configured with a list of host names to which jobs may be submitted, and continually

monitors these hosts to assess their resource usage. The client daemon should be configured on each of the compute nodes to specify a local spool directory and accept job requests from the head node. The Cluster Resources website has plenty of documentation on further configuration details. Advanced scheduling capabilities can be added by installing the Maui software (also distributed freely by Cluster Resources).

§ G.10. Message Passing Interface (MPI)

One common platform for parallelizing computer programs over networked resources is the MPI protocol. The MPICH and MPICH2 implementations, developed at Argonne National Labs, are especially popular among Linux users. MPI provides libraries that handle the network communication details and are relatively simple to use. Simple computer codes may be parallelized with the addition of a few simple instruction lines. Binaries must be compiled with the MPI compilers, and they must be run using the appropriate wrapper program (usually called mpirun or mpiexec). When using MPI with a batch scheduler, such as PBS, it is important to specify the nodes on which the program is to be run. If using MPICH2 and Torque, this can be done by specifying the option `-machinefile $PBS_NODEFILE` to mpirun. Here, $PBS_NODEFILE is an environment variable that is set by the job scheduler.

§ G.11. Other Software and Considerations

This appendix has covered most of the important software needed to run a Linux-based computer cluster. There are, of course, many more useful software

packages that exist. It may be useful, for example, to monitor cluster usage using the web-based graphical logging system Ganglia (www.sourceforge.net/projects/ganglia). If you have many compute nodes in the system, it may be useful to configure one node and use a utility such as SystemImager (www.sourceforge.net/projects/systemimager) to easily load the same configuration on the remaining nodes. On the other hand, specific operating systems can be used, such as MOSIX (www.mosix.org) or Rocks (www.rocksclusters.org). With the recent rise in multicore computer processors, virtualization software can be used to make better use of cluster resources.

While it is likely that the information in this appendix will soon be outdated, it is meant to emphasize that powerful computing resources can be built, with a limited budget and limited expertise. Still, taking on the construction, configuration, and maintenance of a large computer cluster is not a task to be underestimated. It is best done by a person with expertise and experience in the field, and is not suited for the average molecular scientist or engineer. If your organization does not have access to computing facilities, we suggest applying for access to one of the many supercomputing centers around the country, such as the San Diego Supercomputing Center (www.sdsc.org) or the Teragrid (www.teragrid.org). Currently, Clemson University is making strides to become such a computing powerhouse, and we are grateful to have access to the computing systems and support staff here.

APPENDIX H

REFERENCES

[*1*] Sinclair, R. G., "The case for polylactic acid as a commodity packaging plastic". *Journal of Macromolecular Science-Pure and Applied Chemistry*, **A33** (5), 585 (1996).

[*2*] Hakkarainen, M., *Aliphatic Polyesters: Abiotic and Biotic Degradation and Degradation Products*. 2001; pp. 113-138.

[*3*] Mueller, R. J., "Biological degradation of synthetic polyesters - Enzymes as potential catalysts for polyester recycling". *Process Biochemistry*, **41** (10), 2124 (2006).

[*4*] *Municipal Solid Waste Generation, Recycling, and Disposal in the United States: Facts and Figures for 2006*; U.S. Environmental Protection Agency: Washington, D.C., 2007.

[*5*] Vink, E. T. H.; Rabago, K. R.; Glassner, D. A.; Springs, B.; O'Connor, R. P.; Kolstad, J.; Gruber, P. R., "The sustainability of NatureWorks (TM) polylactide polymers and Ingeo (TM) polylactide fibers(a): an update of the future". *Macromolecular Bioscience*, **4** (6), 551 (2004).

[*6*] Lam, K. H.; Nijenhuis, A. J.; Bartels, H.; Postema, A. R.; Jonkman, M. F.; Pennings, A. J.; Nieuwenhuis, P., "Reinforced Poly(L-Lactic Acid) Fibers as Suture Material". *Journal of Applied Biomaterials*, **6** (3), 191 (1995).

[*7*] Mikos, A. G.; Sarakinos, G.; Leite, S. M.; Vacanti, J. P.; Langer, R., "Laminated 3-Dimensional Biodegradable Foams for Use in Tissue Engineering". *Biomaterials*, **14** (5), 323 (1993).

[*8*] Vert, M.; Schwach, G.; Engel, R.; Coudane, J., "Something new in the field of PLA/GA bioresorbable polymers?" *Journal of Controlled Release*, **53** (1-3), 85 (1998).

[*9*] Auras, R.; Harte, B.; Selke, S., "An overview of polylactides as packaging materials". *Macromolecular Bioscience*, **4** (9), 835 (2004).

[*10*] Baiardo, M.; Frisoni, G.; Scandola, M.; Rimelen, M.; Lips, D.; Ruffieux, K.; Wintermantel, E., "Thermal and mechanical properties of plasticized poly(L-lactic acid)". *Journal of Applied Polymer Science*, **90** (7), 1731 (2003).

[*11*] Kenawy, E. R.; Bowlin, G. L.; Mansfield, K.; Layman, J.; Simpson, D. G.; Sanders, E. H.; Wnek, G. E., "Release of tetracycline hydrochloride from electrospun poly(ethylene-co-vinylacetate), poly(lactic acid), and a blend". *Journal of Controlled Release*, **81** (1-2), 57 (2002).

[*12*] Agashe, M.; Raut, V.; Stuart, S. J.; Latour, R. A., "Molecular simulation to characterize the adsorption behavior of a fibrinogen gamma-chain fragment". *Langmuir*, **21** (3), 1103 (2005).

[*13*] Raut, V. P.; Agashe, M. A.; Stuart, S. J.; Latour, R. A., "Molecular dynamics simulations of peptide-surface interactions". *Langmuir*, **21** (4), 1629 (2005).

[*14*] Sun, Y.; Welsh, W. J.; Latour, R. A., "Prediction of the orientations of adsorbed protein using an empirical energy function with implicit solvation". *Langmuir*, **21** (12), 5616 (2005).

[*15*] Flory, P. J., *Principles of Polymer Chemistry*. Cornell University Press: Ithaca, New York, 1953.

[*16*] Painter, P. C.; Coleman, M. M., *Fundamentals of Polymer Science: An Introductory Text*. 2nd ed. CRC Press: Boca Raton, 1997.

[*17*] Odian, G., *Principles of Polymerization*. 4th ed. Wiley: Hoboken, NJ, 2004; p 1.

[*18*] Kolstad, J. J.; Witzke, D. R.; Hartmann, M. H.; Hall, E. S.; Nangeroni, J., *Lactic Acid Residue Containing Polymer Composition and Product Having Improved Stability, and Method for Preparation and Use Thereof*. United States Patent 6,353,086, March 5, 2002.

[*19*] Sperling, L. H., *Introduction to Physical Polymer Science*. 4th ed. Wiley: Hoboken, NJ, 2006.

[*20*] Flory, P. J., *Statistical Mechanics of Chain Molecules*. Wiley: New York, 1969; p 1.

[*21*] Sperling, L. H., *Introduction to Physical Polymer Science*. 4th ed. Wiley: Hoboken, NJ, 2006; pp. 199,207,213.

[*22*] Flory, P. J., *Statistical Mechanics of Chain Molecules*. Wiley: New York, 1969; p 11.

[*23*] Dorgan, J. R.; Janzen, J.; Knauss, D. M.; Hait, S. B.; Limoges, B. R.; Hutchinson, M. H., "Fundamental solution and single-chain properties of polylactides". *Journal of Polymer Science Part B-Polymer Physics*, **43** (21), 3100 (2005).

[*24*] Flory, P. J., *Principles of Polymer Chemistry*. Cornell University Press: Ithaca, New York, 1953; pp. 404-409.

[*25*] Painter, P. C.; Coleman, M. M., *Fundamentals of Polymer Science: An Introductory Text*. 2nd ed. CRC Press: Boca Raton, 1997; pp. 330-335.

[*26*] Stockmayer, W. H.; Fixman, M., "On the estimation of unperturbed dimensions from intrinsic viscositiesxcin". *Journal of Polymer Science Part C: Polymer Symposia*, **1** (1), 137 (1963).

[*27*] Flory, P. J., *Principles of Polymer Chemistry*. Cornell University Press: Ithaca, New York, 1953; pp. 612-613.

[*28*] Lee, J. S.; Lee, H. K.; Kim, S. C., "Thermodynamic parameters of poly(lactic acid) solutions in dialkyl phthalate". *Polymer*, **45**, 4491 (2004).

[*29*] Painter, P. C.; Coleman, M. M., *Fundamentals of Polymer Science: An Introductory Text*. 2nd ed. CRC Press: Boca Raton, 1997; p 209.

[*30*] Painter, P. C.; Coleman, M. M., *Fundamentals of Polymer Science: An Introductory Text*. 2nd ed. CRC Press: Boca Raton, 1997; p 292.

[*31*] Painter, P. C.; Coleman, M. M., *Fundamentals of Polymer Science: An Introductory Text*. 2nd ed. CRC Press: Boca Raton, 1997; pp. 293-297.

[*32*] Sperling, L. H., *Introduction to Physical Polymer Science*. 4th ed. Wiley: Hoboken, NJ, 2006; pp. 381-397.

[*33*] Painter, P. C.; Coleman, M. M., *Fundamentals of Polymer Science: An Introductory Text*. 2nd ed. CRC Press: Boca Raton, 1997; p 294.

[*34*] Sperling, L. H., *Introduction to Physical Polymer Science*. 4th ed. Wiley: Hoboken, NJ, 2006; pp. 381-382.

[*35*] Fox, T. G.; Flory, P. J., "Second-Order Transition Temperatures and Related Properties of Polystyrene. I. Influence of Molecular Weight". *Journal of Applied Physics*, **21** (6), 581 (1950).

[*36*] Fox, T. G.; Flory, P. J., "The glass temperature and related properties of polystyrene. Influence of molecular weight". *Journal of Polymer Science*, **14** (75), 315 (1954).

[*37*] Simha, R.; Boyer, R. F., "On a General Relation Involving the Glass Temperature and Coefficients of Expansion of Polymers". *The Journal of Chemical Physics*, **37** (5), 1003 (1962).

[*38*] Williams, M. L.; Landel, R. F.; Ferry, J. D., "The Temperature Dependence of Relaxation Mechanisms in Amorphous Polymers and Other Glass-forming Liquids". *J. Am. Chem. Soc.*, **77** (14), 3701 (1955).

[*39*] Doolittle, A. K., "Studies in Newtonian Flow. II. The Dependence of the Viscosity of Liquids on Free-Space". *Journal of Applied Physics*, **22** (12), 1471 (1951).

[*40*] Painter, P. C.; Coleman, M. M., *Fundamentals of Polymer Science: An Introductory Text*. 2nd ed. CRC Press: Boca Raton, 1997; p 297.

[*41*] Sperling, L. H., *Introduction to Physical Polymer Science*. 4th ed. Wiley: Hoboken, NJ, 2006; p 387.

[*42*] Painter, P. C.; Coleman, M. M., *Fundamentals of Polymer Science: An Introductory Text*. 2nd ed. CRC Press: Boca Raton, 1997; pp. 237-256.

[*43*] Sperling, L. H., *Introduction to Physical Polymer Science*. 4th ed. Wiley: Hoboken, NJ, 2006; pp. 248-271.

[*44*] Kobayashi, J.; Asahi, T.; Ichiki, M.; Oikawa, A.; Suzuki, H.; Watanabe, T.; Fukada, E.; Shikinami, Y., "Structural and Optical-Properties of Poly Lactic Acids". *Journal of Applied Physics*, **77** (7), 2957 (1995).

[*45*] Sasaki, S.; Asakura, T., "Helix distortion and crystal structure of the alpha-form of poly(L-lactide)". *Macromolecules*, **36** (22), 8385 (2003).

[*46*] Painter, P. C.; Coleman, M. M., *Fundamentals of Polymer Science: An Introductory Text*. 2nd ed. CRC Press: Boca Raton, 1997; pp. 248-250.

[*47*] Kuppa, V. K.; in't Veld, P. J.; Rutledge, G. C., "Monte Carlo simulation of interlamellar isotactic polypropylene". *Macromolecules*, **40** (14), 5187 (2007).

[*48*] Painter, P. C.; Coleman, M. M., *Fundamentals of Polymer Science: An Introductory Text*. 2nd ed. CRC Press: Boca Raton, 1997; pp. 275-277.

[*49*] Keffer, D. J.; Gao, C. Y.; Edwards, B. J., "On the relationship between Fickian diffusivities at the continuum and molecular levels". *Journal of Physical Chemistry B*, **109** (11), 5279 (2005).

[*50*] Sharp, J. S.; Forrest, J. A.; Jones, R. A. L., "Swelling of Poly(DL-lactide) and polylactide-co-glycolide in humid environments". *Macromolecules*, **34** (25), 8752 (2001).

[*51*] Greenfield, M. L.; Theodorou, D. N., "Geometric Analysis of Diffusion Pathways in Glassy and Melt Atactic Polypropylene". *Macromolecules*, **26** (20), 5461 (1993).

[*52*] Palade, L. I.; Lehermeier, H. J.; Dorgan, J. R., "Melt rheology of high L-content poly(lactic acid)". *Macromolecules*, **34** (5), 1384 (2001).

[*53*] Edie, D. D., *Chemical Engineering 818 Polymer Processing Class Notes*. Clemson University: Clemson, SC, 2005.

[*54*] Oldroyd, J. G., "Non-Newtonian Effects in Steady Motion of Some Idealized Elastico-Viscous Liquids". *Proceedings of the Royal Society of London A*, **245**, 278 (1958).

[*55*] Giesekus, H., "A Unified Approach to a Variety of Constitutive Models for Polymer Fluids Based on the Concept of Configuration-Dependent Molecular Mobility". *Rheologica Acta*, **21** (4-5), 366 (1982).

[*56*] Giesekus, H., "A Simple Constitutive Equation for Polymer Fluids Based on the Concept of Deformation-Dependent Tensorial Mobility". *Journal of Non-Newtonian Fluid Mechanics*, **11** (1-2), 69 (1982).

[*57*] Todd, B. D.; Daivis, P. J., "Homogeneous non-equilibrium molecular dynamics simulations of viscous flow: techniques and applications". *Molecular Simulation*, **33** (3), 189 (2007).

[*58*] Zhao, Y.; Pu, J. Z.; Lynch, B. J.; Truhlar, D. G., "Tests of second-generation and third-generation density functionals for thermochemical kinetics". *Physical Chemistry Chemical Physics*, **6** (4), 673 (2004).

[*59*] Levine, I. N., *Quantum Chemistry*. 5th ed. Prentice Hall: Upper Saddle River, New Jersey, 2000; p 287.

[*60*] Levine, I. N., *Quantum Chemistry*. 5th ed. Prentice Hall: Upper Saddle River, New Jersey, 2000; pp. 295-296.

[*61*] Levine, I. N., *Quantum Chemistry*. 5th ed. Prentice Hall: Upper Saddle River, New Jersey, 2000; pp. 134-141.

[*62*] Cook, D. B., *Handbook of Computational Quantum Chemistry*. Oxford University Press: Oxford, 1998; p 28.

[*63*] Frisch, M. J.; Trucks, G. W.; Schlegel, H. B.; Scuseria, G. E.; Robb, M. A.; Cheeseman, J. R.; J. A. Montgomery, J.; Vreven, T.; Kudin, K. N.; Burant, J. C.; Millam, J. M.; Iyengar, S. S.; Tomasi, J.; Barone, V.; Mennucci, B.; Cossi, M.; Scalmani, G.; Rega, N.; Petersson, G. A.; Nakatsuji, H.; Hada, M.; Ehara, M.; Toyota, K.; Fukuda, R.; Hasegawa, J.; Ishida, M.; Nakajima, T.; Honda, Y.; Kitao, O.; Nakai, H.; Klene, M.; Li, X.; Knox, J. E.; Hratchian, H. P.; Cross, J. B.; Bakken, V.; Adamo, C.; Jaramillo, J.; Gomperts, R.; Stratmann, R. E.; Yazyev, O.; Austin, A. J.; Cammi, R.; Pomelli, C.; Ochterski, J. W.; Ayala, P. Y.; Morokuma, K.; Voth, G. A.; Salvador, P.; Dannenberg, J. J.; Zakrzewski, V. G.; Dapprich, S.; Daniels, A. D.; Strain, M. C.; Farkas, O.; Malick, D. K.; Rabuck, A. D.; Raghavachari, K.; Foresman, J. B.; Ortiz, J. V.; Cui, Q.; Baboul, A. G.; Clifford, S.; Cioslowski, J.; Stefanov, B. B.; Liu, G.; Liashenko, A.; Piskorz, P.; Komaromi, I.; Martin, R. L.; Fox, D. J.; Keith, T.; Al-Laham, M. A.; Peng, C. Y.; Nanayakkara, A.; Challacombe, M.; Gill, P. M. W.; Johnson, B.; Chen, W.; Wong, M. W.; Gonzalez, C.; Pople, J. A. *Gaussian 03*, Gaussian, Inc.: 2003.

[*64*] Hehre, W. J.; Stewart, R. F.; Pople, J. A., "Self-Consistent Molecular-Orbital Methods .I. Use of Gaussian Expansions of Slater-Type Atomic Orbitals". *Journal of Chemical Physics*, **51** (6), 2657 (1969).

[*65*] Ditchfield, R.; Hehre, W. J.; Pople, J. A., "Self-Consistent Molecular-Orbital Methods .9. Extended Gaussian-Type Basis for Molecular-Orbital Studies of Organic Molecules". *Journal of Chemical Physics*, **54** (2), 724 (1971).

[*66*] Francl, M. M.; Pietro, W. J.; Hehre, W. J.; Binkley, J. S.; Gordon, M. S.; Defrees, D. J.; Pople, J. A., "Self-Consistent Molecular-Orbital Methods .23. A Polarization-Type Basis Set for 2nd-Row Elements". *Journal of Chemical Physics*, **77** (7), 3654 (1982).

[*67*] Hehre, W. J.; Ditchfield, R.; Pople, J. A., "Self-Consistent Molecular-Orbital Methods .12. Further Extensions of Gaussian-Type Basis Sets for Use in Molecular-Orbital Studies of Organic-Molecules". *Journal of Chemical Physics*, **56** (5), 2257 (1972).

[*68*] Lewars, E., *Computational Chemistry: Introduction to the Theory and Applications of Molecular and Quantum Mechanics*. Kluwer: Boston, 2003; p 223.

[*69*] Szabo, A.; Ostlund, N. S., *Modern Quantum Chemistry: Introduction to Advanced Electronic Structure Theory*. 1st ed., rev. McGraw-Hill: New York, 1989; pp. 186-187.

[*70*] Lewars, E., *Computational Chemistry: Introduction to the Theory and Applications of Molecular and Quantum Mechanics*. Kluwer: Boston, 2003; pp. 227-229.

[*71*] Szabo, A.; Ostlund, N. S., *Modern Quantum Chemistry: Introduction to Advanced Electronic Structure Theory*. 1st ed., rev. McGraw-Hill: New York, 1989; pp. 189-190.

[*72*] Lewars, E., *Computational Chemistry: Introduction to the Theory and Applications of Molecular and Quantum Mechanics*. Kluwer: Boston, 2003; p 226.

[*73*] Dunning, T. H.; Hay, P. J., In *Modern Theoretical Chemistry*, Schaefer, H. F., Ed. Plenum Press: New York, 1976; pp 1-28.

[*74*] Dunning, T. H., "Gaussian-Basis Sets for Use in Correlated Molecular Calculations .1. The Atoms Boron through Neon and Hydrogen". *Journal of Chemical Physics*, **90** (2), 1007 (1989).

[*75*] Kendall, R. A.; Dunning, T. H.; Harrison, R. J., "Electron-Affinities of the 1st-Row Atoms Revisited - Systematic Basis-Sets and Wave-Functions". *Journal of Chemical Physics*, **96** (9), 6796 (1992).

[*76*] Woon, D. E.; Dunning, T. H., "Gaussian-Basis Sets for Use in Correlated Molecular Calculations .3. The Atoms Aluminum through Argon". *Journal of Chemical Physics*, **98** (2), 1358 (1993).

[*77*] Kresse, G.; Furthmuller, J., "Efficient iterative schemes for ab initio total-energy calculations using a plane-wave basis set". *Physical Review B*, **54** (16), 11169 (1996).

[*78*] Kresse, G.; Furthmuller, J., "Efficiency of ab-initio total energy calculations for metals and semiconductors using a plane-wave basis set". *Computational Materials Science*, **6** (1), 15 (1996).

[*79*] Cho, K.; Arias, T. A.; Joannopoulos, J. D.; Lam, P. K., "Wavelets in Electronic-Structure Calculations". *Physical Review Letters*, **71** (12), 1808 (1993).

[*80*] Szabo, A.; Ostlund, N. S., *Modern Quantum Chemistry: Introduction to Advanced Electronic Structure Theory*. 1st ed., rev. McGraw-Hill: New York, 1989.

[*81*] Cook, D. B., *Handbook of Computational Quantum Chemistry*. Oxford University Press: Oxford, 1998; p 74.

[*82*] Lewars, E., *Computational Chemistry: Introduction to the Theory and Applications of Molecular and Quantum Mechanics*. Kluwer: Boston, 2003; p 168.

[*83*] Szabo, A.; Ostlund, N. S., *Modern Quantum Chemistry: Introduction to Advanced Electronic Structure Theory*. 1st ed., rev. McGraw-Hill: New York, 1989; p 73.

[*84*] Szabo, A.; Ostlund, N. S., *Modern Quantum Chemistry: Introduction to Advanced Electronic Structure Theory*. 1st ed., rev. McGraw-Hill: New York, 1989; pp. 67-68.

[*85*] Lewars, E., *Computational Chemistry: Introduction to the Theory and Applications of Molecular and Quantum Mechanics*. Kluwer: Boston, 2003.

[*86*] Hohenberg, P.; Kohn, W., "Inhomogeneous Electron Gas". *Physical Review*, **136** (3B), B864 (1964).

[*87*] Allen, M. P.; Tildesley, D. J., *Computer Simulation of Liquids*. Oxford University Press: Oxford, 1987.

[*88*] Frenkel, D.; Smit, B., *Understanding Molecular Simulation*. 2nd ed. Academic Press: San Diego, 2002.

[*89*] Haile, J. M., *Molecular Dynamics Simulation*. Wiley: New York, 1992.

[*90*] Steinbach, P. J. *Classical vs. Quantum Mechanics: The Harmonic Oscillator in One Dimension* http://cmm.cit.nih.gov/intro_simulation/node3.html (accessed June 16, 2009).

[*91*] Jorgensen, W. L.; Maxwell, D. S.; TiradoRives, J., "Development and testing of the OPLS all-atom force field on conformational energetics and properties of organic liquids". *Journal of the American Chemical Society*, **118** (45), 11225 (1996).

[*92*] Kaminski, G. A.; Friesner, R. A.; Tirado-Rives, J.; Jorgensen, W. L., "Evaluation and reparametrization of the OPLS-AA force field for proteins via comparison with accurate quantum chemical calculations on peptides". *Journal of Physical Chemistry B*, **105** (28), 6474 (2001).

[*93*] Hess, B.; Bekker, H.; Berendsen, H. J. C.; Fraaije, J. G. E. M., "LINCS: A linear constraint solver for molecular simulations". *Journal of Computational Chemistry*, **18** (12), 1463 (1997).

[*94*] Miyamoto, S.; Kollman, P. A., "Settle - an Analytical Version of the Shake and Rattle Algorithm for Rigid Water Models". *Journal of Computational Chemistry*, **13** (8), 952 (1992).

[*95*] Brooks, B. R.; Bruccoleri, R. E.; Olafson, B. D.; States, D. J.; Swaminathan, S.; Karplus, M., "Charmm - a Program for Macromolecular Energy, Minimization, and Dynamics Calculations". *Journal of Computational Chemistry*, **4** (2), 187 (1983).

[*96*] Cornell, W. D.; Cieplak, P.; Bayly, C. I.; Gould, I. R.; Merz, K. M.; Ferguson, D. M.; Spellmeyer, D. C.; Fox, T.; Caldwell, J. W.; Kollman, P. A., "A Second Generation Force Field for the Simulation of Proteins, Nucleic Acids, and Organic Molecules". *Journal of the American Chemical Society*, **117** (19), 5179 (1995).

[*97*] Sun, H., "COMPASS: An ab initio force-field optimized for condensed-phase applications - Overview with details on alkane and benzene compounds". *Journal of Physical Chemistry B*, **102** (38), 7338 (1998).

[*98*] London, F., "The General Theory of Molecular Forces". *Transactions of the Faraday Society*, **33**, 8 (1937).

[*99*] Mie, G., "Zur kinetischen Theorie der einatomigan Körper". *Annalen der Physik*, **11** (8), 657 (1903).

[*100*] Charifson, P. S.; Hiskey, R. G.; Pedersen, L. G., "Construction and Molecular Modeling of Phospholipid Surfaces". *Journal of Computational Chemistry*, **11** (10), 1181 (1990).

[*101*] Allen, M. P.; Tildesley, D. J., *Computer Simulation of Liquids*. Oxford University Press: Oxford, 1987; p 21.

[*102*] Jorgensen, W. L.; Chandrasekhar, J.; Madura, J. D.; Impey, R. W.; Klein, M. L., "Comparison of Simple Potential Functions for Simulating Liquid Water". *Journal of Chemical Physics*, **79** (2), 926 (1983).

[*103*] Mahoney, M. W.; Jorgensen, W. L., "A five-site model for liquid water and the reproduction of the density anomaly by rigid, nonpolarizable potential functions". *Journal of Chemical Physics*, **112** (20), 8910 (2000).

[*104*] Dick, B. G.; Overhauser, A. W., "Theory of the dielectric constants of alkali halide crystals". *Physical Review*, **112**, 90 (1958).

[*105*] van Maaren, P. J.; van der Spoel, D., "Molecular dynamics simulations of water with novel shell-model potentials". *Journal of Physical Chemistry B*, **105** (13), 2618 (2001).

[*106*] Kaminski, G. A.; Stern, H. A.; Berne, B. J.; Friesner, R. A., "Development of an accurate and robust polarizable molecular mechanics force field from ab initio quantum chemistry". *Journal of Physical Chemistry A*, **108** (4), 621 (2004).

[*107*] Rick, S. W.; Stuart, S. J.; Berne, B. J., "Dynamical Fluctuating Charge Force-Fields - Application to Liquid Water". *Journal of Chemical Physics*, **101** (7), 6141 (1994).

[*108*] Rick, S. W.; Stuart, S. J.; Bader, J. S.; Berne, B. J., "Fluctuating Charge Force-Fields for Aqueous-Solutions". *Journal of Molecular Liquids*, **65-6**, 31 (1995).

[*109*] Morse, P. M., "Diatomic molecules according to the wave mechanics. II. Vibrational levels". *Physical Review*, **34**, 57 (1929).

[*110*] Bird, R. B.; Dotson, P. J.; Johnson, N. L., "Polymer-Solution Rheology Based on a Finitely Extensible Bead-Spring Chain Model". *Journal of Non-Newtonian Fluid Mechanics*, **7** (2-3), 213 (1980).

[*111*] Brenner, D. W.; Shenderova, O. A.; Harrison, J. A.; Stuart, S. J.; Ni, B.; Sinnott, S. B., "A second-generation reactive empirical bond order (REBO) potential energy expression for hydrocarbons". *Journal of Physics-Condensed Matter*, **14** (4), 783 (2002).

[*112*] van der Spoel, D.; Lindahl, E.; Hess, B.; Kutzner, C.; Buuren, A. R. v.; Apol, E.; Meulenhoff, P. J.; Tieleman, D. P.; Sijbers, A. L. T. M.; Feenstra, K. A.; Drunen, R. v.; Berendsen, H. J. C., *GROMACS User Manual, Version 4.0*. Groningen, The Netherlands, 2008; p 62.

[*113*] Maple, J. R.; Hwang, M. J.; Stockfisch, T. P.; Dinur, U.; Waldman, M.; Ewig, C. S.; Hagler, A. T., "Derivation of Class-Ii Force-Fields .1. Methodology and Quantum Force-Field for the Alkyl Functional-Group and Alkane Molecules". *Journal of Computational Chemistry*, **15** (2), 162 (1994).

[*114*] Martin, M. G., "Comparison of the AMBER, CHARMM, COMPASS, GROMOS, OPLS, TraPPE and UFF force fields for prediction of vapor-liquid coexistence curves and liquid densities". *Fluid Phase Equilibria*, **248** (1), 50 (2006).

[*115*] Haile, J. M., *Molecular Dynamics Simulation*. Wiley: New York, 1992; p 42.

[*116*] Gear, C. W., *Numerical initial value problems in ordinary differential equations*. Prentice-Hall: Englewood Cliffs, NJ, 1971.

[*117*] Swope, W. C.; Andersen, H. C.; Berens, P. H.; Wilson, K. R., "A Computer-Simulation Method for the Calculation of Equilibrium-Constants for the

Formation of Physical Clusters of Molecules - Application to Small Water Clusters". *Journal of Chemical Physics*, **76** (1), 637 (1982).

[*118*] Verlet, L., "Computer Experiments on Classical Fluids .I. Thermodynamical Properties of Lennard-Jones Molecules". *Physical Review*, **159** (1), 98 (1967).

[*119*] Hockney, R. W.; Goel, S. P.; Eastwood, J. W., "Quiet High-Resolution Computer Models of a Plasma". *Journal of Computational Physics*, **14** (2), 148 (1974).

[*120*] van der Spoel, D.; Lindahl, E.; Hess, B.; Kutzner, C.; Buuren, A. R. v.; Apol, E.; Meulenhoff, P. J.; Tieleman, D. P.; Sijbers, A. L. T. M.; Feenstra, K. A.; Drunen, R. v.; Berendsen, H. J. C., *GROMACS User Manual, Version 4.0*. Groningen, The Netherlands, 2008; p 22.

[*121*] Allen, M. P.; Tildesley, D. J., *Computer Simulation of Liquids*. Oxford University Press: Oxford, 1987; p 80.

[*122*] Allen, M. P.; Tildesley, D. J., *Computer Simulation of Liquids*. Oxford University Press: Oxford, 1987; p 46.

[*123*] Andersen, H. C.; Allen, M. P.; Bellemans, A.; Board, J.; Clarke, J. H. R.; Ferrario, M.; Haile, J. M.; Nose, S.; Opheusden, J. V.; Ryckaert, J. P., "New molecular dynamics methods for various ensembles". *Rapport d'activité scientifique du CECAM*, (1984).

[*124*] Berendsen, H. J. C.; Postma, J. P. M.; Vangunsteren, W. F.; Dinola, A.; Haak, J. R., "Molecular-Dynamics with Coupling to an External Bath". *Journal of Chemical Physics*, **81** (8), 3684 (1984).

[*125*] Nosé, S., "A Molecular-Dynamics Method for Simulations in the Canonical Ensemble". *Molecular Physics*, **52** (2), 255 (1984).

[*126*] Hoover, W. G., "Canonical Dynamics - Equilibrium Phase-Space Distributions". *Physical Review A*, **31** (3), 1695 (1985).

[*127*] Haile, J. M., *Molecular Dynamics Simulation*. Wiley: New York, 1992; pp. 46-53.

[*128*] Martyna, G. J.; Klein, M. L.; Tuckerman, M., "Nose-Hoover Chains - the Canonical Ensemble Via Continuous Dynamics". *Journal of Chemical Physics*, **97** (4), 2635 (1992).

[*129*] van der Spoel, D.; Lindahl, E.; Hess, B.; Kutzner, C.; Buuren, A. R. v.; Apol, E.; Meulenhoff, P. J.; Tieleman, D. P.; Sijbers, A. L. T. M.; Feenstra, K. A.; Drunen, R. v.; Berendsen, H. J. C., *GROMACS User Manual, Version 4.0*. Groningen, The Netherlands, 2008; pp. 23-24.

[*130*] Allen, M. P.; Tildesley, D. J., *Computer Simulation of Liquids*. Oxford University Press: Oxford, 1987; p 232.

[*131*] van der Spoel, D.; Lindahl, E.; Hess, B.; Kutzner, C.; Buuren, A. R. v.; Apol, E.; Meulenhoff, P. J.; Tieleman, D. P.; Sijbers, A. L. T. M.; Feenstra, K. A.; Drunen, R. v.; Berendsen, H. J. C., *GROMACS User Manual, Version 4.0*. Groningen, The Netherlands, 2008; pp. 25-26.

[*132*] Parrinello, M.; Rahman, A., "Polymorphic Transitions in Single Crystals: a New Molecular Dynamics Method". *Journal of Applied Physics*, **52** (12), 7182 (1981).

[*133*] Metropolis, N., "The Beginning of the Monte Carlo Method". *Los Alamos Science*, (15), 125 (1987).

[*134*] Metropolis, N.; Rosenbluth, M. N.; Teller, A. H.; Teller, E., "Equation of State Calculations by Fast Computing Machines". *Journal of Chemical Physics*, **21** (6), 1087 (1957).

[*135*] Allen, M. P.; Tildesley, D. J., *Computer Simulation of Liquids*. Oxford University Press: Oxford, 1987; pp. 123-131.

[*136*] Kirkpatrick, S.; Gelatt, C. D.; Vecchi, M. P., "Optimization by Simulated Annealing". *Science*, **220** (4598), 671 (1983).

[*137*] Flory, P. J., *Statistical Mechanics of Chain Molecules*. Wiley: New York, 1969.

[*138*] Flory, P. J., *Statistical Mechanics of Chain Molecules*. Wiley: New York, 1969; pp. 16-17.

[*139*] Brant, D. A.; Flory, P. J., "The Configuration of Random Polypeptide Chains. II. Theory". *Journal of the American Chemical Society*, **87** (13), 2791 (1965).

[*140*] Brant, D. A.; Tonelli, A. E.; Flory, P. J., "The Configurational Statistics of Random Poly(lactic acid Chains. II.Theory". *Macromolecules*, **2** (3), 228 (1969).

[*141*] Zhu, C. Y.; Byrd, R. H.; Lu, P. H.; Nocedal, J., "Algorithm 778: L-BFGS-B: Fortran subroutines for large-scale bound-constrained optimization". *Acm Transactions on Mathematical Software*, **23** (4), 550 (1997).

[*142*] O'Brien, C. P. *Quantum and Molecular Modeling of Polylactide*. Ph. D. Thesis, Clemson University, Clemson, SC, 2005.

[*143*] de Santis, P.; Kovacs, J., "Molecular conformation of poly(S-lactic acid)". *Biopolymers*, **6** (3), 299 (1968).

[*144*] Hoogsteen, W.; Postema, A. R.; Pennings, A. J.; Tenbrinke, G.; Zugenmaier, P., "Crystal-Structure, Conformation, and Morphology of Solution-Spun Poly(L-Lactide) Fibers". *Macromolecules*, **23** (2), 634 (1990).

[*145*] Kang, S. H.; Hsu, S. L.; Stidham, H. D.; Smith, P. B.; Leugers, M. A.; Yang, X. Z., "A spectroscopic analysis of poly(lactic acid) structure". *Macromolecules*, **34** (13), 4542 (2001).

[*146*] Yang, X. Z.; Kang, S. H.; Hsu, S. L.; Stidham, H. D.; Smith, P. B.; Leugers, A., "A spectroscopic analysis of chain flexibility of poly(lactic acid)". *Macromolecules*, **34** (14), 5037 (2001).

[*147*] Yang, X. Z.; Kang, S. H.; Yang, Y. N.; Aou, K.; Hsu, S. L., "Raman spectroscopic study of conformational changes in the amorphous phase of poly(lactic acid) during deformation". *Polymer*, **45** (12), 4241 (2004).

[*148*] Alemán, C.; Lotz, B.; Puiggali, J., "Crystal structure of the alpha-form of poly(L-lactide)". *Macromolecules*, **34** (14), 4795 (2001).

[*149*] Wales, D., *Energy Landscapes : Applications to Clusters, Biomolecules and Glasses (Cambridge Molecular Science)*. Cambridge University Press: 2004.

[*150*] Dougill, M. W.; Jeffrey, G. A., "The Structure of Dimethyl Oxalate". *Acta Crystallographica*, **6**, 831 (1953).

[*151*] McNaught, A. D.; Wilkinson, A., *Compendium of Chemical Terminology: IUPAC Recommendations*. 2nd ed.; Blackwell Scientific Publications: Oxford, 1997; p.

[*152*] Curl, R. F., "Microwave Spectrum, Barrier to Internal Rotation, and Structure of Methyl Formate". *The Journal of Chemical Physics*, **30** (6), 1529 (1959).

[*153*] O'Gorman, J. M.; Shand, W.; Schomaker, V., "An Electron Diffraction Investigation of Methyl Formate, Methyl Acetate, and Methyl Chloroformate". *Journal of the American Chemical Society*, **72**, 4222 (1950).

[*154*] Tonelli, A. E.; Flory, P. J., "Configuration Statistics of Random Poly(Lactic Acid) Chains. I. Experimental Results". *Macromolecules*, **2** (3), 225 (1969).

[*155*] Eling, B.; Gogolewski, S.; Pennings, A. J., "Biodegradable Materials of Poly(L-Lactic Acid) .1. Melt-Spun and Solution-Spun Fibers". *Polymer*, **23** (11), 1587 (1982).

[*156*] Zugenmaier, P.; Sarko, A., "Packing Analysis of Carbohydrates and Polysaccharides .4. New Method for Detailed Crystal-Structure Refinement of Polysaccharides and Its Application to V-Amylose". *Biopolymers*, **15** (11), 2121 (1976).

[*157*] León, S.; Navas, J. J.; Alemán, C., "PCSP: a computer program to predict and analyze the packing in crystalline polymers". *Polymer*, **40** (26), 7351 (1999).

[*158*] Arnott, S.; Wonacott, A. J., "Atomic Coordinates for an Alpha-Helix Refinement of Crystal Structure of Alpha-Poly-L-Alanine". *Journal of Molecular Biology*, **21** (2), 371 (1966).

[*159*] Rietveld, H. M., "A Profile Refinement Method for Nuclear and Magnetic Structures". *Journal of Applied Crystallography*, **2**, 65 (1969).

[*160*] Blomqvist, J.; Ahjopalo, L.; Mannfors, B.; Pietila, L. O., "Studies on aliphatic polyesters I: Ab initio, density functional and force field studies of esters with one carboxyl group". *Journal of Molecular Structure-Theochem*, **488**, 247 (1999).

[*161*] Blomqvist, J.; Mannfors, B.; Pietila, L. O., "Studies on aliphatic polyesters. Part II. Ab initio, density functional and force field studies of model molecules with two carboxyl groups". *Journal of Molecular Structure-Theochem*, **531**, 359 (2000).

[*162*] Korpelainen, V.; Mannfors, B.; Pietila, L. O., "Studies on Aliphatic Polyesters. Part III. Ab Initio, Density Functional and Force Field Studies of Esters with Tartaric Units". *Journal of Molecular Structure- Theochem*, **624**, 287 (2002).

[*163*] Sun, H., "Force-Field for Computation of Conformational Energies, Structures, and Vibrational Frequencies of Aromatic Polyesters". *Journal of Computational Chemistry*, **15** (7), 752 (1994).

[*164*] Sun, H., "Ab-Initio Calculations and Force-Field Development for Computer-Simulation of Polysilanes". *Macromolecules*, **28** (3), 701 (1995).

[*165*] Sun, H., "Molecular structures and conformations of polyphosphazenes - A study based on density functional calculations of oligomers". *Journal of the American Chemical Society*, **119** (15), 3611 (1997).

[*166*] Sun, H.; Mumby, S. J.; Maple, J. R.; Hagler, A. T., "An Ab-Initio Cff93 All-Atom Force-Field for Polycarbonates". *Journal of the American Chemical Society*, **116** (7), 2978 (1994).

[*167*] Price, M. L. P.; Ostrovsky, D.; Jorgensen, W. L., "Gas-phase and liquid-state properties of esters, nitriles, and nitro compounds with the OPLS-AA force field". *Journal of Computational Chemistry*, **22** (13), 1340 (2001).

[*168*] Carlson, H. A.; Nguyen, T. B.; Orozco, M.; Jorgensen, W. L., "Accuracy of Free-Energies of Hydration for Organic-Molecules from 6-31g-Asterisk-Derived Partial Charges". *Journal of Computational Chemistry*, **14** (10), 1240 (1993).

[*169*] Breneman, C. M.; Wiberg, K. B., "Determining Atom-Centered Monopoles from Molecular Electrostatic Potentials - the Need for High Sampling Density in Formamide Conformational-Analysis". *Journal of Computational Chemistry*, **11** (3), 361 (1990).

[*170*] van der Spoel, D.; Lindahl, E.; Hess, B.; Kutzner, C.; Buuren, A. R. v.; Apol, E.; Meulenhoff, P. J.; Tieleman, D. P.; Sijbers, A. L. T. M.; Feenstra, K. A.; Drunen, R. v.; Berendsen, H. J. C., *GROMACS User Manual, Version 4.0*. Groningen, The Netherlands, 2008.

[*171*] Blomqvist, J., "RIS Metropolis Monte Carlo studies of poly(L-lactic), poly(L,D-lactic) and polyglycolic acids". *Polymer*, **42** (8), 3515 (2001).

[*172*] Honeycutt, J. D., "A general simulation method for computing conformational properties of single polymer chains". *Computational and Theoretical Polymer Science*, **8** (1-2), 1 (1998).

[*173*] Blomqvist, J.; Mannfors, B.; Pietila, L. O., "Amorphous cell studies of polyglycolic, poly(L-lactic), poly(L,D-lactic) and poly(glycolic/L-lactic) acids". *Polymer*, **43** (17), 4571 (2002).

[*174*] Theodorou, D. N.; Suter, U. W., "Detailed Molecular-Structure of a Vinyl Polymer Glass". *Macromolecules*, **18** (7), 1467 (1985).

[*175*] Theodorou, D. N.; Suter, U. W., "Atomistic Modeling of Mechanical-Properties of Polymeric Glasses". *Macromolecules*, **19** (1), 139 (1986).

[*176*] Entrialgo-Castaño, M.; Lendlein, A.; Hofmann, D., "Molecular modeling investigations of dry and two water-swollen states of biodegradable polymers". *Advanced Engineering Materials*, **8** (5), 434 (2006).

[*177*] Karst, D.; Yang, Y. Q., "Molecular modeling study of the resistance of PLA to hydrolysis based on the blending of PLLA and PDLA". *Polymer*, **47** (13), 4845 (2006).

[*178*] Lee, W. K.; Iwata, T.; Gardella, J. A., "Hydrolytic behavior of enantiomeric poly(lactide) mixed monolayer films at the air/water interface: Stereocomplexation effects". *Langmuir*, **21** (24), 11180 (2005).

[*179*] Duan, Y.; Wu, C.; Chowdhury, S.; Lee, M. C.; Xiong, G. M.; Zhang, W.; Yang, R.; Cieplak, P.; Luo, R.; Lee, T.; Caldwell, J.; Wang, J. M.; Kollman, P., "A point-charge force field for molecular mechanics simulations of proteins based on condensed-phase quantum mechanical calculations". *Journal of Computational Chemistry*, **24** (16), 1999 (2003).

[*180*] Meaurio, E.; Zuza, E.; Lopez-Rodriguez, N.; Sarasua, J. R., "Conformational behavior of poly(L-lactide) studied by infrared spectroscopy". *Journal of Physical Chemistry B*, **110** (11), 5790 (2006).

[*181*] *Jaguar 4.2*, Schrodinger, Inc.: Portland, OR, 1991-2000.

[*182*] St.-Amant, A.; Cornell, W. D.; Kollman, P. A.; Halgren, T. A., "Calculation of Molecular Geometries, Relative Conformational Energies, Dipole Moments, and Molecular Electrostatic Potential Fitted Charges of Small Organic Molecules of Biochemical Interest by Density Functional Theory". *Journal of Computational Chemistry*, **16** (12), 1483 (1995).

[*183*] Sigfridsson, E., "Comparison of Methods for Deriving Atomic Charges from the Electrostatic Potential and Moments." *Journal of Computational Science*, **19** (4), 377 (1997).

[*184*] Becke, A. D., "Density-Functional Exchange-Energy Approximation with Correct Asymptotic-Behavior". *Physical Review A*, **38** (6), 3098 (1988).

[*185*] Vosko, S. H.; Wilk, L.; Nusair, M., "Accurate spin-dependent electron liquid correlation energies for local spin density calculations: a critical analysis". *Canadian Journal of Physics*, **58**, 1200 (1980).

[*186*] Lee, C. T.; Yang, W. T.; Parr, R. G., "Development of the Colle-Salvetti Correlation-Energy Formula into a Functional of the Electron-Density". *Physical Review B*, **37** (2), 785 (1988).

[*187*] Lewars, E., *Computational Chemistry: Introduction to the Theory and Applications of Molecular and Quantum Mechanics*. Kluwer: Boston, 2003; p 407.

[*188*] Tomasi, J.; Persico, M., "Molecular-Interactions in Solution - an Overview of Methods Based on Continuous Distributions of the Solvent". *Chemical Reviews*, **94** (7), 2027 (1994).

[*189*] Cramer, C. J.; Truhlar, D. G., "Implicit solvation models: Equilibria, structure, spectra, and dynamics". *Chemical Reviews*, **99** (8), 2161 (1999).

[*190*] Ben-Naim, A.; Marcus, Y., "Solvation thermodynamics of nonionic solutes". *Journal of Chemical Physics*, **81** (4), 2016 (1984).

[*191*] Cortis, C. M.; Friesner, R. A., "Numerical solution of the Poisson-Boltzmann equation using tetrahedral finite-element meshes". *Journal of Computational Chemistry*, **18** (13), 1591 (1997).

[*192*] Cortis, C. M.; Friesner, R. A., "An automatic three-dimensional finite element mesh generation system for the Poisson-Boltzmann equation". *Journal of Computational Chemistry*, **18** (13), 1570 (1997).

[*193*] Kanchanasopa, M.; Runt, J., "Broadband dielectric investigation of amorphous and semicrystalline L-lactide/meso-lactide copolymers". *Macromolecules*, **37** (3), 863 (2004).

[*194*] Wright, J. R., *Jaguar User's Guide, Version 4.2*. Schrodinger, Inc.: 2002.

[*195*] Kodaka, M., "Correlation between molecular size and packing density of solvents". *Journal of Physical Chemistry B*, **108** (3), 1160 (2004).

[*196*] Painter, P. C.; Coleman, M. M., *Fundamentals of Polymer Science: An Introductory Text*. 2nd ed. CRC Press: Boca Raton, 1997; pp. 313-335.

[*197*] Tannor, D. J.; Marten, B.; Murphy, R.; Friesner, R. A.; Sitkoff, D.; Nicholls, A.; Ringnalda, M.; III, W. A. G.; Honig, B., "Accurate First Principles Calculation of Molecular Charge Distributions and Solvation Energies from Ab Initio Quantum Mechanics and Continuum Dielectric Theory". *Journal of the American Chemical Society*, **116** (26), 11875 (1994).

[*198*] Flory, P. J., *Statistical Mechanics of Chain Molecules*. Wiley: New York, 1969; p 265.

[*199*] Flory, P. J., *Statistical Mechanics of Chain Molecules*. Wiley: New York, 1969; p 25.

[*200*] Flory, P. J., *Statistical Mechanics of Chain Molecules*. Wiley: New York, 1969; pp. 19-25,274-276.

[*201*] Wiberg, K. B.; Laidig, K. E., "Barriers to Rotation Adjacent to Double-Bonds .3. The C-O Barrier in Formic-Acid, Methyl Formate, Acetic-Acid, and Methyl Acetate - the Origin of Ester and Amide Resonance". *Journal of the American Chemical Society*, **109** (20), 5935 (1987).

[*202*] Joziasse, C. A. P.; Veenstra, H.; Grijpma, D. W.; Pennings, A. J., "On the chain stiffness of poly(lactide)s". *Macromolecular Chemistry and Physics*, **197** (7), 2219 (1996).

[*203*] McAliley, J. H.; O'Brien, C. P.; Bruce, D. A., "Continuum electrostatics for electronic structure calculations in bulk amorphous polymers: Application to polylactide". *Journal of Physical Chemistry A*, **112** (31), 7244 (2008).

[*204*] Sato, Y.; Inohara, K.; Takishima, S.; Masuoka, H.; Imaizumi, M.; Yamamoto, H.; Takasugi, M., "Pressure-volume-temperature behavior of polylactide, poly(butylene succinate), and poly(butylene succinate-co-adipate)". *Polymer Engineering and Science*, **40** (12), 2602 (2000).

[*205*] Dorgan, J. R.; Lehermeier, H.; Mang, M., "Thermal and rheological properties of commercial-grade poly(lactic acid)s". *Journal of Polymers and the Environment*, **8** (1), 1 (2000).

[*206*] Bopp, R., Personal Communication, February 5, 2008

[*207*] Kofke, D. A., "On the acceptance probability of replica-exchange Monte Carlo trials". *Journal of Chemical Physics*, **117** (15), 6911 (2002).

[*208*] Kone, A.; Kofke, D. A., "Selection of temperature intervals for parallel-tempering simulations". *Journal of Chemical Physics*, **122** (20), 206101 (2005).

[*209*] Patriksson, A.; van der Spoel, D., "A temperature predictor for parallel tempering simulations". *Physical Chemistry Chemical Physics*, **10** (15), 2073 (2008).

[*210*] Rathore, N.; Chopra, M.; de Pablo, J. J., "Optimal allocation of replicas in parallel tempering simulations". *Journal of Chemical Physics*, **122** (2), (2005).

[*211*] Boyd, R. H., "Glass transition temperatures from molecular dynamics simulations". *Trends in Polymer Science*, **4** (1), 12 (1996).

[*212*] Han, J.; Gee, R. H.; Boyd, R. H., "Glass-Transition Temperatures of Polymers from Molecular-Dynamics Simulations". *Macromolecules*, **27** (26), 7781 (1994).

[*213*] Rigby, D.; Roe, R. J., "Molecular-Dynamics Simulation of Polymer Liquid and Glass .1. Glass-Transition". *Journal of Chemical Physics*, **87** (12), 7285 (1987).

[*214*] Buchholz, J.; Paul, W.; Varnik, F.; Binder, K., "Cooling rate dependence of the glass transition temperature of polymer melts: Molecular dynamics study". *Journal of Chemical Physics*, **117** (15), 7364 (2002).

[*215*] Soldera, A.; Metatla, N., "Glass transition of polymers: Atomistic simulation versus experiments". *Physical Review E*, **74** (6), (2006).

[*216*] O'Brien, C. P.; Stuart, S. J.; Bruce, D. A.; Latour, R. A., "Modeling of Peptide Adsorption Interactions with a Poly(lactic acid) Surface". *Langmuir*, **24** (24), 14115 (2008).

[*217*] Mackerell, A. D.; Feig, M.; Brooks, C. L., "Extending the treatment of backbone energetics in protein force fields: Limitations of gas-phase quantum mechanics in reproducing protein conformational distributions in molecular dynamics simulations". *Journal of Computational Chemistry*, **25** (11), 1400 (2004).

[*218*] Lewars, E., *Computational Chemistry: Introduction to the Theory and Applications of Molecular and Quantum Mechanics*. Kluwer: Boston, 2003; pp. 400-406.

[*219*] Zhang, J.; Liang, Y.; Yan, J. Z.; Lou, J. Z., "Study of the molecular weight dependence of glass transition temperature for amorphous poly(L-lactide) by molecular dynamics simulation". *Polymer*, **48** (16), 4900 (2007).

[*220*] Giesen, D. J.; Storer, J. W.; Cramer, C. J.; Truhlar, D. G., "General Semiempirical Quantum-Mechanical Solvation Model for Nonpolar Solvation Free-Energies - N-Hexadecane". *Journal of the American Chemical Society*, **117** (3), 1057 (1995).

[*221*] Greenfield, M. L., "Sorption and Diffusion of Small Molecules Using Transition-State Theory". In *Simulation Methods for Polymers*, Kotelyanskii, M.; Theodorou, D. N., Eds. Marcel Dekker: New York, 2004; pp 389-490.

[*222*] Mourits, M. *The Silicon Graphics Refrigerator Project, or: How To Turn a $175,000 High-End SGI Challenge DM Server into a Fridge*. http://home.planet.nl/~mourits/koelkast/ (accessed June 16th, 2009).

[*223*] "Completion of a one-petaflops computer system for simulation of molecular dynamics". Press Release, RIKEN, 19 June 2006. http://www.riken.jp/engn/r-world/info/release/press/2006/060619/index.html, Accessed on 28 March 2008.

[*224*] Susukita, R.; Ebisuzaki, T.; Elmegreen, B. G.; Furusawa, H.; Kato, K.; Kawai, A.; Kobayashi, Y.; Koishi, T.; McNiven, G. D.; Narumi, T.; Yasuoka, K., "Hardware accelerator for molecular dynamics: MDGRAPE-2". *Computer Physics Communications*, **155** (2), 115 (2003).

[*225*] Kuskin, J. S.; Young, C.; Grossman, J. P.; Batson, B.; Deneroff, M. M.; Dror, R. O.; Shaw, D. E. "Incorporating Flexibility in Anton, a Specialized Machine for Molecular Dynamics Simulation". In *Proceedings of The 14th International Symposium on High-Performance Computer Architecture (HPCA '08)*, Salt Lake City, UT, 2008, 343-354.

[*226*] Shaw, D. E.; Deneroff, M. M.; Dror, R. O.; Kuskin, J. S.; Larson, R. H.; Salmon, J. K.; Young, C.; Batson, B.; Bowers, K. J.; Chao, J. C.; Eastwood, M. P.; Gagliardo, J.; Grossman, J. P.; Ho, C. R.; lerardi, D. J.; Kolossvary, I.; Klepeis, J. L.; Layman, T.; McLeavey, C.; Moraes, M. A.; Mueller, R.; Priest, E. C.; Yibing, S.; Spengler, J.; Theobald, M.; Towles, B.; Wang, S. C., "Anton, a special-purpose machine for molecular dynamics simulation". *Computer Architecture News*, **35** (2), 1 (2007).

[*227*] Kofke, D. A.; Cummings, P. T., "Quantitative comparison and optimization of methods for evaluating the chemical potential by molecular simulation". *Molecular Physics*, **92** (6), 973 (1997).

[*228*] Widom, B., "Some Topics on the Theory of Fluids". *Journal of Chemical Physics*, **39** (11), 2808 (1963).

[*229*] Shing, K. S.; Gubbins, K. E., "The Chemical-Potential from Computer-Simulation Test Particle Method with Umbrella Sampling". *Molecular Physics*, **43** (3), 717 (1981).

[*230*] Bennett, C. H., "Efficient Estimation of Free-Energy Differences from Monte-Carlo Data". *Journal of Computational Physics*, **22** (2), 245 (1976).

[*231*] Boulougouris, G. C.; Economou, I. G.; Theodorou, D. N., "Calculation of the chemical potential of chain molecules using the staged particle deletion scheme". *Journal of Chemical Physics*, **115** (17), 8231 (2001).

[*232*] Torrie, G. M.; Valleau, J. P., "Non-Physical Sampling Distributions in Monte-Carlo Free-Energy Estimation - Umbrella Sampling". *Journal of Computational Physics*, **23** (2), 187 (1977).

[*233*] Han, K. K., "A New Monte-Carlo Method for Estimating Free-Energy and Chemical-Potential". *Physics Letters A*, **165** (1), 28 (1992).

[*234*] Frenkel, D. "Free energy computation and first order phase transitions". In *Proceedings of International School of Physics "Enricho Fermi"*, Varenna, Italy, 1985,

[*235*] Fitts, D. D., *Nonequilibrium Thermodynamics: A Phenomenological Theory of Irreversible Processes in Fluid Systems*. McGraw-Hill: New York, 1962.

[*236*] de Groot, S. R.; Mazur, P., *Nonequilibrium Thermodynamics*. North-Holland: Amsterdam, 1962.

[*237*] Evans, D. J.; Sarman, S., "Equivalence of Thermostatted Nonlinear Responses". *Physical Review E*, **48** (1), 65 (1993).

[*238*] Evans, D. J.; Morriss, G. P., "Nonlinear-Response Theory for Steady Planar Couette-Flow". *Physical Review A*, **30** (3), 1528 (1984).

[*239*] Ladd, A. J. C., "Equations of Motion for Non-Equilibrium Molecular-Dynamics Simulations of Viscous-Flow in Molecular Fluids". *Molecular Physics*, **53** (2), 459 (1984).

[*240*] Hoover, W. G.; Evans, D. J.; Hickman, R. B.; Ladd, A. J. C.; Ashurst, W. T.; Moran, B., "Lennard-Jones Triple-Point Bulk and Shear Viscosities - Green-Kubo Theory, Hamiltonian-Mechanics, and Non-Equilibrium Molecular-Dynamics". *Physical Review A*, **22** (4), 1690 (1980).

[*241*] Hoover, W. G.; Hoover, C. G.; Petravic, J., "Simulation of two- and three-dimensional dense-fluid shear flows via nonequilibrium molecular dynamics: Comparison of time-and-space-averaged stresses from homogeneous Doll's and Sllod shear algorithms with those from boundary-driven shear". *Physical Review E*, **78** (4), (2008).

[*242*] Lees, A. W.; Edwards, S. F., "Computer Study of Transport Processes under Extreme Conditions". *Journal of Physics Part C Solid State Physics*, **5** (15), 1921 (1972).

[*243*] Evans, D. J.; Morriss, G. P., "Transient-Time-Correlation Functions and the Rheology of Fluids". *Physical Review A*, **38** (8), 4142 (1988).

[*244*] Morriss, G. P.; Evans, D. J., "Isothermal Response Theory". *Molecular Physics*, **54** (3), 629 (1985).

[*245*] Morriss, G. P.; Evans, D. J., "Application of Transient Correlation-Functions to Shear-Flow Far from Equilibrium". *Physical Review A*, **35** (2), 792 (1987).

[*246*] Scott, A. P.; Radom, L., "Harmonic vibrational frequencies: An evaluation of Hartree-Fock, Moller-Plesset, quadratic configuration interaction, density functional theory, and semiempirical scale factors". *Journal of Physical Chemistry*, **100** (41), 16502 (1996).

[*247*] Frisch, Æ., *Essential System Administration*. 3rd ed. O'Reilly & Associates: Sebastopol, CA, 2002.

[*248*] Liu, C.; Albitz, P., *DNS and BIND*. 5th ed. O'Reilly & Associates: Sebastopol, CA, 2006.

[*249*] Stern, H.; Meisler, M.; Labiaga, R., *Managing NFS and NIS*. 2nd ed. O'Reilly & Associates: Sebastopol, CA, 2001.